OPTIMISATION OF THE PROCESS PARAMETERS FOR PRODUCTION OF MAGNESIUM OXIDE FROM IKPESHI DOLOMITE ORE IN EDO STATE, NIGERIA

BY

ARE, Comfort Temitope
PhD/SPS/2017/908

DEPARTMENT OF CHEMISTRY

FEDERAL UNIVERSITY OF TECHNOLOGY, MINNA NIGERIA

NOVEMBER, 2023

OPTIMISATION OF THE PROCESS PARAMETERS FOR PRODUCTION OF MAGNESIUM OXIDE FROM IKPESHI DOLOMITE ORE IN EDO STATE, NIGERIA

BY

ARE, Comfort Temitope
PhD/SPS/ 2017/908

A THESIS SUBMITTED TO THE POSTGRADUATE SCHOOL
FEDERAL UNIVERSITY OF TECHNOLOGY, MINNA, NIGERIA
IN PARTIAL FULFILMENT OF THE REQUIREMENTS FOR THE AWARD OF THE DEGREE OF DOCTOR OF PHILOSOPHY (PhD) IN ANALYTICAL CHEMISTRY

NOVEMBER, 2023

DECLARATION

I hereby declare that this thesis titled: "**Optimisation of the Process Parameters for Production of Magnesium Oxide from Ikpeshi Dolomite Ore in Edo State, Nigeria."** is a collection of my original work and it has not been presented for any other qualification anywhere. Information from other sources (published or unpublished) has been duly acknowledged.

ARE, Comfort Temitope
PhD/SPS/2017/908
FEDERAL UNIVERSITY OF TECHNOLOGY,
MINNA, NIGERIA

_____
Signature & Date

CERTIFICATION

The thesis titled: "**Optimisation of the Process Parameters for Production of Magnesium oxide from Ikpeshi Dolomite Ore in Edo State, Nigeria."** by: ARE, Comfort Temitope (PhD/SPS/2017/908) meets the regulations governing the award of the degree of PhD of the Federal University of Technology, Minna and it is approved for its contribution to scientific knowledge and literary presentation.

PROF. J. YISA
MAJOR SUPERVISOR _____ Signature & Date

PROF. M.A.T SULEIMAN
CO-SUPERVISOR _____ Signature & Date

DR. M. AUTA
CO-SUPERVISOR _____ Signature & Date

DR. (MRS.) L. A. FADIPE
HEAD OF DEPARTMENT _____ Signature & Date

PROF. M. JIYA
DEAN, SCHOOL OF PHSICAL SCIENCES, _____ Signature & Date

ENGR. O. K. ABUBAKRE
DEAN, POSTGRADUATE SCHOOL _____ Signature & Date

DEDICATION

This thesis is dedicated to the Almighty God, the Creator of heaven and earth, who spared my life and made my dreams to come to reality. All glory and honour be to his name.

ACKNOWLEDGEMENTS

I give all glory to God for sparing my life, for His divine assistance, provision, guidance, and protection over my life, and for the grace bestowed upon me to complete this program successfully. All honor and glory to Your Sacred Name.

Special appreciation to my major supervisor, Prof. J.Yisa, for giving me the privilege of working with him at such a crucial time in my career. Sir, your guidance, teaching, and encouragement played a vital role in the completion of this research and the composition of this thesis. May the Lord bless and promote you. My appreciation also goes to my co-supervisor, Prof. M.A.T. Suleiman and Dr. M. Auta, for their guidance, teaching and encouragement, which played a vital role in the completion of this research and the composition of this thesis advice and their contributions in the course of this research. The Lord will prosper you in all that you do.

I would like to appreciate the Head of Department, Dr. (Mrs.) L. A. Fadipe, for her meaningful contributions during my seminar presentation and her words of encouragement throughout this program. To my able internal examiner, Dr. S.O Salihu, thank you for taking the pain to read through my thesis, page by page, within a short period of time, God will elevate you. To the postgraduate coordinator, Dr. (Mrs). R.A. Lafia- Araga, thank you for giving me the opportunity to do my seminar presentation within the stipulated time frame; indeed, you are a mother. Thanks to all the Departmental Lecturers and laboratory Technologist at FUT Minna. God will bless you all.

Now to my one and only loving, darling, and caring sweetheart (*Ademi),* Mr. Joseph Isaac Adekunle, thank you for giving me the privilege to upgrade my knowledge. Your words of encouragement, prayers, sacrificial love and support, we shall live to enjoy the fruits together in Jesus name. Indeed, you are special and a God send, and I love you, sir. I thank my son,

Miracle, for his patience and understanding while Mummy was away from home. God will continue to bless and preserve you all. My sincere appreciation also goes to my beloved parents, Mr. and Mrs. Are for their prayers, encouragement, and sacrificial giving; may God bless and keep you so that you can enjoy the fruits of your labour. My sincere appreciation goes to the family of Mr. Olundu Kolade Raphael for their magnanimous contribution and encouragement in the course of the program. I also appreciate my wonderful siblings (Mr. Femi, Tosin, and Seun) for their concern and prayers. May the good Lord bless you all.

Many thanks to Dr. Yahaya A., (H.O.D Chemistry Department Prince Abubakar Audu University (PAAU), Anyigba), Dr. Larayetan R., and Mrs. Idowu L., Mr. Ochalla A. of Chemistry Department, PAAU), Dr. Gideon Y.B of the (Department of Earth Sciences PAAU) for their support and encouragement, may the good Lord reward you. My sincere gratitude goes to Mr. Umoru .T of the Department of Geology, Federal Polytechnic Auchi and Mr Segun Abifarin for their assistance on the location of the mining site and geological mapping of the mining site. Finally, I would like to thank all those that have contributed to the success of my postgraduate study in one way or the other. My God will always be there for you.

ABSTRACT

The optimization study for the production of magnesium oxide (MgO) from dolomite via the nitric acid route (NAR) and the hydrochloric-perchloric acid System route (HPASR) was investigated. Dissolution of dolomite ore in nitric acid (HNO_3) and in hydrochloric acid (HCl)-perchloric acid ($HClO_4$) systems was optimised using the Box-Behnken methodology. The effect of reaction temperature ranging from 30 to 70 ^oC, acid concentration ranging from 0.5 to 2.5 $moldm^{-3}$, and reaction time ranging from 20 to 60 min, on leaching efficiency was investigated, while stirring speed was kept constant at 250 revolution per minute (rpm). An optimum leaching efficiency of 99.16 % was predicted while 98.6 % was validated for the dissolution in Nitric acid at a leaching temperature of 55.3 ^oC, an acid concentration of 2.2 $moldm^{-3}$, and a leaching time of 20 minutes. Second-order quadratic polynomial regression model which established the relationship between the dissolution efficiency of dolomite and the process variables was developed based on the statistical analysis of the data. The model was sufficient enough to predict the dissolution of dolomite in HNO_3 with a 0.977 coefficient of determination and a desirability of 1. For dolomite leaching in an HCl-$HClO_4$ system, a dissolution efficiency of 99.7 % was predicted at a temperature of 57 ^oC, a reaction time of 20 Mins, and an acid concentration of 2.03 $moldm^{-3}$, while 98.39 % was validated experimentally. A significant model equation with a Prov>F of < 0.0001 was developed, the effect of acid concentration, leaching temperature, leaching time, and interactive effect of leaching temperature and acid concentration; interactive effects of temperature and time, all have significant effects on the leaching process, while the interactive effects of acid concentration and leaching time have no significant effect on the leaching process. The study of the reaction kinetics and mechanism of the reaction between dolomite and HNO_3 as well as between dolomite and HCl-$HClO_4$ was also investigated. The fraction of dolomite that reacted in HNO_3 and in HCl-$HClO_4$ increased as the temperature and concentration increased. The highest fraction of 0.995 of dolomite dissolution in HNO_3 was achieved at 50 Mins reaction time, acid concentration of 2.5 $moldm^{-3}$, agitation speed of 250 revolution per minutes (rpm) and reaction temperature of 55 ^oC while the highest fraction of 0.995 of dolomite dissolution in HCl-$HClO_4$ was achieved at 40 Mins reaction time, acid concentration of 2.2 M, agitation speed of 250 revolution per minutes (rpm) and reaction temperature of 60 ^oC. The reaction mechanism followed the surface chemical reaction control mechanism and it is first order with a hydrogen ion concentration and activation energy of 16.68 $KJmol^{-1}$. Central Composite Design was used to optimize $Mg(OH)_2$ precipitation from pregnant solution in both NAR and HPASR. For NAR, the concentration of the calcium hydroxide $Ca(OH)_2$ (precipitant) and precipitation time were studied between 24% to 34 % and 2 minutes to 8 minutes respectively, while for HPASR, the concentration of the $Ca(OH)_2$ (precipitant) and precipitation time were studied between 32% to 39 % and 2 minutes to 8 minutes respectively. For NAR, 98.5 % $Mg(OH)_2$ precipitation was predicted to be optimal, while 98.1% was validated with a desirability of 0.93 at the optimum conditions of 34 % concentration of calcium hydroxide and time of 8 minutes. For HPASR, 97.63 % $Mg(OH)_2$ precipitation was predicted as optimal, and 97.1 % was validated at the optimum conditions of 35.3 % concentration of calcium hydroxide and 5 minutes with a desirability of 0.93.The mineral phase of the synthesized MgO that was obtained from calcination process in this study from both NAR and HPASR were confirmed by XRD analysis with most prominent peaks of periclase. From the XRF results, the highest MgO of 56.8 % and 72.72 % were achieved from HPASR and NAR respectively. NAR is more preferred for MgO production. Further study should explore the use of full factorial design for the optimization process.

TABLE OF CONTENT

CHAPTER TWO

CHAPTER FIVE

LIST OF TABLES

LIST OF FIGURES

LIST OF PLATES

LIST OF APPENDICES

ABBREVIATIONS, GLOSSARIES AND SYMBOLS

Abbreviations	Descriptions
HNO_3	Nitric acid
HCl	Hydrochloric acid
$HClO_4$	Perchloric acid
XRD	X-Ray Diffraction
XRF	X-ray Fluorescence
EDX	Energy Dispersive X-ray
CaO	Calcium Oxide
SEM	Scanning Electron Microscopy
RSM	Response Surface Methodology
H_2O	Water
NAR	Nitric acid Route
HPASR	Hydrochloric perchloric acid system route
FTIR	Fourier transform infrared
CCD	Central composite design
RPM	Revolution per minutes
SiO2	Silica
MgO	Magnesium oxide
$Mg(OH)_2$	Magnesium hydroxide
PPT	Precipitate
AAS	Atomic Absorption spectrometry
SCM	Shrinking Core Model

RP	Residue from Hydrochloric-Perchloric acid route
RN	Residue from Nitric route

CHAPTER ONE

1.0 INTRODUCTION

1.1 Background to the Study

Dolomite is a double carbonate mineral known as calcium magnesium carbonate ($CaCO_3.MgCO_3$) (Priya 2014; Sivrikaya, 2018) with a variable amount of impurities which determined its industrial applications (Sunil *et al.,* 2013). These impurities are also responsible for it appearance in various colours such as white, pink, green, gray, brown, and black (Brady *et al.,* 2002). The impurities include iron-dominant ankerite and the manganese-dominant kutnohorite, silica, alumina, lead, sulphur, and zinc (Kaufmann, 2013; Jakic *et al.,* 2016; Sivrikaya, 2018). The crystals yellow-to-brown color is caused by the little quantity of iron in the structure. When a French geologist named Deodat Gratet De Dolomieu noticed exposure in the dolomite Alps of Northern Italy, Saussare, N. T. gave the mineral its original name, "dolomite," in his honor in 1792 (Robert *et al.,* 1990). Dolomite and limestone are both sedimentary rocks that formed in warm, shallow marine settings where calcium carbonate mud accumulated as coral pieces, feces, check debris, and carbonate precipitate (Sivrikaya, 2018).

There are currently many uses of dolomite as refractories in the steel industry in some nations including China, England, France, and India (Moorkah *et al.,* 2005). Due to its chemical makeup, it is utilized for numerous industrial and agricultural purposes, such as steel and iron production, refractory construction, production of glass, as filler for paints, rubber, and plastics, and as a soil conditioner/neutralizer in agriculture (Mahmut *et al.,* 2016). Also, dolomite is a good source of magnesium oxide (MgO) (Lingling and Deng, 2005 Galai *et al.,* 2007: Beruto *et al.*, 2003; Yildirim, 2008; Samtani *et al.,* 2001; Li *et al.*, 2013) and the chemical industries considered dolomite to be the best sources of magnesium salt due to the

high content of MgO in it (Jakic *et al.,* 2016). Beneficiation of minerals is a process of improving the inherent properties and quality of ore to maximize its utility (Olokesusi, 2010). Separation is achieved by utilizing some specific variation in chemical or physical properties between valuable and gangue minerals in the ore (Sirajo, 2008). Beneficiation processes may be classified into (i) Physical separation process: Magnetic, gravity, froth flotation (fine particle separation method), high tension or electrostatic and sorting, and optical. (ii) Chemical separation process: Leaching, solvent extraction, precipitation, autoclaving, carbon adsorption, electro-winning, chlorination. (iii) Biological separation: Bacterial leaching. (iv) Pyro-metallurgical separation: Thermal treatments, which may include roasting, calcination, pelletizing, and sintering.

The dissolution of dolomite in a solvent is an important unit process that leads to the production of MgO. To obtain a high percentage separation of magnesia from dolomite, optimization of the dissolution process is necessary. (Solihin *et al.*, 2018).

The mineral periclase, also known as magnesium oxide or magnesia, is a rare occurrence in nature and is most typically seen as clusters of crystals in marble. Typically, magnesium oxide is synthesised from magnesium hydroxide [$Mg(OH)_2$] derived from brine or by calcining the mineral magnesite ($MgCO_3$) (Ding *et al.*, 2001 and Jakic *et al.*, 2016). Also, it can be produced through the thermal hydrolysis (pyrohydrolysis) of, magnesium sulphide (MgS), hydrated magnesium chloride ($MgCl_2$), magnesium sulphate ($MgSO_4$), and basic carbonate (Duhaime *et al.,* 2002 and Ding *et al.,* 2001). One of these carbonates is a sedimentary carbonate rock name dolostone mostly composed of magnesium and calcium carbonates. Among the industrial uses of magnesium oxide (from as magnesium hydroxide) are the treatment of wastewater and sewage (such as the precipitation of heavy metals and silica), the use of the compound as a catalyst in the production of biodiesel, the removal of

sulphur trioxide and sulphur dioxide from industrial flue gases. Magnesium oxide is also employed in some metallurgical processes. For instance, in the synthesis of lateritic nickel, caustic-calcined or lightly burned magnesia is used in crude nickel-cobalt hydroxide precipitating from the H_2SO_4 leach liquid. The primary application of refractory grade magnesia is in the manufacturing of direct reduction iron and steel (Aral, *et al.*, 2004).

Considering the various industrial application of MgO, it then becomes necessary to further research into the improvement of the synthesis of Magnesium oxide from locally sourced dolomite. This study will help to establish its chemical separation by acid leaching followed by precipitation of MgO from dolomite ore. The characterisation in this study will be carried out by chemical methods such as Fourier transform infrared (FTIR), X-Ray Fluorescence (XRF), X-Ray Diffraction (XRD), Energy Dispersive X-ray Fluorescence (EDXRF), and Scanning Electron Microscope (SEM). This approach to the MgO production process was carefully chosen to cater for the problem of high energy consumption and the environmental problem associated with the current methods of electrolysis and silicothermic process of MgO production as well as overcoming the over-dependence of Nigerians on imported MgO.

1.2 Statement of the Resarch Problem

Despite having extensive deposits of dolomite that can be used for the production of MgO in Nigeria. This country continues to depend on external sources to meet its local demand (Trend Economy, 2022). The silicothermic process and molten salt electrolysis used to beneficiate dolomites for the recovery of valuables, are expensive and extremely energy-intensive. The pyrohydrolysis technique, a well-known way to extract magnesium oxide from dolostone, is linked to the liberation of hydrochloride gas and has destructive effects, hence it is not an environmentally friendly procedure (Yildrim *et al.*, 2010). Seawater is currently

the main source of commercial magnesium oxide. Boron in seawater occurs as the non-dissociated orthoborate acid (H_3BO_3) and the borate ion ($H_2BO_3^{2-}$ and BO_3^{2-}). At a high temperature, this boron is adsorbed onto the produced MgO, lowering both its purity and strength (Matrinac *et al.*, 2004; Fraga, 2020).

1.3 Justification of the Study

The optimization of the process parameters for the production of magnesium oxide (MgO) from Ikpeshi dolomite ore via nitric acid and hydrochloric-perchloric acid system does not exist in literarture to the best of our knownledge. The production of MgO from dolomite in this study will help in meeting its growing global demands in cement, agricultural, iron and steel, wastewater treatment, and other industrial sectors. Production of MgO from Nigerian dolomite ore will minimize the cost of importation of refractories and increase the gross domestic product of the country. Leaching via acid medium and precipitation will bring about a low energy usage route as well as a reduced cost of production. The separation and purification method of magnesium oxide from dolomite in this study is environmentally friendly and corrosion-free compared to the silicothermic process, pyrohydrolysis techniques been used. Sourcing from dolomite ore will also help to achieve high purity MgO free from boron.

1.4 Aim and Objectives of the Study

The study is aimed at optimizing the production process parameters of MgO from dolomite ore obtained from Ipkeshi mines, Edo State, Nigeria . The objectives of the research are:

i. Characterisation of dolomite ores from Ipkeshi mines, Edo State
ii. Optimization of the leaching conditions such as reaction temperature, time, and acid concentration HNO_3 and HCl-$HClO_4$ respectively

iii. Evaluation of the kinetics of dolomite ores in HNO_3 and HCl-$HClO_4$ at the optimum points

iv. Optimization of $Mg(OH)_2$ precipitation parameters such as time and concentration of the precipitant ($Ca(OH)_2$ from the leachate

v. Production of MgO from calcination of $Mg(OH)_2$ and characterisation of the MgO produced.

1.5 Scope of the Study

The scope of this research is restricted to the use of dolomite from Ipkeshi mines, Edo State, Nigeria as starting material for the production of magnesium oxide (MgO). Each of the stages was optimized to achieve the best operating conditions for the production process. The leaching kinetics of dolomite in the hydrochloric acid-perchloric acid system and nitric acid, precipitation of magnesium hydroxide and magnesium oxide synthesis via calcination process were also studied.

CHAPTER TWO

2.0 LITERATURE REVIEW

2.1 Occurrence and Sources of Dolomite.

Dolomite is considered to be formed from calcite and aragonite (alteration of limestone) by the action of magnesium-rich solution from marine or hydrothermal sources (Chang *et al.*, 1998). The process is called diagenesis and believed that most of the extensive dolomite beds were beneath the sea (Chang *et al.,* 1998) Organo-genic dolomite forms in deep seas where organic matter content is high.

The dolomite formation also occurs in supersaturated saline conditions, as found in some lagoons in Brazil, Baffin Bay (Texas, USA), and Kuwait. (Chang *et al.,* 1998). Primary dolomite is found in the tidal flats of Andros Island, Bahamas, Sugarloaf Key, Florida, USA, and Bonaire, Netherlands Antilles. Dolomite also occurs in hydrothermal veins along with fluorite, barite, and quart. In igneous rocks dolomite mainly occurs in carbonatites with calcite, ankerite, and siderite. For siliceous dolomites, a progressive series of reactions occur with a rise in temperature, from which talc, tremolite, forsterite, disposed e.t.c are formed. The carbonate sediment dolomitization is possible with normal seawater without modification (Kozehevnikov *et al.*, 1973). A small percentage of dolomite can be found in some limestones. However, this does not make it to be categorized as a dolomite rock before a rock can be termed dolomite, it must have a minimum of 15 % $MgCO_3$ (Akande and Agbalajobi, 2013).

2.2 Dolomite Deposit Formation

Based on the mode of formation, dolomite can be classified into two groups: primary and secondary dolomite (Pichler and Humphery, 2001; Amalan, 2016).

2.2.1 Primary Dolomite Deposit

Primary dolomite is formed by direct precipitation of particles from seawater or other aqueous solution between temperature windows of 20 -35 ^{o}C and this does not involve the dissolution of $CaCO_3$ (Chakrabarti *et al.,* 2011), not all precipitation falls into primary classification. Dolostones are primary in origin, meaning that they did not originate as dolostone but rather as calcite and aragonite, which were changed into dolomite by the passage of magnesium-rich water through limestone. Dolomite, which precipitates straight from a fluid rather than developing as an alteration of an already-existing mineral, is the principal exception to this rule (Department of Geology Minnesota Mineral (DGMM), 2018).

2.2.2 Secondary Dolomite Deposit

Dolomitization, the conversion of $CaCO_3$ to $CaMg(CO_3)_2$, is the process by which secondary dolomite is formed. When Mg^{2+} ions substitute Ca^{2+} ions in the mineral calcite, the carbonate mineral dolomite is created as a result of a geological process. It can also be referred to as the dissolution of the calcite process involving the transformation of limestone into dolomite as well as its precipitation. It is common for this mineral change into dolomite to take place due to the loss of water (Whitaker *et al.,* 2010; Amlan, 2016). Recrystallization occurs frequently during the dolomitization process.

$$2CaCO_3 + Mg^{2+} \rightarrow CaMg(CO_3)_2 + Ca^{2+} \qquad (2.1)$$

The precursor mineral calcite provides the needed calcium ion (Ca^{2+}) whereas magnesium ion (Mg^{2+}) and the carbonate ions (CO_3^{2-}) are provided by the dolomitizing fluid; this results in a significant amount of recrystallization during dolomitization dissolution. Equation 2.1 is a representation of the stoichiometric equation involved in the dolomitization process (Whitetaker *et al.,* 2010; Rahimi *et al.,* 2016; Anakoli, 2020).

Reactant surface area, Low Ca:Mg ratio in solution, reactant mineralogy, a high temperature which indicates the thermal stability of inhibitors like sulphate, and other specific parameters are all necessary for dolomitization (Whitaker *et al.,* 2010 and Amlan 2016). Dolomitization can occur in salty settings above the thermodynamic and kinetic saturation for dolomite if the kinetic inhibitors and high temperatures can coexist. This type of environment includes areas where seawater and freshwater mingle, subtidal environments that range from being normally salty to being hyper-salty, and schizohaline settings (Whitaker *et al.,* 2010).

2.3 Hydrothermal Vein Dolomite Deposit

In carbonate rocks, dolomite can form as a pore-filling mineral or in hydrothermal veins. In carbonate limestone and dolostone rocks with hydrothermal veins, dolomite crystals also border or fill pores. Dolomite vein deposits can be found alongside quartz and other vein minerals like calcite ($CaMgCO_3$), magnesite ($MgCO_3$), fluorite (CaF_2), siderite ($FeCO_3$), and sphalerite (ZnS), as well as with metallic ore minerals such galena (PbS), pyrite (FeS_2), and chalcopyrite ($CuFeS_2$) (Hips and Argyelan 2007; Mubashir *et al.,* 2018).

2.4 Occurrence of Dolomite in the World

The main dolomite resources can be found in the United States, Ontario (Canada), Pamplona (Spain), Mexico, and countries in South America like Brazil and Argentina. Primary dolomite is found in the tidal flats of Andros Island, Bahamas, Sugarloaf Key, Florida, USA, and Bonaire, Netherlands Antilles (Sunil *et al*., 2013). Dolomite of the lower cretaceous Edwards formation in Texas, USA, and Zeechstein dolomite of Northwest Europe, and dolomite in the Northern Michigan Reef Belt, USA are associated with evaporates. They are formed from evaporation and sulphate precipitation of Mg-rich fluids from lagoon water or tidal flat pore waters which further seep into the carbonate sediment below and initiate dolomitization (Graf

and Goldsmith, 1956). The most prominent European occurrence are Navarra, Eugu, Castilla Quarry, Setiles in Spain, Italy, Switzerland, Syria, and Austria. In Africa deposits have been discovered in Kolwezi, Katanga (Shaba), Congo (Zaire), and BouAzzer, Morocco, Tsumeb, and Namibia. In Asia, the major deposits are found in China, the Philippines, Indonesia, Kyrgyzstan, Azerbaijan, Uzbekistan, and Oman (Warren, 2000). Figure 2.2 maps out the various locations of dolomite in the World.

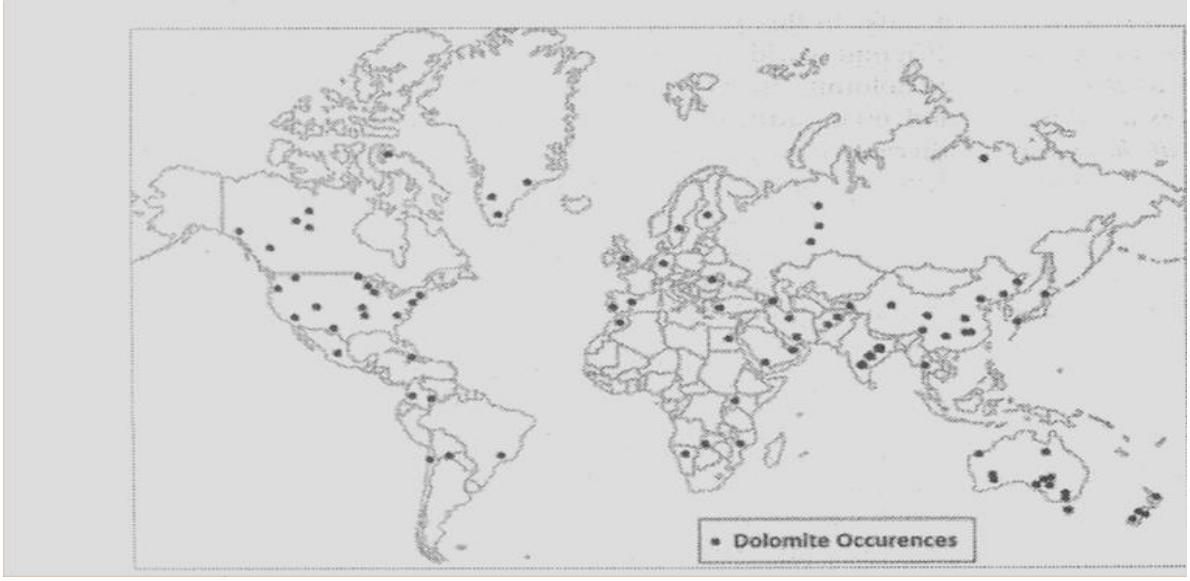

Figure 2.1: Occurrence of dolomite in the world (Sunil *et al.,* 2013)

2.5 World Production and Consumption of Dolomite

The world's major producers of dolomite are China with about 160 million tones, India with 7533.1 million tones, Spain with 1.5 million tones, and Bhutan with 1.2 million tones. Other major producers are Germany, Russia, and Brazil (Hamilton minerals and Metals Ltd's 2013).

2.6 Occurrence of Dolomite in Nigeria

By 1994, few solid minerals were known from the early days of independence and the late colonial era. To diversify the economy of the country, the Nigerian government advocated

for a private sector-led economic revitalization program in the industry, agriculture, and solid minerals. It was decided to create the Ministry of Solid Mineral Development (MSMD). Geological survey improvements were finished in 1987. 13 of these minerals are currently being mined, processed, and sold. They consist of iron minerals, coal, kaolin, barites, limestone, dolomite, feldspar, glass sand, and gemstones. There are also some small amounts of the gold present (Akande and Agbalajobi, 2013). Despite being in demand, the remaining 21 minerals remain unexplored (MSMD, 2003).

Historically, the production of dolomite in Nigeria could be traced back to 1960 when it was first found in Kogi State (Lokoja) and secondly in Oyo State (Igbeti marble development). Other locations where dolomite was also discovered are Kwara State (Oreke in Ifelodun Local Government Area), Alaguntan in Oyo State, and Ikpesi in Edo State (Moorkah and Abolarin, 2005; Akanji *et al.,* 2013). Figure 2.1 and Table 2.1 is showing the various locations of dolomite in Nigeria.

Table 2.1: Location of Dolomite in Nigeria

Location	**Local Government**	**State**
Oreke	Ifelodun	Kwara
Alagutan	Orile	Oyo
Igbeti	Olorunsogo	Oyo
Ikpeshi	Akoko-Edo	Edo
Akoko	Akoko-Edo	Edo

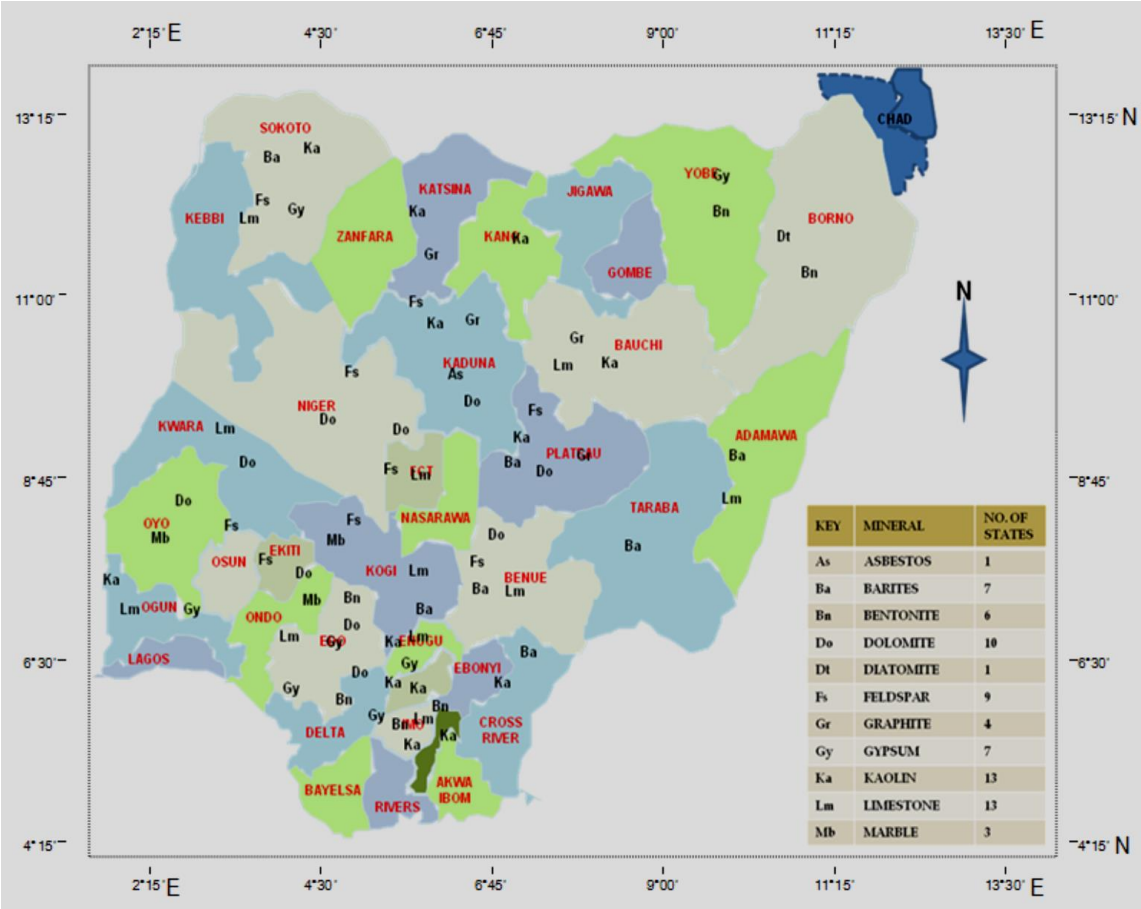

Figure 2.2: Some Industrial Minerals in Nigeria (Dolomite Denoted by Do (MSMD, 2003)

2.7 Chemistry of Dolomite

Dolomite has the chemical formula $CaCO_3.MgCO_3$, it's usually found in combination with other minerals (Sunil *et al.*, 2013), and is rare to find it pure. The chemistry of dolomite is affected by mineral contamination, such as Iron, silica, alumina, lead, and zinc which also affect its refractoriness (Brady *et al.*, 2002). Dolomite is a mineral that forms in metamorphic rocks and is frequently found in contact with or locally metamorphosed with magnesian or dolomitic limestones, where it may re-crystallize to produce a dolomitic marble. Dolomite may fracture in two stages at a higher level of metamorphism (Deer *et al.*, 1992). Causing

periclase (MgO) and later brucite ($Mg(OH)_2$ to form, resulting in the rock types pencatite or Predazzite, which contains more calcite. These are illustrated by equation 2.2 and 2.3

$$CaMg(CO_3)_2 \rightarrow CaCO_3 + MgO + CO_2 \qquad (2.2)$$

$$MgO + H_2O \rightarrow Mg(OH)_2 \qquad (2.3)$$

From the dolomite two dimensional structure in Figure 2.1, the carbonate sub-structure shows that carbon and oxygen are sharing electron which account for the double and single valence bond existing between oxygen and carbon.

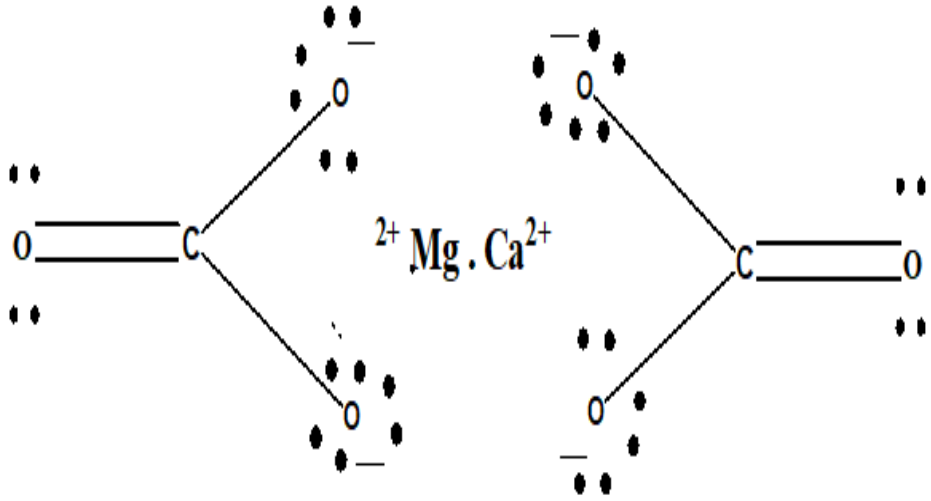

Figure 2.3: Structure of Dolomite (Solihin *et al.*, 2018)

The structure in Figure 2.3 shows that one carbon atom is singly bonded to two atoms of oxygen and shares a double bond with another oxygen atom. Each of the oxygen shares a single covalent bond with carbon as an electron (negative charge) that makes it form an ionic bond with the positive charge of calcium and magnesium to form a dolomite molecule (Solihin *et al.*, 2018)

2.8 Dolomite Mineralogy

The structure of dolomite was first established by Wyckoff and Merwin. Dolomite exhibits trigonal rhombohedral crystallization (Sunil *et al.,* 2013). Layers of magnesium and calcium alternate in a highly organized pattern along the axis of dolomite, defining its structure. During initial crystallization at temperatures below 100 ^{o}C, dolomites with such high cation orders cannot form by direct precipitation (Zvir *et al*., 2021).

2.9 Dolomite Associate Mineral

Some of the minerals associated with dolomite are Fluorite, barite, calcite, siderite, quartz, metal sulphide (hydrothermal vein), celestine, gypsum (Sedimentary) talc, serpentine, magnesite, magnetite, diopside, tremolite, forsterite, wollastonite and aragonite (metamorphic) ankerite, siderite, apatite (carbonatites) (Chang, 1998).

2.9.1 Quartz

Quartz is typically white or clear, with slight impurities which can give it different colors. Quartz is the source of most of our society's glass from windowpanes and crystal goblets to eyeglasses and cathedral stained glass (DGMM, 2018; Gonidanga *et al.,* 2019).

2.9.2 Fluorite

When fluorite is pure, it is colorless or transparent, however, color can vary greatly due to minute chemical impurities. While smelting metallic ores, fluorite is employed as a flux because it melts easily. Flux is a substance that aids in cleaning ore of impurities while it is processed into metal (DGMM, 2018)

2.9.3 Gypsum ($CaSO_4.H_2O$)

Hydrated calcium sulphate is gypsum. Crystals are often clear, transparent to translucent in large form, and are typically white, colorless, or gray. Gypsum is frequently used for sculpture and casting even though it might seem red when impurities are present. This is because it easily loses the water necessary for crystallization (DGMM, 2018).

2.9.4 Magnetite (Fe_2O_3)

Iron oxide is magnetite. It is typically magnetic, opaque, and black. It is formed when magma cools down slowly for crystals to form and separate out of the magma. Usually, these crystals are dodecahedrons (eight-sided to twelve-sided shapes) or octahedrons. Steel utilized nearly universally in the physical infrastructure of modern society comes from deposits of magnetite and hematite iron (DGMM, 2018).

2.9.5 Calcite and aragonite

A polymorph is a mineral that has the same chemical make-up but a slightly different crystal structure, such as calcite ($CaCO_3$) and aragonite. Both minerals are so similar to one another that they can coexist. Calcite occurs with dolomite and other minerals in the sedimentary environment (DGMM, 2018).

2.10 Physical and Chemical Properties of Dolomite

Dolomite can be colourless, white, pink, green, gray, brown, and black. One of the major pertinent properties of dolomite is that they have good flow properties when they are abundant in water. Dolomite has 3 orders of perfect. When the dolomite is fine-grained it may not be obvious. Conversely, for coarsely crystal-like dolomite, the angle of cleavage is easily seen using a hand lens. Dolostone has a Mohs, hardness of 3.5 to 4, and is occasionally

found in rhombohedral crystals with curved faces. Dolomite also has a good bulk density which enhances its abrasion resistance and slag resistance (Moorkah and Abolarin, 2005). These properties are shown in Table 2.2. The porosity of dolomite decreased with increased temperature which makes it suitable for use in steel-making furnaces and converters. Dolomite has the chemical formula $CaCO_3.MgCO_3$ and the summary of their properties are listed below:

Table 2.2: Physical Properties of Dolomite

Parameters	**Properties**
Colour	Brown, black, green, pink, colorless, and white
Luster	Pearly, Vitreouss
Cleavage	Perfect, rhombohedral, 3 –direction
Specific gravity	2.8-2.9
Mohs hardness	3.5-4.0
Crystal system	Hexagonal
Optical properties	Transparent to transparent

(Source: Department of Geology, University of Minnesota, 2021)

2.11 Dolomite Crystallography

Rhombohedral carbonate dolomite is made up of layers of carbonate anions and cations that alternate. There are Ca and Mg ions grouped with CO_3^{2-} in the crystal structure (Gregg *et al.,* 2015, Kaczmarek *et al.,* 2017).

2.12 Typical Uses and Industrial Applications of Dolomite

The economic importance of dolomite can be credited to its distinct mineralogical, chemical, and physical properties (Akande and Agbalajobi, 2013). The various uses and applications of dolomite are listed below:

2.12.1 Glass making

In the glass business, premium dolomites with little iron content are used (Hycnar *et al.*, 2020). Dolomite used to make glass is known for its uniformity and cleanliness. The content of calcium oxide and magnesium oxide shouldn't fluctuate by more than 5 %. Iron, chromium, manganese, vanadium, and lead are the main unwanted impurities that give glass its color and contribute to glass flaws. Commercial colorless glass may have a Fe_2O_3 level of up to 0.25 %, while a Fe_2O_3 content of 0.04 % is required occasionally (Sunil *et al.*, 2013).

2.12.2 Iron and steel making

MgO 18 % (minimum), CaO 29–30 %, and acid-insoluble 6–10 % should all be present in dolomite used in blast furnaces and steel mills. Dolomite of the highest quality is required for fluxing during the melting of steel (Songtao *et al.,* 2017)

2.12.3 Production of lime and magnesium metal

$CaCO_3$ should make up 58-75 % of the dolomite used to make lime, $MgCO_3$ should make up 28-48 %, and the remaining should be less than 3 %. Magnesium metal is extracted using calcined dolomite (Sunil *et al.,* 2013).

2.12.4 Filler/Extender

Dolomite used as fillers must be very pure and free from coloring impurities such as oxides of iron, chromium, and manganese (Sunil *et al.,* 2013).

2.12.5 Ferro-Manganese

The dolomite used in ferromanganese should be hard and fine grains since crystalline dolomite erode the furnace (Sunil *et al.*, 2013).

2.12.6 Agricultural uses

Dolomite powder is a crucial part of many fertilizers and animal feeds used in agriculture. Dolomite is currently in use in Indonesia as a fertilizer and as a source of magnesium for coconut palm trees (Wulandari *et al.*, 2015; Solihin *et al.*, 2018).

2.13 Dolomite Hazards

Dust of dolomite can irritate the eyes on the contact tract, irritate mucus membrane, sneezing and coughing, causing difficulty in breathing, short-term contact with the skin is not poisonous but elongated contact will dehydrate the skin. (Buttrick *et al.*, 2011)

2.13.1 Safety measures in handling of dolomite

The following safety measures should be observed (Lhoist North America, Inc, 2018):

i. approved respirator should be used to eliminate exposure
ii. Exhaust fan should be recommended in controlling any dusting
iii. Protective gloves should be used.
iv. This product's waste can either be dumped on the spot or at a facility that has been given the go-ahead.
v. Avoid storing in wet or moist areas.

2.14 Dolomite Processing

Mineral processing of dolomite can be achieved through the following processes:

2.14.1 Pyrometallurgy

Pyrometallurgy is a method used in the heat treatment of metallurgical ores and minerals to enable the recovery of metal interest (Brent, 2000). This method may be used to produce readymade products such as pure metals and alloys. Examples of metal oxides recovered by the method include oxides of less or reactive elements like iron, aluminium, copper, manganese, magnesium and calcium (Aldalbert, 2005). In the treatment of low-grade ores, it requires large amounts of energy to melt the associated gangues. The energy is usually supplied in form of combustion or electrical heat (Sefiu *et al.*, 2020).

2.14.2 Hydrometallurgy

The hydrometallurgical route is the process of extraction and recovery of metals from their ores using aqueous (water-based) solutions (Boundless, 2016). Leaching, the first stage of the hydrometallurgical process, is the extraction of a metal from ore using a lixiviant or solvent. When the solution has been extracted from the ore, it must undergo some procedures, including concentration and purification, before the desired metal can be extracted (Boundless, 2016). These procedures could involve solvent extraction, distillation, and precipitation, among others (Boundless, 2016).

2.14.3 Electrometallurgy

Electrometallurgy is a technique that involves the use of electricity to refine metals. The most well-known electrometallurgical processes are electrowinning and electrorefining. In essence, an electric current is applied to bring about chemical changes that extract (electrowin) or purify (electrorefining) the ore (Sanni, 2016). To recover metals from an aqueous solution, an electrolysis technique called electrowinning has been used, typically

after the ore has passed one or more hydrometallurgical procedures. The desired metal is plated onto the cathode, while an inert electrical conductor is the anode (Shamsuddin, 2016).

2.15 Beneficiation of Dolomite

Beneficiation is the process of removing unusable component (gangue minerals) from a mineral ore in order to improve on its quality (Haldar, 2020). The beneficiation of dolomite can be achieved through the following means.

2.15.1 Milling

A mill is a machine that uses cutting, crushing, or grinding to reduce solid materials into smaller bits. There are many distinct kinds of mills, and they handle a wide variety of materials. In the past, mills were propelled by human force (such as a hand crank), an animal's labor (such as a horse mill), the wind (a windmill), or water (watermill). Nowadays, electricity is typically used to power them. Dolomite is typically ground under exposure to mechanical forces that overcome the internal bonding forces and trench the structure. Upon grinding, the solid-state is altered, including the grain shape, grain size disposition, and grain size (Balasubramanian, 2017).

The procedure of sorting out, sizing, or grouping aggregate material such as dolomite is sometimes referred to as milling. For instance, the sorting of soil, aggregate material, and rock for land reclamation activities or structural fill. Rock crushing or grinding to generate consistent aggregate size for building applications to create "dry fills" before being used for transportation or structural filling, collective milling operations are also used to separate or eliminate contamination or moisture from soil or aggregate (Rizwan, 2018).

2.15.2 Cementation

Cementation is a form of precipitation that involves the heterogeneous process in which ions are reduced to zero valences at a solid metallic surface. Leach solutions are frequently refined using this method. According to Younesi *et al.* (2006), cementation is used industrially to recover a range of heavy metals, including cadmium. The Merrill-Crowe method, which uses zinc to cement gold, is responsible for a sizable portion of the world's gold production (Walton, 2005).

The cementation method is more efficient, faster, cost-effective in purifying ammonia solution compared to its use for the purification of acid solution (Scholle and Ulmer-Scholle, 2013). Cementation involves the reduction of soluble metal ion impurities to insoluble - and thus separable - metal particles by dissolving valuable metal into the leaching solution. Precipitation under cementation process is used in the recovery of magnesium and calcium hydroxide from dolomite (Younesi *et al.* 2006).

2.15.3 Electrowinning

Leaching, which is a process of pulling metals from their ores in solution, is another name for electrowinning, which is the electrode deposition of the metals from their ores. Similar techniques are used in electroextraction to purge metals of impurities. This method make extensive use of electroplating and are crucial methods for the quick and affordable purification of non-ferrous metals. The finished metals are referred to as electro won (Alexander, 2008).

In electrowinning, the metal is removed as it is being electroplated onto the cathode by passing a current from an inert anode through a leach-liquor solution that contains the metal. In electroextraction, the anodes are made of unrefined, impure metal, which is corroded into

the solution as the current flows through the acidic electrolyte. This allows the electroplating process to deposit refined, pure metal onto the cathodes. Electrowinning process is used in the recovery of magnesium metal from dolomite ore (Yu, 2015).

2.15.4 Flotation and flocculation studies

For beneficiation of fine dolomite tribo-electrostatic separation and froth flotation are viable methods that have been used. A well-known method for separating silica from dolomite particles is flotation. Chen and Tao (2004) studied how magnesite and dolomite's flotability was affected by the surface conversion phenomenon, rate of leaching, surface electrical characteristics, and species distribution solubility. The pH change of the solution to mixing time was used to gauge the dissolving rate. It was determined that managing the solution chemistry improved the flotation process ability to separate magnesite from dolomite.

Using an unconventional, medium-anionic polyacrylamide-based flocculent in borax solutions, the flocculation behavior of two clay rock samples from Kirka and Turkey that had varying amounts of dolomite and clay minerals was investigated. It was found that raising the borax concentration had some positive effects on reducing the flocculated dispersions supernatant turbidity (Hosten and Cirak, 2013).

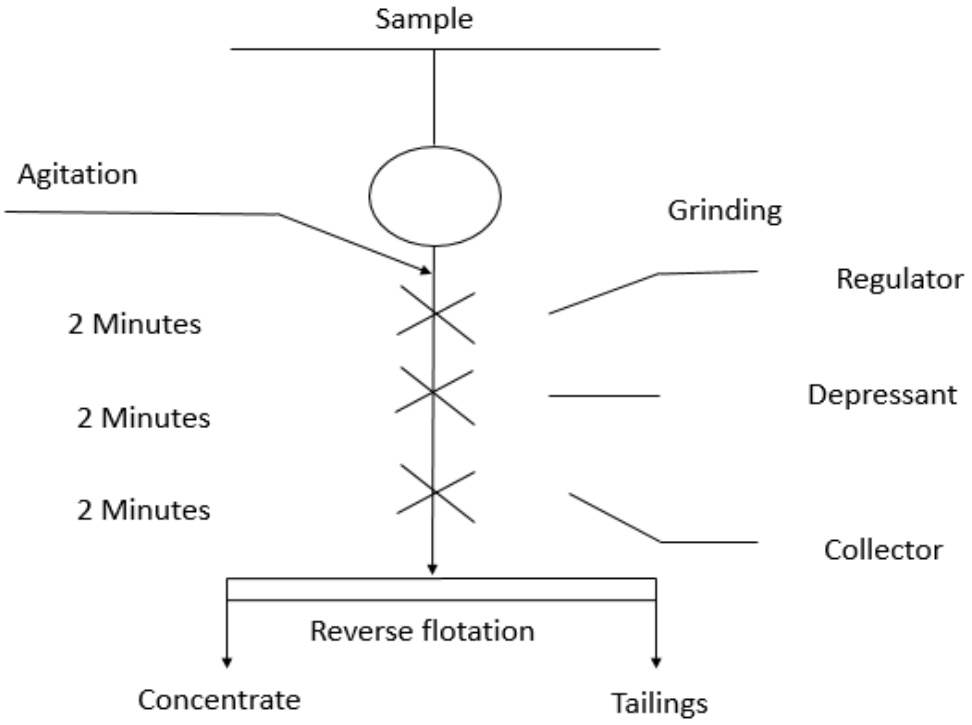

Figure 2.4: Flotation Flow Sheet (Chen and Tao, 2004)

2.16 Leaching Description

Leaching is the term used to describe the process of extracting metal from ore using a lixiviant or solvent. The goal of leaching is to maximize the amount of valuable that can be recovered from the ore (Green and Perry, 2008; Binnemans and Jones, 2017).

The solid phase, which is usually permeable and insoluble, takes the form of membrane with a porous surface or permeable cell walls (Perry and Green, 2008). This increases the surface area available for chemical reactions by allowing the leachant to penetrate the particle.

There are numerous leaching mechanisms, which can take the form of one of two methods depending on the solubility of the solid in a solvent. The second kind of leaching involves chemical processes (Green and Perry, 2008). The rate of leaching is influenced by several

variables. These variables may include, interfacial resistance, the level at which the liquid is moved to the location where the material desired is present, the degree of the material solubility in the reagent, and the rate at which the chemical reaction occurs (Green and Perry, 2008).

At the boundary between various phases, heterogeneous reactions called leaching reactions occurs. Chemical leaching reactions include the interaction of the liquid phase (the leachant), and the solid phase (which is made up of the desired material to be dissolved into a reagent), though all three phases may be involved (Web, 2012). There are a few steps that can be used to condense the leaching process. The lixiviant first diffuses via the diffusion layer to the solid particle's surface (step 1). This reactant adheres to the solid surface (step 2), where the solid and leachant undergo a chemical reaction to produce the product (step 3). The next process is for the product to desorb from the solid surface (step 4), moves from the solid surface through the diffusion layer (step 5), and then dissolve in the solvent in the immediate vicinity (Web, 2012). Figure 2.5 displays a diagram of the leaching procedure.

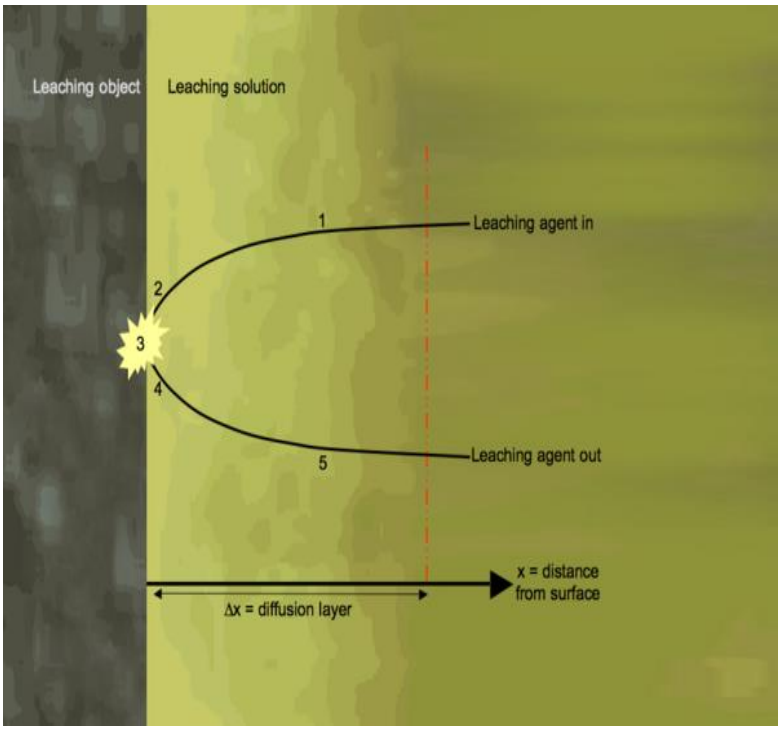

Figure 2.5: Schematic Representation of Stages in the Leaching Process (Web, 2012)

Equation (2.4) which is the mathematical expression of Fick's law used to to describe the diffusion rate in a solution:

$$N = \frac{dn}{dt} = -A.D.\frac{dC}{dx} \tag{2.4}$$

A is the responding particle's surface area, D is the diffusivity constant, and dC/dx is the concentration change in equation (1). The diffusion layer's thickness is influenced by the concentration gradient. So, it can be said that each of these elements will have an impact on how quickly leaching occurs (Web, 2012).

2.16.1 Factors affecting leaching

The rate of leaching may be impacted by several process variables and physical elements, depending on which phase in the leaching process controls the rate (Sitando *et al.,* 2018).

At fixed concentration, the reaction rate of heterogeneous reaction can be used to determine which factors will influence the chemical reaction speed if the process is chemical reaction regulated (Equation 2). (Web, 2012).

$$-\frac{dW}{dt} = K.A.C \qquad (2.5)$$

Here, W denotes the particle's weight at time t, K denotes the rate constant, and the surface area of the particle is denoted by A. The reactant's concentration is given by C. It seems that altering the temperature will have an impact on the response rate because the rate is constant and k is temperature dependant. The response rate will also be impacted by changes to the particle's surface area.

2.16.1.1 Temperature

Leaching kinetics speed up when the temperature in a system that is leaching rises. This results from $K= Ae^{-Ea/RT}$ which is Arrhenius equation for reaction rate controlled by chemical reaction systems due to the link between the rate constant and temperature. The dependency of the diffusion coefficient on temperature results in this pattern for diffusion-controlled leaching (Web, 2012; Abali *et al.,* 2011). The reaction between dolomite and H_2SO_4, HNO_3, and HCl is an uncatalyst reaction as well as an irreversible heterogeneous reaction that is temperature-sensitive. Previous studies have shown that the rate of dolomite conversion in an acidic solution increase with temperature (Pultar *et al.,* 2019; Sitando *et al.,* 2018)

2.16.1.2 Particle size

Usually, reduced particle size will accelerate leaching (Souza *et al.,* 2007; Abali *et al.,* 2011). The rate-controlling step will determine the extent of the effect of particle size. The connection between particle size and leaching kinetics is made evident by taking into account how the diffusion speed influences the surface area of the particle. As the particle size is

decreased, porous particles may recover very little or not at all. This is due to the initial particle's enormous surface area, which is brought on by the porosity of the particle. Hence, reducing the particle size may not significantly affect the material's surface area. (Souza *et al.,* 2007).

2.16.1.3 Reagent concentration

Lixiviant concentration often affects leaching kinetics since a rise in concentration leads to a rise in kinetics up to a point, which has been documented to positively improve reactant conversion (Web, 2012; Abali *et al.,* 2011). Moreover, altering the reagent concentration might alter the leaching mechanism, which would alter the rate-controlling step (Web, 2012; Pultar *et al.*, 2018).

2.16.1.4 Rate of agitation

Agitating the leaching slurry maximizes the contact between the various phases, causing thorough mixing of the liquid and solid particles. This causes the dolomite and acid to effectively collide, accelerating the leaching reaction (Sitando *et al.,* 2018; Pultar *et al.,* 2019). The speed at which a system is stirred can change the thickness of the diffusion layer, which typically gets thinner as the speed is raised. The dissolution rate of the system controlled by diffusion-controlled will rise with increasing agitation speed as a result of this reduction in diffusion layer thickness. The mixing rate would not affect a lixiviating system that is chemically reaction-controlled, though (Web, 2012). Pultar *et al.* (2019) reported that at low stirring speeds (200 to 400 rpm), an increasing degree of conversion was observed while at higher stirring speeds (400 to 800 rpm) no significant increase in the degree of conversion was observed between dolomite and nitric acid.

2.16.1.5 pH

In general, the concentration of the lixiviant affects a system's pH. Hence, pH will typically have an impact on the rate of leaching as well as the volume of extraction. Equation 2.6 illustrates the link between pH and hydrogen ion concentration (associated with acid concentration).

$$pH = -log\{H^+] \quad (2.6)$$

Low pH values suggest a higher H^+ content in the solution. On the other side, low H^+ concentrations are implied by high pH values. The OH- concentration will be low while the H^+ concentration in the solution is high, and vice versa. (Erik *et al.*, 2020).

The dissolution of dolomite in HCl, HNO_3, and H_2SO_4 at an acidic condition of pH<5 is represented in equations 2.7 and 2.8

$$CaMg(CO_3)_2 + 2H^+ \rightarrow Ca^{2+} + MgCO_3 + H_2O + CO_2 \quad (2.7)$$

$$MgCO_3 + 2H^+ \rightarrow Mg^{2+} + H_2O + CO_2 \quad (2.8)$$

At a low pH value, fractional-order is obeyed as the rate of leaching of dolomite depends on the pH, an empirical relationship in equation 2.9 helps to describe the rate of the dissolution

$$r = k.a^m H^+ c \qquad (0 < m < 1) \quad (2.9)$$

were K = rate constant, m = order of reaction a aH^+,c is the activity of hydrogen ion in the bulk of the solution. From equation 2.10 the plot of log(r) against $logaH^+$,b for any given experiment at constant temperature will give a straight line graph having intercept equal to logk and slop equal to n (Yidrim and Akaras, 2010).

$$logr = nlog\, aH^+ b + logk \quad (2.10)$$

2.16.1.6 Liquid-solid ratio

Maximizing the solid-liquid ratio or pulp density, one can reduce the amount of lixiviant utilized by making sure there is no extra reagent in the tank that is not being used for leaching (Sitando *et al.*, 2018). It is critical to maximizing this factor because reagent usage represents one of the key costs associated with leaching procedures.

In general, there will be less lixiviant per unit of solid as the solid-liquid ratio rises. As a result, there is a chance that certain particles will not interact with the leachant and would not fully leach. Also, it is important to make sure that all of the particles leach at the same time when the pulp density is reduced because doing so would increase the leaching rate and raise the cost of the process. It is crucial to keep in mind that lixiviant will be diluted if the volume of liquid used for slurring is increased (Lottering, 2016).

2.16.1.7 Residence time

Residence time in leaching operations is the time required for the leach mixture to circulate through all the leaching reactors. This implies that each concentration of slurry uses a certain period referred to as the residence time in each leach tank. Up until the point at which equilibrium is attained, generally speaking, the more the solid material interacts with the leachant, the more the quantity dissolved (Sitando *et al.*, 2018).

A lot of other things play a role in this, and sometimes it takes a while before precipitation starts. Moreover, there is a chance for chemical interactions between dissolved reactant, with these interactions becoming more prevalent as the residence duration is prolonged. To ascertain the impact that operating time will have on the degree of reaction, it is crucial to understand both the chemistry and the mechanism of the leaching process (Lottering, 2016; Faraji, 2020). Yildrim and Akaru (2010) investigated the influence of leaching time on the

leaching of dolomite in HCl and reported that a rapid dissolution rate of Mg^{2+} and Ca^{2+} was recorded initially with 92.43 % efficiency within 5 min and this clearly shows that dissolution increases with time.

2.16.2 Dolomite leaching in an acidic medium

The leaching of dolomite is usually carried out in an acidic medium due to its basic oxide composition. Acid leaching of dolomite leads to the formation of calcium and magnesium salt and water while carbon (IV) oxide is released in the process. The slurry is then subjected to filtration to separate the filtrate and the residue. The residue consists of impurities which do not go into the solution while the filtrate is a combination of calcium and magnesium salts.

The filtrate is further precipitated to recover magnesium oxide from it. This research will consider the comparative study of dolomite leaching using an acidic medium of HCl-$HClO_4$ and HNO_3 (Yildirim and Akarsu, 2010; Manivannan, 2016).

Some of the relevant works on dolomite mineral treatments in different media are reported thus: Dolomite leaching in water with low CO_2 saturation was studied by Herman and White (1985). It was discovered that the rate was decreased and the effect of grain size was negligible at lower temperatures.

The leaching of dolomite in hydrochloric acid was done by Lund *et al.* (1973). The dissolving process was discovered to have a surface reaction rate restricted at 25 ^{o}C. Even at relatively high stirring speeds of (500 min^{-1}), the dissolving process approaches diffusion control as the temperature rises by 100 ^{o}C.

Busenberg and Plummer (1989), studied dolomite leaching in water with insufficient CO_2 saturation. In their study, Gautlier *et al.*,(1999), studied the effect of pH on the dissolution of dolomite. The rate was discovered to rise from 0.63 at 25 ^oC to 0.8 at 80 ^oC.

Abdel Aal (1995) utilized dolomite ore obtained from Egypt for the production of Magnesia by Nitric acid. It was found that the temperature of the reaction was 60 ^oC and 55 ^oC, the time of reaction was 2.5 and 2.0 hours, and the mole ratio of nitric acid to calcium and magnesium oxides was 1.10 and 1.05, and the particle size for both was 0.5 mm.

Abali *et al.,* (2011) investigated the optimization of Kutahya dolostone ore leaching in HCl. The variables were liquid-to-solid ratio, temperature acid initial concentration, stirring speed, and leaching time. It was established that the leaching acid concentration was 2 $moldm^{-3}$, the temperature was 50 ^oC, the leaching time of 5 minutes, the solid-to-liquid ratio was 2 %, and the stirring speed was 450 rpm

Baba *et al.,* (2014) investigated the optimization of Nigeria dolomite ore dissolution by HCl acid. The optimized parameters were temperature, particle size, acid concentration, and time. It was reported that the reaction time was 60 minutes, the reaction temperature was 80 ^OC, acid reaction concentration was 2 M, while 0.01 mm reactant particle size was recorded. The dolomite ore dissolution efficiency of 99.3 % was achieved and dissolution kinetic data followed the diffusion control mechanism.

Mahmut *et al.,* (2016) examined the Leaching of Mersin/Aydicink dolomite ore in HCl acid. The experimental condition is acid/dolomite ratio, solid/liquid ratio, particle size, stirring speed, temperature, and time. It was found that reaction order changed from 1.55 to 1.339

and between 3.17 and 10.49×10^{-2} $moldm^{-3}$/sec respectively and the minimum energy requirement was 16.69 kJ/mol.

In a study conducted by Yildrm and Akarsu (2010), leaching of dolomite ore in 22 % hydrochloric acid achieved 98.2 % dissolution within 30 Minutes to produce magnesium chloride, decomposition was carried out via pryrohydrolysis at 600 ^{o}C for 1 hour leading to the liberation of hydrogen chloride gas and MgO deposited.

Mubarok and Kumiawan (2015), synthesized magnesium oxide (MgO) from East Java dolomite The authors observed optimum dissolution of dolomite at 1.5 M HCl, particle size -323#, liquid-solid ratio of 20:1 cm3/g, stirring speed of 200 rpm at room temperature after one second. Precipitation of Magnesium hydroxide yielded 97.5 %. Calcination of magnesium hydroxide was performed at temp 550 ^{0}C and 800 ^{o}C. 88 % pure magnesium oxide was recovered.

Dong *et al.*, (2017) synthesized $Mg(OH)_2$ from rejected brine using ammonium hydroxide as a precipitant at a 6:1 molar ratio of NH_4OH/magnesium ion (Mg^{2+}). Reactive MgO was further produced from $Mg(OH)_2$ by calcination at 500 °C for 120 minutes.

Amrulloh *et al.*,(2020) applied an electrochemical method in a 2-compartment electrochemical cell with a constant potential of 18 V, for 4 h at room temperature in the production of $Mg(OH)_2$ from Pamekasan, Madura, Indonesia seawater and bittern obtained from the local salt industry MgO was obtained by calcination of $Mg(OH)_2$ at a temperature of 500 °C for 240 minutes.

Also, some of the important studies on dolomite beneficiation and purification studies are summarized below:

Table 2.3: Some of the Reported works on the Beneficiation of the Dolomite for Magnesium oxide Production ore by Different Authors

Reference/Location	Work done	Achievement	Gaps
Abdel Aal (1995) Khaboba (Egypt ore)	Possibility of utilizing Egyptian dolomite ores for the production of magnesium oxide by acid leaching.	The temperature of the reaction were 60 and 55 ^{o}C, time of reaction were 2.5 and 2.0 hours, the mole ratios of nitric acid to calcium and magnesium oxides were 1.10 and 1.05	Optimization of leaching parameter was not studied
Akarus & Yilidrim (2007)(Ice-Yava ore)	Leaching rates of icel-yavca dolomite in hydrochloric acid solution.	Dissolution of dolomite was observed to increase as the reaction time increases and attained about 92.43 % in the first 5 min, then rose to 98.2 % after 30 minutes. The minimum energy requirement obtained at study temperatures between 25 to 85 ^{o}C was 0.130 kJ/mol	Further purification not for recovery of valuable components not studied
Yildrim (2008)	Dissolution kinetics of ice-Aydincik dolomite in hydrochloric acid	The reaction conditions were acid concentration ranging from 3.00 to 9.02 moldm^{-3}, temp 20-80 ^{o}C and reaction time 2-14 mins. The dissolution rate of the ore rises with increasing time, temperature, acid/dolomite mole ratio, stirring speed. Chemical surface model best fit the leaching process.	Characterisation after leaching was not done.
Yildrim & Akarus (2010)(Yavca Turkey ore)	Preparation of magnesium oxide from dolomite by leach-precipitation–Pyrohydrolysis process	Leaching rate depended on the pH ,high purity magnesium chloride brine containing 98.8 % MgO and thermal decomposition recovery of 98.10 %	Optimization of leach parameter was not carried

Table 2.3 Continues

Abali *et al.*, (2011) Turkey ore	Optimization of dolomite ore leaching in hydrochloric acid solution	The leaching parameter level were found to be temperature 50 ^{o}C, solid-liquid ratio 2 %, acid concentration 2moldm^{-3}, stirring speed 450 rpm, leaching time 5mins. Leaching efficiency of 83 %	Characterisation of the ore not carried out
Danda *et al.*, (2013)	Characterisation of dolomite fines and their implications in beneficiation	The primary minerals present were dolomite, calcite, and quartz in addition to a trace of apatite, pyrite, and siderite	Leaching and purification not studied.
Mohammed *et al.,(*2013) Malaysian ore	Preparation and characterisation of Malaysian dolomite as a Tar cracking catalyst in biomass gasification process	Effect of calcination on the catalytic activity and properties of dolomite, scanning electron micrography of dolomite reveals that the calcination process affected its morphological properties; The result also indicates that calcined Malaysian dolomites can be used as tar-cracking catalyst during the gasification of biomass.	Leaching of the ore via chemical was not conducted
Baba *et al.*, (2014) Nigeria ore	Optimization study of a Nigerian dolomite ore dissolution by HCl	The leaching temperature was found to be acid concentration 2 mol/L, 80 ^{o}C, 60 Mins while particle size was 0.01mm. 99.3 % leaching efficiency was reached	Further purification was not studied
Al-Zahrani and Abdel-Majeed (2015) Al-Shaba dolomite	Production of magnesia from local dolomite ores and rejected brines from local desalination plants.	Calcinations of dolomite and adding of lime from desalinated plant effluent and to stimulated liquor to precipitate magnesium hydroxide which is then Separated, dried, and calcined to give magnesium oxide.	Ore characterisation of MgO produced was not done
Mubarok and Kurniawan (2015	Synthesis of magnesia powder from Java dolomite through leaching, precipitation, and calcination	The of magnesia obtained was 88 % with main impurities as of calcium and chloride.	Optimization was not done

Table 2.3 Continues

Mahmut *et al.*, (2016)	Leaching of Mersin/Aydincik Dolomite ore in hydrochloric acid.	The reaction conditions were particle size 5.00 mm-1.00 mm, reaction time 1minutes-24 minutes,reaction temperature 25 - 85 ^{0}C. The author observed that reaction orders and rate constants due to temperatures, changed from 1.505 to 1.339 and between 3.17 and 10.49×10^{-2} moldm^{-3}/secs respectively.	Further purification was not done

2.16.3 Research Gaps

From the literature review, the following research gaps have been observed:

i. There is high energy demand for Silicothermic process of MgO synthesis

ii. Leaching of dolomite in HCl-$HClO_4$ has not been reported

iii. Process development through the crude optimization methods is limited in terms of data generation

iv. The reaction mechanism for the synthesis of MgO from dolomite was not established

v. Despite the huge local demand for MgO, Nigerian dolomite deposit is yet to be fully utilized for MgO synthesis

2.17 Response Surface Methodology (RSM)

The process of choosing the optimum input conditions from a set of accessible parameters to provide the best results at the lowest feasible cost is known as optimization. This is accomplished using effective quantitative techniques (Abdulkareem *et al*., 2011; Umar *et al*., 2016; Joseph *et al.,* 2022). Several academic disciplines, including engineering, science, and business, use optimization.

2.18 Reaction Kinetics Study of Dolomite in Acid Medium

An exothermic reaction occurs between acid and dolomite and this can be categorized as a non-catalyzed irreversible heterogeneous reaction (equation 2.11).

$$CaMg(CO_3)_2 + AB \rightarrow Ca(B) + MgB + CO_2 + H_2O \quad (2.11)$$

A= Hydrogen ion, B = Anion

A complex reaction system between dolomite and mineral acid (HCl-$HClO_4$ and HNO_3) at the solid-liquid interface occurs that involves the movement of reagent and products through phase interphases, desorption, and adsorption on the solid phase surface as well as the heat transfer. To evaluate the kinetics from the experimental data, a mathematical description that will help to give a simplified model will be used in this study (Are *et al.*, 2021).

2.19 Precipitation

Precipitation in the chemical treatment of minerals involves the release of both metals and their compounds or the contaminants from aqueous solutions. It occurs by temperature manipulation, evaporation, reagent addition, pH change. (Mubarok and Kurniawan, 2015).

2.20 Magnesium Oxide

Magnesium is found naturally in the form of periclase, a white, hygroscopic solid mineral known as magnesium oxide or magnesia. It is made up of an interconnected lattice of Mg^{2+} and O_2 ions (Tooma, 2021; Drake, 2021).

2.20.1 Physical properties of magnesium oxide

Magnesium oxide has the chemical formula MgO, It usually appears as a white powder, it is colorless, it dissolves in acid, and ammonia, and is not soluble in alcohol. The coordination geometry is octahedral and the crystal structure is cubic. Table 2.3 present the properties of

magnesium oxide while Figure 2.5 presents the crystal structure of magnesium oxide. Magnesium oxide is often synthesized through the calcination of the mineral magnesite ($MgCO_3$) or magnesium hydroxide that is extracted through liming from seawater or brine. Also, it can be obtained from thermal hydrolysis of magnesium sulphate ($MgSO_4$), magnesium sulphide (MgS), basic carbonate hydrated, and magnesium chloride ($MgCl_2$), (Ding *et al.*, 2001; Duhaime *et al.*, 2002). The refractory industry considered MgO a very important raw material due to its high hydration resistance, its ability to retain chemical stability at high temperatures, and its high degree of refractoriness (Martinac *et al.*, 2004)

Table 2.4: Physical Properties of Magnesium Oxide (Kirk-Othmer, 2005)

Property	**Values**
Appearance	White powder
Molar weight (g/m)	40.304
Density (g/cm^3)	3.581
Melting point (^OC)	2827
Hardness	5.5-6.0
Co-ordination geometry	Octahedral

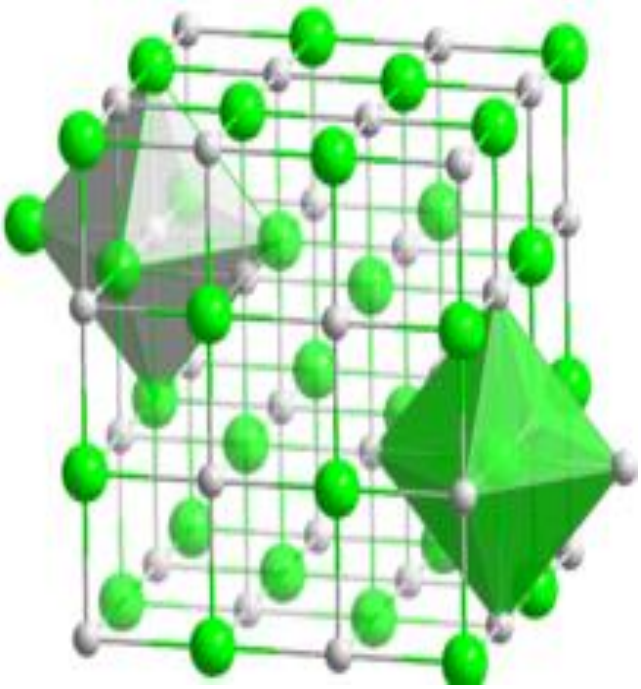

Figure 2.6: Crystal Structure of Magnesium oxide (Haynes, 2011)

2.20.2 Industrial application of magnesium oxide

MgO is a very important and useful material to the refractory industry, agricultural industry, metallurgy industry, and pharmaceutical industry. Its relevance to any of the aforementioned industry depend on the calcination temperature used for its production (Buckman, 2020). Its importance to the refractory industry is attributed to its resistance to hydration, ability to retain its chemical stability in a basic medium at high temperatures, and excellent degree of refractoriness.

Industrial applications of magnesium oxide include:

- Magnesium oxide is used in industry to treat wastewater and sewage, remove sulphur dioxide and sulphur trioxide from industrial flue gases, and act as a neutralizer for some industrial effluent streams (Roy and Sardar, 2015).
- Magnesium oxide is also employed in several metallurgical processes. For instance, in the manufacture of lateritic nickel, caustic-calcined or light-burned magnesia is

used to precipitate a crude nickel-cobalt hydroxide from the sulphuric acid leach liquid.

- The main application for refractory grade magnesia is the production of direct reduction iron and steel (Aral, *et al.,* 2004).
- Magnesium is also utilized in agriculture as a fertilizer and in animal feed. Magnesium is a structural component of the chlorophyll molecule, a substance required for photosynthesis in plants. Plants might perish if their soil or fertilizer supply is insufficient in magnesium. Among the crops that respond very well to magnesium fertilization are corn, potatoes, cotton, citrus, tobacco, and sugar beets. Another crucial aspect of animal nutrition is the use of fertilizers containing magnesium to nourish pasture (NORDFEED, 2021). Cattle and sheep that forage on grass need magnesium in their diets to prevent the potentially fatal condition known as grass tetany and hypomagnesia. While the animals are grazing on grass that has recently experienced a rapid growth spurt, this sickness most frequently develops in cool weather. The two most widely used ways to add magnesium to bovine diets are adding caustic-calcined or moderately burned magnesia to purchased feed or mixing the mineral with molasses in a liquid lick (Kirk-Othmer, 2005).
- Magnesium cement also uses magnesium oxides. Sorel cement and the much more recent magnesium phosphate cement are the two main categories of magnesium cement. In industrial and institutional structures, so-called "magnesite" flooring is a common use of sorel cement. Additionally, they are used in the production of tiles, wallboards, fiberboards, refractory boards for fire doors, and non-abrasive binders for grinding wheels and disks. Due to the cement's possible instability in damp outdoor

circumstances, its use is limited to indoor applications. For roads, parking lots, and airport runways, magnesium phosphate cement is utilized in rapid-setting formulations and patching mortars. Because it is resistant to moisture, magnesium phosphate cement can be used in contact with steel reinforcing, where the phosphate passivates the steel to stop corrosion (Aral, *et al.,* 2004).

- Electric furnaces and appliances heating elements are insulated using fused, boron-free magnesia or periclase (Kirk-Othmer, 2005)

2.21 Basic Instrumentation for Dolomite Mineral Processing

The following instrumentation is used for dolomite mineral processing:

2.21.1 X-Ray Diffraction (XRD)

X-ray diffraction (XRD) methods have been employed for many years to characterize microstructures. If a specimen has different crystal structures, XRD can be used to identify the percentages of different phases that are present in the material. Based on the crystal structure and lattice parameters, a specific phase can be identified by XRD if it can be chemically isolated from bulk material. EDS and/or WDS analysis, which quantifies the chemical composition, can be used to supplement this study. However, applying EDS and WDS to particles with a diameter of less than 2-3 micrometers is laborious. Smaller particles can be identified using diffraction techniques on the TEM, and EDS can be used on them if they are separated from the matrix using replication procedures. This prevents the detection of the matrix along with the precipitate (Ohtaki, 1993).

According to the XRD theory of operation, when X-ray radiation enters a material, it interacts with the atoms' electrons to scatter the radiation. Positive and negative interference will happen when the atoms are arranged in planes, which implies that the matter is crystalline and their spaces are equal to the wavelength of X-rays. When the atoms are arranged in

crystalline patterns called planes, this causes diffraction, where X-rays are released at distinctive angles. The majority of crystals allow for multiple sets of planes to travel through their atoms. Each set of planes has a unique interplanar distance that results in a distinctive X-ray diffracted angle (Kaczmarek *et al.*, 2017).

Dolomite has a similar structure to that of calcite, however, there is an alteration of Mg and Ca layers. There is a large difference of 33 % between the Mg^{2+} and Ca^{2+}which is responsible for the alteration. An excess of Ca^{2+}, with the composition of up to $Ca_{1.2}Mg_{0.8}(CO_3)_2$ exist in many naturally occurring dolomite which is different from the dolomite stoichiometric $CaMg(CO_3)_2$. An increase in the unit cell parameter exists due to the excess Ca^{2+} in the dolomite structure and that of Mg^{2+} (Nowak *et al.*, 2022, Warren 2000; Shen *et al.*, 2013) reported that dolomite crystals from Platteville formation are both microstructure and compositionally heterogeneous in a partially dolomitized limestone. Three phases are usually associated with a single dolomite crystal which is calcite inclusions, Fe-bearing dolomite ($Ca_{1.06}Mg_{0.8}Fe_{0.14}(CO_3)_2$), and the host Ca-rich dolomite ($Ca_{1.14}Mg_{0.8}(CO_3)_2$). A similar orientation is shown in the three phases: a modulated microstructure is shown in Ca-rich dolomite while it was not evident in Fe- bearing minerals.

2.21.2 X-Ray Fluorescence (XRF)

The bombardment of a substance with high-energy X-rays or gamma rays leads to excitement, it emits characteristic secondary X-rays. The process is frequently utilized for chemical and elemental analysis, especially in the study of materials, glass, metals, ceramics, and construction materials, as well as for academic fields in areas like archaeology, and art products, such as creating sand murals, geochemistry, and forensic science. The chemistry of a sample can be analyzed by Energy Dispersive X-Ray Fluorescence (EDXRF) analyzers by

analyzing the spectrum of the distinctive X-rays that each element in the sample emits when it is treated by high-energy photons (X-rays or gamma rays). When striking an atom in the sample by a photon with enough energy, it releases one of the atom's inner orbital shells' electrons and produces a luminous X-ray (lower quantum energy states). When an electron from one of its higher quantum energy orbital shells fills the gap left in the inner orbital, the atom stabilizes once more. (Geochemical Instrumentation and Analysis, 2022).

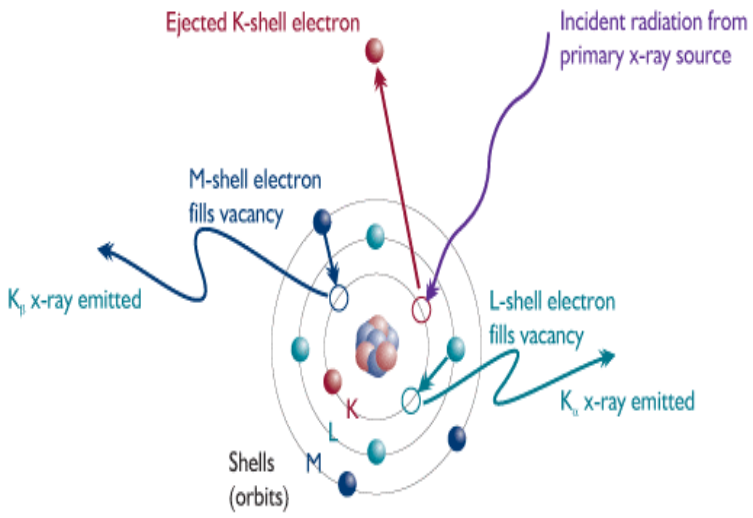

Figure 2.7: X-ray Fluorescence Phenomenon (Geochemical Instrumentation and Analysis, 2022)

By using XRF analysis, the chemical makeup of dolomite ore is often identified. The various analyses reported in table 2.4 clearly shows that CaO and MgO are the main components of dolomite ore (Mohammed *et al.*, 2013) however variation of the oxides from different locations could be attributed to different geological formations. The trace amount of other oxides such as SiO_2, Al_2O_3, and Fe_2O_3 are usually considered to be impurities (Abdel-Aal

1995; Mohammed *et al.,* 2013) and the composition of these other oxides goes a long way to determining their industrial applications (Mohammed *et al.,* 2013).

Table 2.5: Chemical Composition of Dolomite Ore

Compound Content (% weight)	**Kamang-Agam district (Olivia *et al.*, 2017)**	**Batu, Perlis, Malaysia (Salleh *et al.*, 2006)**	**Daye, ahubei, China (Xiaoli *et al.*, 2016**	**Oreke, Ifelodun LGA, Kwara State**	**Khaboba, Sinai, Egypt (Abdel-AAl, 1995)**	**Mersin/ Aydincik Turkey (Mahmut *et al.*, 2016)**
CaO	31.25	42.56	29.68	55.23	28.1	32.37
MgO	20.17	22.73	16.55	40.15	17.5	22.84
SiO_2	3.65	0.8	5.13	4.62	11.15	0.17
Al_2O_3	0.61	-	-	-	0.11	-
Fe_2O_3	0.46	0.51	-	-	0.81	0.42
CO_2	-	-	-	-	41.2	-
Moisture	-	-	-	-	0.77	-
MnO	-	-	-	-	-	0.009
PbO	-	-	-	-	-	0.019
LOI	43.86	-	-	-	41.5	

2.21.3 Scanning Electron Microscopy (SEM)

Scanning electron microscope (SEM) also known as an electron microscope produce the image of an object by directing electrons beams on the object for scanning. Several signals are produced by the sample's atoms and electron interactions, and these signals give information about the sample's surface composition and topography (Griffiths and Hasseth, 2007). An image is produced by fusing the position of the electron beam with the detected

data during a normal raster scan of the electron beam. The fundamental idea is that an appropriate source, usually a tungsten filament, generates an electron beam. After being thinned out by a set of electromagnetic lenses and apertures and being accelerated by a high voltage, the electron beam uses scan coils to scan the surface of the specimen (AAS, 2015). SEM uses a direct electron beam to irradiate a tiny area of the material specimen, producing distinctive x-rays that are used for both qualitative and quantitative analysis. The beam interacts with the sample to produce a variety of signals, including photon emission, internal currents, secondary electrons, and others, all of which can be monitored in an appropriate manner (Bindell, 1992). The most important of the produced electrons (x-rays), called backscattered or primarily reflected electrons are detected and amplified. The output from this is a function of the composition of the area irradiated by an electron beam (Thomas, 2007). The atomic number of the specimen determines the intensity of the backscattered electron signal, therefore surfaces with varied chemical makeup will create varying signal intensities and appear differently on the SEM screen.

The signal intensities are used for quantitative analysis. The identification of secondary electrons produced by atoms that have been stimulated by an electron beam is the most popular SEM technique. The topography of the specimen, among other factors, affects the number of secondary electrons that can be found. By scanning the sample and utilizing a specific detector to capture the secondary electrons that are released, an image showing the topography of the surface is produced.

2.21.4 Atomic Absorption Spectroscopy (AAS)

The electroanalytical method known as atomic absorption spectroscopy (AAS) determines the quantitative composition of chemical components by measuring the amount of optical

radiation (light) that unbound atoms in a gaseous state absorb. (McCarthy, 2012). The technique is used in analytical chemistry to determine the amount of a certain element (the analyte) in a sample that will be subjected to analysis. In the fields of toxicology, biophysics, and pharmacology, around 70 distinct elements can be identified using AAS either directly in solid samples or solutions.

In nuclear absorption, the clinical study of metals in biological tissues and fluids, such as whole saliva, blood, liver tissue, brain tissue, plasma, urine, muscle tissue, and semen, as well as in some pharmaceutical production processes, to find minute levels of a catalyst that remain in the finished medication are just a few applications for spectrometry in various branches of chemistry.

CHAPTER THREE

3.0 MATERIAL AND METHODS

3.1 Materials

Table 3.1 shows the list of materials, chemicals/reagent, and their uses in the production of magnesium oxide and their sources.

Table 3.1 Sources and uses of Materials/Chemicals used for the Study

S/N	Materials/Chemicals	Source/location	Uses
1	Dolomite ore	Ikpeshi Akoko, Edo state mines	Leachee
2	Nitric acid (HNO_3)	Central Drug House (P) Ltd, India	Leachant
3	Hydrochloric acid(HCl)	Central Drug House (P) Ltd, India	Leachant
4	Perchloric acid ($HClO_4$)	Central Drug House (P) Ltd, India	Leachant
5	Calcium oxide	Loba chemie PVT. LTD., India	Precipitant
6	Citric acid	Loba chemie PVT. LTD., India	Inhibitor
7	Distilled water	Step –B central Research lab FUT Minna	Leachant preparation

3.1.1 Equipment used

Table 3.2 presents the list of equipment used for this research work

Table 3.2: Equipment and their Models

	Equipment	Model	Manufacturer
1	Mortar and pestle	-	Sim best Minna
2	Muffle furnace	S336RD	Carbolite, England
3	Digital Weighing Balance	US – 6000g	Cyberlab, USA
4	Oven	N505F	Genlab, England
5	Hot plate with Magnetic stirrer	Model 400	Gallenkamp, England
6	X-ray fluorescence	NEX CG	Rigaku Tech. Japan
7	X-ray diffractometer	AXS D8	Brunker Germany
8	HRSEM	T150T	Zeiss Auriga
9	FT-IR	Nicolet iS5	Perkin Elmer, UK
10	AAS	PG-90	England

3.2 Methods

3.2.1 Sample collection and preparation

Ikpeshi/Egbigere clan also known as Marble city in Akoko-Edo Local Government Area of Edo State (Plate I) is blessed with a large amount of dolomite ore deposit (Plate II). The location mapping of Ikpeshi dolomite ore mine site was conducted with the aid of a global position system to locate and determine the elevation and co-ordinates of sample points (Figure 3.1). Six different samples were collected at an interval of 5 meters apart within the

dolomite deposit to form a composite (Plate III). It was crushed, ground, and sieved into particle sizes ranging from 0.15-0.3 µm mesh (Plate IV).

Plate I: Ikpeshi

Plate II: Dolomite Ore Deposit

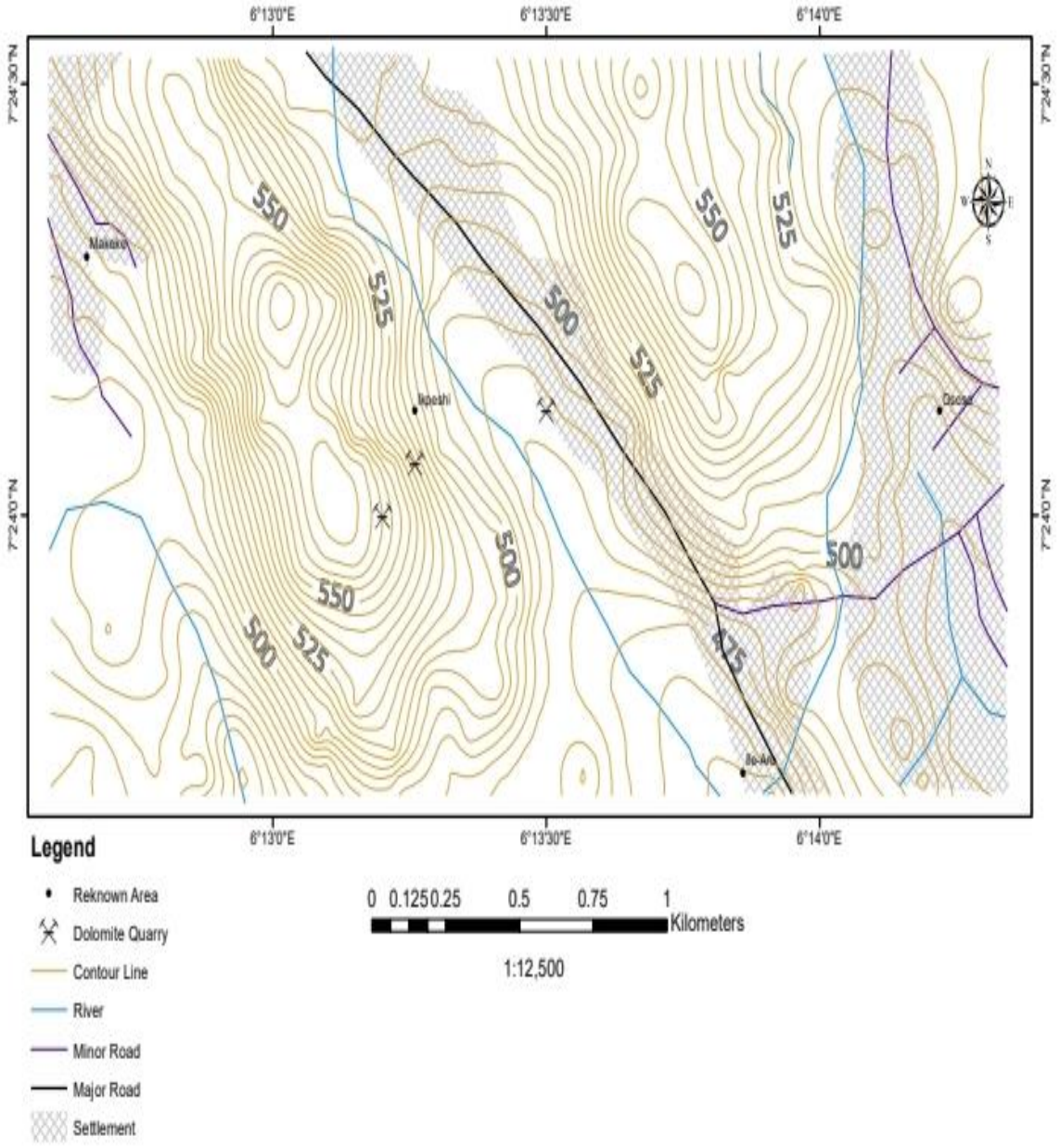

Figure 3.1: Location Map of Ikpeshi Dolomite Ore Deposit

Plate III: Mined Dolomite Ore **Plate IV: Sieved Dolomite Sample**

3.2.2 Dolomite ore characterisation

The collected dolomite ore was subjected to the following analyse:

3.2.2.1 Dolomite ore characterisation using x-ray diffraction

The mineral phases of the dolomite ore were determined using powder X-ray diffraction (XRD). This was carried out using Cu-Kα radiation on a Bruker AXS D8 Advance. On a degreased glass slide, some of the crystals were sprinkled, and the diffractograms between diffraction two angles were recorded. Run settings were chosen, including step size, start angle, finish angle, and speed (Table 3.3). The analysis was done in Ithemba Laboratory, South Africa.

Table 3.3: Parameter Setting for the XRD Analysis of Dolomite Ore

Parameter	Setting
Voltage	20 kV
Current	5 Ma
Start angle	5^{o}
End angle	70^{o}
Angular stop	0.05^{o}
Scanning speed	2.5o/min
Time/step	0.02^{o}
Reduction wavelength	1.5405 Å (Cu)

3.2.2.2 Dolomite ore characterisation using x-ray fluorescence

This was conducted to ascertain the oxide composition of the dolomite ore. This was done using Thermo Scientific ARL OP-TIM'X 166 in Ithemba Laboratory, South Africa.

3.2.2.3 Dolomite ore characterisation using SEM/EDX analysis

SEM analyzer model JEOL JSM-6030 was used for the dolomite ore. SEM/EDX analysis, and INCAX-sight, an OXFORD instrument, was used for elemental analysis of the ore and X-ray energy dispersive analysis (EDX), which allowed for the quantification of every element present on the surface. A pure silver sample is typically used to calibrate the SEM/EDX spectrophotometer before the working curve is chosen based on the sample and the output is sent to an excel spreadsheet. Table 3.4 present the SEM/EDX analysis's parameters. The analysis was done in Physics Department, University of Wester EDS Cape (UWC), South Africa

Table 3.4: Parameter Setting for SEM/EDX Analysis of Dolomite Ore

Parameter	Setting
Voltage	40 Kv
Test time	100 s
Current	350 µA

3.2.3 Box-Behnken design for dissolution of dolomite in HNO_3 and HCl-$HClO_4$

Preliminary investigations were conducted on one-factor-at-a-time and variables such as temperature, leaching time, and HNO_3 concentration show a significant effect on the leaching efficiency. Therefore, these factors were selected for further study. Leaching time was studied between 20 minutes to 60 minutes, leaching temperature was varied between 30 ^oC to 70 ^oC and HNO_3 Concentration ranged from 0.5 $moldm^{-3}$ to 2.5 $moldm^{-3}$. Table 3.5 lists the codes, ranges, and levels of the independent variables of time (t), temperature (T), and acid concentration (C).

Table 3.5: Levels and Coded Variables for Box-Behnken Design

Symbol	Independent variable	Low (-1)	Centre (0)	High (1)
A	Temperature (^oC)	30	50	70
B	Concentration ($moldm^{-3}$)	0.5	1.5	2.5
C	Time (minutes)	20	40	60

Table 3.6 shows the 17 generated experiments using the Box-Behnken Design matrix. Each of the independent parameters was studied at three levels, coded as +1, 0, and -1, which are high, intermediate, and low values respectively.

Table 3.6: Box-Behnken Design for Leaching Efficiency

Run	A (°C)	B ($moldm^{-3}$)	C (Minutes)
1	30	0.5	40
2	70	0.5	40
3	30	2.5	40
4	70	2.5	40
5	30	1.5	20
6	70	1.5	20
7	30	1.5	60
8	70	1.5	60
9	50	0.5	20
10	50	2.5	20
11	50	0.5	60
12	50	2.5	60
13	50	1.5	40
14	50	1.5	40
15	50	1.5	40
16	50	1.5	40
17	50	1.5	40

3.2.4 Dissolution of dolomite ore in both HNO_3 and HCl-$HClO_4$

100 cm^3 of 0.5 $moldm^{-3}$ trioxonitrate (V) acid was dispensed into a conical flask equipped with a thermometer and it was heated on a hot plate magnetic stirrer (Plate V) to a temperature of 30 ^oC. Three grams of powdered dolomite sample was measured into the conical flask at a constant stirring speed of 250 rpm. After allowing the reaction to run for 40 minutes, it was filtered. The remnant was dried in an oven at 110 ^oC and the weight was used to compute the leaching efficiency in equation 3.1. The experiment was repeated under various conditions in Table 3.6. The Above procedures were repeated for optimization of the leaching of dolomite in HCl-$HClO_4$. Using the same parameters.

$$\text{Leaching efficiency (\%)} = \frac{Mass\ of\ dissolved\ dolomite\ X\ 100\ \%}{Initial\ Mass\ of\ dolomite} \qquad (3.1)$$

Plate V: Dissolution of Dolomite in HNO_3

3.2.5 Leaching kinetics of the dolomite ore in both HNO_3 and $HCl\text{-}HClO_4$

100 cm^3 of 0.5 $moldm^{-3}$ trioxonitrate (V) acid was dispensed into a conical flask equipped with a thermometer and it was heated on a hot plate magnetic stirrer (Plate V) to a temperature of 55 ^oC. Three grams of powdered dolomite sample was measured into the conical flask at a constant stirring speed of 250 rpm According to Baba *et al*. (2014). After allowing the reaction to run for 10 minutes, it was filtered using watchman filter paper . The remnant was dried in an oven at 110 ^oC and the weight was used to compute the fraction of dolomite that dissolved equation 3.1. The experiment was repeated under various conditions in Table presented in Appendice A1 to examine the influence of concentration. The Above procedures were repeated for condition in table presented in Appendice A2 at the 2.2 $moldm^{-3}$ to investigate the influence of concentration.The experimental data was used to generate the kinetics charts. For the kinetic analysis of the reaction between dolomite and $HCl\text{-}HClO_4$, the aforementioned steps were repeated.

3.2.6 Central composite design for the precipitation of magnesium hydroxide from Nitric acid Route (NAR)

Preliminary experiments was conducted on one-factor at-a-time, variables such as concentration of precipitant ($Ca(OH)_2$) and precipitation time shows a significant effect on the quantity of precipitate formed. Therefore, these factors were selected for further investigation. Precipitation time was studied between 2 minutes to 8 minutes and calcium hydroxide concentration was 24 % to 34 % w/v. Table 3.7 shows the code, ranges, and levels of independent parameters of time (t), and concentration of calcium hydroxide. Table 3.8 shows the 13 composite experimental runs generated using central composite. Each of the

independent parameters was studied at three levels, coded -1, 0, and +1 which are low, intermediate, and high respectively.

Table 3.7: Process Variables for Central Composite Design

Factor	Name	Units	Type	Minimum	Maximum	Coded Low	Coded High	Mean	Std. Dev.
A	Conc.of $Ca(OH)_2$	%	Numeric	21.93	36.07	-1 ↔ 24.00	+1 ↔ 34.00	29.00	4.08
B	Time	Min	Numeric	0.7574	9.24	-1 ↔ 2.00	+1 ↔ 8.00	5.00	2.45

Table 3.8: Central Composite Design for Precipitation

Run	A: Concentration of $Ca(OH)_2$ (%)	B: Time (Min)	Yield (%)
1	34	2	
2	22	5	
3	29	5	
4	24	2	
5	34	8	
6	29	5	
7	29	10	
8	29	5	
9	29	5	
10	29	5	
11	37	5	
12	24	8	
13	29	1	

3.2.7 Precipitation of magnesium hydroxide from nitric acid filtrate

50 cm^3 of the filtrate collected from the dissolution of dolomite in Nitric at optimum was measured into a 250 cm^3 beaker fitted with a pH meter and submerged in ice water to control the temperature to minimize the co-precipitation of calcium oxide (Plate VI). 1 cm^3 of 0.1 $moldm^{-3}$ citric acid was added also to minimize the Co-precipitation of calcium oxide (Szilvester *et al.,* 2020). 34 % calcium hydroxide was added drop wise until pH of 10.2. Precipitation time was monitored for 2 minutes with the aid of a stopwatch. The resulting precipitate was then separated using watchman filter paper and funnel (Plate VII**)**. The precipitate was collected and oven-dried at 120 ^oC (Plate VIII and Plate XI**)** for each of the runs (Mubarok and Kurniawan, 2015). The resulting filtrate from each of the runs was subjected to AAS analysis to ascertain the quantity of magnesium ion left in the solution. The above process was repeated for other conditions in Table 3.6 and also for precipitation from the filtrate of dissolution of dolomite in $HCl/HClO_4$.

$$Yield\ of\ magnesium\ precipitated(\%) = \left(\frac{p1 - p2}{p1}\right) \times 100 \qquad (3.2)$$

Where P1 is the concentration of magnesium ion before precipitation

P2 is the concentration of magnesium ions after precipitation

Plate VI: Experimental Setup for the Precipitation of $Mg(OH)_2$

Plate VII: Precipitate of $Mg(OH)_2$

Plate VIII: Laboratory Oven

Plate IX: Dried $Mg(OH)_2$ Precipitate

3.2.8 Pentagonal experimental design for the calcination of magnesium hydroxide

During a preliminary experiment, variables such as time and temperature had a major impact on the calcination magnesium hydroxide. Therefore, these factors were selected for further

investigation. The calcination period was monitored from 10 to 40 minutes and the temperature was 500 to 900 ^{o}C. Table 3.7 presents the ranges, codes, and levels of independent variables of time (t) and temperature (T). Table 3.8 shows the 8 experimental runs generated using a pentagonal design. Each independent variable was examined at three different levels, denoted by the codes +1, 0, and -1, which represent high, middle, and low levels, respectively.

Table 3.9: Boundary Conditions for Pentagonal Experimental Design

Factor	Name	Units	Type	Minimum	Maximum	Coded Low	Coded High	Mean	Std. Dev.
A	Time	Minutes	Numeric	12.86	40.00	-1 ↔ 10.00	+1 ↔ 40.00	25.00	8.96
B	Temperature	^{o}C	Numeric	509.80	890.20	-1 ↔ 500.00	+1 ↔ 900.00	700.00	119.53

Table 3.10: Pentagonal Experimental Design for the Synthesis of MgO through Nitric Acid System (NAR)

Run	A: Time (Minutes)	B: Temperature (^{o}C)	Yield (%)
1	30	890	
2	13	582	
3	25	700	
4	25	700	
5	40	700	
6	30	510	
7	13	818	
8	25	700	

3.2.9 Calcination of dried precipitate

The furnace (Plate X) was preheated to the calcination temperature for each of the experimental runs, after which 4 g of the oven-dried precipitate was measured in a crucible and charged into the muffle furnace for each of the runs with time monitored using a stopwatch. After complete calcination, the crucible (plate XI) was withdrawn from the furnace and allowed to cool inside the desiccator (Plate XII**)**, the weight for each of the runs was recorded using a digital weighing balance. The above procedure was repeated for other runs in Table 3.8 and for calcination of the precipitate obtained via HCl/ $HClO_4$ (Al-Zahrani and Abed-Majeed 2015).

Plate X: Electric Muffle Furnance

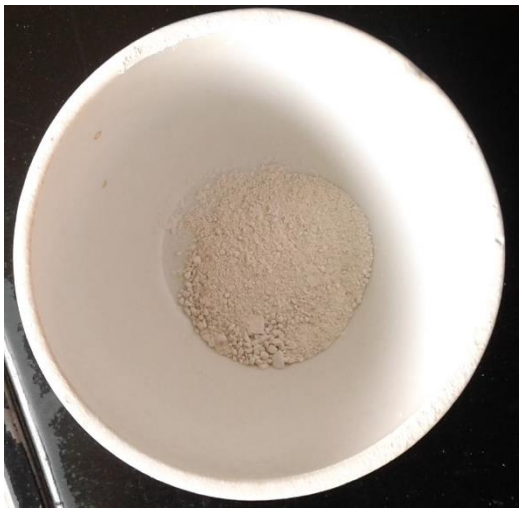

Plate XI: Synthesized MgO **Plate XII: Desiccator**

3.2.9.1 Characterisation of the synthesized magnesium oxide (MgO)

The synthesized magnesium oxide was analyzed using XRF, SEM/EDX, and XRD to identify the mineralogical phases and morphological properties of the ore.

3.2.9.2 X-ray fluorescence

This was conducted to ascertain the oxide composition of the synthesized magnesium oxide. This was done using Thermo Scientific ARL OP-TIM'X 166. The analysis was done in Ithemba Laboratory, South Africa

3.2.9.3 *X-ray diffraction*

The phases of the minerals in the synthesized magnesium oxide were determined using powder X-ray diffraction (XRD). This was carried out using Cu-Kα radiation on a Bruker AXS D8 Advance. On a degreased glass slide, some of the crystals were sprinkled, and the diffractograms between diffraction two angles were recorded. Run settings were chosen,

including step size, start angle, finish angle, and speed. The analysis was done in Ithemba Laboratory, South Africa

3.2.9.4 SEM/EDX Analysis

SEM analyzer model JEOL JSM-6030 was used for the synthesized magnesium oxide analysis, and INCAX-sight, an OXFORD instrument, was used for elemental analysis. The X-ray energy dispersive analysis (EDX) allowed for the quantification of every element present on the surface. A pure silver sample is typically used to calibrate the SEM/EDX spectrophotometer before the working curve is chosen based on the sample and the output is sent to an excel spreadsheet. The analysis was done in Pysics Department, University of West Cape (UWC), South Africa

3.2.9.5 Determination of FTIR of the synthesized magnesium oxide

The functional group present in the synthesized MgO was identified via FTIR analysis. FTIR analyzer model Nicolet iS5 spectrometer located in the University Central Laboratory, Umar Musa Yar'adua University Katsina was used. The spectra were recorded from 500 to 4000 cm^{-1}.

3.2.9.6 Determination of differential thermal and thermo-gravimetric (DTA-TGA)

The DTA/TGA was used to determine the synthesized MgO stability using a PerkinElmer TGA 4000 (Netherlands) instrument (Model STA 409) under nitrogen flow in the temperature range of 35-1100 ℃. Plate II shows the TGA machine used. A clean empty crucible with the wire basket was loaded onto the hang-down wire. The hang down wire was connected to the microbalance at the top of the instrument. After the crucible has been installed, the furnace was selected and raised up over the crucible. When the furnace is in position the crucible was allowed to stabilize and the balance was zeroed repeatedly until it

stabilized (Babatunde, 2021). The analysis was done in STEP-B, Federal University of Technology, Minna, Niger Satate

CHAPTER FOUR

4.0 RESULTS AND DISCUSSION

4.1 Characterisation of Dolomite Ores from Ikpeshi

4.1.1 XRD analysis of dolomite

The XRD spectra of the dolomite sample analysis is given in Figure 4.1. The different phases of components in the ore are indicated by the various peaks. The main component, with a 2θ of 29^{o} – 32 ^{o}, represents dolomite, while the other components are calcite with 2θ of 28 ^{o} – 29 ^{o}, magnesite of 2θ of 50 ^{o} – 52 ^{o} and quartz with a 2θ of 24^{o} -25^{o}. The ore can be classified as high-grade ore with small impurities (Baba *et al.*, 2014).

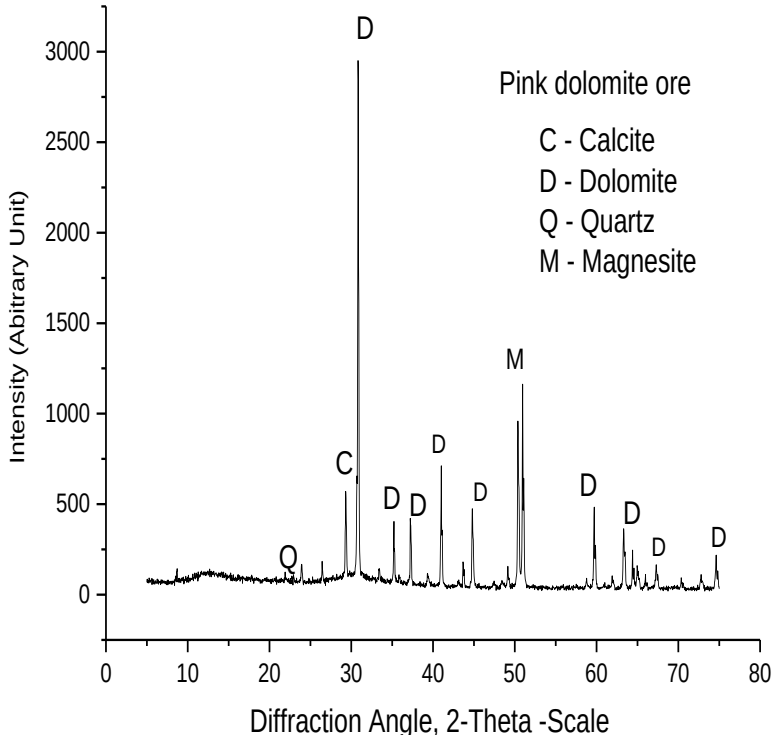

Figure 4.1: XRD Pattern of dolomite Ore.

4.1.2 XRF characterisation of dolomite

The XRF result in Table 4.1 shows the various percentage compositions of metal oxides in the ore. The ore contained about 30.6 % CaO, which agrees with the theoretical composition

of 30.4 % CaO (Sunil *et al.,* 2013; Sivrikaya, 2018). The value is also close to the 31.7 % CaO and 33.0 % CaO recorded by Yildrim *et al.,* (2010) and Olaiya *et al.* (2015) respectively. The amount of MgO present in the dolomite is 18.84 %, with a value that is comparable to the theoretical value of 21.90 % MgO (Sunil *et al.,* 2013; Sivrikaya, 2018). It is also in line with the values of 20.6 % and 21.3 % MgO reported by Yildrim *et al.* (2010) and Olaiya *et al.,* (2015), respectively. 45.91 % lost on ignition (LOI) could be attributed to the presence of CO_2, and tends to agree with the 47.75 % CO_2 reported by Sunil *et al.* (2013); Sivrikaya (2018) as part of the theoretical composition of dolomite. All other oxides are considered to be impurities with a total sum of 2.55 %, this suggests that the Ikpeshi used for this study has low impurities.

Table 4.1: Metal Oxide Composition (%) of Ikpeshi Dolomite Ore

Fe_2O_3	CaO	TiO_2	MgO	K_2O	Al_2O_3	P_2O_5	SiO_2	LOI	Total
0.10	30.62	0.02	18.84	0.07	0.44	0.05	1.87	45.91	97.92

4.1.3 EDX characterisation of dolomite

The EDX spectra shown in Figure 4.2 reveal the peaks of the three main elements that make up dolomite, which are magnesium (13.93 %), oxygen (65.99 %), and calcium (20.09 %), as well as their corresponding percentage compositions.

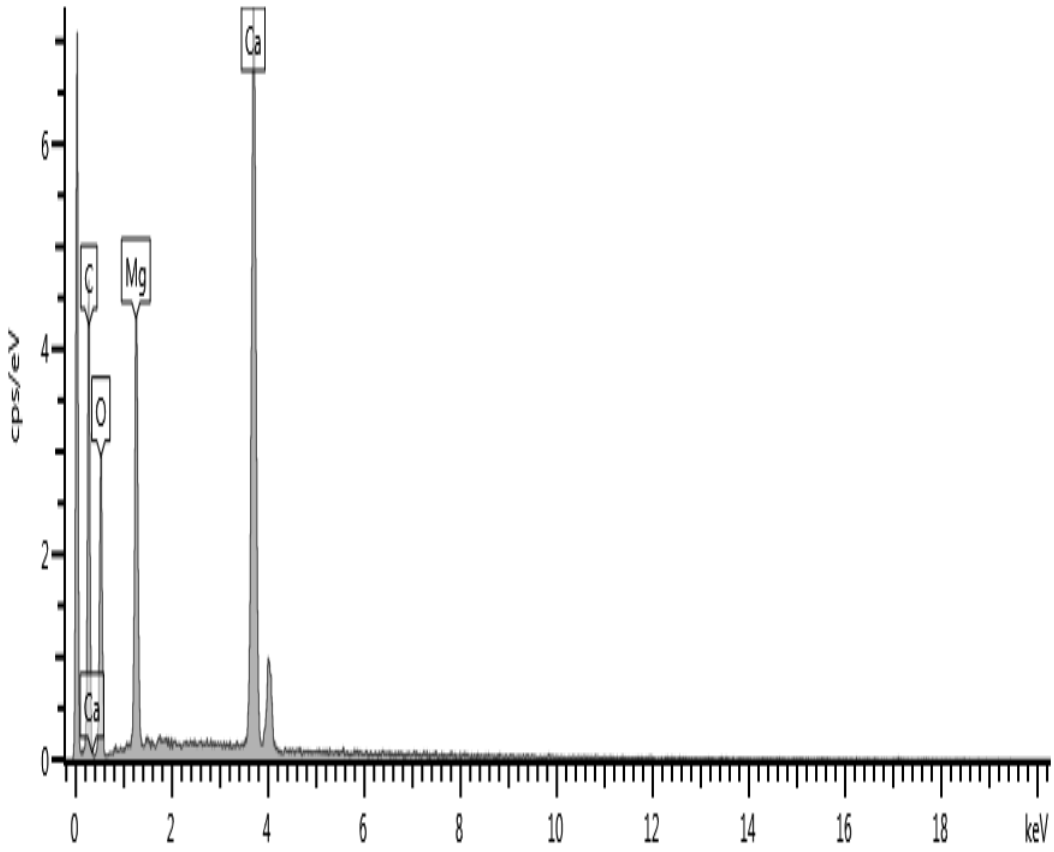

Figure 4.2: EDX of Dolomite Ore

4.1.4 SEM characterisation of dolomite

The result of the SEM image of the collected dolomite ore is presented in plate XIII. The dolomite has distinct, sharp-edged particles Fahad *et al*. (2011). This implies that most of the dolomite particles can be categorized as fine particles since the 1 µm measurement in plate XI falls between 0.1 µm to 2.5 µm for any particle to be regarded as fine (Mertens *et al.*, 2020).

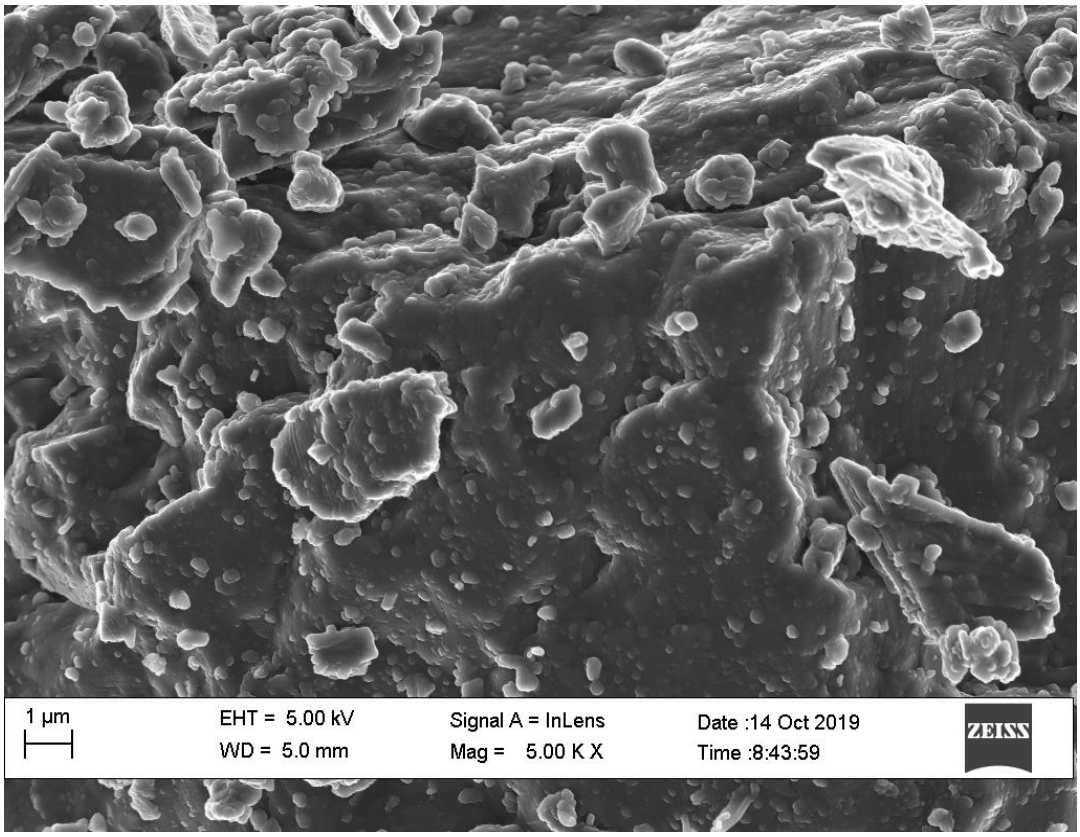

Plate XIII: SEM Micrographs of Dolomite

4.2 Optimization of the Leaching Parameters Temperature, Acid Concentration and Reaction Time in HNO_3 and HCl-$HClO_4$ Respectively

4.2.1 Regression model and statistical analysis of leaching of dolomite in HNO_3

Design Expert 11.0 was used for the regression and graphical analysis, and the response of the experimental design represents the leaching efficiency. Optimal point prediction was based on the statistical model which gave a coefficient of regression (R^2) of 0.977 for a quadratic model, and 0.7018 for a linear model. Hence, the interaction between the independent and dependent (leaching efficiency) variables is best described by the second-order polynomial regression model. Equation (4.1) gives the following description of the relationship:

$$Y= \beta_o + \beta_1X_1 + \beta_2X_2 + \beta_3X_3 + \beta_{12}X_1X_2 + \beta_{13}X_1X_3 + \beta_{23}X_2X_3 + \beta_{11}X^2_1 + \beta_{22}X^2_2 + \beta_{33}X^2_3 \quad (4.1)$$

Y denotes the expected response, βo denotes the model constant, X1, X2, and X3 are independent factors, β1, β2, and β3 denote linear coefficients, and β11, β12, and β13 denote quadratic coefficients (Rahman *et al.,* 2011). The results in Table 4.2 show that the experimental values obtained tend to agree very closely with the predicted values. The residual total of 0.01 further demonstrates how closely the projected values match the experimental value. Figure 4.3 displays a plot of the predicted values versus the experimental leaching efficiency. The bulk of the values are quite close to the straight line, indicating that the predicted values are consistent with the actual findings.

Table 4.2: Box-Behnken Design for Leaching Efficiency of Dolomite in HNO_3

Run	A (^oC)	B ($moldm^{-3}$)	C (minutes)	Experimental L E (%)	Predicted L E (%)	Residual
1	30	0.5	40	49.70	46.04	3.66
2	70	0.5	40	73.00	74.76	-1.76
3	30	2.5	40	87.00	85.24	1.76
4	70	2.5	40	99.00	102.66	-3.66
5	30	1.5	20	57.30	62.42	-5.12
6	70	1.5	20	97.70	97.40	0.30
7	30	1.5	60	81.70	82.00	-0.30
8	70	1.5	60	98.30	93.18	5.13
9	50	0.5	20	60.70	59.24	1.46
10	50	2.5	20	98.30	94.94	3.36
11	50	0.5	60	65.70	69.06	-3.36
12	50	2.5	60	99.00	100.46	-1.46
13	50	1.5	40	98.30	98.12	0.18
14	50	1.5	40	98.00	98.12	-0.12
15	50	1.5	40	98.10	98.12	-0.02
16	50	1.5	40	98.00	98.12	-0.12
17	50	1.5	40	98.20	98.12	0.08
Sum						**0.01**

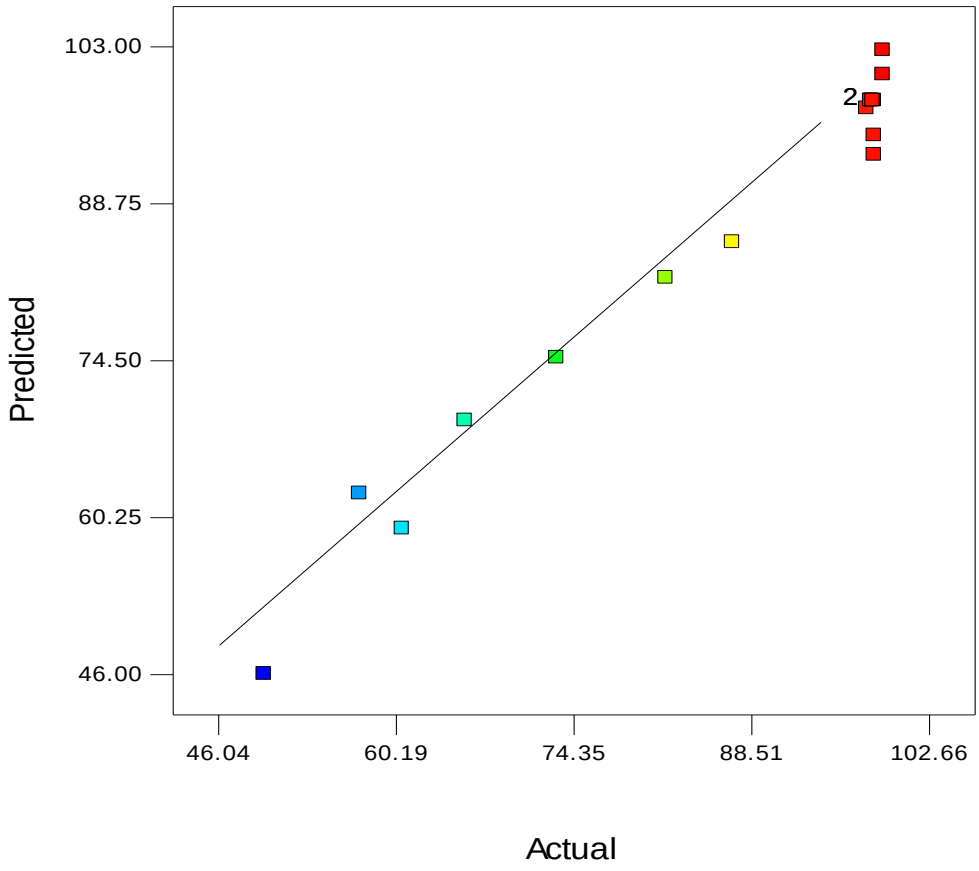

Figure 4.3: Predicted against Actual Leaching Efficiency

4.2.2 Response analysis for dissolution of dolomite in HNO_3

A quadratic model in equation (4.2) was generated by Box-Behnken experimental design which can predict the leaching efficiency in terms of the coded variable.

$$(Y\%) = +98.12 + 11.54A + 16.78B + 3.84C - 2.83AB - 5.95AC - 1.07BC - 9.06A^2 - 11.89B^2 - 5.31C^2 \quad (4.2)$$

Where Y is the leaching efficiency (%), A, B, and C are coded the temperature (^oC), coded concentration (M), and coded time (Mins) respectively. A final model equation (4.3) in terms of the real factors that predict the leaching efficiency when the variables are specific was also developed

$$(Y\%) = -111.73625 + 3.64875A + 61.64250B + 2.07825C - 0.14125AB - 0.014875AC - 0.053750BC - 0.022650A^2 - 11.88500B^2 - 0.013275C^2 \quad (4.3)$$

Where Y is the leaching efficiency (%), A, B, and C are the actual temperature (^oC), actual concentration (M) and actual time (min) respectively.

In table Table 4.3, the F-value from ANOVA was applied to test the second-order response surface model equation 4.4. This demonstrated that, at a 95 % confidence level, the regression is statistically significant. Model significance is indicated by the model's F-value, which is 32.99, there is only an 0.01 % chance of noise. Any model term must have ProbF less than 0.05 to be significant. Hence, the key model terms are A, B, C, AC, A^2, B^2, and C^2 (Table 4.3). The regression coefficient (R^2) value of 0.977 indicated that the experimental result was well-fitted into the model (Table 4.4). The model was reduced from equation 4.2 to equation 4.4 to enhance it because the lack of fit test F-value of 2208.68 indicates that it is considerable.

$$(Y\%) = +98.12 + 11.54A + 16.78B + 3.84C - 5.95AC - 9.06A^2 - 11.89B^2 - 5.31C^2 \quad (4.4)$$

Table 4.3: ANOVA for the Quadratic Model of Dolomite Dissolution

Source	Sum of Squares	Df	Mean Square	F Value	p-value Prob > F	
Model	4780.408	9	531.157	32.988	< 0.0001	Significant
A-Temperature	1064.911	1	1064.911	66.137	< 0.0001	
B-Concentration	2251.205	1	2251.205	139.813	< 0.0001	
C-Time	117.811	1	117.811	7.317	0.0304	
AB	31.923	1	31.923	1.983	0.2019	
AC	141.610	1	141.610	8.795	0.0209	
BC	4.623	1	4.623	0.287	0.6087	
A^2	345.615	1	345.615	21.465	0.0024	
B^2	594.750	1	594.750	36.938	0.0005	
C^2	118.720	1	118.720	7.373	0.0300	
Residual	112.7105	7	16.1015			
Lack of Fit	112.6425	3	37.5475	2208.6760	< 0.0001	Significant
Pure Error	0.0680	4	0.0170			
Cor Total	4893.1190	16				

Df = degree of freedom

Table 4.4: Lack of Fit Tests for the Leaching Efficiency of Dolomite in HNO_3

Source	SD	R-Squared	Adjusted R-Squared	Predicted R-Squared	Remarks
Linear	10.5946	0.7018	0.6330	0.5262	
2FI	11.3183	0.7382	0.5811	0.2803	
Quadratic	4.0127	0.9770	0.9474	0.6317	**Suggested**
Cubic	0.1304	0.9999	0.9999		Aliased

SD = Standard deviation

4.2.3 Effect of process variable on the leaching efficiency of dolomite in HNO_3

Figure 4.4 indicates that temperature has a positive influence on the leaching efficiency, as temperature increases from 30 ^oC to 70 ^oC the leaching efficiency increases from 77 % to 95 % this could be because as temperatures increase the reactant (dolomite particles) gain more kinetic energy to react. Figure 4.4 also shows that concentration has a positive effect on the leaching efficiency as it increases from 0.5 $moldm^{-3}$ to 2.5 $moldm^{-3}$, leaching efficiency also increases from 75 % to 99 % which is because as concentration increases the bond-breaking between the dolomite particles and bond formation between the products is sufficiently high. It is observed in Figure 4.4 that as time shows an increase from 20 to 60 minutes, the leaching efficiency also shows an increase from 90 % to 99 % which implies that at a prolonged time the dolomite particles have sufficient time to react. The P-value (0.0001) for both temperature and concentration and the P-value (0.00304) for the effect of time shows that all three parameters have a positive effect on the leaching efficiency.

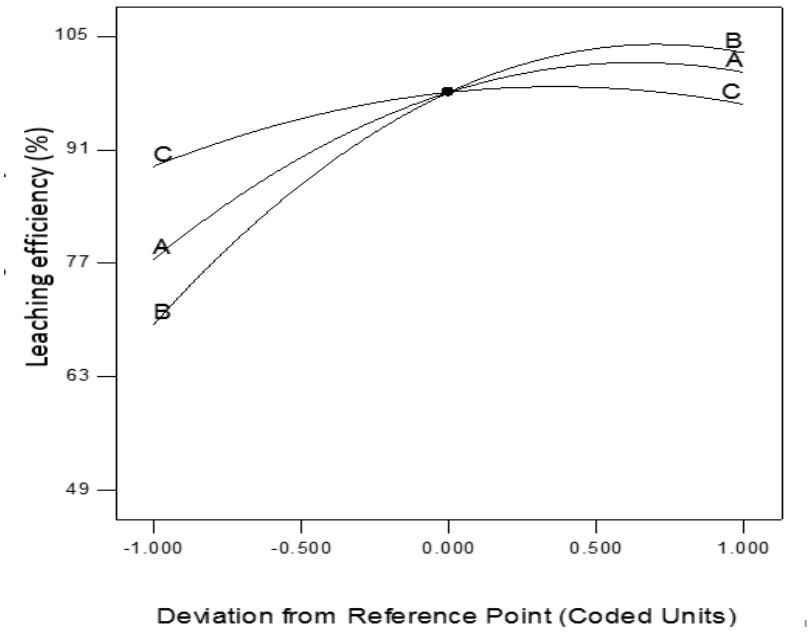

Key	
A	Temperature
B	Concentration
C	Time

Figure 4.4: Influence of Dissolution Temperature, Concentration, and Time on Leaching Efficiency

4.2.4 Interactive effect of temperature and concentration on the leaching efficiency

The interactive influence of dissolution temperature and concentration on the leaching efficiency of dolomite in HNO_3 is clearly shown in Figure 4.5. There is an improvement in the leaching efficiency from 56.13 % to 95.50 % as there is a rise in temperature from 30 ^oC to 70 ^oC and the concentration increased from 0.5 to 2.5 $moldm^{-3}$ while the time remained constant at 40 minutes. This could be as a result of improvement in the effective collision of dolomite particles resulting from a rise in temperature and concentration.

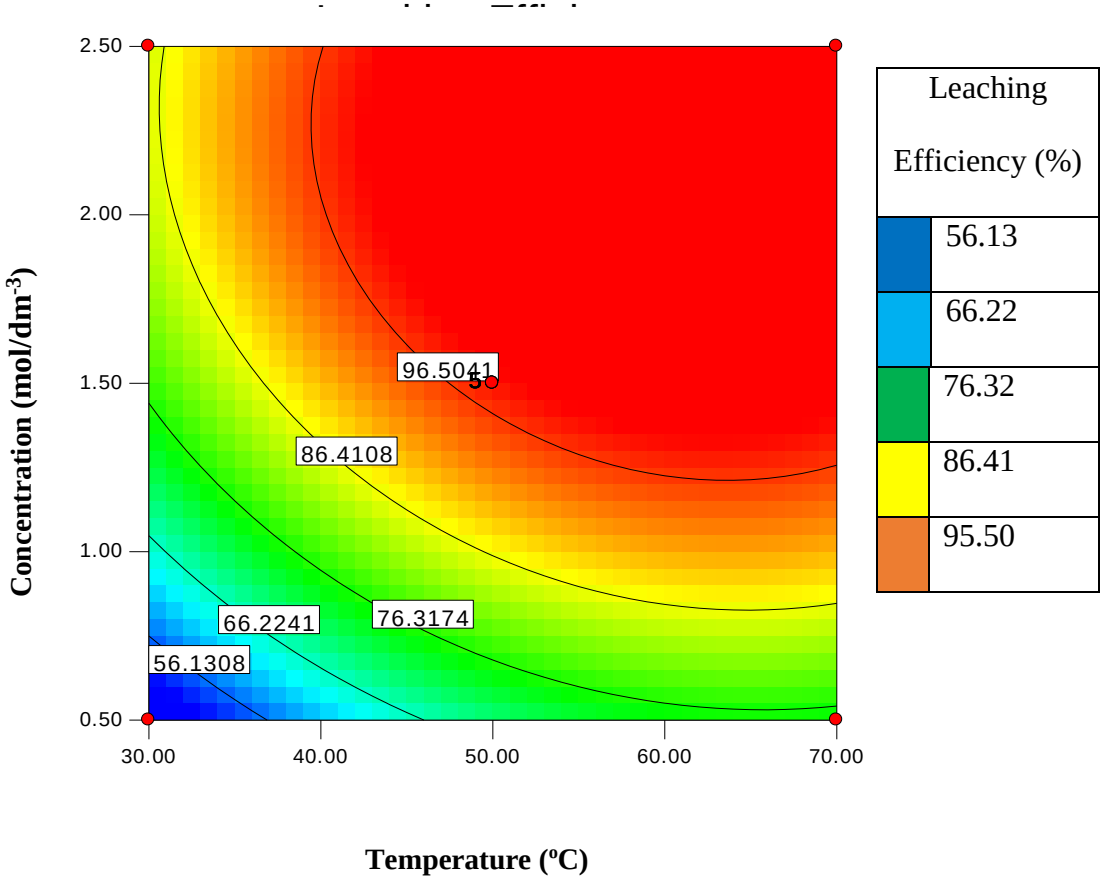

Figure 4.5: Contour Plot of the Interactive Influence of Temperature and Concentration on Leaching Efficiency

Figure 4.6 shows that the leaching efficiency increased from 68.99 % to 95.23 % as there was a rise in temperature from 30 to 70 ^{o}C, while there was also an increment in time from 20 to 60 minutes. The positive influence of the leaching time and temperature on the leaching efficiency could be due to a rise in temperature, which increased the reaction speed thereby leading to the conversion of reactants to products in time.

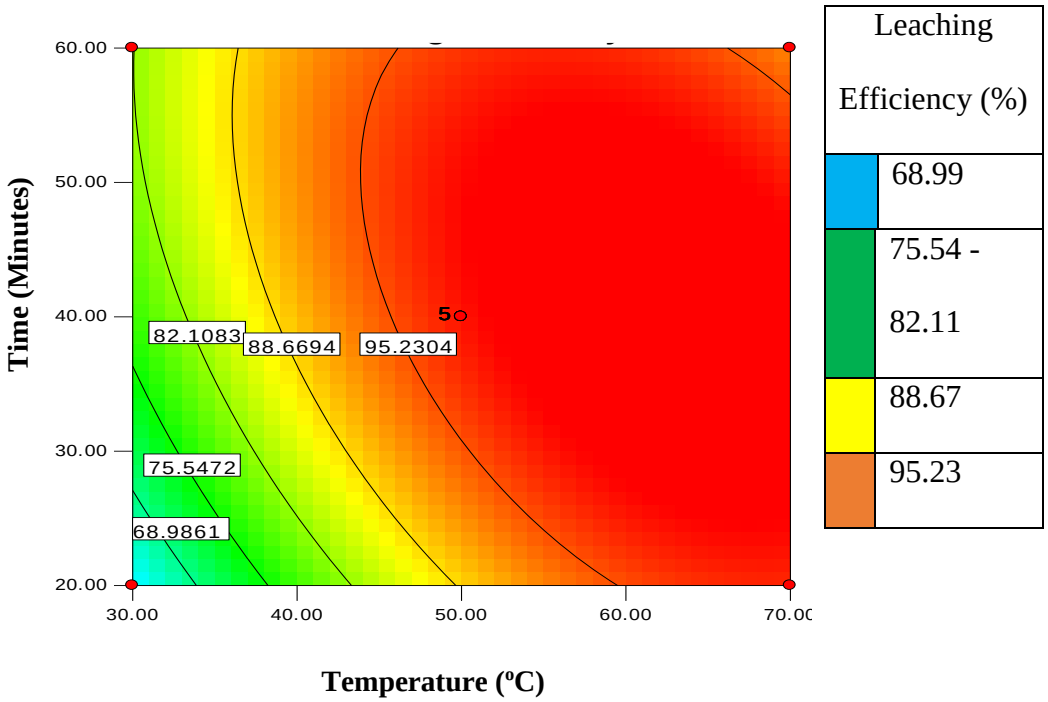

Figure 4.6: Contour plot of the Interactive Influence of (a) Temperature and Concentration, (b) Temperature and Time on Leaching Efficiency

Figure 4.7 indicates a arise in the leaching efficiency from 66.78 to 96.95 % as the concentration of HNO_3 increases from 0.5 to 2.5 $moldm^{-3}$, while the leaching time increases from 20 to 60 Mins. The improvement in the leaching efficiency as time changes from 20 to 60 Mins could be due to the abundance of HNO_3 acid to dissolve the dolomite. This could be attributed to the availability of more acid to dissolve the dolomite in sufficient time.

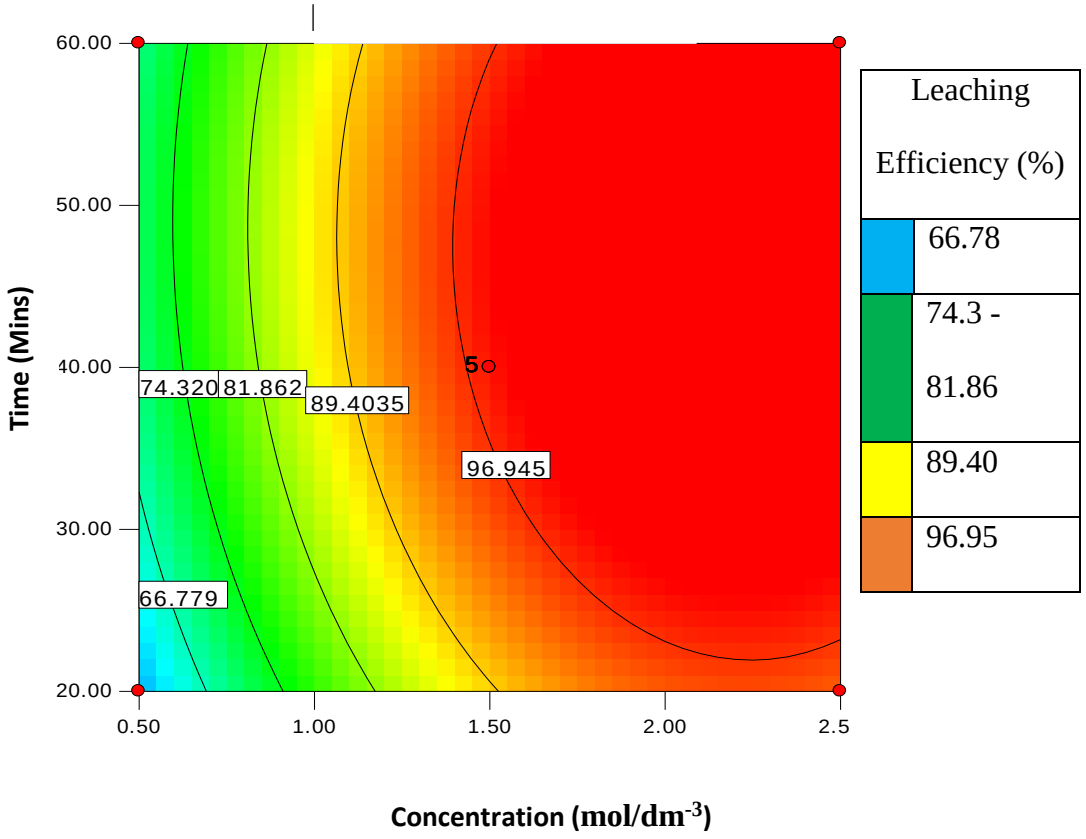

Figure 4.7: Contour Plot presenting the Interactive Influence of Concentration and leaching Time on Leaching Efficiency

4.2.5 Experimental validation

Following the statistical analysis of the leaching efficiency of dolomite in HNO_3, a numerical optimization method was applied to the optimization process of parameters. The following criteria were selected for the optimization process; Optimizing the effect of temperature within the range of 30 to 70 ^{O}C the concentration of acid within the range of 0.5 to 2.5 $moldm^{-3}$, and minimizing the leaching time at 20 minutes helps in realizing the objective of maximizing the leaching efficiency. The optimum leaching efficiency of 99.16 % was predicted by Design Expert 11.0 using the Box-Behnken Design method at a 55.32 ^{o}C leaching temperature, 2.22 $moldm^{-3}$ acid concentration, and 20 Minutes of leaching time with desirability of 1.00. An experimental run was then carried out to validate the data predicted

by the design. At the optimum prediction, a leaching efficiency of 98.6% was achieved, which is very close to the 99.16 % predicted with 0.56 % experimental error.

4.3 Optimization of Process Variables on the Dissolution of Dolomite in Hydrochloric (HCl)/Perchloric ($HClO_4$) Acid System

4.3.1 Box-Behnken design

Preliminary experimental investigation on one-factor-at-a-time shows that leaching time, HCl/$HClO_4$ concentration, and temperature all show a positive contribution to dissolution efficiency. Therefore, these factors were selected for further study. The leaching time was investigated from 20 to 60 minutes, the temperature was studied from 30 to 70 ^{o}C, and the HCl and $HClO_4$ concentrations were varied from 0.5 to 2.5 moldm^{-3}. Table 4.5 shows the 17 experimental conditions obtained from the Box-Behnken Design matrix. Each of the independent variables was studied at three stages, coded as -1, 0, and +1, which are the low, center, and high values, respectively.

Table 4.5: Box-Benkhen Experimental Design of Dolomite Dissolution Leaching Efficiency

Run	Temp (ºC)	Conc. (mol/dm^{-3})	Time (Minutes)	Actual L.E (%)	Predicted L.E (%)	Residual
1	30	0.5	40	54.30	52.18	2.13
2	70	0.5	40	80.00	80.20	-0.20
3	30	2.5	40	91.00	90.80	0.20
4	70	2.5	40	99.00	101.13	-2.13
5	30	1.5	20	62.30	66.51	-4.21
6	70	1.5	20	99.00	100.89	-1.89
7	30	1.5	60	92.70	90.81	1.89
8	70	1.5	60	99.00	94.79	4.21
9	50	0.5	20	64.00	61.91	2.09
10	50	2.5	20	98.70	94.69	4.01
11	50	0.5	60	70.00	74.01	-4.01
12	50	2.5	60	98.70	100.79	-2.09
13	50	1.5	40	98.70	98.72	-0.02
14	50	1.5	40	99.00	98.72	0.28
15	50	1.5	40	98.60	98.72	-0.12
16	50	1.5	40	98.80	98.72	0.08
17	50	1.5	40	98.50	98.72	-0.22
Sum						**0**

L.E: Leaching Efficiency

4.3.2 Regression model and statistical analysis

Seventeen (17) experimental runs were produced using the experimental design performed by Design Expert 11.0. To obtain the graphical analysis and regression, the responses (leaching efficiencies) from the experimental findings were simulated. The highest coefficient of regression (R^2) of 0.98, a predicted R-Squared value of 0.63, and an adjusted R-Squared of 0.95 led to the selection of a quadratic model (Table 4.6). The relationship between the dependent and independent factors is best described by the quadratic regression model, as shown in Equation 4.5.

$$Y= \beta_o + \beta_1X_1 + \beta_2X_2 + \beta_3X_3 + \beta_{12}X_1X_2 + \beta_{13}X_1X_3 + \beta_{23}X_2X_3 + \beta_{11}X^2_1 + \beta_{22}X^2_2 + \beta_{33}X^2_3 \quad (4.5)$$

Where Y is the output, β_o is the model constant, the independent factors are X_1, X_2, and X_3, β_1, β_2, β_3 are linear coefficients, and the coefficients of quadratic are depicted β_{11}, β_{12}, and β_{13} (Rahman *et al.*, 2011). Table 4.5's findings demonstrate that the established quadratic model in equations (4.6 and 4.7) was successful in the prediction of the leaching efficiency under different experimental settings. With a residual value of 0, the predicted leaching efficiency values are quite close to the experimental findings. In Figure 4.8, the leaching efficiency experimental findings are plotted against the expected values.

Coded Equation:

$$L.E(\%) = +98.72 + 9.59A + 14.89B + 4.55C - 4.42AB - 7.60AC - 1.50BC - 6.12A^2 - 11.52B^2 \quad - 4.35C^2 \quad (4.6)$$

Actual Equation:

$$L.E(\%) = -97.35500 + 3.10187A + 63.51750B + 2.15950C - 0.22125AB - 0.019000AC - 0.07500BC - 0.015306A^2 - 11.52250B^2 - 0.010869C^2 \quad (4.7)$$

Table 4.6: Statistical Model Summary

Source	SD	R^2	Adjusted R^2	Predicted R^2	
Linear	9.9289	0.67602	0.6012	0.4524	
2FI	9.8143	0.7565	0.6104	0.2918	
Quadratic	3.6408	0.9765	0.9464	0.6252	Suggested
Cubic	0.1924	0.99996	0.99985		Aliased

SD = Standard Deviation

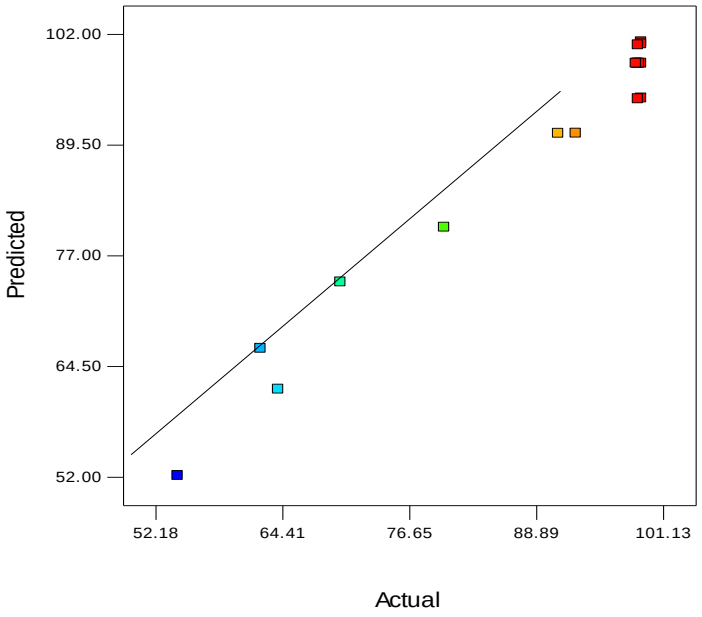

Figure 4.8: Predicted against Actual Leaching Efficiency

The developed models in equations (4.6 and 4.7) are relevant, with a 32.38 F-value. A Model F-Value this large might be caused by noise only 0.01 % of the time. A, B, C, AB, AC, A^2, B_2, and C^2 are significant model terms as shown because model terms are only deemed significant when the values of Prob > F are less than 0.0500. (Table 4.7). As a result, model

reduction (Equation 4.6) was done to improve the model (Equation 4.8). This study's ratio of 17.530 denotes a sufficent signal, hence this model can be used to explore the design space.

Reduced Coded Equation:

$$LE(\%) = +98.72 + 9.59A + 14.89B + 4.55C - 4.42AB - 7.60AC - 6.12A^2 - 11.52B^2 - 4.35C^2 \quad (4.8)$$

Where A, is the temperature, B is the Concentration and C is the time

Table 4.7: Response Surface Quadratic Model from ANOVA

Source	Sum of Squares	Df	Mean Square	F Value	p-value Prob > F	
Model	3862.8650	9	429.2072	32.3789	< 0.0001	Significant
A-Temperature	735.3613	1	735.3613	55.4747	0.0001	
B-Concentration	1773.1010	1	1773.1010	133.7606	< 0.0001	
C-Time	165.6200	1	165.6200	12.4942	0.0095	
AB	78.3225	1	78.3225	5.9086	0.0454	
AC	231.0400	1	231.04	17.4294	0.0042	
BC	9.0000	1	9.0000	0.6789	0.4371	
A^2	157.8316	1	157.8316	11.9066	0.0107	
B^2	559.0232	1	559.0232	42.1720	0.0003	
C^2	79.58213	1	79.5821	6.0036	0.0441	
Residual	92.7905	7	13.2558			
Lack of Fit	92.6425	3	30.8808	834.6171	< 0.0001	Significant
Pure Error	0.1480	4	0.0370			

Df = degree of freedom

4.3.3 Effect of process variable on the leaching efficiency of dolomite in HCl-$HClO_4$

The single influence of acid concentration, temperature, and time on the dolomite leaching efficiency in HCl-$HClO_4$ is plotted in Figure 4.9. The leaching efficiency is positively influenced by temperature, time, and concentration because it rises as each of those variables does. This might be because the reactant molecules have more kinetic energy to contribute to the reaction at high temperatures. At higher acid concentrations, both the bond breaking between the reactants and the bond formation between the products are sufficiently high, and at prolonged leaching time, the dolomite has sufficient time to go into the solution. The single effects of concentration, temperature, and time are relevant, with a p-value of 0.0001, < 0.0001, and 0.0095 respectively. The influence of concentration is the most significant factor, followed by temperature, and time is the least significant process variable. The leaching efficiency of the temperature curve ranges from 83.01 to 98.9 %, the concentration curve ranges from 72.31 to 98.9 % and the time curve ranges from 89.82 to 98.9 %.

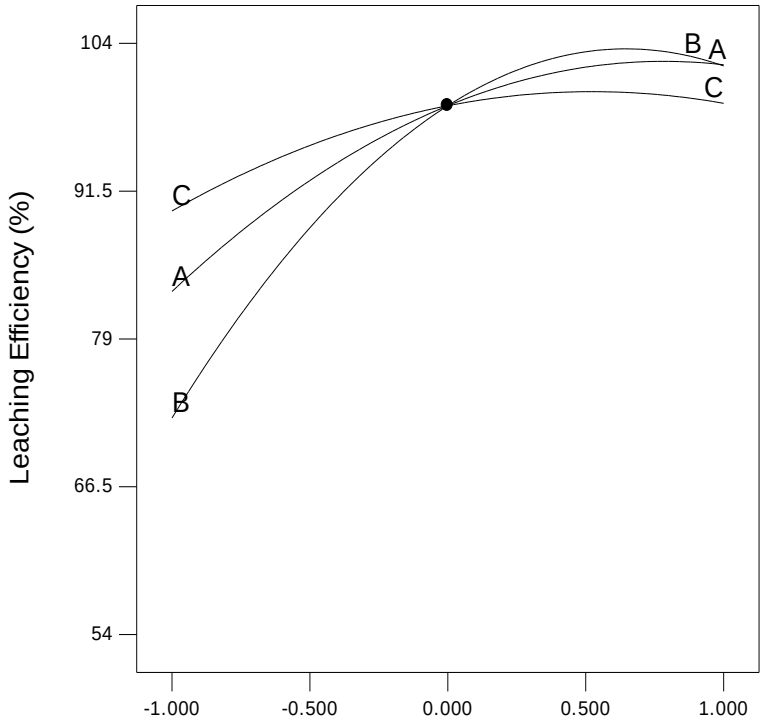

Key	
A	Temperature
B	Concentration
C	Time

A: Temperature = 50 ^{o}C, B: Concentration: 1.5 moldm^{-3}, Time = 40 Mins

Figure 4.9: Effect of Concentration, Temperature, and Time on Leaching Efficiency

4.3.4 Interactive effect of the process variables on the leaching efficiency of dolomite

The contour plot illustrating the interaction between temperature and acid concentration on the dolomite leaching efficiency in an HCl-$HClO_4$ mixture is shown in Figure 4.10. As the temperature rises from 30 to 70 ^{o}C and the concentration rises from 0.5 to 2.5 moldm^{-3}, the leaching efficiency increased from 61.06 to 96.62 % while the reaction time remained constant at 40 minutes. The interactive effect of concentration and temperature has a positive contribution to the prediction of the leaching efficiency of dolomite in a mixture of HCl-$HClO_4$. The three-dimensional plot of the interactive effect is shown in Figure 4.10b

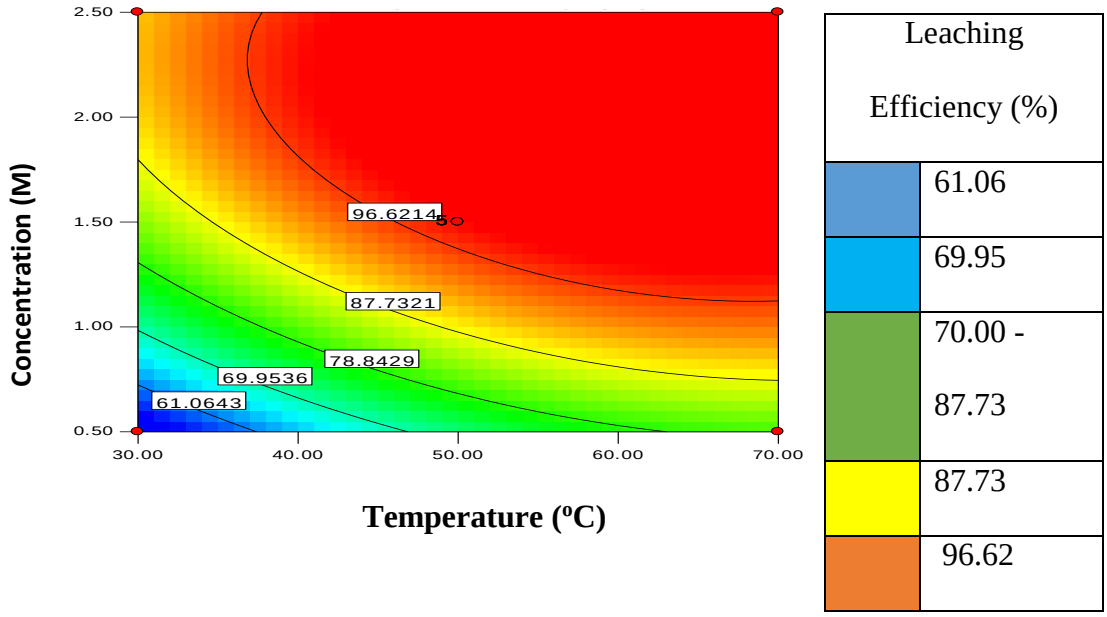

Figure 4.10: (a) Contour of the Interactive Influence of Temperature and Concentration on the Leaching Efficiency

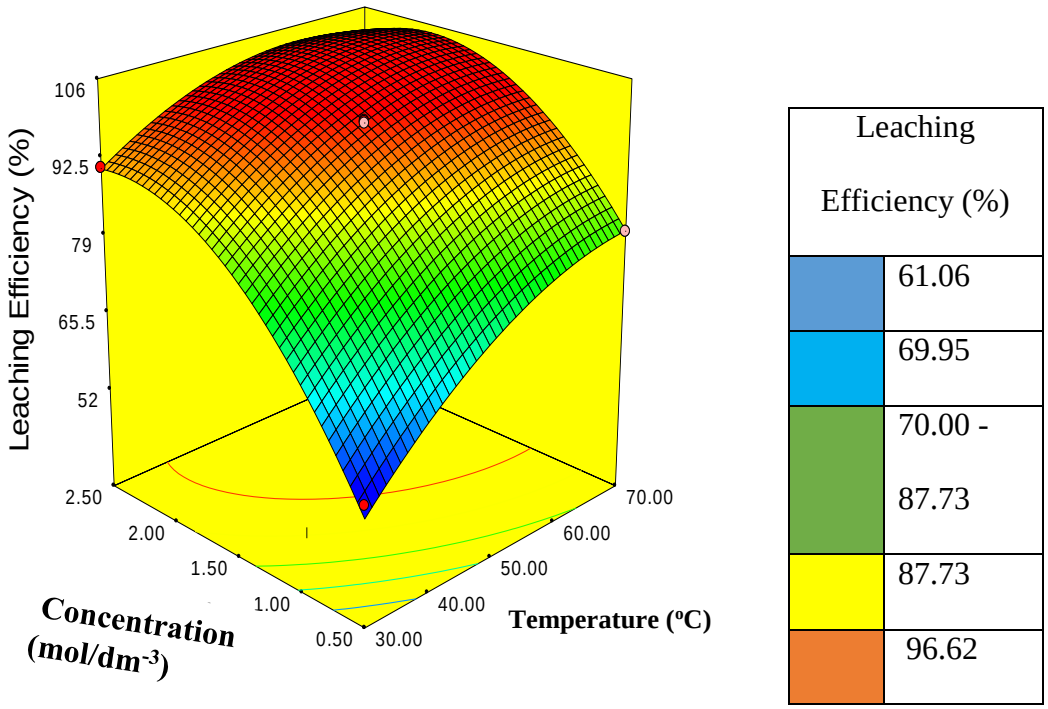

Figure 4.10: (b) 3D of the Interactive Influence of Temperature and Concentration Leaching Efficiency

Time and concentration interact to affect the efficiency of leaching, as shown in Figures 4.11a and 4.11b. The leaching efficiency shows an improvement from 72.55 to 97.21 % with a

concentration rise from 0.5 to 2.5 moldm^{-3} and a reaction time increase from 20 to 60 minutes, while the temperature remained constant at 40 ^{o}C. The outcome of the ANOVA in Table 4.8 confirmations that the whole contribution from the interactive influence of time and concentration on the developed models (3 and 4) is insignificant with a P-value of 0.4371, hence the interaction of temperature and time was not considered for model reduction.

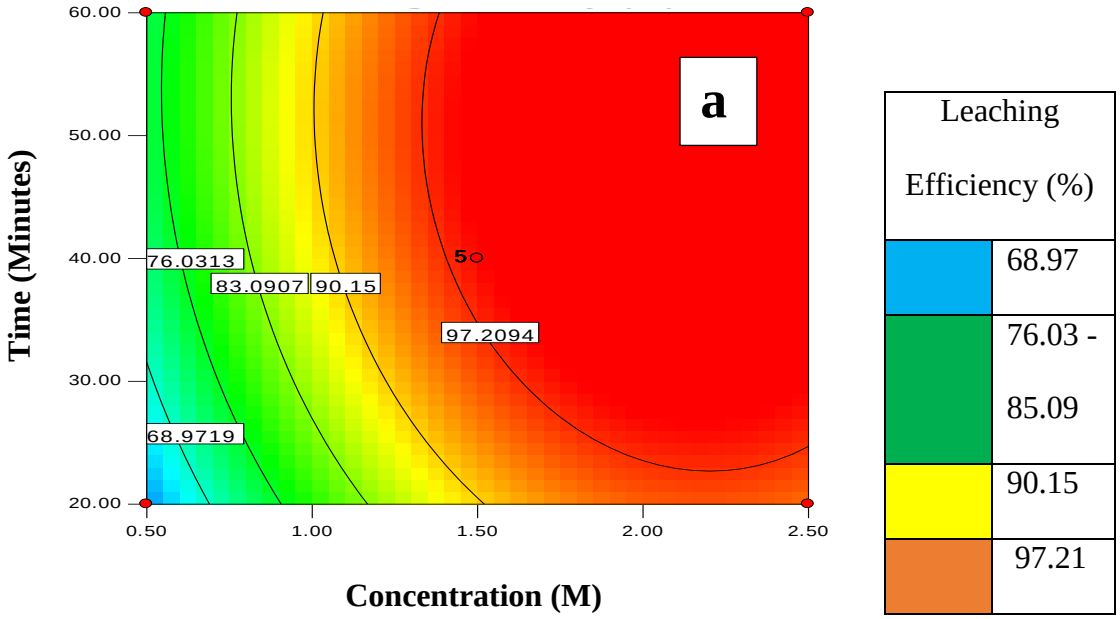

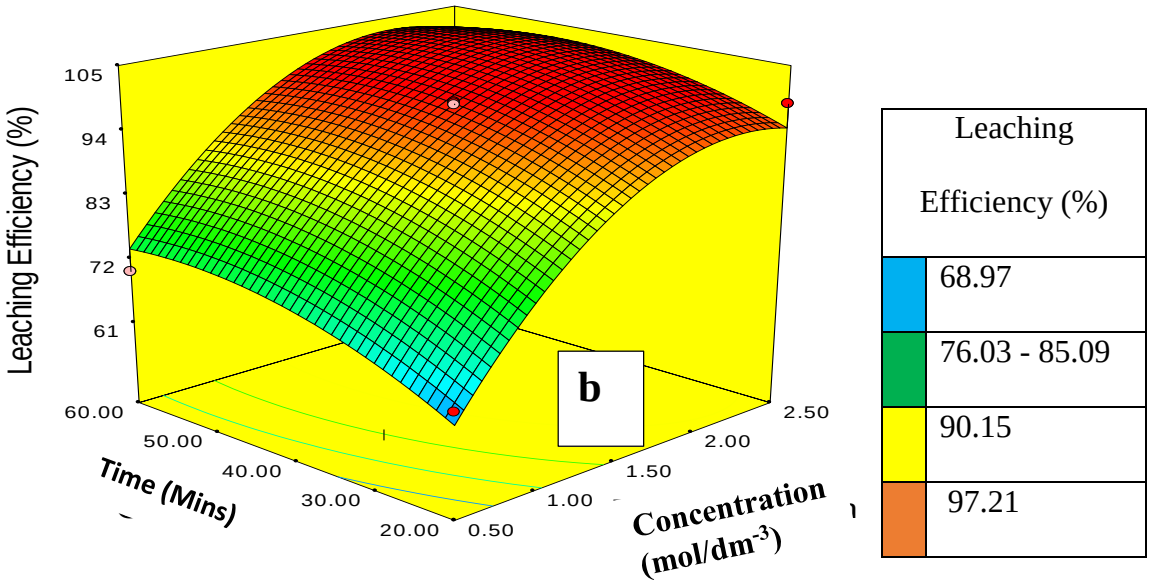

Figure 4.11: (a) Contour Plot of the Interactive Influence of Time and Concentration, (b) 3D plot of the Interactive Effect of Time and Concentration

Figure 4.12 contour plot illustrates how time and temperature interact to affect how effectively dolomite dissolves in HCl-$HClO_4$ solution. When the temperature of the reaction rises from 30 to 70 ^{o}C and the reactant molecules have enough opportunity to collide with one another between 20 and 30 Mins, the leaching efficiency increases from 72.55 to 96.68 % as a result of an increase in the kinetic energy of the reactant molecules.

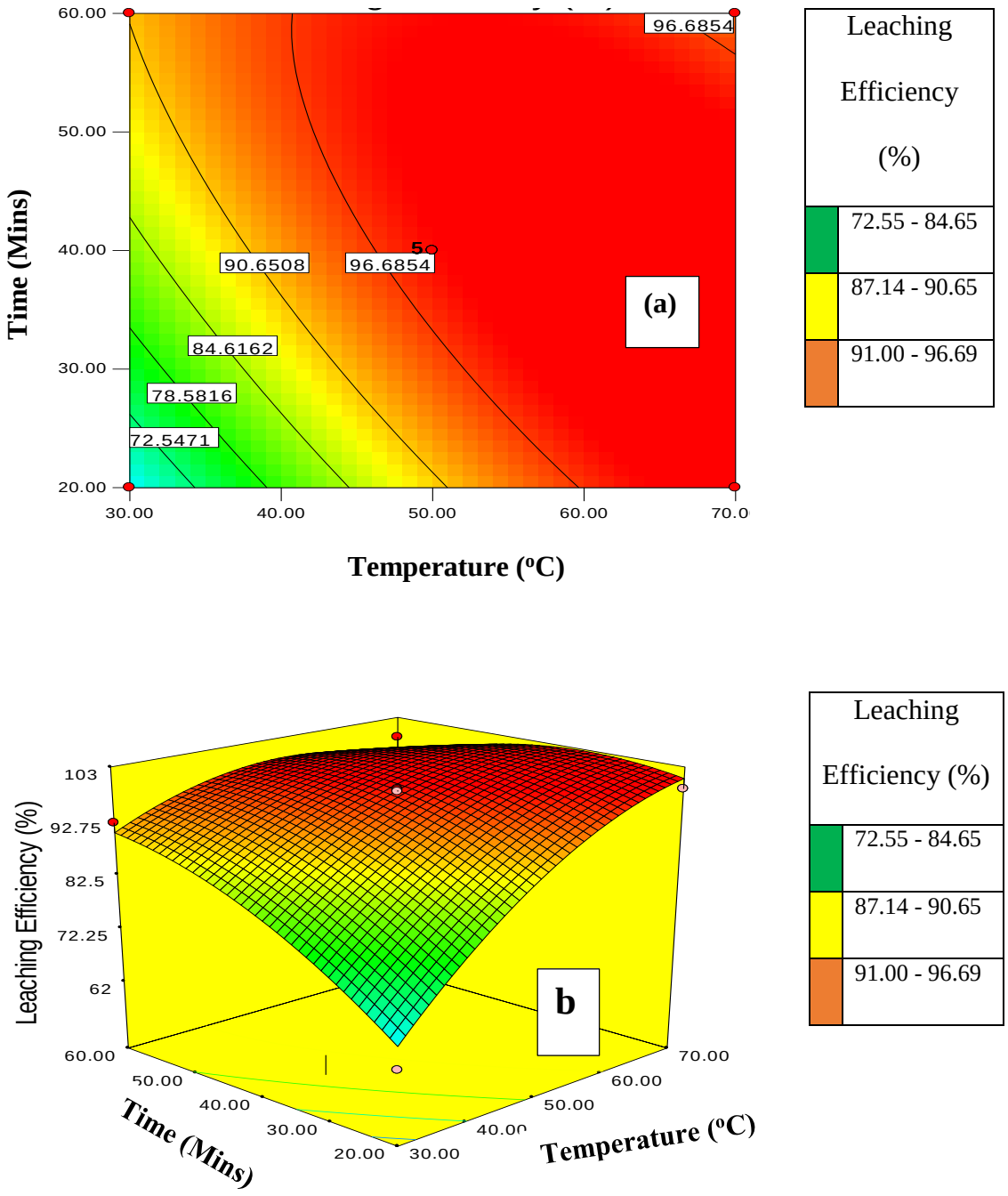

Figure 4.12: (a) Contour Plot of the Interactive Influence of Temperature and Time, (b) 3D plot of the Interactive Influence of Temperature and Time

4.3.5 Experimental validation

The numerical optimization of the experimental leaching efficiency of dolomite in HCl-$HClO_4$ was carried out by simulation using Design Expert 11.0 software. To get the best point prediction of the leaching efficiency, the HCl-$HClO_4$ concentration was optimized from 0.5 to 2.5 $moldm^{-3}$, the temperature was optimized from 30 to 70 ^oC, and the time of reaction was set at 20 minutes minimum. Point prediction of leaching efficiency was proposed at a temperature of 57 ^oC, time of 20 minutes, and HCl-$HClO_4$ concentration of 2.03 $moldm^{-3}$. A laboratory experiment was conducted at the predicted process conditions to determine the accuracy of the prediction. A leaching efficiency of 98.3 % was validated at desirability of 1, this is a bit close to the 99.7 % predicted by the design model with only a 1.4 % error.

4.3.6 Comparison between XRD of dolomite, residue from HNO_3 route and residue from HCl-$HClO_4$

It was reported in the literature that dolomite is soluble in mineral acids while quartz is insoluble (Yildrim *et al.,* 2010; Pultar *et al.,* 2019; Baba *et al.,* 2014; Are *et al.,* 2021). The reaction mechanism developed (equations 4.9 to 4.16) in this study also shows that dolomite reacts with HNO_3 and HCl-$HClO_4$. The XRD spectra presented in Figure 4.13 also verify this claim. Dolomite ore was subjected to XRD analysis before dissolving it in HNO_3 and HCl-$HClO_4$. After the dissolution at the optimum points, the undissolved component was analyzed using XRD for identification of the component left.

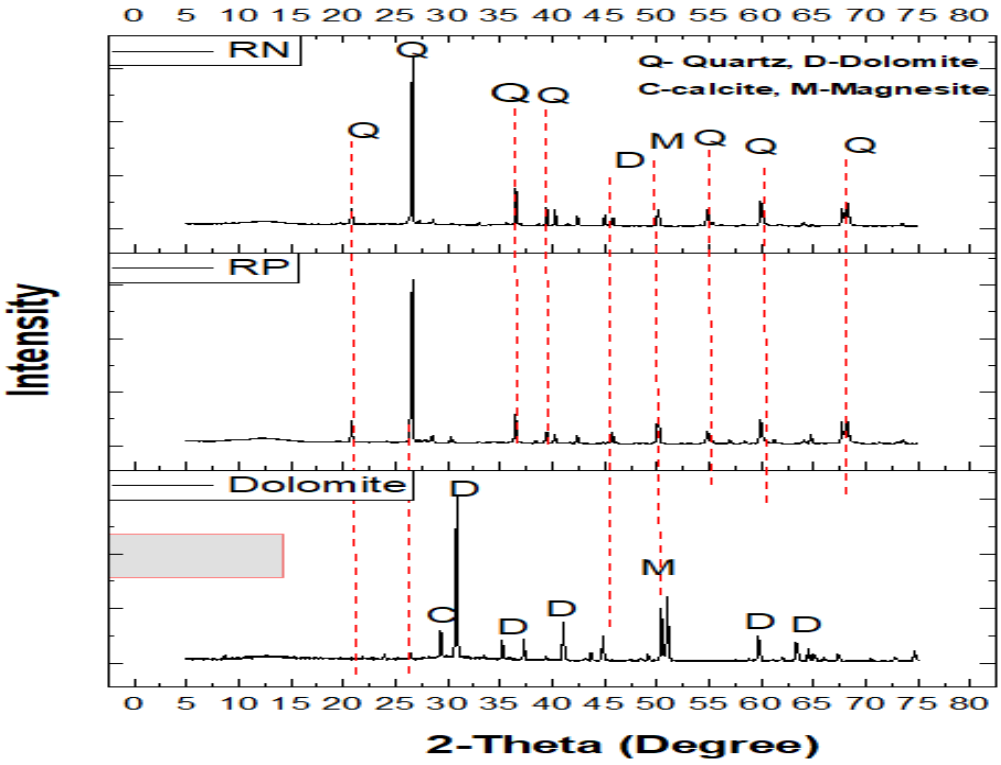

Figure 4.13: XRD Analysis of Dolomite, RN and RP

Table 4.8: Mineral Phase Composition of Dolomite Ore and Residues

Mineral Phase /2-Theta (2θ)	D. O	R .P	R.N
D (30.82^0)	P.P	ABS	ABS
D (45.00^0)	ABS	P.P	P.P
C (29.32^0)	P.P	ABS	ABS
M (50.98^0)	P.P	S.P	S.P
Q (21.91^0)	S.P	ABS	ABS
Q (20.81^0)	ABS	P.P	P.P
Q (26.61^0)	ABS	P.P	P.P
Q (26.61^0)	ABS	P.P	P.P

D.O: Dolomite Ore, R.P: Residue from HCl-$HClO_4$, R.N: Residue from HNO_3, P.P: Prominent peak, S.P: Smaller Peak, ABS: Absent.

The mineral phase composition of dolomite ore and residues is presented in Table 4.8. At the diffraction angle of 30.82^{o}, the dolomite mineral phase with prominent peaks is present in the dolomite ore while it is absent in both R.P and R.N, this could be a result of the dissolution of the dolomite phase in the mineral acids. However, at a diffraction angle of 45 ^{o}, smaller peaks of the dolomite mineral phase were only present in both R.P and R.N but absent in the dolomite ore, this implies that only a small fraction of dolomite was left undissolved in the residue. The calcite mineral phase is present at the diffraction angle of 29.32^{0} in dolomite ore but absent in the R.P and R.N, this is an indication that all the calcite reacted with the mineral acids. The magnesite mineral phase corresponds to a diffraction angle of 50.98^{0}, prominent peaks of the M were observed in dolomite ore while smaller peaks are present in both R.N and R.P. This shows that a larger proportion of the magnetite went into the solution while only a small fraction is left undissolved in the residue. The quartz mineral phase with a small peak at the diffraction angle of 21.91^{0} is only present in the dolomite ore, but absent in the R.P and R.N, this shows that the dolomite ore has very small impurities. Prominent quartz mineral peaks at the diffraction angles of 20.81^{0}, 26.61^{0}, and 26.61^{0} were identified in both R.P and R.N but absent in the dolomite ore, this is because all other mineable phases were able to dissolve in the mineral acid leaving behind the quartz.

4.4 Kinetic Investigation of the Interaction between Trioxonitrate (V) Acid (HNO_3) and Dolomite Ore

The investigation of dissolution kinetics was carried out for proper understanding of reaction mechanism between trioxonitrate (V) acid (HNO_3) and dolomite ore.

4.4.1 Effect of trioxonitrate (v) acid concentration on the dissolution of dolomite

The stoichiometric Equation (4.9) governs the interaction between Dolomite and HNO_3 solution

$$4HNO_{3(aq)} + CaCO_3\,MgCO_{3(S)} \rightarrow Mg(NO_3)_{2(aq)} + Mg(NO_3)_{2(aq)} + 2H_2O + 2CO_2 \quad (4.9)$$

Equation 4.9 shows that the reactions of calcium carbonate and magnesium carbonate with HNO_3 occur in two stages.

(Appendix-A1) Figure 4.14 shows the plot of the dolomite fraction that reacted with the concentration of HNO_3 which was varied from 0.5 and 2.5 moldm^{-3}. It is evident that the fraction of dolomite that has reacted with time is enhanced by an increase in acid concentration. This is in line with the findings of Baba *et al*. (2014). Pultar *et al*. (2019) found that the rate of dolomite dissolution increases as hydrogen ion (H^+) concentration increases. The result showed that the aim of increasing the fraction of dolomite that reacted and reducing reaction time was achieved at 0.995 fractions in 60 Mins, with a reaction temperature of 55 ^oC and a concentration of 2.5 moldm^{-3}. Slightly higher than 0.8 fractions of reacted dolomite recorded by Pultar *et al*. (2019) in 0.1 moldm^{-3} concentration at 25 hours reaction time and 4^oC reaction temperature. 0.759 portion of reacted dolomite at 120 Mins in 2 moldm^{-3} of HCl was recorded by Baba *et al.* (2014). In Figure 4.14 and Appendix-A1, there is a steady increase in the fraction of dolomite that dissolves in HNO_3 at 0.5 moldm^{-3} when the dissolution time is increased from 10 to 60 Mins, a similar increase was recorded for dissolution at concentrations of 1, 1.2, and 1.5 moldm^{-3}. However, fractions of dolomite that are dissolved at a concentration of 2 and 2.5 moldm^{-3} tend to have constant values at different dissolution times.

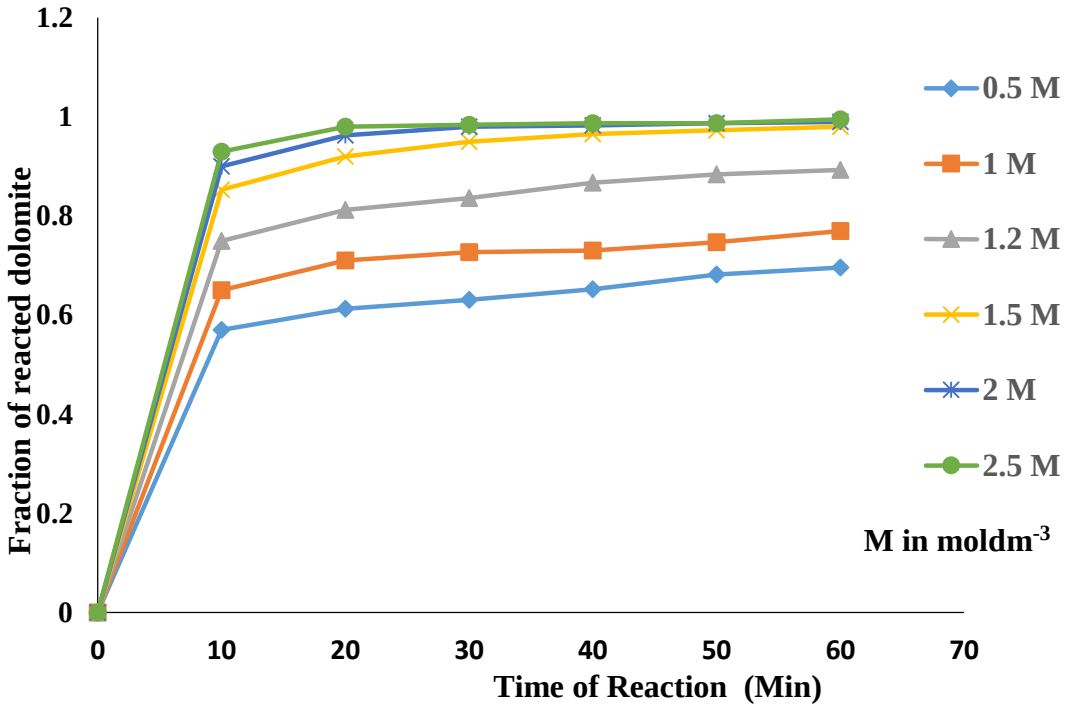

Figure 4.14: Influence of HNO_3 Concentration on the kinetic Study of Dolomite (Reaction Temperature of 55 ^oC and 3 g of Dolomite)

4.4.2 Effect of temperature on dissolution of dolomite in HNO_3

The process parameters on the study of the influence of temperature on the kinetic study were based on the optimization of the reaction of dolomite in HNO_3 (Appendix-A2). The temperature was varied between 30 to 70 ^oC leaching time interval of 20 to 60 Mins, while the concentration and agitation speed were kept constant at 2.2 $moldm^{-3}$ and 250 rpm, respectively. Figure 4.15 and Appendix-A2 show that the amount of dolomite that reacted increases from 0.777 to 0.993 with a temperature increases from 30 to 70 ^oC. This may be explained by the fact that as more reactants were changed into products, the uncatalyzed heterogeneous reaction system kinetic energy increased.

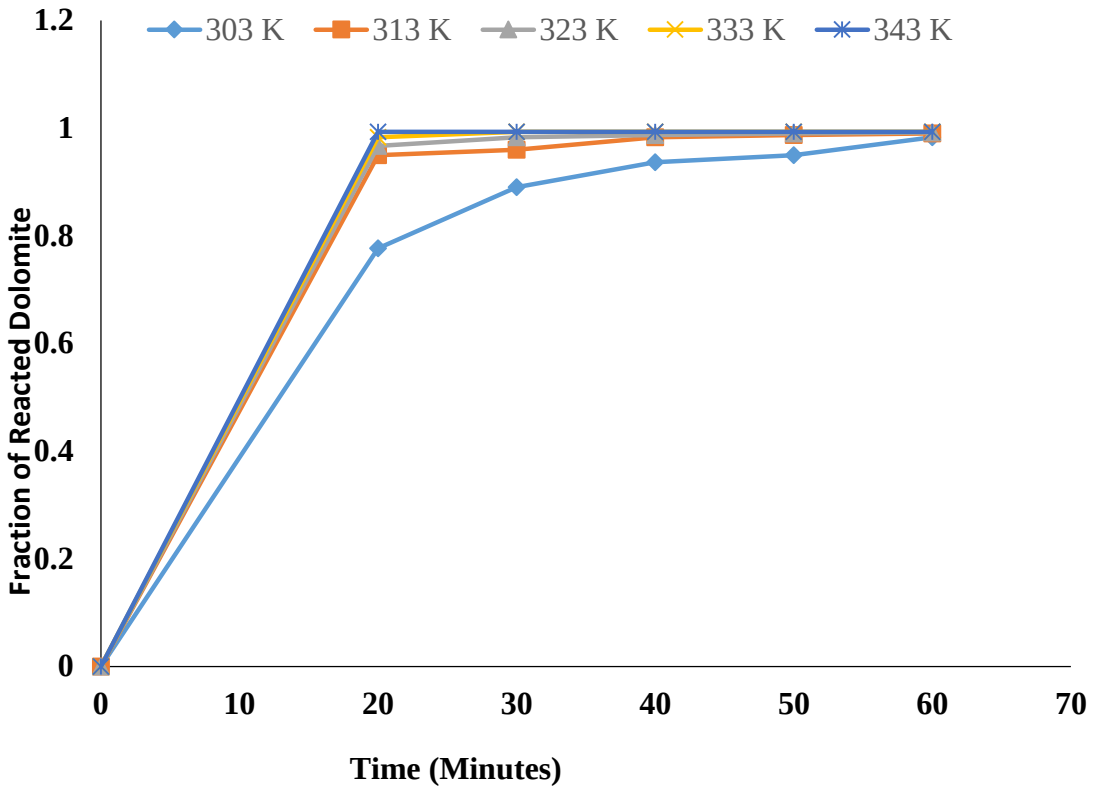

Figure 4.15: Influence of Temperature on the Efficiency of Dolomite Leaching (HNO_3 concentration of 2.22 moldm^{-3} and reacting dolomite of 3 g mass)

4.4.3 Kinetic Study of dissolution of dolomite in HNO_3

The chemical reaction for the dissolution of dolomite in HNO_3 is expressed by the mechanism in equations 4.10-4.17.

$$CaMg(CO_3)_2 + 4HNO_3 \rightarrow Mg(NO_3)_2 + Ca(NO_3)_2 + 2H_2O + 2CO_2 \quad (4.10)$$

$$CaMg(CO_3)_2 \rightarrow CaCO_3 + MgCO_3 \quad (4.11)$$

$$CaCO_3 \rightarrow Ca^{2+} + CO_3^{2-} \quad (4.12)$$

$$MgCO_3 \rightarrow Mg^{2+} + CO_3^{2-} \quad (4.13)$$

$$4HNO_3 \rightarrow 4NO_3^- + 4H^+ \quad (4.14)$$

$$Ca^{2+} + 2NO_3^- \rightarrow Ca(NO_3)_2 \quad (4.15)$$

$$Mg^{2+} + 2NO_3^- \rightarrow Mg(NO_3)_2 \quad (4.16)$$

$$4H^+ + 2CO_3^{2-} \rightarrow 2CO_2 + 2H_2O \quad (4.17)$$

Complex reactions are involved between dolomite and HNO_3. The shrinking core model (SCM) was applied to a mathematical model of the experimental outcome (data) to describe the reaction kinetics to have a simplified model. Three steps (4.18 – 4.20) are involved in the heterogeneous reaction between HNO_3 and dolomite. Film diffusion control (FDC) involves the movement of a liquid film around a solid particle (Gerald *et al.*, 2013).

$$X = 6bDC_A/P_oR_o^2t = k_1t \quad (4.18)$$

Surface chemical reaction control (SCRC):

$$1 - (1-x)^{1/3} = 6bDC_A/P_oR_o^2t = k_2t \quad (4.19)$$

Product layer diffusion control (PLDC):

$$1 + 2(1-x) - 3(1-x)^{2/3} = 6bDC_A/P_oR_o^2t = k_3t \quad (4.20)$$

Where P_o is the solid reactant's molar density ($molm^3$), Ro is a sphere's radius (m), b is the solid's stoichiometric coefficient, D is the effective diffusion coefficient (m^2/s), and C_A is the concentration of A in the bulk solution ($molm^3$), K_1, K_2, and K_3 are rate constants for FDC, SCRC, and PLDC, respectively (Ajemba and Onukwuli, 2012).

An SCM is usually assumed for spherical particles like dolomite. The linearization of a plot of the fraction of reacted dolomite at different concentrations and temperatures versus the time was investigated at the three conditions of Equations (4.18), (4.19), and (4.20). The experimental outcome (data) was examined for the line of best fits, which is also the slowest and rate-determining step. The reaction's sequence and activation energy were studied.

The apparent rate constants for the various models shown in Appendices A3 to A14 are compared in Table 4.9 using the slopes and regression coefficients (R^2). The study shows

that, in descending order, the PLDC, SCRC, and FDC were responsible for controlling the process. Hence, the experimental outcome (data) is best suited by the PLDC method, which is also the rate-determining step.

Table 4.9: Apparent Rate Constants, and Correlation Coefficients (R^2) at Different Temperatures and HNO_3 Concentrations

Process Variable	**Kinetic Equation**					
	$X = k_1t$ (FDC**)**		**$1 – (1 – X)1/3 = k_2t$ (**SCRC**)**		**$1 + 2(1 – X) – 3(1 – X) 2/3 = k_3t$ (**PLDC**)**	
Temp (^oC)	$K_1 \times 10^{-3}$	R^2	$K_2 \times 10^{-3}$	R^2	$K_2 \times 10^{-3}$	R^2
30	4.7200	0.867	8.078	0.9687	11.974	0.9804
40	1.0700	0.8959	4.126	0.9313	5.05	0.9699
50	0.5700	0.8147	2.833	0.9035	3.523	0.9397
60	0.2000	0.5000	1.318	0.5	1.608	0.7272
70	0.0000	0.0000	0.0000	0.0000	0.000	0.000
		0.7694		**0.8259**		**0.9043**
Conc ($moldm^{-3}$)						
0.5	2.4510	0.9782	1.4150	0.9829	1..2430	0.8924
1	2.040	0.8727	0.6680	0.9482	1.4200	0.9502
1.2	2.7490	0.9198	2.5590	0.9749	2.8310	0.9753
1.5	2.3110	0.8214	3.8720	0.9154	3.505	0.9535
2	1.5000	0.6721	2.7190	0.9656	3.9210	0.9363
2.5	0.9970	0.6235	2.1780	0.8327	3.9420	0.9363
		0.8146		**0.9366**		**0.9407**

4.4.4 Kinetics of the reaction between dolomite and HNO_3

The evaluation of the influence of acid concentration on the kinetic reaction of dolomite with HNO_3 was achieved by plotting the natural logarithm of apparent reaction rate constants

obtained from the slopes of Appendix-A14 against the natural logarithm of the concentrations (Appendix-A15). The sequence of a reaction tells us how quickly or slowly a reaction will take place. This confirms that the PLDC mechanism best explains the reaction mechanism. Using the model equation, Figure 4.16 was plotted. The slope was calculated as 0.9152 as a result. This implies that the reaction between dolomite and HNO_3 was first order in terms of the concentration of hydrogen ions. Baba *et al*. (2014) reported that dolomite dissolves in HCl in a half-order reaction, as opposed to Pultar *et al.* (2019) who reported that the reaction order is 0.77.

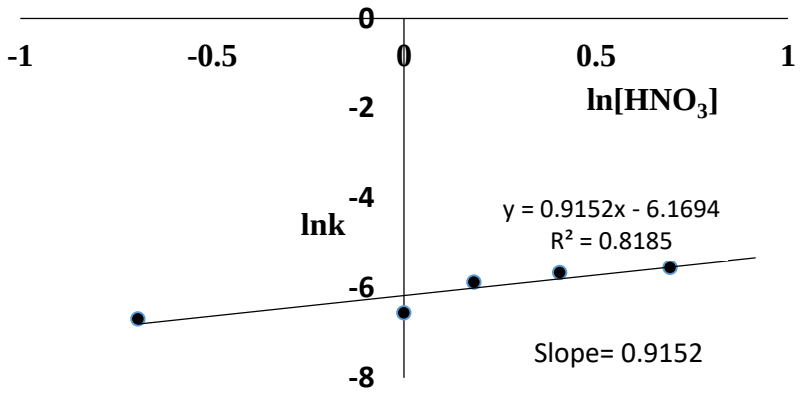

Figure 4.16: Plot of lnk Vs ln[HNO_3]

4.4.5 Activation energy required for the reaction of dolomite with HNO_3

The activation energy which is the minimum amount of energy necessary for a chemical reaction to occur, is determined by the Arrhenius equation (4.21). The equation establishes the relationship between temperature, activation (Ea) energy, and rate constant (K).

$$K = Aexp\left(\frac{-Ea}{RT}\right) \quad (4.21)$$

To evaluate the minimum energy requirement for the reaction between HNO_3 and dolomite the apparent rate constant estimated from the slopes of Appendix-A8 was plotted against the inverse of temperature, as shown in Figure 4.17. According to equation 4.21, which yields

$lnK = lnA - \frac{Ea}{RT}$ (4.22) and contrasts equation (4.22) with the equation of a straight line $Y = mX + C$, the slope of Figure 4.18 (Appendix-A16) is equal to $\frac{Ea}{R}$

$$Slope = -3200.10\ K, R = 8.31450\ Jmol^{-1}k^{-1}$$

$$Ea = -(-3200.10)Kx8.3145\ J/molK$$

$$26605.60\ Jmol^{-1}k^{-1}\ \ or\ 26.0KJmol^{-1}k^{-1}$$

The reaction between dolomite and HNO_3 yielded an activation of 26.605 $KJmol^{-1}k^{-1}$. This number falls below Pultar *et al.* (2019) reported an activation energy range of 30-57 KJmol-$1k^{-1}$. Since activation energy and reaction rate are strongly connected, the reaction system improved with reduced activation energy. The higher the reaction's pace and, thus, the higher fractions that respond, the lower the activation energy. The reaction between the molecules will continue once the activation energy barrier is overcome. A reduced barrier will allow more molecules to cross because they have sufficient energy. (Khan Academy, 2020). This could be the cause of the higher reaction fraction of dolomite (0.995) in the short reaction period of 60 mins as compared to the lower reaction fraction of 0.800 in the longer reaction time of 25 h by Pultar *et al.,* (2019). The activation energy (26.6050 $KJmol^{-1}$) between HCl and dolomite in this study is a little bit higher than the 20.77 KJ/mol reported by Baba *et al.,* (2014).

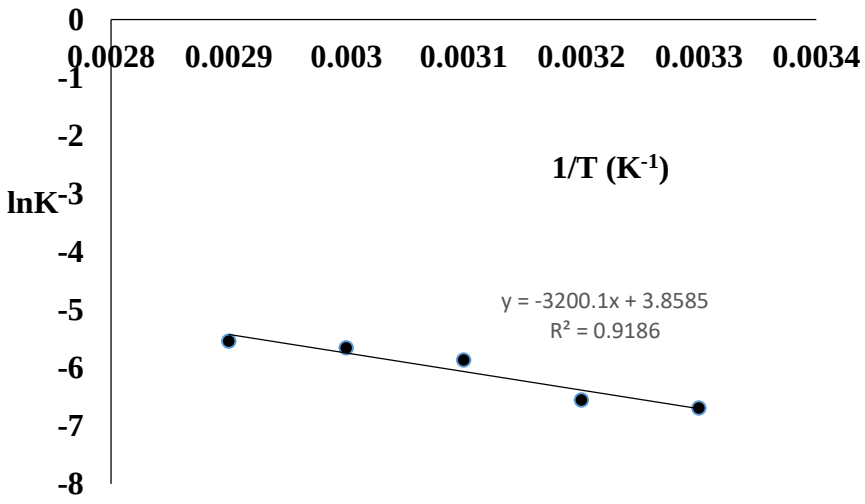

Figure 4.17: Plot of lnk Vs 1/T (K^{-1})

4.5 Dissolution Kinetic of Dolomite in HCl-$HClO_4$

The equation of reaction between dolomite and the HCl-$HClO_4$ system is represented in equations 4.23 and 4.24.

$$CaCO_3.MgCO_{3(S)} + 4HClO_4 \rightarrow Ca(ClO_4)_2 + Mg(ClO_4)_2 + 2H_2O + 2CO_2 \quad (4.23)$$

$$CaCO_3.MgCO_{3(S)} + 4HCl \rightarrow CaCl_2 + MgCl_2 + 2H_2O + 2CO_2 \quad (4.24)$$

From the equation of reaction, four reaction stages occur, which are: reaction between calcium carbonate and perchloric acid, the reaction between $MgCO_3$ and $HClO_4$, the reaction between $CaCO_3$ and HCl, and reaction between $MgCO_3$ and HCl.

4.5.1 Effect of HCl-$HClO_4$ concentration on the dissolution of dolomite

The influence of HCl-$HClO_4$ concentration on dolomite dissolution was studied between 0.5 and 2.5 $moldm^{-3}$ (Appendix-B1). From Figure 4.18, there was an increase in the amount of dolomite that reacted as the acid concentration and time increased. This is in contrast with Pultar *et al.* (2019) and Baba *et al.* (2014) that as the acid concentration is raised, more

hydrogen ions will be available to react with dolomite, thereby increasing the rate of dolomite dissolution. The least fraction of dolomite dissolution (0.61) was obtained at an acid concentration of 0.5 moldm^{-3} reaction time of 10 Mins, and a temperature of 57 ^{o}C, while the highest fraction of dolomite dissolution of 0.93 was first recorded at 2 moldm^{-3} concentration, a reaction time of 60 Mins and a temperature of 57 ^{o}C. The result of the study shows a significant improvement with the acid combination of HCl and $HClO_4$ as compared with the use of only HCl by Baba *et al.*, (2014) with a 0.759 fraction of dissolved dolomite in 2 moldm^{-3} HCl at a reaction time of 120 Mins.

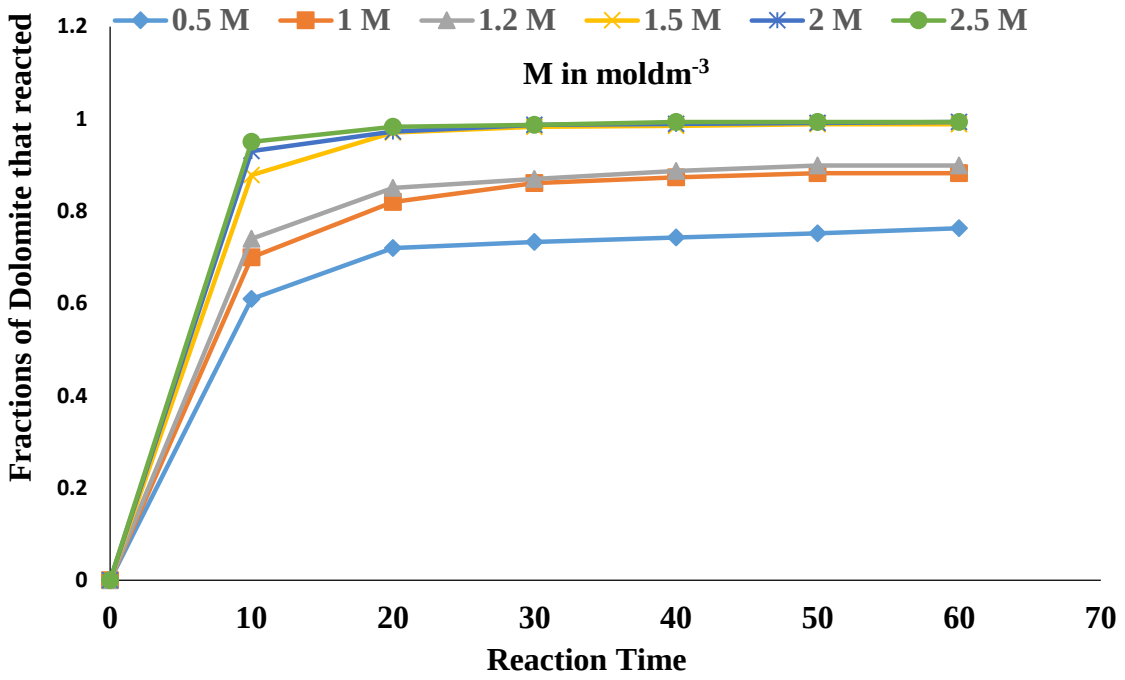

Figure 4.18: Effect of Concentration on Dissolution of Dolomite in HCl-$HClO_4$

4.5.2 Effect of temperature on dolomite on dissolution

The Design expert 11.0 was used to get the optimum condition for the study of the influence of temperature on the kinetics study. In Appendix-B2, the dissolution temperature was varied between 30 to 70 ^{o}C, while the agitation speed and acid concentration were kept constant at

250 rpm and 2.2 moldm^{-3}, respectively. In the study, the least dissolution fraction of 0.83 was attained at a reaction temperature of 30 ^{o}C in 20 Mins while the highest dolomite dissolution of 0.995 was first recorded at a dissolution temperature of 60 ^{o}C and a reaction time of 40 Mins. The increase in the fraction of dolomite that reacted as temperature increased in Figure 4.19 could be due to an increase in the average kinetic energy of the dolomite particle going into reaction with HCl-$HClO_4$ at elevated temperatures, which favours increased bond breaking and bond formation between reactant and products, respectively.

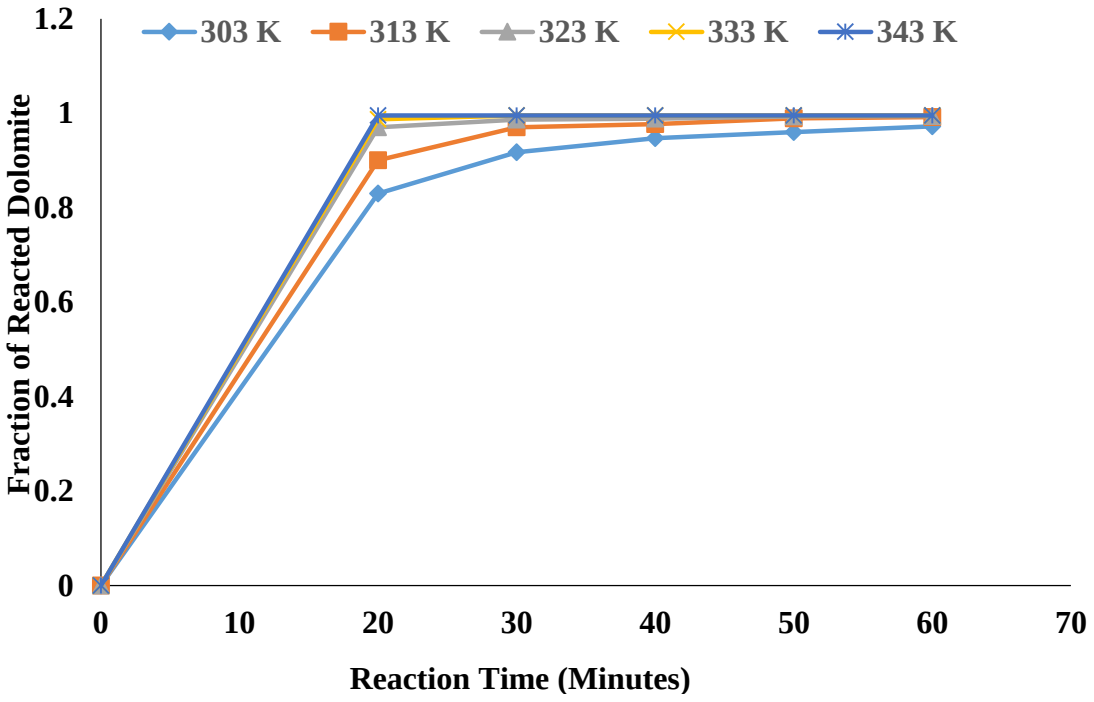

Figure 4.19: Effect of Temperature on Dissolution of Dolomite in HCl- $HClO_4$

4.5.3 Kinetic study

The reaction mechanism between dolomite and HCl-$HClO_4$ is represented in equations 4.25 to 4.35 below:

$$4HClO_4 \rightarrow 2H^+ + 2ClO_4^- \quad (4.25)$$

$$CaCO_3 \rightarrow Ca^{2+} + CO_3^{2-} \quad (4.26)$$

$$Ca^{2+} + 2ClO_4^- \rightarrow Ca(ClO_4)_2 \quad (4.27)$$

$$2H^+ + CO_3^{2-} \rightarrow CO_2 + H_2O \quad (4.28)$$

$$2HClO_4 \rightarrow 2H^+ + 2ClO_4^- \quad (4.29)$$

$$MgCO_3 \rightarrow Mg^{2+} + CO_3^{2-} \quad (4.30)$$

$$Mg^{2+} + 2ClO_4^- \rightarrow Mg(ClO_4)_2 \quad (4.31)$$

$$2H^+ + CO_3^{2-} \rightarrow CO_2 + H_2O \quad (4.32)$$

$$HCl \rightarrow H^+ + Cl^- \quad (4.33)$$

$$Ca^{2+} + 2Cl^- \rightarrow CaCl_2 \quad (4.34)$$

$$Mg^{2+} + 2Cl^- \rightarrow MgCl_2 \quad (4.35)$$

The rate of the reaction was studied via the shrinking core model (SCM). The experimental data were fitted with a shrinking core (SCM) to create a valid model that will provide more relevant information about the complex reaction between dolomite and HCl-$HClO_4$.

The particles of dolomite in this study are assumed to be spherical, hence SCM best suits this assumption. The experimental data were fitted into equations 4.18 to 4.20 to identify the rate-determining step and the slowest step that correspond to the best line of fit to explain the behavior of the dissolution of dolomite in HCl-$HClO_4$. As a result, the minimum energy and the order of the reactions were established. The slopes of the plots were used to calculate the regression coefficient (R^2), which was then compared to the apparent rate constant to produce the values shown in Table 4.11. The information supplied in Appendix-B3 to Appendix-B14 was utilized to calculate the correlation coefficient and apparent rate constants at various temperatures and HCl-$HClO_4$ concentrations.

Table 4.10: Apparent Rate Constants, Correlation Coefficients, and R^2 Values at Various Temperatures and Concentrations of HCl-$HClO_4$

Process Variable	**Kinetic Equation**					
	$X = k_1t$ (FDC)		**$1 - (1 - X)^{1/3} = k_2t$ (SCRC)**		**$1 + 2(1 - X) - 3(1 - X)^{2/3} = k_3t$ (PLDC)**	
Temp (^oC)	$K_1 \times 10^{-3}$	R^2	$K_2 \times 10^{-3}$	R^2	$K_2 \times 10^{-3}$	R^2
30	3.2700	0.8221	5.9480	0.9254	8.5400	0.9130
40	2.0300	0.7233	6.1680	0.8791	7.8780	0.8379
50	0.5500	0.8114	3.0790	0.9047	3.3560	0.8757
60	0.1600	0.5000	1.2840	0.5000	1.2420	0.5000
70	0.0000	0.0000	0.0000	0.000	0.0000	0.0000
Average		**0.7142**		**0.8023**		**0.7817**
Concentration ($moldm^{-3}$)						
0.5	2.4890	0.9961	0.9650	0.9453	1.1980	0.9977
1	3.1660	0.7865	1.7590	0.8108	2.6310	0.8287
1.2	2.7400	0.7545	1.7230	0.9245	2.3180	0.8116
1.5	1.7310	0.7545	1.9180	0.8106	2.2390	0.7926
2	1.0690	0.7979	2.5200	0.8495	2.7760	0.7996
2.5	0.7170	0.7972	1.7220	0.7982	1.8100	0.7996
Average		**0.8078**		**0.8565**		**0.8383**

From the assessment of the results of R^2 in Table 4.10, it can be deduced that the mechanism of the reaction is higher in the surface chemical reaction, followed by product layer diffusion control, while the film diffusion controls have the least. Hence, the surface chemical reaction control mechanism better describes the experimental data which is also the rate-determining step.

4.5.4 Reaction order of dolomite in HCl-$HClO_4$

The order of reaction in this study is related to the speed of the reaction between dolomite and HCl-$HClO_4$. The slopes of Apendix-B6 shown in Apendix-B5 corresponds to the apparent rate constant, its natural logarithm was plotted against the natural logarithm of the HCl-$HClO_4$ concentration in Apendix-B15. Since the reaction follows a surface chemical reaction mechanism. The slope of Figure 4.20 is 0.6583, this corresponds to a first-order reaction with hydrogen ion concentration. This value is very close to the reaction order of 0.77 reported for the reaction between HCl and dolomite by Pultar *et al.* (2019) and above the half order reported by Baba *et al.* (2014) of dolomite in HCl.

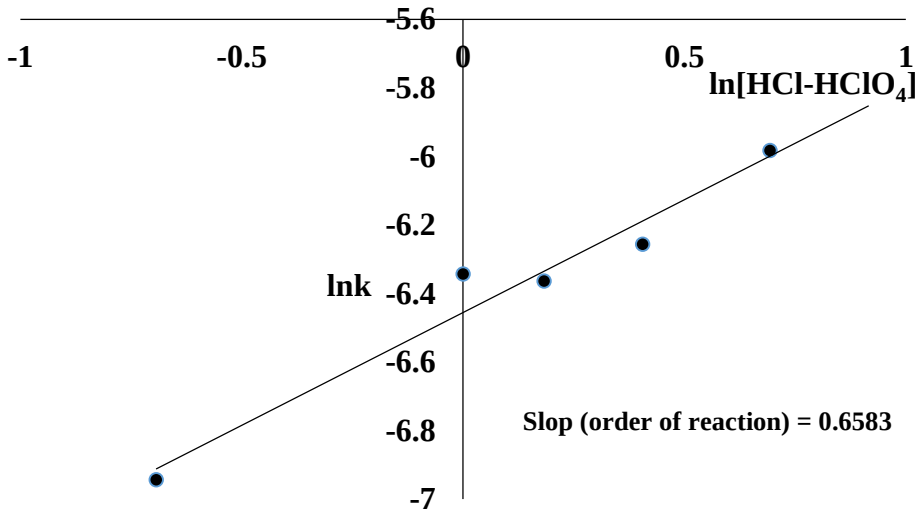

Figure 4.20: Plot of lnk Vs ln[HCl-$HClO_4$]

4.5.5 Activation energy dolomite in HCl-$HClO_4$

The least amount of energy needed for a reaction to take place is activation energy. The relationship between the minimum energy requirement (Ea), temperature (T), and rate constant is mathematically expressed in equation (4.21).

The frequency factor is denoted with an A. The activation energy between dolomite and HCl-$HClO_4$ was determined by evaluating the apparent rate constant from the slope (Apendix-B16) and it was plotted against the temperature inverse in kelvin units shown in Figure 4.21. Linearization of equation 4.21 gives rise to 4.22. This is similar to the equation of a straight line, hence the slope of Figure 4.22 is equal to Ea/R, that is, Ea = slope R

Slope =-2006.30K, R = 8.31450$Jmol^{-1}K^{-1}$

Ea = -(-2006.30)K × 8.31450J/molk = 16,681.38130 $Jmol^{-}K^{-1}$

The dissolution of dolomite in HCl-$HClO_4$ required an activation energy of 16.681 $kJmol^{-1}k^{-1}$ which is lower than the 26.605 $kJ/mol^{-1}k^{-1}$ reported in this study for the dissolution of dolomite in HNO_3. This is an indication that there is less energy barrier in the dissolution of dolomite in HCl-$HClO_4$ than in HNO_3. The 16 $kJmol^{-}k^{-1}$ reported in this study is also below the 20.77 kJ/mol/k reported by Baba *et al.* (2014) for the dissolution of dolomite in HCl. In terms of activation energy, HCl-$HClO_4$ offers a lower energy barrier than HNO_3 in the dissolution of dolomite.

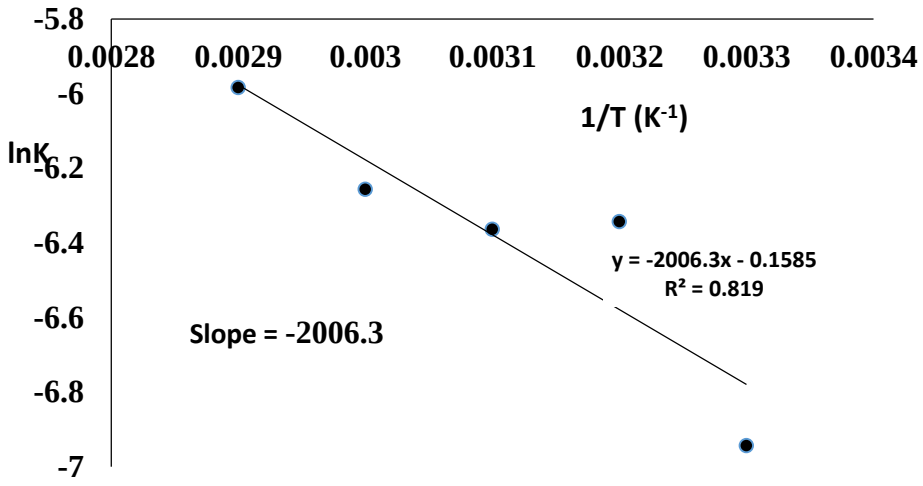

Figure 4.21: Plot of lnk Vs 1/T (K^{-1})

4.6 First-order Linear Regression Model and Statistical Analysis for Precipitation of Magnesium ion through Nitric Acid Route

The dolomite dissolution in nitric acid solution has restricted application, hence the selective separation of magnesium compounds becomes necessary to enhance wide industrial application. The precipitation reaction in equation 4.36 governs the selective separation of magnesium hydroxide from dissolved dolomite while the mechanism of the precipitation is shown in equations 4.36 to 4.40.

$$Ca(OH)_2 + Mg(NO_3)_2 + \rightarrow Ca(NO_3)_2 + Mg(OH)_2 \quad (4.36)$$

$$Mg(NO_3)_2 \rightarrow Mg^{2+} + 2NO_3^- \quad (4.37)$$

$$Ca(OH)_2 \rightarrow Ca^{2+} + 2OH^- \quad (4.38)$$

$$Mg^{2+} + 2OH^- \rightarrow Mg(NO_3)_2 \quad (4.39)$$

$$Ca^{2+} + 2NO_3^- \rightarrow Ca(NO_3)_2 \quad (4.40)$$

The extent of the precipitation was determined by measuring the difference in the amount of magnesium ion in the solution before and after precipitation using AAS analysis. Central Composite Design (CCD) is considered to be more suitable for optimization studies were there are only two independent variables. In this, the concentration of $Ca(OH)_2$ and precipitation time are the two independent variables that have a significant effect on the $Mg(OH)_2$ precipitation from a saturated solution of dolomite in nitric acid. Table 4.11 present the factors studied for the precipitation reaction which is the concentration of calcium oxide slurry and precipitation time. The coded low and high are the lower and upper boundary conditions that must be specified for the software to generate the optimization matrix. The minimum and the maximum values are the two predicted extreme conditions by the software to determine the extent of the precipitation.

Table 4.11: Factors for the Precipitation $Mg(OH)_2$

Factor (Numeric)	Minimum	Maximum	Coded		Mean	SD
			Low	High		
A – Concentration of $Ca(OH)_2$ (%)	21.93	36.07	-1 ↔ 24.00	+1 ↔ 34.00	29.00	4.08
B- Time (Mins)	0.7574	9.24	-1 ↔ 2.00	+1 ↔ 8.00	5.00	2.45

SD: Standard deviation

The variables were simulated using the central composite experimental design method in Design Expert 11.0 software and thirteen experimental runs were generated. The software helps in the determination of the most appropriate model for the experiment by plugging the results of the experimental runs into it. The experimental and predicted magnesium ion in PPT through the nitric acid route (NAR) is presented in Table 4.12. The actual magnesium

ion were the responses from the experimental work while the predicted magnesium ion was obtained by simulation. To know how near the predicted outcome is to the experimental outcome, each residual value was calculated. The residual value of 0.01, which is nearly equal to zero, shows how well the expected values match the results of the experiment.

Table 4.12: Experimental and Predicted Magnesium ion in PPT from NAR

Run	Concentration of $Ca(OH)_2$ (%)	Time (Min)	Magnesium ion In PPT (%)		Residual
			Actual	Predicted	
1	34	2	97.83	85.25	12.57
2	22	5	78.72	78.56	0.16
3	29	5	85.10	85.49	-0.39
4	34	8	98.81	95.54	3.27
5	24	2	75.35	75.45	-0.10
6	29	5	85.00	85.49	-0.49
7	29	9	97.61	92.77	4.84
8	29	5	85.20	85.49	-0.29
9	29	5	85.12	85.49	-0.37
10	29	5	85.00	85.49	-0.49
11	36	5	79.59	92.43	-12.84
12	24	8	83.28	85.73	-2.45
13	29	1	74.81	78.22	-3.41
Sum					**0.01**

In Figure 4.22, the predicted Mg^{2+} values in the PPT are plotted against the actual values. At the actual Mg^{2+} value of 98.81 %, the predicted Mg^{2+} value of 95.54 % was determined from the plot, while at the actual value of 85 .00 % Mg^{2+} a close predicted Mg^{2+} value of 85.49 % was determined from the plot. This implies that the plot can be used to determine the predicted Mg^{2+} in PPT. The blue colour represents the lower Mg^{2+} concentration in the PPT, the green colour represents the Mg^{2+} concentration at the intermediate, while the red colour represents the high Mg^{2+} concentration in the PPT.

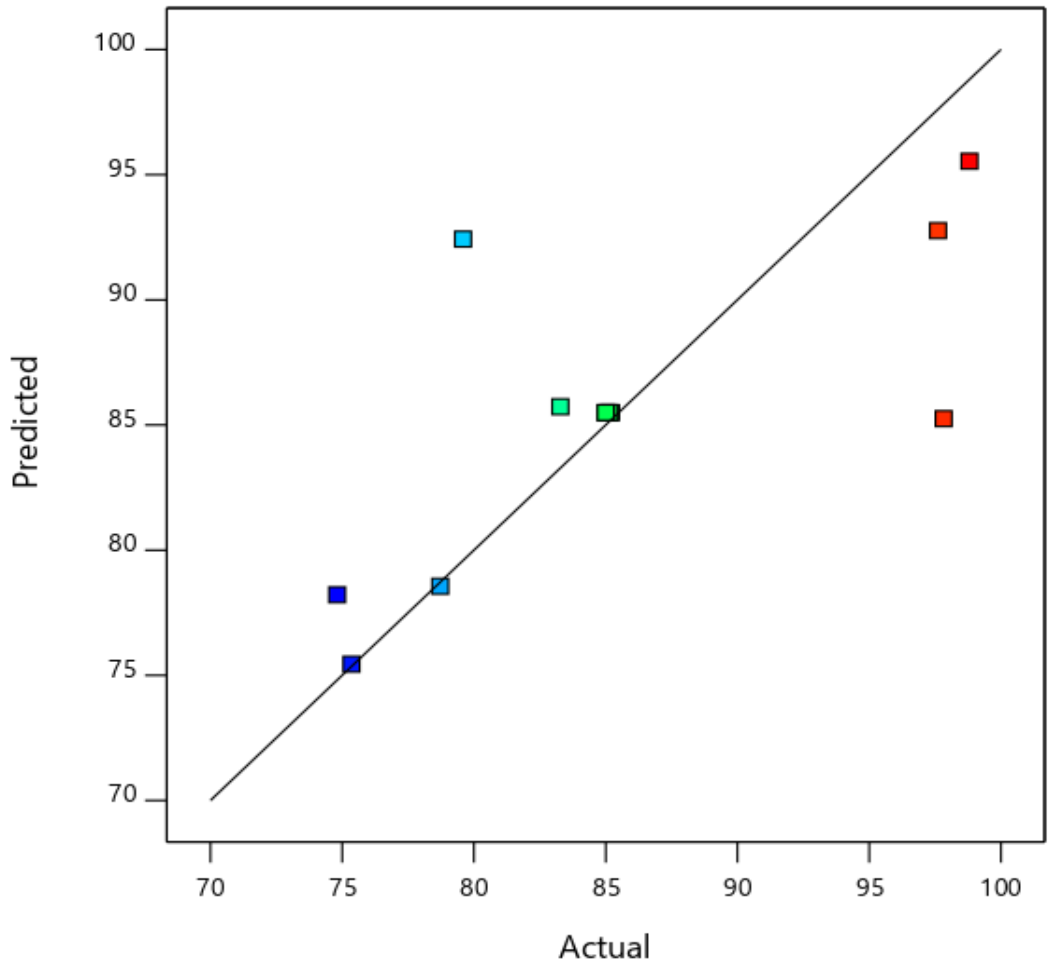

Figure 4.22: Plot of Predicted Mg^{2+} Value against the Actual in PPT

The model summary statistics are shown in Table 4.13. The thirteen experimental responses were subjected to four different models (cubic, quadratic, two-factor interaction (TFI), and

linear) to get the one with the best regression (R^2), predicted R^2 and adjusted R^2 values. The cubic model has the best R^2 of 0.9034 but it was rejected because it is aliased, the quadratic model with an R^2 value of 0.5993 could have been the next available option but the sequential p-value (0.5881) indicates the model is not appropriate (insignificant), and this lead to it rejection. The linear model has a significant sequential p-value (0.026), an R^2 **(**0.5182), and an adjusted R^2 (0.4218), hence the choice of the linear model.

Table 4.13: Model Summary Statistic Magnesium Ion in PPT

Source	**SD**	**Sequential p-value**	**R^2**	**Predicted R^2**	**Adjusted R^2**	
Linear	**6.13**	**0.0260**	**0.5182**	**-0.0624**	**0.4218**	**Suggested**
2FI	6.36	0.5979	0.5337	-0.7336	0.3782	
Quadratic	6.68	0.5881	0.5993	-1.8493	0.3131	
Cubic	3.88	0.0285	0.9034	-5.1780	0.7682	Aliased

SD: Standard Deviation

The ANOVA for linear model magnesium hydroxide precipitation is presented in Table 4.14. The F-value of 5.38 suggests that the model is relevant in the prediction of the magnesium hydroxide precipitation. The chance that there will be noise in the F-value is merely 2.60 %. A P-value less than 0.05000 is an indication that the model terms have a reasonable amount of influence on the model. $Ca(OH)_2$ concentration (A), which has a P-value of 0.0471, and precipitation time (B), which has a P-value of 0.039, are important model terms. A lack of fit with an F-value of 8567.89, suggests that its value is considerable. The model reduction was used to enhance the model because there is only a 0.01 % probability that noise may result in a significant lack of fit F-value. For any model to have good adequate precision, it

must have a minimum value of 4, the value of 6.825 in this study is above the minimum acceptable value of 4. This indicates that the model is appropriate for predicting the amount of Mg^{2+} that can be precipitated from a saturated solution of dissolved dolomite in nitric acid.

Table 4.14: Linear model ANOVA for Magnesium Hydroxide Precipitation

Source	Sum of Squares	df	Average Square	F-value	p-value	
Model	404.04	2	202.02	5.38	0.0260	significant
A- Conc.of $Ca(OH)_2$	192.38	1	192.38	5.12	0.0471	
B-Time	211.66	1	211.66	5.63	0.0390	
Residual	375.69	10	37.57			
Lack of Fit	375.66	6	62.61	8567.89	< 0.0001	
Pure Error	0.0292	4	0.0073			
Cor Total	779.72	12				

Df: Degree of freedom, P: probability, Adequate Precision: 6.8247

Coded factor equation

$$Magnesium\ ion\ PPT(\%) = +85.49 + 4.90A + 5.14B \quad (4.41)$$

Where A and B are the concentration of $Ca(OH)_2$ and reaction time respectively.

Equation 4.41 represent the model equation with the factors being coded, magnesium ion precipitation can be predicted via the equation. Equation 4.42 is the model equation that was developed with the factor being at the actual experimental conditions.

Actual factor equation

$$Magnesium\ ion\ PPT(\%) = +48.47852 + 0.980765A + 1.71455B \quad (4.42)$$

Where A and B are the concentration of $Ca(OH)_2$ and reaction time respectively.

4.6.1 Single influence of precipitation time and $Ca(OH)_2$ concentration on the precipitation of $Mg(OH)_2$

Figure 4.23 depicts the individual effects of $Ca(OH)_2$ concentration and precipitation time on $Mg(OH)_2$ precipitation. The magnesium ion concentration rises from 80.59 to 90.35 % as the $Ca(OH)_2$ concentration in the solution rises from 24 to 34 %, implying that increasing the concentration of $Ca(OH)_2$ in the solution raises the saturation point, allowing more $Mg(OH)_2$ to precipitate. The magnesium ion concentration increases from 80.34 to 90.58 % as the precipitation time increases from 2 to 8 minutes. This implies that an increase in precipitation time increases the contact period between the calcium hydroxide and the molecules of the magnesium nitrate in the solution.

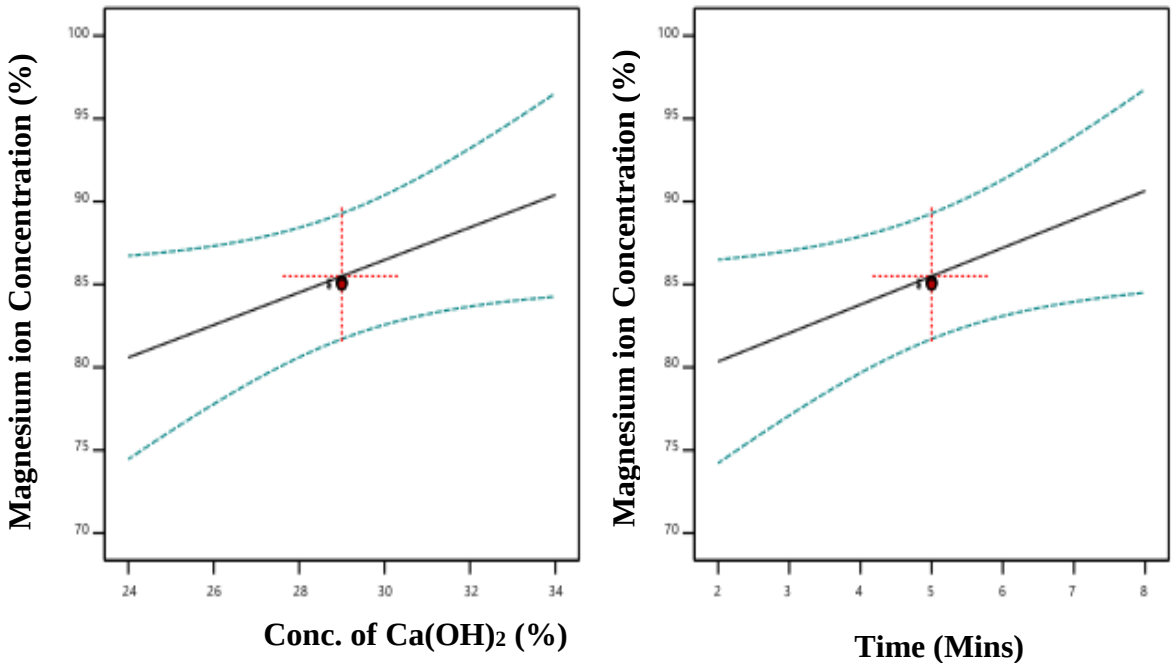

Figure 4.23: Individual Influence of Precipitation Time and $Ca(OH)_2$ Concentration on the Precipitation of $Mg(OH)_2$

4.6.2 Interactive influence of precipitation time and $Ca(OH)_2$ concentration on the precipitation of $Mg(OH)_2$

The interactive effect between precipitation time and $Ca(OH)_2$ concentration is presented in Figure 4.24.

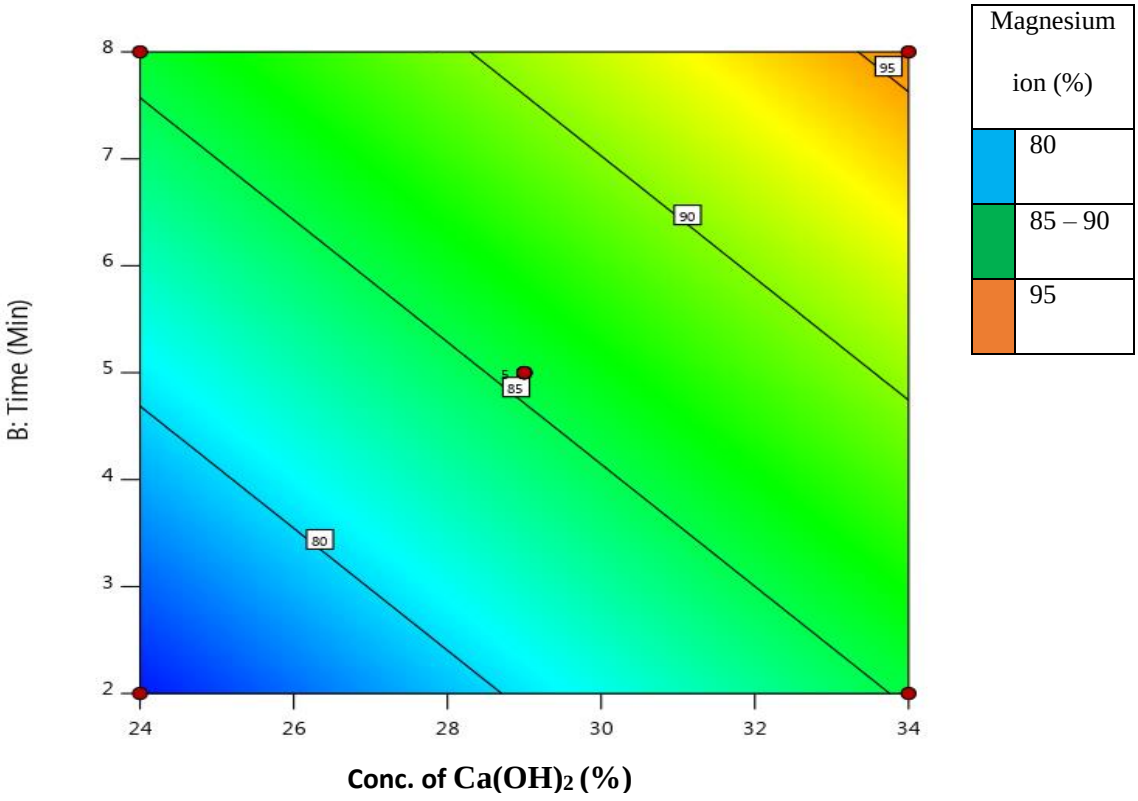

Figure 4.24: Interactive Influence of Time and $Ca(OH)_2$ Concentration on the Precipitation of $Mg(OH)_2$

The time increases from 2 to 8 minutes and the $Ca(OH)_2$ concentration increases from 24 to 34 % the amount of magnesium ion concentration increases from 80 to 95 %. This indicates that an increase in the concentration of precipitant is more effective with a sufficient precipitation period as longer interaction between the reactant molecules [$Mg(NO_3)_2$ and $Ca(OH)_2$] enhances the liberation of the magnesium ion from the saturated solution. Figure 4.25 depicts a graphical plot in three-dimensions of the interactive influence of time and $Ca(OH)_2$ concentration on $Mg(OH)_2$ precipitation.

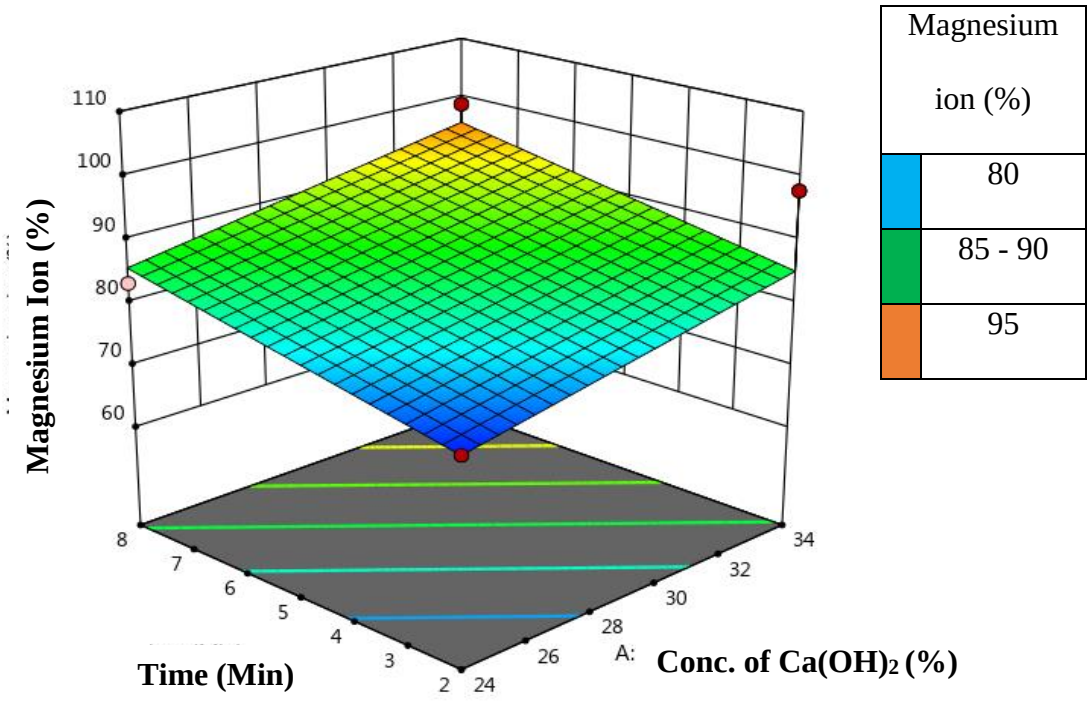

Figure 4.25: Three-Dimensional Plot of the Combined Influence of Time and $Ca(OH)_2$ Concentration on the Precipitation of $Mg(OH)_2$

In this study, the interest was in having precipitates with high magnesium content and low calcium content. To achieve this, an evaluation of the amount of both magnesium ion and calcium ion was carried out and presented in Figure 4.26 and Appendix-C1. It is obvious that runs 4 with a precipitation condition of 34 %v/v $Ca(OH)_2$ and 8 minutes has the highest magnesium content (98.81 %) and the least calcium content (1.19 %). This implies that a higher proportion of the $Ca(OH)_2$ was able to go into the precipitation and that the experimental condition does not favour the co-precipitation of CaO. The yield of $Mg(OH)_2$ precipitate of 98.81 % is very close to the 99 % report by Mohammed and Kurniawan (2015). Run 7 has the least magnesium ion content of 74.81 % and the highest calcium ion content of 25.19 %. The high calcium content could be attributed to undissolved $Ca(OH)_2$ from the precipitant and co-precipitate of $Ca(OH)_2$ at the experimental condition.

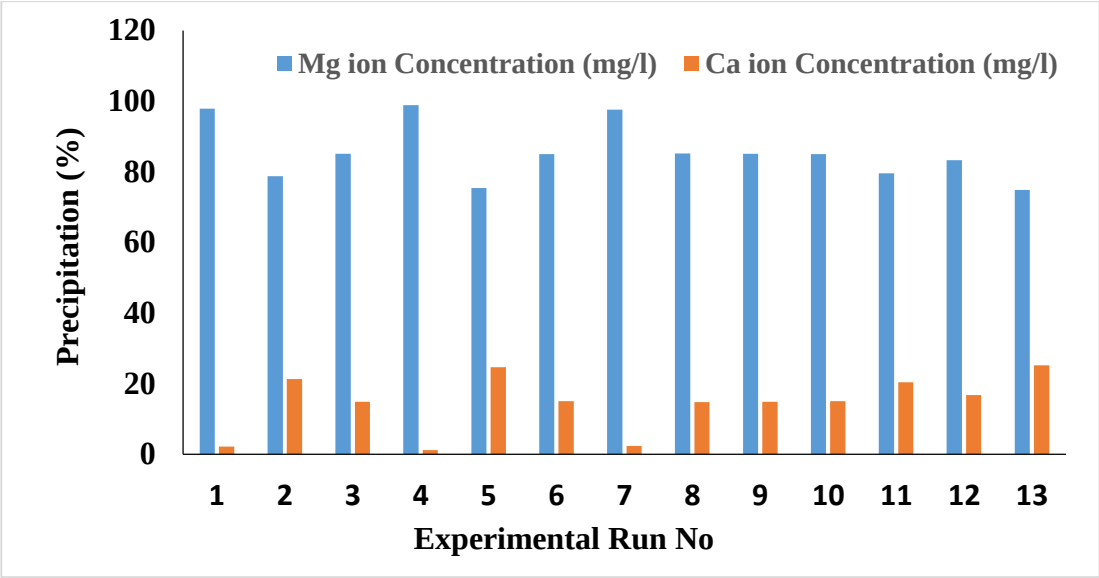

Figure 4.26: Amount of the Magnesium Ion and Calcium Ion Content in the Precipitated Sample from NAR

The optimization constraints in Table 4.15 for precipitation of $Mg(OH)_2$ were chosen due to the significance of their effect on the precipitation process.

Table 4.15: Optimization Constraints of $Mg(OH)_2$ Precipitation

Name	Goal	Lower Limit	Upper Limit
Concentrationof $Ca(OH)_2$ (%)	maximize	24	34
Time (Mins)	is in range	2	8
Magnesium ion Concentration (%)	maximize	74.81	98.8056

Maximizing the concentration of the calcium hydroxide and setting the time within the range of 2 to 8 minutes resulted in the best optimum prediction of 34 % concentration of calcium hydroxide and 8 minutes precipitation time at 98.54 % $Mg(OH)_2$ precipitation (Figure 4.27) from the saturated solution with desirability of 0.929 (Figure 4.28), which is much closer to

the 97.5% magnesium ion precipitate obtained by Mubarok and Kurniawan (2015) from dissolved dolomite. At the predicted conditions, a confirmatory experiment revealed 98.1 % magnesium ion precipitation.

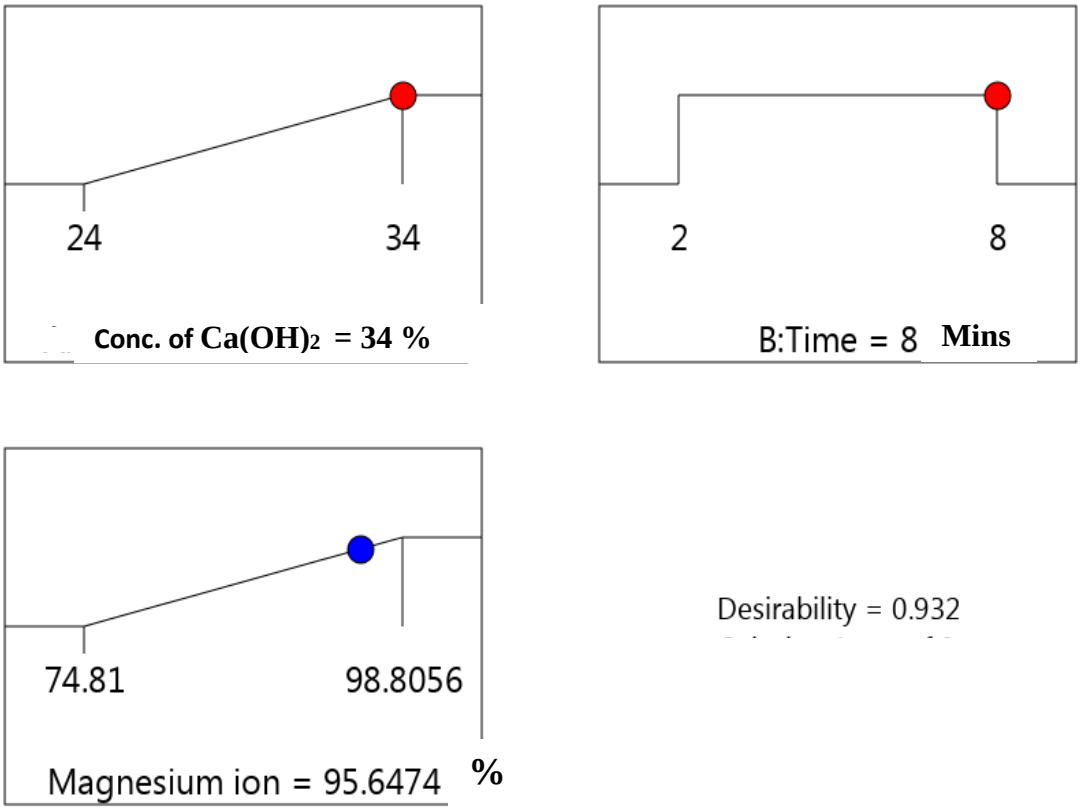

Figure 4.27: Optimum Predicted Point of $Mg(OH)_2$ Precipitation

The desirability plot of $Mg(OH)_2$ precipitation presented in Figure 4.28 helps to access the degree of acceptance of the predicted optimum condition. The desirability of one implies 100 % acceptance. In this study, both the $Ca(OH)_2$ concentration and the time have a dierability of 1 (100 %) while the combined has a desirability of 0.9295 (92.95 %).

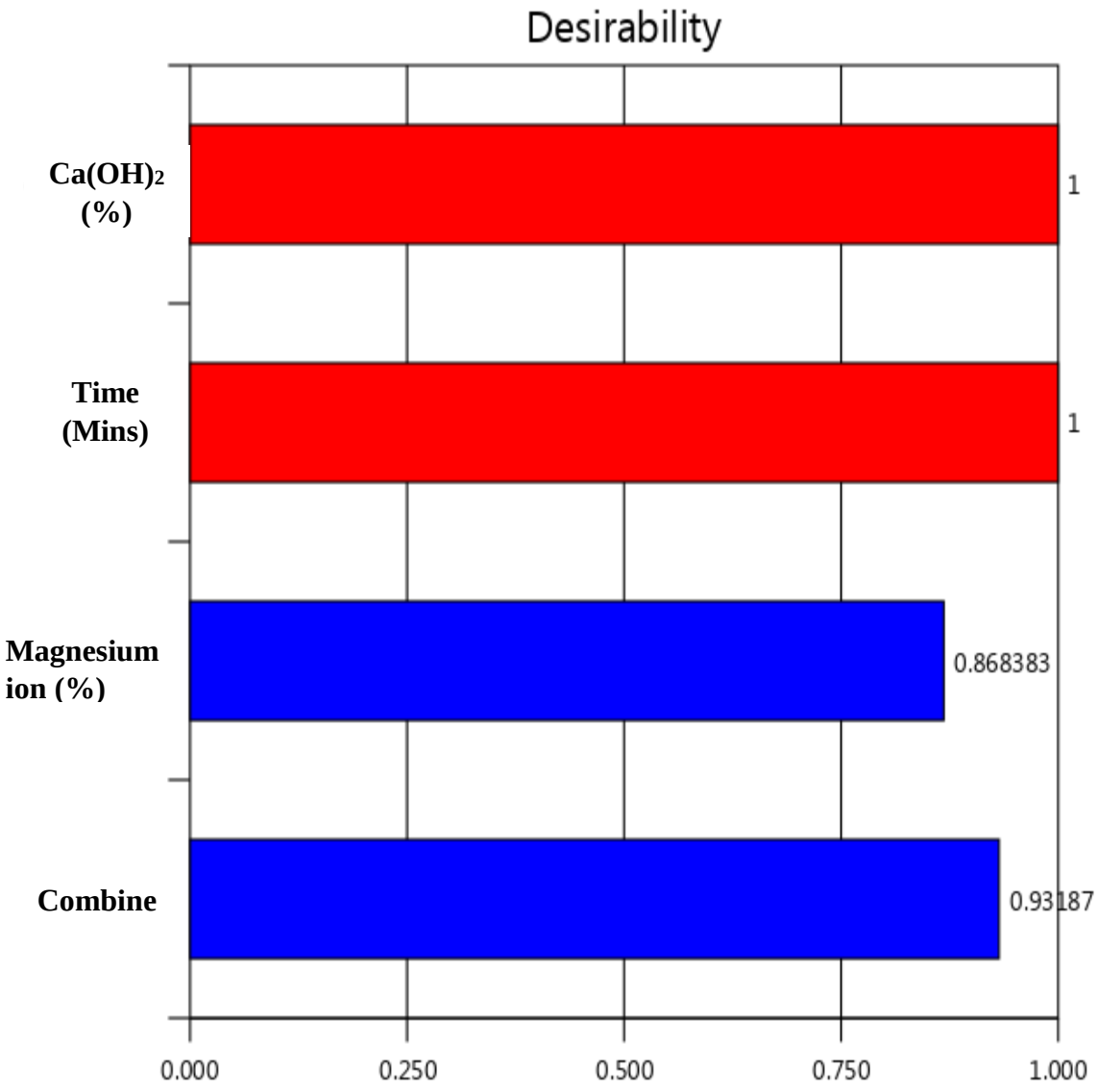

Figure 4.28: Desirability Plot of $Mg(OH)_2$ Precipitation

4.7 Quadratic Model and Statistical Analysis for Precipitation of Magnesium ion from Hydrochloric/Perchloric Acid Route (HPASR)

This study has been able to establish that HCl-$HClO_4$ is suitable for the dissolution of dolomite. The recovery of value-added products from the dissolved dolomite could be a serious challenge if appropriate techniques are not employed. The reaction mechanism of $Mg(OH)_2$ precipitation from HPASR is described in Equations 4.43 to 4.52.

$$MgCl_2 + Ca(OH)_2 \rightarrow CaCl_2 + Mg(OH)_2 \quad (4.43)$$

$$MgCl_2 \rightarrow Mg^{2+} + 2Cl^- \quad (4.44)$$

$$Ca(OH)_2 \rightarrow Ca^{2+} + 2OH^- \quad (4.45)$$

$$Mg^{2+} + 2OH^- \rightarrow Mg(OH)_2 \quad (4.46)$$

$$Ca^{2+} + 2Cl^- \rightarrow CaCl_2 \quad (4.47)$$

$$Mg(ClO_4)_2 + Ca(OH)_2 \rightarrow Ca(ClO_4)_2 + Mg(OH)_2 \quad (4.48)$$

$$Mg(ClO_4)_2 \rightarrow Mg^{2+} + 2ClO_4^- \quad (4.49)$$

$$Ca(OH)_2 \rightarrow Ca^{2+} + 2OH^+ \quad (4.50)$$

$$Mg^{2+} + 2OH^+ \rightarrow Mg(OH)_2 \quad (4.51)$$

$$Ca^{2+} + 2ClO_4^- \rightarrow Ca(ClO_4)_2 \quad (4.52)$$

Sequel to a preliminary experimental study, the boundary conditions in Table 4.16 for the selective precipitation were selected for the generation of the experimental conditions by the software.

Table 4.16: Process Conditions for the $Mg(OH)_2$ Precipitation from Dissolved Dolomite in HCl-$HClO_4$

Factor (Numeric)	Minimum	Maximum	Coded		Mean	SD
			Low	High		
A – Concentration of $Ca(OH)_2$ (%)	30.55	40.45	-1 ↔ 32.00	+1 ↔ 39.00	35.50	2.86
B- Time (Mins)	0.7574	9.24	-1 ↔ 2.00	+1 ↔ 8.00	5.00	2.45

SD: Standard Deviation

The optimization matrix as well as the experimental and the predicted Mg^{2+} in the PPT from HPASR is presented in Table 4.17. AAS was used to determine the amount of the Mg^{2+} and

Ca^{2+} in the solution before and after precipitation and the percentage of precipitation was calculated. The amount of Mg^{2+} precipitated was taken as the response of each of the thirteen experimental runs. This was simulated to get close to the predicted values and it was confirmed by the residual sum of 0.07. At 30.55 % $Ca(OH)_2$ concentration and precipitation time of 5 minutes, the least Mg^{2+} actual yield of 72.81 % and predicted yield of 77.84 % was recorded. Similarly, at 35.5 % $Ca(OH)_2$ concentration and precipitation time of 5 minutes, the highest Mg^{2+} actual yield of 97.63 % and predicted yield of 97.50 % was recorded. This shows that the concentration of $Ca(OH)_2$ influenced the precipitation.

Table 4.17: Experimental and Predicted Magnesium Ion in PPT form HPASR

Run	Concentrationof $Ca(OH)_2$ (%)	Time (Min)	Magnesium ion (%)		Residual
			Actual	Predicted	
1	36	5	97.63	97.51	0.12
2	32	8	85.84	81.00	4.84
3	36	1	80.72	81.84	-1.12
4	39	2	90.28	90.98	-0.70
5	36	5	97.54	97.49	0.05
6	31	5	72.81	77.84	-5.03
7	40	5	96.61	95.72	0.89
8	36	5	97.43	97.50	-0.07
9	32	2	80.35	76.86	3.49
10	39	8	92.81	92.16	0.65
11	36	5	97.35	97.49	-0.14
12	36	10	82.59	85.61	-3.02
13	36	5	97.52	97.49	0.03
Sum					**-0.07**

The quadratic models in equations 4.53 and 4.54 were developed in terms of coded factors and real factors respectively for predicting the amount of magnesium ion ($Mg(OH)_2$ precipitate at any of the experimental runs in Table 4.17

Coded Factor equation

Magnesium ion (%) = +97.50 + 6.32A + 1.33B - 0.7397AB - 5.36A² - 6.89B² (4.53)

Actual Factor Equation

$$Magnesium\ ion\ conc.(\%) = -551.69433 + 33.21352A + 10.59714B - 0.070450AB - 0.437406A^2 - 0.765221B^2 \quad (4.54)$$

The graph of the actual against predicted, clearly indicates that the magnesium ion for both actual and predicted are very close and are above 75 % for both Figure 4.29.

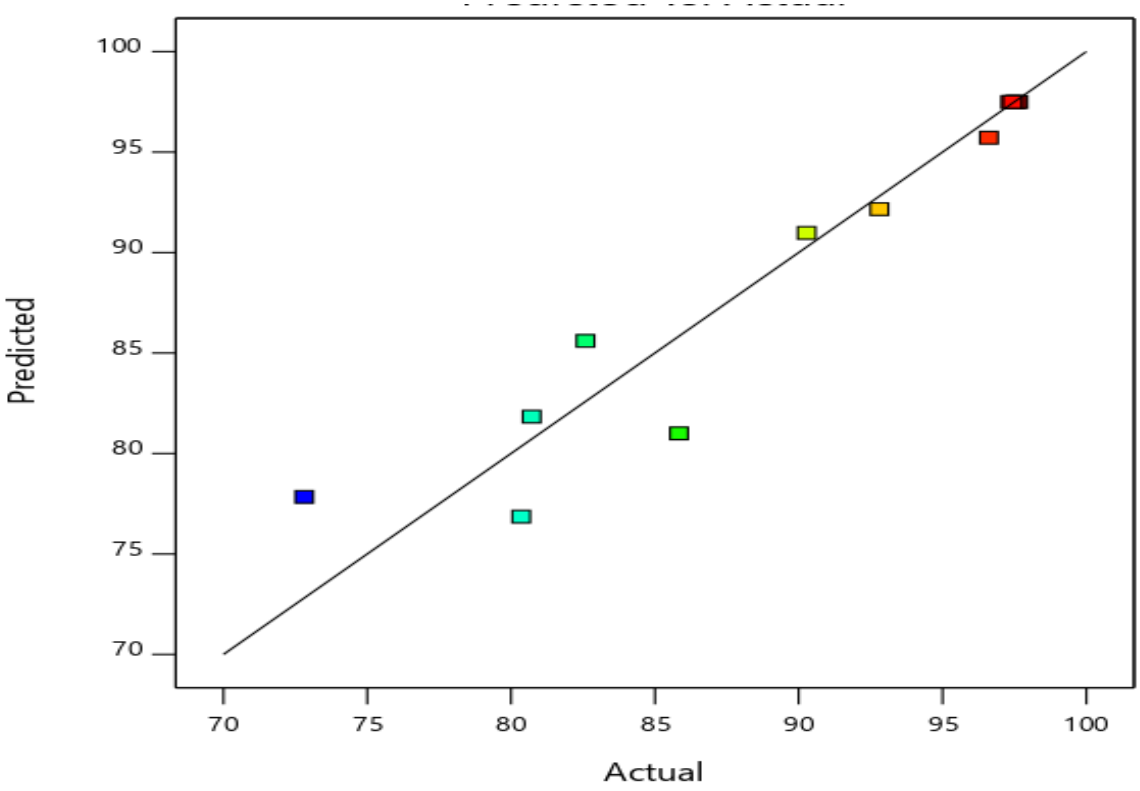

Figure 4.29: Plot of Predicted against the Actual Magnesium Ion Yield from HPASR

Table 4.18: Summary of the Statistics Model for the Precipitation of $Mg(OH)_2$ through HPASR

Source	Std. Dev.	R^2	Predicted R^2	Adjusted R^2	
Linear	7.390	0.3793	-0.0363	0.25520	
2FI	7.77	0.3818	-0.2124	0.1758	
Quadratic	**3.23**	**0.9170**	**0.4099**	**0.8577**	**Suggested**
Cubic	2.62	0.9610	-1.4909	0.9065	Aliased

Model selection for any set of experimental values is usually based on its R^2, predicted R^2, and adjusted R^2 values close to unity, and the model should not be aliased. In this study, the quadratic model best fit into these conditions with 0.9170 R^2, 0.8577 adjusted R^2, and an R^2 predicted of 0.4099. The other tested models in Table 4.18 failed to meet these set conditions and were therefore rejected.

Table 4.19: ANOVA for Quadratic Model Precipitation of $Mg(OH)_2$ through HPASR

Source	Sum of Squares	Df	F-value	Mean Square	p-value	
Model	806.55	5	15.46	161.31	0.0012	Significant
A-Concentration of $Ca(OH)_2$	319.46	1	30.62	319.46	0.0009	
B-Time	14.19	1	1.36	14.19	0.2817	
AB	2.19	1	0.2098	2.19	0.6608	
A^2	199.73	1	19.15	199.73	0.0033	
B^2	329.95	1	31.63	329.95	0.0008	
Residual	73.02	7		10.43		
Lack of Fit	72.98	3	2075.10	24.33	< 0.0001	Significant
Pure Error	0.0469	4		0.0117		
Cor Total	879.58	12				
			Adequate Precision: 9.4045			

The HPASR-based quadratic model ANOVA of $Mg(OH)_2$ precipitation is presented in Table 4.19. The 15.46 F-value is an indication of model significance. From the F-value, there are only a 0.12 % chance of noise. The criteria for selecting significant model terms is that the terms must have P-values less than 0.0500. A, A^2, and B^2. The signal-to-noise ratio is determined by enough precision. A ratio of at least 4 is desired. The ratio of 9.405 is appropriate for moving around the design space.

4.7.1 Single influence of $Ca(OH)_2$ concentration and precipitation time on the precipitation of $Mg(OH)_2$ via HPASR

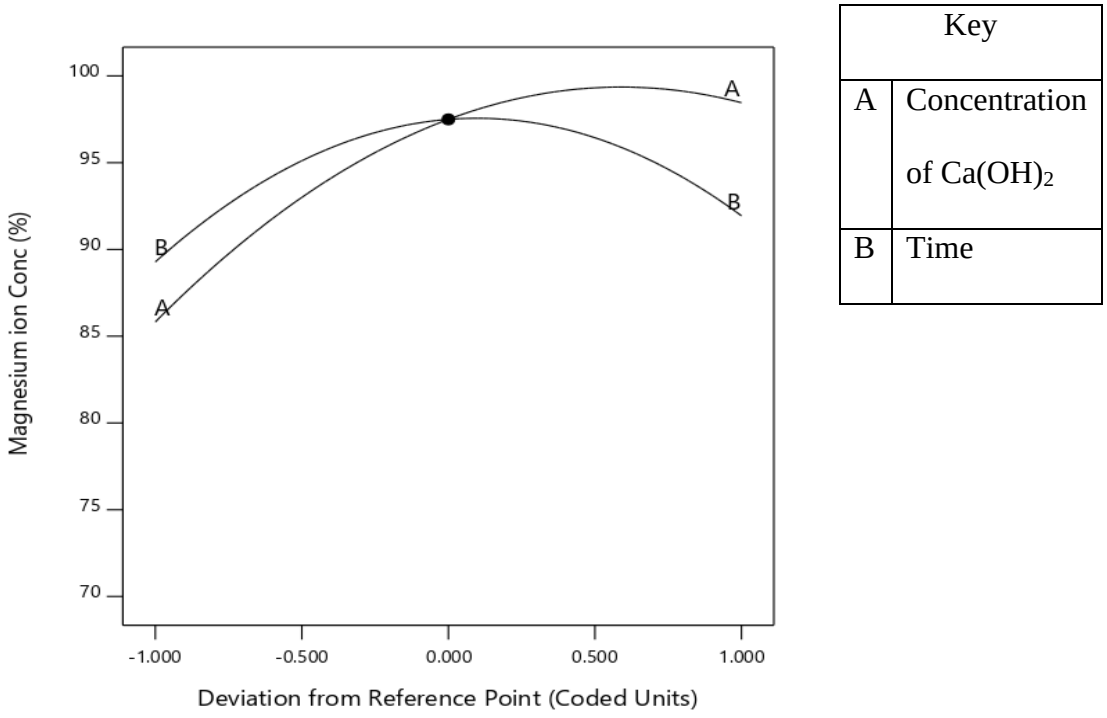

Figure 4.30: Effect of Concentration of $Ca(OH)_2$ and Precipitation Time on the Precipitation of $Mg(OH)_2$ via HPASR

Figure 4.30 depicts the individual effects of $Ca(OH)_2$ concentration and precipitation time on the precipitation of $Mg(OH)_2$ from dissolved dolomite in HPASR. The center point of the design is concentrationat 35.5 % and 5 mins precipitation time. The amount of magnesium ion removed from the solution in the form of precipitate increases from 85.82 % to 98.55 %

as the $Ca(OH)_2$ conc with respect to the solution increases from 12 to 39 %. This reveals that the precipitation is positively and significantly influenced by the $Ca(OH)_2$ concentrationThe results of the ANOVA, which likewise demonstrate the significance of the $Ca(OH)_2$ concentration with a p-value of 0.0009, are consistent with this. It can also be noted that when the precipitation duration was raised from 2 to 5 minutes, the amount of magnesium ion first increased from 89.27 % to 97.5 %. However, there was a decrease in the amount of magnesium ion removed in the form of precipitate from 97.5 % to 91.93 % as the precipitation time increased from 5 to 8 minutes. The dissolution of $Mg(OH)_2$ already precipitated can be attributed to the decrease in the amount of magnesium ion after 5 minutes of precipitation time.

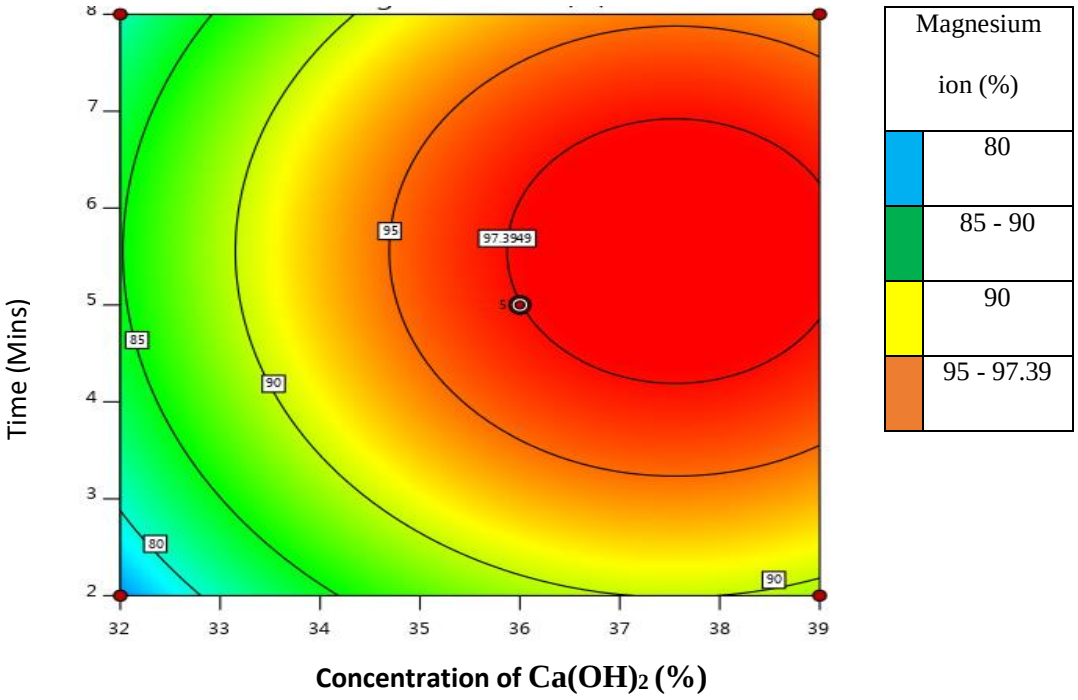

Figure 4.31: Interactive Effect of Concentration of $Ca(OH)_2$ and Time on thePrecipitation of $Mg(OH)_2$ Via HPASR

The interactive effect between precipitation time and $Ca(OH)_2$ concentration is represented in Figure 4.31. It suggests that as the time increases from 2 to 8 minutes and the $Ca(OH)_2$

concentration increases from 24 to 34 % the amount of magnesium ion concentration increases from 80 to 97.46 %. This shows that an increase in the concentration of precipitant is more effective with a sufficient precipitation period as longer interaction between the reactant molecules enhances the liberation of the magnesium ion from the saturated solution. Figure 4.32 depicts a three-dimensional plot of the combined effect of $Ca(OH)_2$ concentration and time on $Mg(OH)_2$ precipitation.

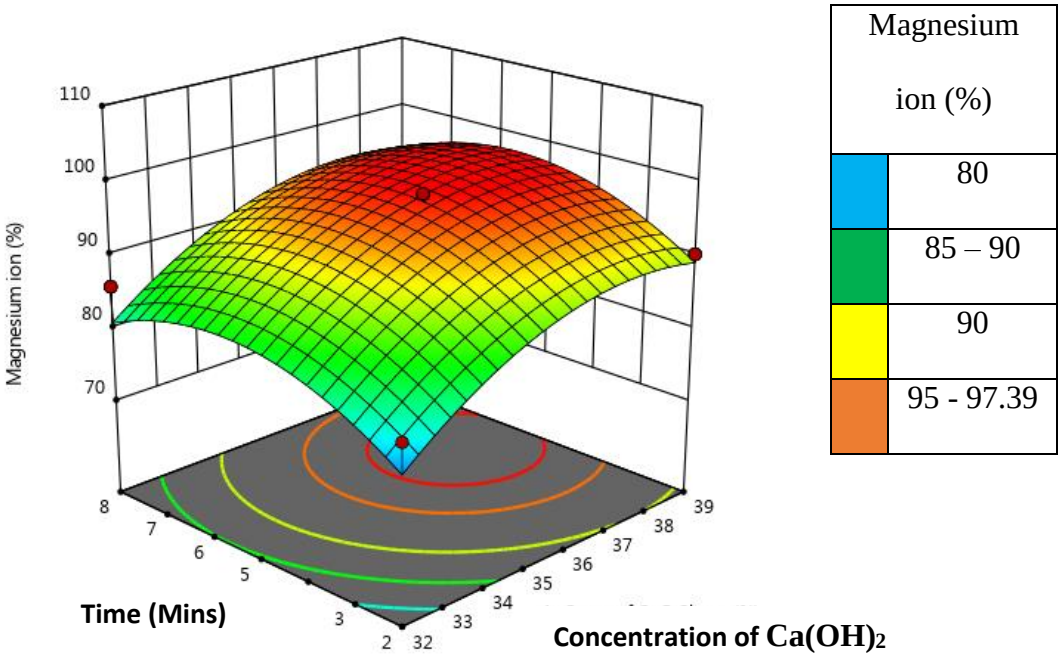

Figure 4.32: Three Dimensional Plot of The Interactive Effect of $Ca(OH)_2$ Concentration and Time on The Precipitation of $Mg(OH)_2$ Via HPASR

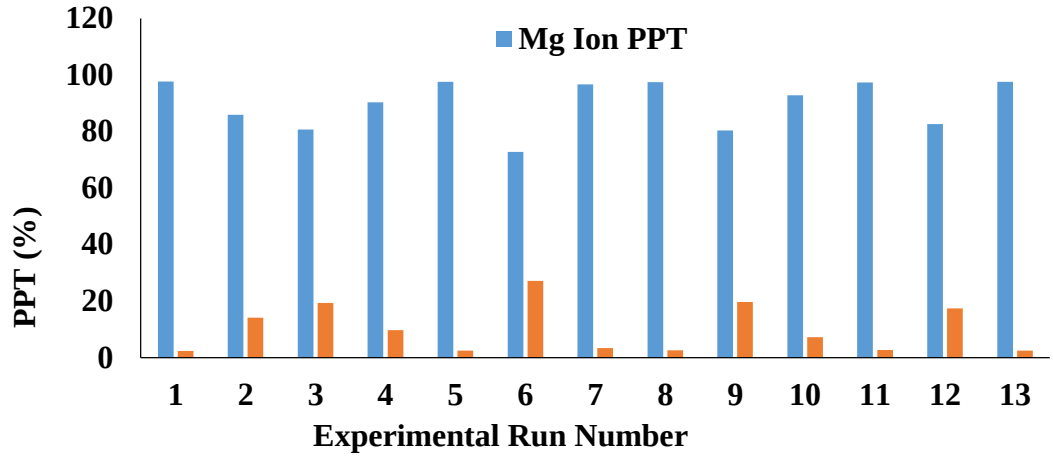

Figure 4.33: Amount of the Magnesium Ion and Calcium Ion Content in the Precipitated Sample from HPASR

This aspect of this study is interested in having precipitate with high magnesium content and low calcium content. To achieve this, an evaluation of the amount of both magnesium ion and calcium ion was carried out and reported in Figure 4.33 and Appendix-D1. It can be seen that run 10 has the highest magnesium content (97.54 %) and the least calcium content (2.46 %). This implies that a higher proportion of the $Ca(OH)_2$ was able to go into the precipitation and the experimental condition does not favour the co-precipitation of $Ca(OH)_2$. Run 7 has the least magnesium ion content (72.81 %) and the highest calcium ion content. The high calcium content could be attributed to undissolved $Ca(OH)_2$ from the precipitant and co-precipitate of CaO at the experimental condition.

Table 4.20: Optimization Constraints of the Precipitation of $Mg(OH)_2$ Via HPASR

Name	Goal	Lower Limit	Upper Limit
Concentrationof $Ca(OH)_2$ (%)	is target = 35.5	32	39
Time (Mins)	is target = 5	2	8
Magnesium ion Conc (%)	Maximize	72.81	97.6341

The optimization boundaries in Table 4.20 for $Mg(OH)_2$ precipitation are based on the influence of $Ca(OH)_2$ concentration, precipitation time, and the amount of magnesium and calcium ions in the precipitate. Setting the concentration of the calcium hydroxide at 35.3 % of the saturated solution and settling the time at 5 minutes gave the best optimum prediction of 97.63 % magnesium ion (Figure 4.34) from the saturated solution with desirability of 0.998 (Figure 4.35). A confirmatory experiment shows 97.1 % magnesium ion precipitation at the predicted conditions, which is much closer to Mubarok and Kurniawan's (2015) 97.5 % magnesium ion precipitate obtained from dissolved dolomite in HCl.

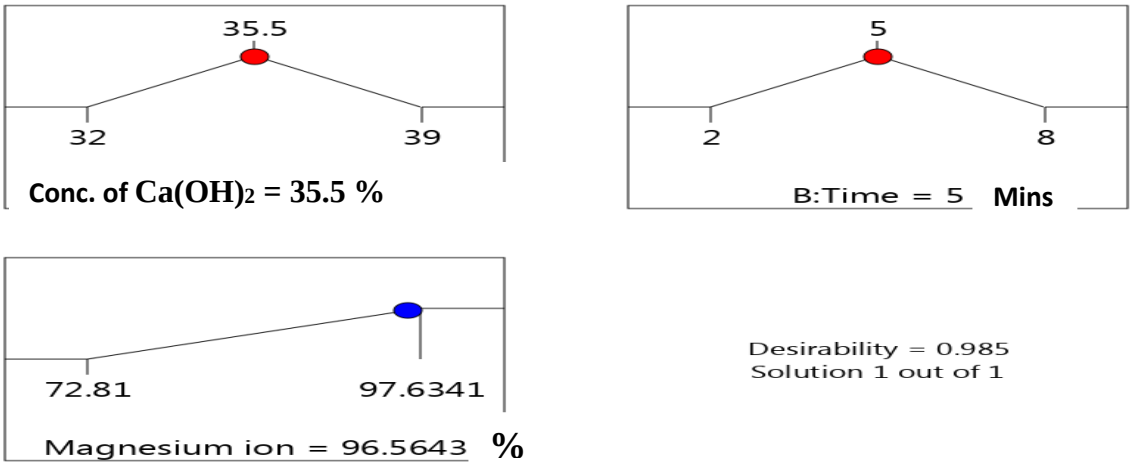

Figure 4.34: Optimum Predicted Point of $Mg(OH)_2$ Precipitation Via HPASR

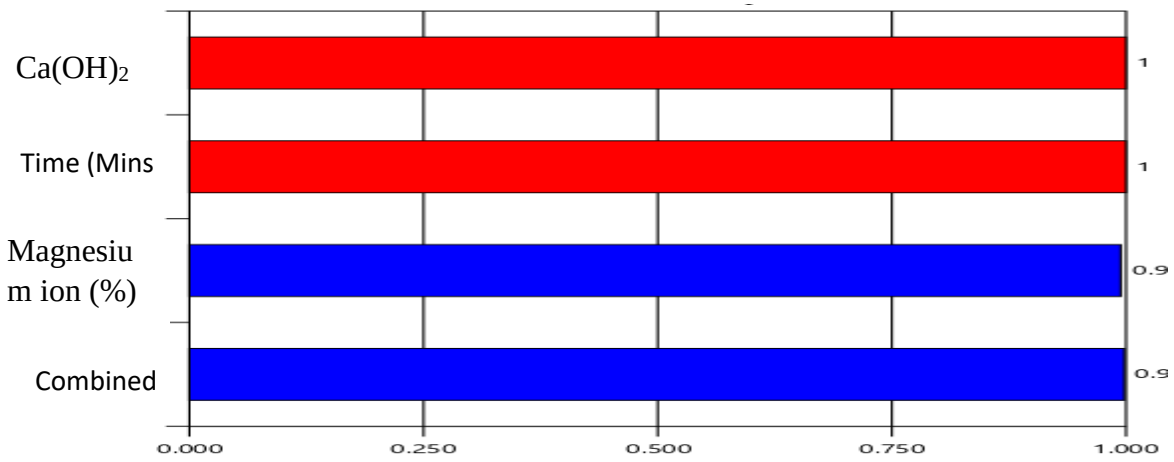

Figure 4.35: Desirability Plot of $Mg(OH)_2$ Precipitation Via HPASR

4.8 Optimization of the Calcination Process Using Pentagonal Experimental Design for the Production of MgO from Dolomite via Nitric Acid Route (NAR)

The Pentagonal experimental design method in Design Expert software 11.0 was used in the optimization study of two independent variables, where the first variable, A, has 4 levels and P variable B, has 5 levels. Pentagonal design helps in minimizing the number of experiments required to decide on the optimum point. A preliminary experiment was conducted on the one-factor-at-a-time, parameters such as temperature, and calcination time, which show significant influence on the yield of MgO from magnesium hydroxide. Therefore, the two factors of time and temperature were selected for further study. The time of calcination was investigated between 10 to 40 Mins, while calcination temperature was varied between 400 to 800 ^{o}C as seen in Table 4.21. The developed mechanism of reactions for this study is the disintegration of $Mg(OH)_2$ which is depicted by equations 4.55 to 4.58. The $Mg(OH)_2$ was obtained by dissolving dolomite in nitric acid and then precipitating it with calcium hydroxide.

Table 4.21: Pentagonal Design of Experimental for Calcination Study

Factor (Numeric)	Minimum	Maximum	Coded		Mean	SD
			Low	High		
A - Time (Minutes)	12.86	40.00	-1 ↔ 10.00	+1 ↔ 40.00	25.00	8.96
B- Temperature (°C)	509.80	890.20	-1 ↔ 500.00	+1 ↔ 900.00	700.00	119.53

$$Mg(OH)_2 \rightarrow MgO + H_2O \quad (4.55)$$

$$Mg(OH)_2 \rightarrow Mg^{2+} + 2OH^- \quad (4.56)$$

$$OH^- + OH^- \rightarrow H_2O + O^{2-} \quad (4.57)$$

$$Mg^{2+} + O^{2-} \rightarrow MgO \quad (4.58)$$

Table 4.22 shows eight experimental runs developed using a pentagonal design. The calcination yield of MgO represents the outcome of the experimental design.

Table 4.22: Pentagonal Design for the Synthesis of MgO from $Mg(OH)_2$ via Nitric Acid System Route (NAR)

Run	Time (Minutes)	Temperature (°C)	Calcination Yield (%)		Residual
			Actual	Predicted	
1	30	890	61.30	61.30	0.0
2	13	582	59.50	59.50	0.0
3	25	700	61.50	61.30	0.2
4	25	700	61.21	61.30	-0.09
5	40	700	60.30	60.30	0.0
6	30	510	60.50	60.50	0.0
7	13	818	62.00	62.00	0.0
8	25	700	61.21	61.30	-0.09
Sum					**0.02**

Three statistical models, which are linear, two-factor interactions (2FI), and quadratic, were tested on the response for model fitness. The model fitness is chosen based on the highest set of coefficient of regression (R^2), predicted $R^{2,}$ and adjusted R^2 values, but values close to unity are preferred. In Table 4.23, adjusted R^2 (0.9536) and R^2 (0.9868) for the quadratic model are much closer to unity compared with the R^2 of 0.46560 and adjusted R^2 of 0.2519 for the linear model, while the 2FI has an 0.7974 R^2 and 0.6455 adjusted R^2. Hence, the connection between the independent (calcination time and temperature) and dependent (calcination product) variables is best described by the quadric model. The prediction of the calcination yield for each of the experimental conditions was carried out using the selected model. The result in Table 4.22 shows that the actual results were very accurate as the model predicted figures and the actual figures were very close with a residual sum of 0.02. Residual is the difference between the predicted values and the experimental result. The plot of the predicted against the experimental yield is shown in Figure 4.37 with almost all the points on the line. This also shows the closeness between the experimental and the actual calcination yield.

Table 4.23: Model Summary Statistics for the Production of MgO through Nitric Acid System (NAR)

Source	Std. Dev.	R^2	Adjusted R^2	Predicted R^2	
Linear	0.6845	0.4656	0.2519	-1.0429	
2FI	0.4712	0.7974	0.6455	-2.6830	
Quadratic	**0.1704**	**0.9868**	**0.9536**		**Suggested**
Cubic					Aliased

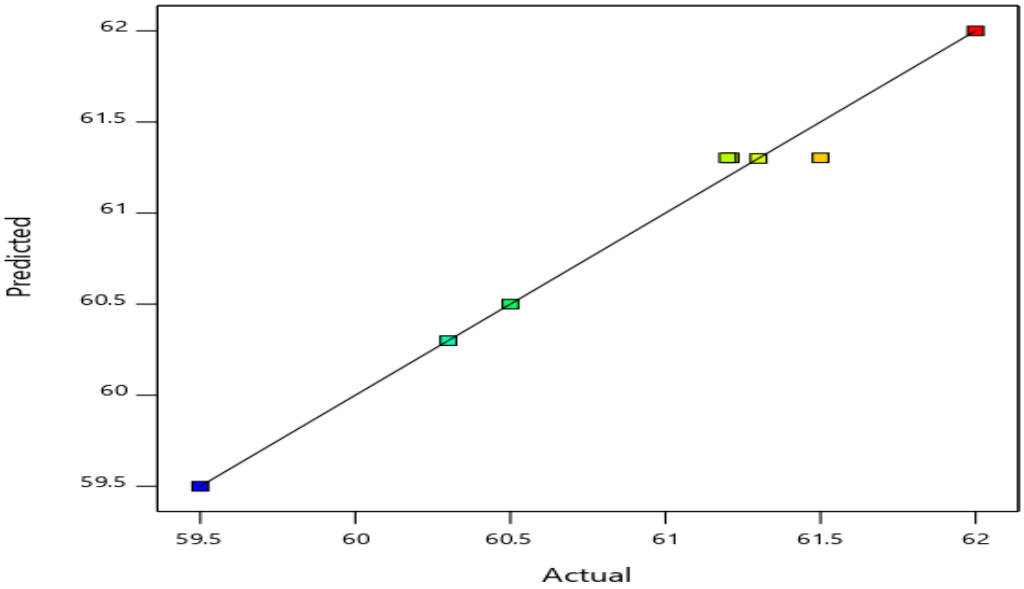

Figure 4.36: The Predicted against the Actual Calcination Product from NAR

Table 4.24: ANOVA for Quadratic Model of Calcination Yield through NAR

Source	Sum of Squares	df	Mean Square	F-value	p-value	
Model	4.33	5	0.8652	29.80	0.0328	Significant
A-Time	0.0511	1	0.0511	1.76	0.3158	
B-Temperature	1.99	1	1.99	68.51	0.0143	
AB	1.45	1	1.45	50.10	0.0194	
A^2	0.7931	1	0.7931	27.32	0.0347	
B^2	0.1005	1	0.1005	3.46	0.2039	
Pure Error	0.0581	2	0.0290			
Cor Total	4.38	7				

Adequate Precision:16.9419

The quadratic model from ANOVA of calcination yield through NAR is represented in Table 4.24. The 29.80 F-value suggests that the model gives a satisfactory prediction of the experimental outcome with only a 3.28 % chance of noise. The choice of a significant model term is based on 0.0500 P-values benchmark. B, AB, and A^2 are relevant to model terms that are suitable for the prediction of the responses. Precision is the measure of the signal-to-noise ratio. For any model to have an acceptable precision, it must have a minimum value of 4. A precision value of 16.942 in this study shows that the model is satisfactory.

Equation 4.59 of the pentagonal experimental design served as the basis for the quadratic model that predicts the outcome of the thermal decomposition yield with the coded variables, while equation 4.60 uses actual factors.

$$Calcination\ yield(\%) = +61.30 - 0.1430A + 0.8920B - 1.530AB - 0.860A^2 - 0.3063B^2 \quad (4.59)$$

$$\text{Calcination yield (\%)} = +43.3806 + 0.53756A + 0.02789B - 0.00051AB - 0.00382A^2 - 7.65723E06B^2 \quad (4.60)$$

4.8.1 Individual influence of time and temperature on the calcination product from NAR

Figure 4.37 depicts the singular impact of calcination temperature and time respectively, on the calcination product. This suggests that the calcination time of $Mg(OH)_2$ is insignificant and is consistent with the ANOVA report, which shows that the influence of calcination time has a 0.3158 P-value. As the thermal decomposition time raised from 10 to 25 Mins, the calcination percentage slightly increases from 60.27 to 61.30 %, whereas increasing the thermal decomposition time to 40 minutes causes a decline in the calcination product back to 60.30 %. The thermal decomposition yield slightly increases from 60.11 to 61.9 % when the temperature rises from 500 to 652.8 ^oC. This suggests that temperature has a considerable

impact on the calcination yield, which is consistent with an ANOVA finding that the temperature effect on calcination yield has a P-value of 0.0143.

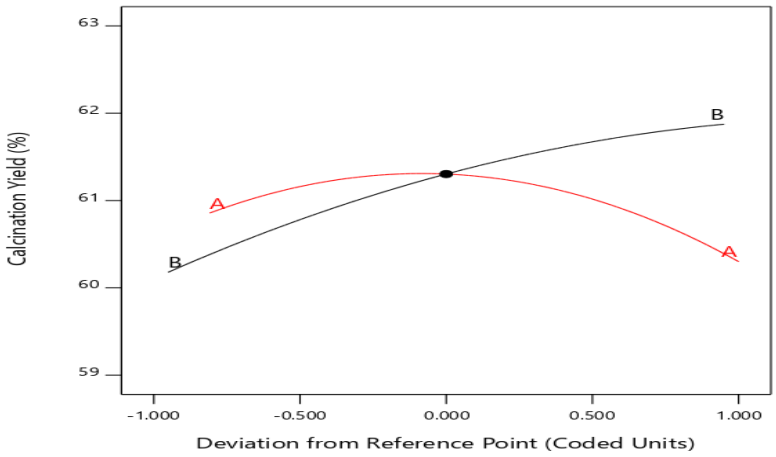

Key	
A	Time
B	Temperature

Figure 4.37: Effect of Time and Temperature on the Calcination Yield from NAR

4.8.2 Combined impact of temperature and time on the calcination yield from NAR

Figure 4.38 (a) depicts the plot of the combined influence of decomposition time and temperature on the calcination product from HPASR, and Figure 4.38 (b) depicts the three-dimensional plot (b). The simultaneous rise in the decomposition temperature from 500 to 900 ^{o}C and the calcination period from 10 to 40 Mins, brings about an increase in the calcination product from 59 to 62 %. Only small portions of the calcined samples fall inside the smallest blue band, which suggests calcination yields of between 59 and 60 %. The high proportion of the decomposition occurs within the calcination yield of 61 % since the green region has the largest area. The red zone with the average area has the highest calcination yield, 62 %, which indicates that a significant portion of the decomposition falls inside this region.

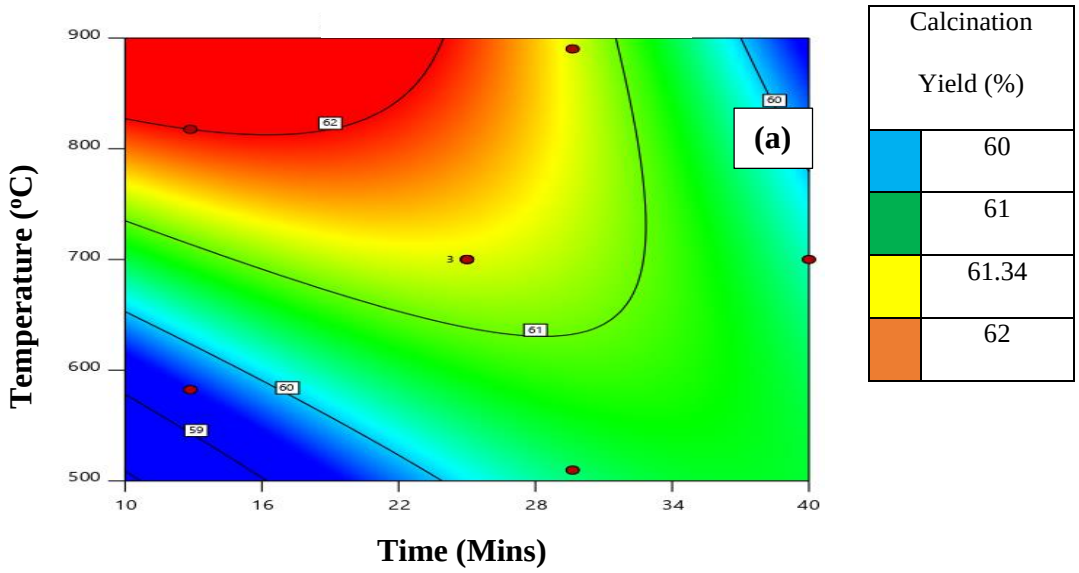

Figure 4.38: (a) Contour Plot of Interactive effect of Time and Temperature on the Calcination Yield from NAR

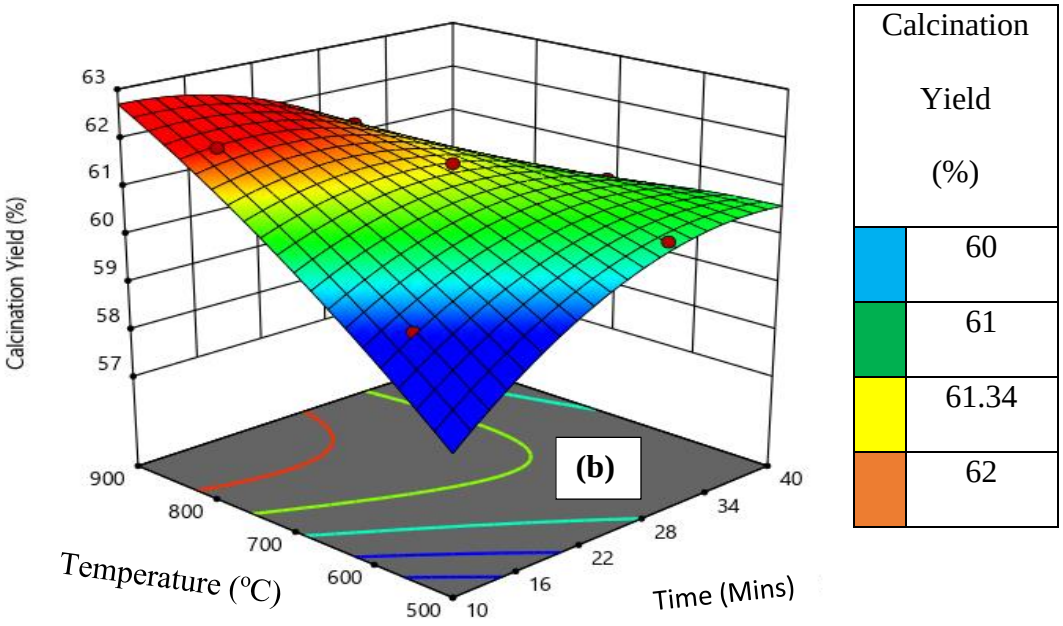

Figure 4.38: (b) Three Dimensional Plot of Interactive Effect of Time and Temperature on the Calcination Yield from NAR

Table 4.25 Optimization Boundaries for the Calcination Product from NAR

Name	Goal	Lower Boundary	Upper Boundary
Decomposition Time (Mins)	Minimize	10.00	40.00
Decomposition Temperature (°C)	is target = 700.00	500.00	900.00
Calcination Product (%)	is in range	59.50	62.00

Table 4.25 illustrates the boundary conditions for the optimization of the calcination product. The ANOVA reveals that the influence of the decomposition time on the calcination product is negligible, necessitating the reduction of this influence. The calcination yield is somewhat influenced by temperature, thus its influence was first set at the midpoint to determine the optimum point. With desirability of 1 (Figure 4.40), the numerical optimization approach predicts that a calcination product of 60.59 % can be attained at a 700 °C decomposition temperature within 10 Mins. A calcination product of 60.51 % was validated under the expected process parameters.

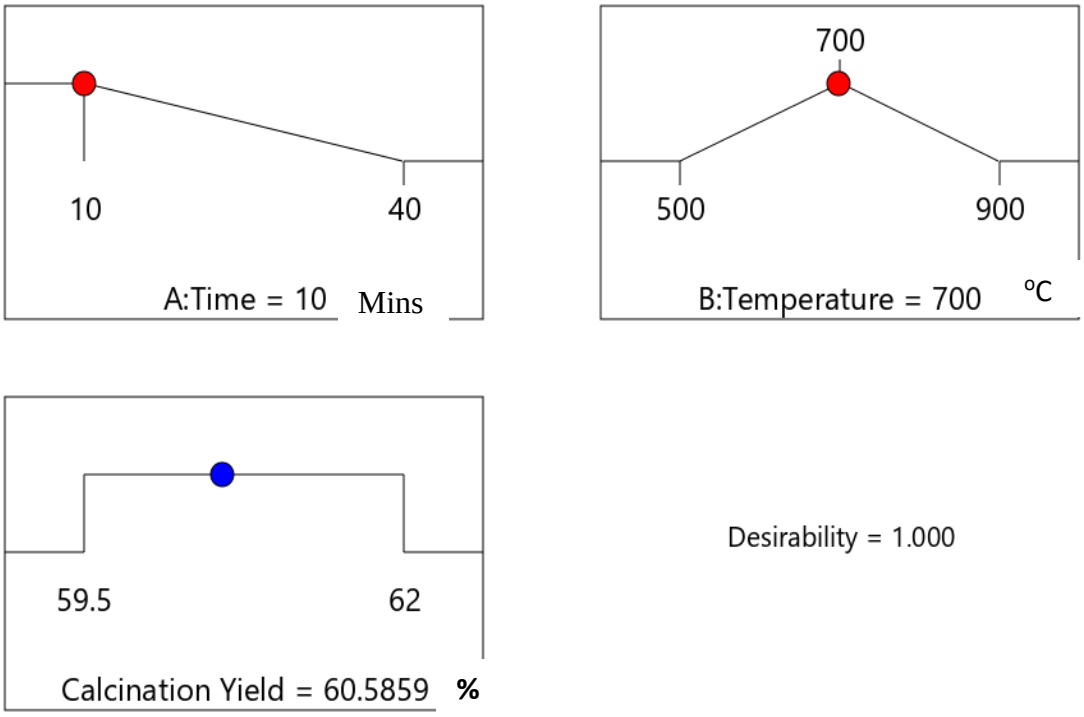

Figure 4.39: Optimum Point Prediction for the Calcination Product from NAR

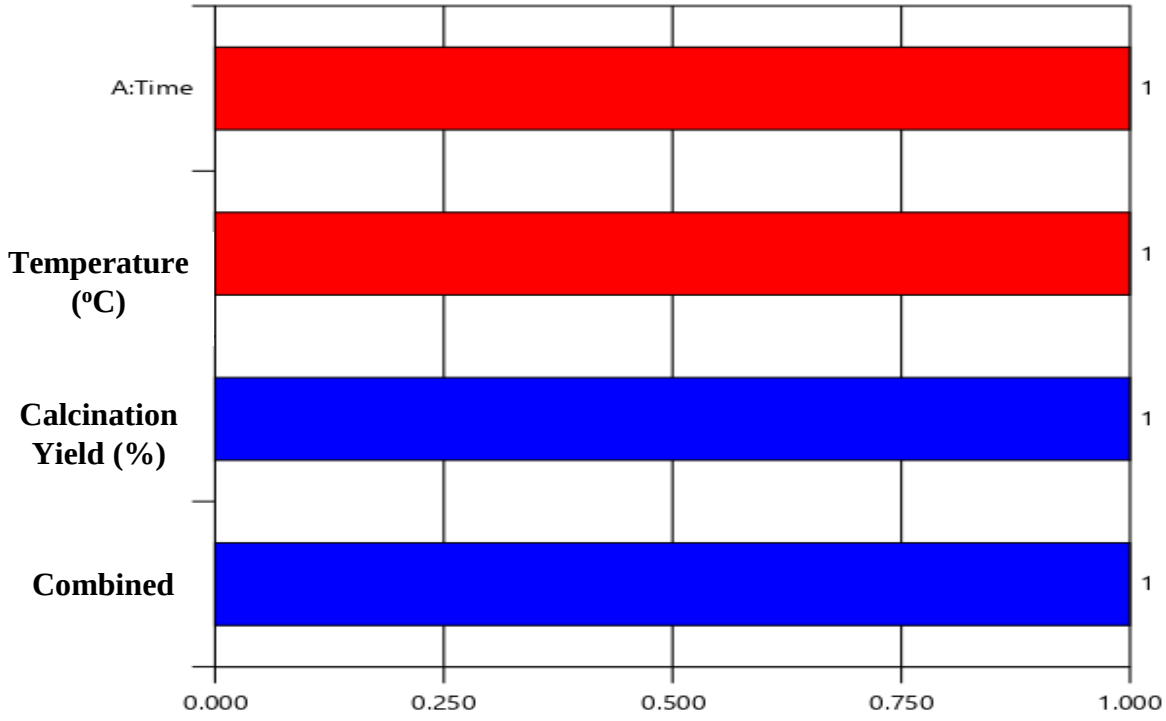

Figure 4.40: Desirability Plot of Calcination Yield from NAR

4.9 Optimization of the Calcination Process Using Pentagonal Experimental Design for the Synthesis of MgO from Dolomite (HPASR)

The pentagonal experimental design (PED) method in Design Expert software 11.0 was used in the optimization study of two independent variables, where the first variable, A, has 4 levels and variable B has 5 levels. The PED further enhanced the reduction of the number of experimental runs required to arrive at the optimum point. A preliminary experiment investigated the one-factor-at-a-time, parameters such as calcination time, and temperature, which show significant effects on the yield of MgO from magnesium hydroxide. Therefore, the two factors of time and temperature were selected for further study. Decomposition time was investigated between 10 to 40 Mins, while calcination temperature was varied between 500 to 900 ^{o}C as seen in Table 4.26. The developed mechanism of reactions in this study in Equation 4.56 to 4.59 represents the decomposition reaction of $Mg(OH)_2$ to MgO.

Table 4.26: Conditions for Pentagonal Experimental Design of the production of MgO

Factor (Numeric)	Minimum	Maximum	Coded		Mean	SD
			Low	High		
A - Time (Minutes)	12.86	40.00	-1 ↔ 10.00	+1 ↔ 40.00	25.00	8.96
B- Temperature (^{o}C)	509.80	890.20	-1 ↔ 500.00	+1 ↔ 900.00	700.00	119.53

SD: Standard Deviation

Three statistical models, which are linear, two-factor interactions (2FI), and quadratic, were tested on the response for model fitness. The model fitness was chosen based on the highest set of R^2, predicted $R^{2,}$ and adjusted R^2 values, but values close to unity are preferred. In Table 4.28, the R^2 of 0.9988 and adjusted R^2 of 0.9957 for the quadratic is much closer to unity compared with the R^2 of 0.3904 and adjusted R^2 of 0.1466 for the linear model, while

the 2FI has an R^2 of 0.6533 and an adjusted R^2 of 0.3933. Hence, the interaction between the independent (calcination time and temperature) and dependent (calcination product) parameters is best described by the second-order quadratic regression model.

Table 4.27: Model Summary Statistics Calcination Yield of MgO from Hydrochloric-Perchloric Acid System Route (HPASR)

Source	Standard Deviation	R^2	Predicted R^2	Adjusted R^2	
Linear	3.54	0.3904	-1.2057	0.1466	
2FI	2.99	0.6533	-1.6860	0.3933	
Quadratic	**0.2517**	**0.9988**		**0.9957**	**Suggested**

Table 4.28 shows the eight experimental runs generated using a pentagonal design. The calcination yield of MgO represents the response of the experimental design. The experimental results were very accurate as the model predicted values and the actual values were very close with a residual sum of -0.01. This represents the discrepancy between the experimental results and the expected values.

Table 4.28: Pentagonal Design for the Production of MgO through Hydrochloric-Perchloric Acid System (HPASR)

Run	A: Time (Minutes)	B: Temperature (°C)	Calcination Yield (%)		
			Actual	Predicted	Residual
1	13	818	58.00	58.00	0.00
2	25	700	67.80	67.77	0.03
3	30	510	64.50	64.50	0.00
4	13	582	68.50	68.50	0.00
5	25	700	67.50	67.77	-0.27
6	30	890	61.50	61.50	0.00
7	40	700	67.75	67.750	0.00
8	25	700	68.00	67.77	0.23
Sum					**-0.01**

The plot of the predicted against the observed yield is given in Figure 4.41 with practically all the spots on the line. As can be observed, the projected calcination yield of MgO is 58 %, which is in line with the actual calcination yield of MgO of 58 %. The projected calcination yield of MgO is 68 %, compared to the actual calcination yield of 68 % for MgO. This suggests that the actual and projected MgO calcination yields in this investigation have a proportionate connection.

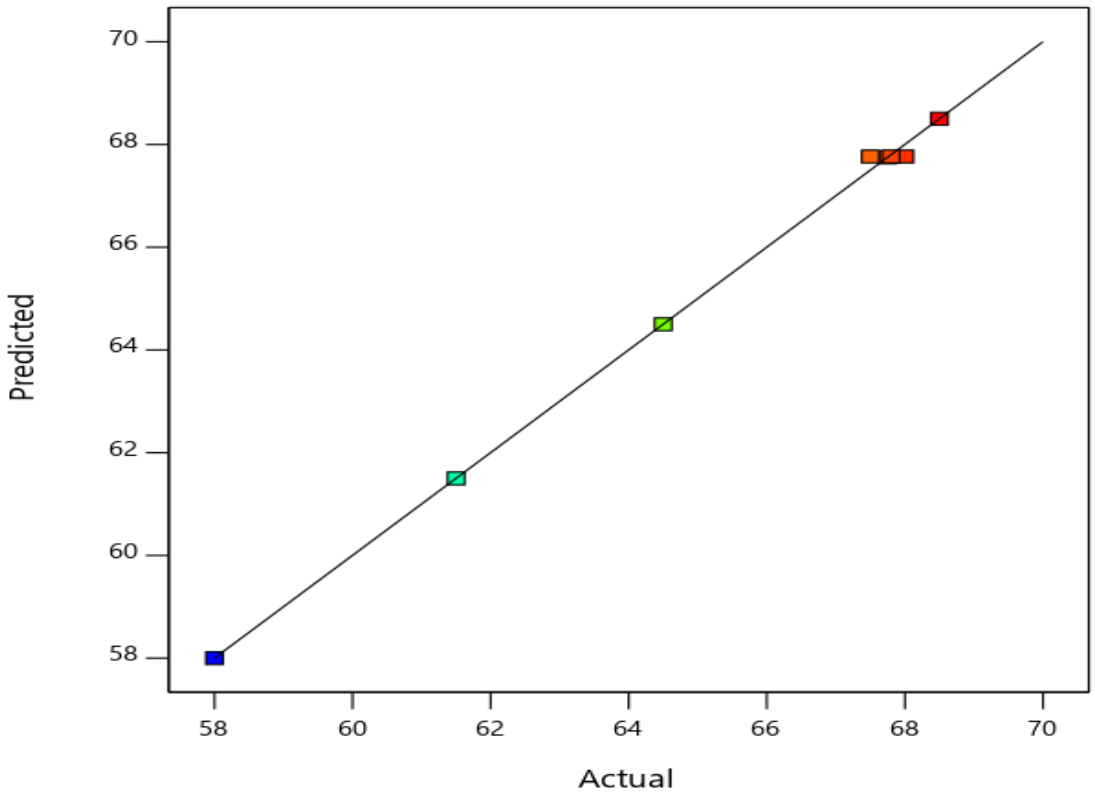

Figure 4.41: Predicted against the Actual Calcination Product of MgO from HPASR

4.9.1 Response analysis on the calcination yield of MgO from HPASR

Equation illustrates the development of the quadratic model from the pentagonal experimental design that predicted the calcination product in terms of coded variables (4.61). Model equation 4.62 was designed to forecast the calcination product in terms of the real component.

$$Calcination\ yield(\%) = +67.77 + 1.74A - 3.61B + 6.58AB - 1.75A^2 - 5.68B^2 \quad (4.61)$$

A and B are Time (Minutes) and temperature (^oC) respectively.

$$\text{Calcination yield (\%)} = 41.42142 - 1.02870A + 0.125921B + 0.002192AB - 0.007795A^2 - 0.000142B^2 \quad (4.62)$$

Table 4:29: ANOVA for Quadratic Model Calcination Yield of MgO from HPASR

Source	Sum of Squares	df	Mean Square	F-value	p-value	
Model	102.70	5	20.54	324.32	0.0031	Significant
A-Time	7.54	1	7.54	119.12	0.0083	
B-Temperature	32.57	1	32.57	514.22	0.0019	
AB	27.03	1	27.03	426.85	0.0023	
A^2	3.30	1	3.30	52.04	0.0187	
B^2	34.55	1	34.55	545.50	0.0018	
Pure Error	0.1267	2	0.0633			
Cor Total	102.83	7				

Df: Degree of freedom; Adequate Precision: 48.1773

The proposed quadratic model equation was tested for model relevance using the F-value from ANOVA. The model is suggested to be significant with a 324.32 F-value, hence, only 0.31 % noise can be recorded. A, B, AB, A^2, and B^2 are significant model terms, as shown in Table 4.29 since values below 0.0500 P-values imply significance. The signal-to-noise ratio corresponds to the model precision, a minimum of 4 is mostly desired. This model can be utilized to navigate the design space as the ratio of 48.177 shows a high adequate precision

4.9.2 Single effect of process parameters on the calcination product from HPASR

Figure 4.42 shows the relationship between the individual effects of the control factors of calcination temperature and time on the calcination product. The center point temperature is 700 ^{o}C (0) while that of time is 25 Mins (0). The calcination product increases from 64.27 to

67.75 % as the time increases from 10 (-1) to 40 (1) minutes, implying that the resident time of $Mg(OH)_2$ during the calcination is important because it allows more molecules to undergo decomposition and form MgO. It was observed that as the temperature rises from 500 (-1) to 652.8 ^{O}C (1) the calcination product also increases from 65.69 to 68.33 % after which a further increase in temperature up to 900 ^{o}C resulted in a drop in the calcination yield of 58.55 %. The initial increase in calcination yield could be due to an increase in the rate of calcination of $Mg(OH)_2$ to MgO as the molecules gain kinetic energy, whereas the decrease in calcination yield could be attributed to the loss of calcination yield at elevated temperatures.

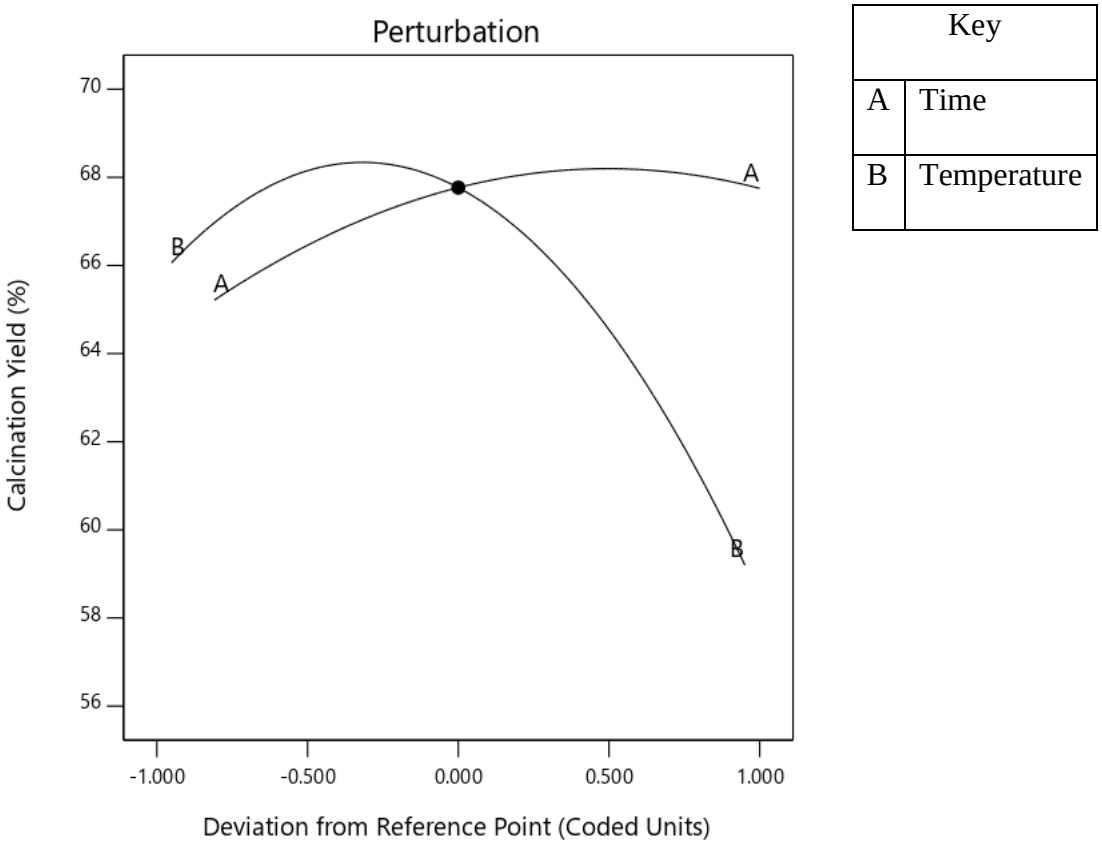

Figure 4.42: Single Influence of Temperature and Time on the Calcination Product from HPASR

4.9.3 Interactive influence of calcination time and temperature on the calcination products from HPASR

The plot of the interactive influence of calcination temperature and time on the calcination product from HPASR is shown in Figure 4.43a, while the three-dimensional view plot is presented in Figure 4.43b. It observed that as the temperature changes from 500 to 900 ^{o}C and time changes from 10 to 40 minutes, the calcination product decreases from 68.28 to 55 %. This implies that calcination at high temperatures for an extended time resulted in a significant loss of calcination yield. The red, green, and blue colours represent calcination yield at 68.28 %, 65, and 60 to 55 % respectively.

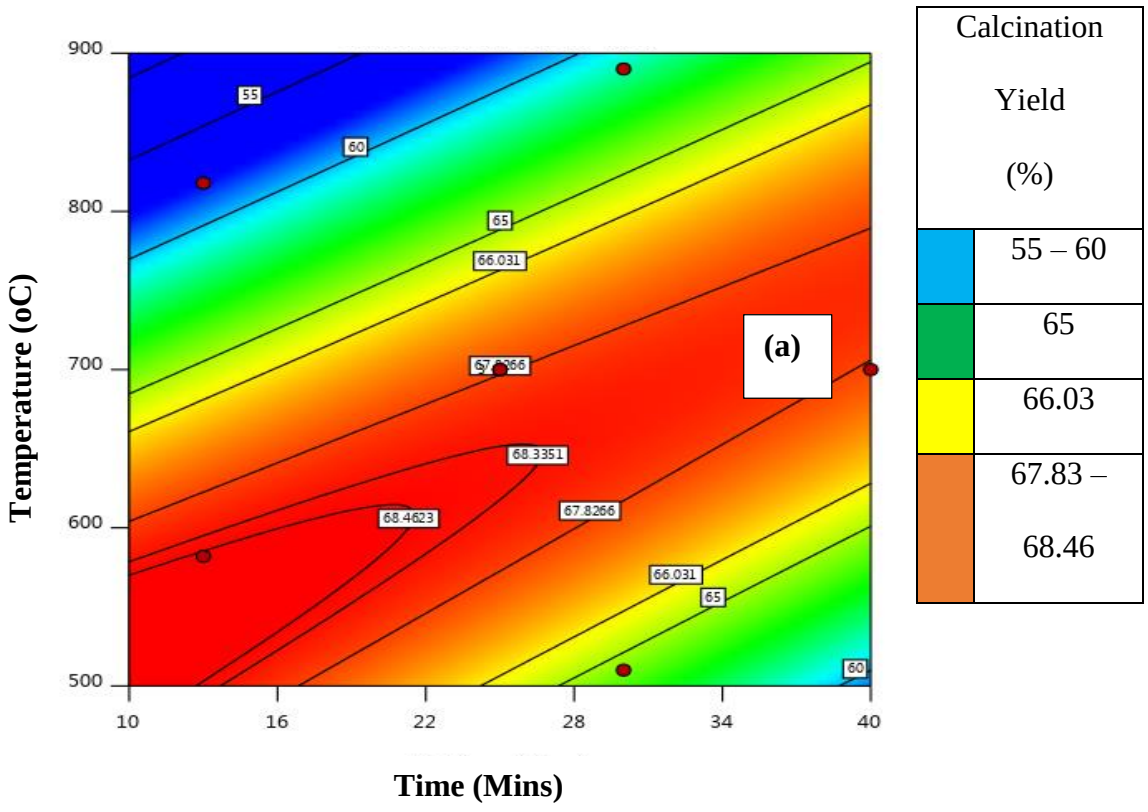

Figure 4.43: (a) Contour plot of Interactive Influence of Time and Temperature on the Calcination Product from HPASR

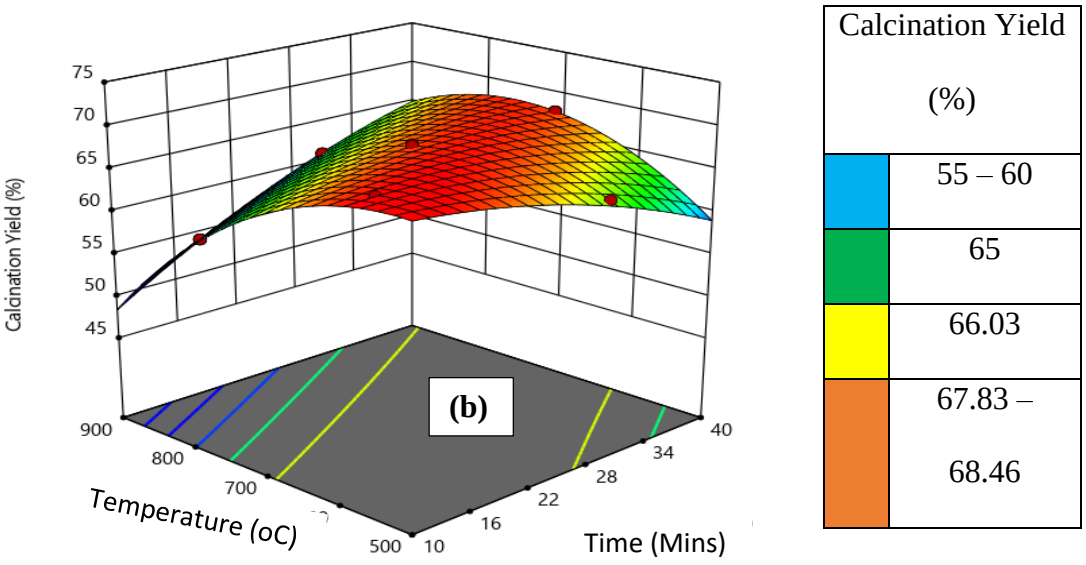

Figure 4.43: (b) Three-dimensional Plot of Interactive Influence of Time and Temperature on the Calcination Product from HPASR

According to the statistical and regression analysis, both temperature and time showed significant effects on the calcination yield, but at higher process variables, a loss of calcination yield was recorded. To maintain balance in the calcination yield, both the effects of time and temperature were set in the range shown in Table 4.30 to predict the optimum calcination yield.

Table 4.30: Optimization Controls for the Calcination Product from HPASR

Name	**Goal**	**Lower Boundary**	**Upper Boundary**
Time (Minutes)	is in range	10	40
Temperature (^{o}C)	is in range	500	900
Calcination Yield (%)	Maximize	58	68.5

The highest predicted points for the calcination yield of MgO from HPASR are presented in (Figure 4.44). The best prediction using the numerical optimization technique shows that a calcination product of 68.5 % can be obtained at a temperature of 582.5 ^{o}C and a time of 13 minutes. The predicted point was validated through a laboratory experiment with a calcination yield of 68.1 % at the desirability of 1, as shown in Figure 4.45.

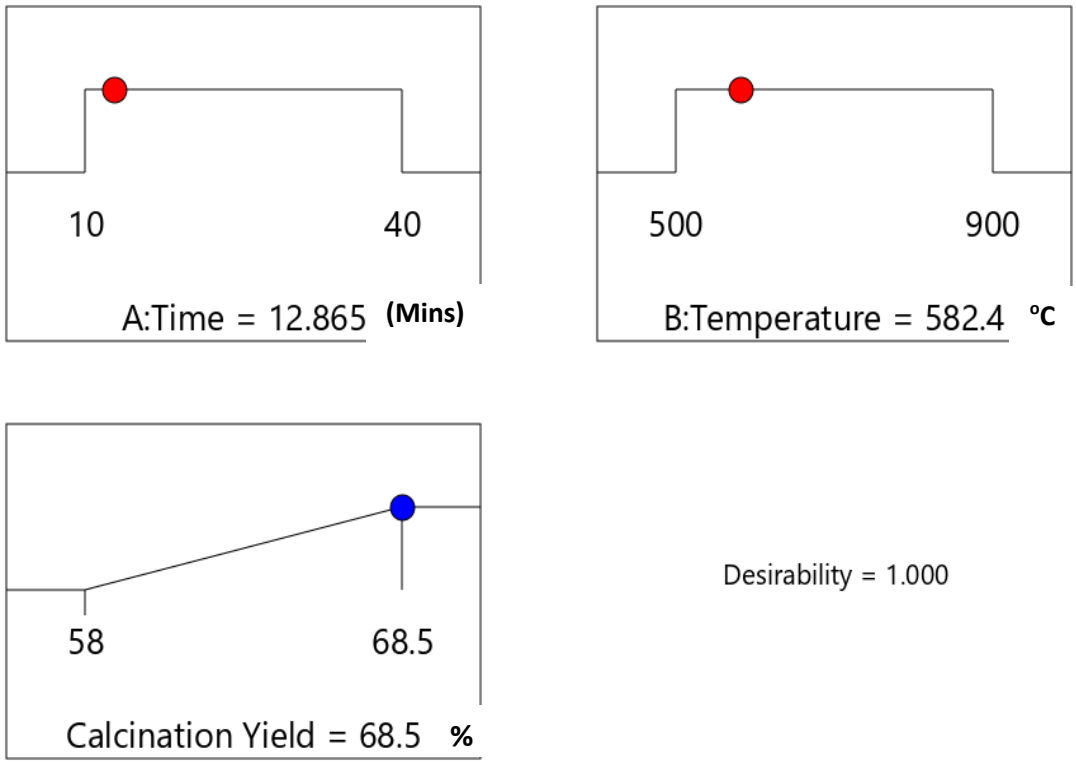

Figure 4:44: Optimum Points Prediction for the Calcination Product of MgO from HPASR

The desirability plot of the calcination yield of MgO from HPASR presented in Figure 4.45 shows that the temperature, time, and the combined effect all have a desirability of 1. This implies that the optimization method used in this study to arrive at the optimum predicted point is a perfectly fit for the calcination yield of MgO from HPASR.

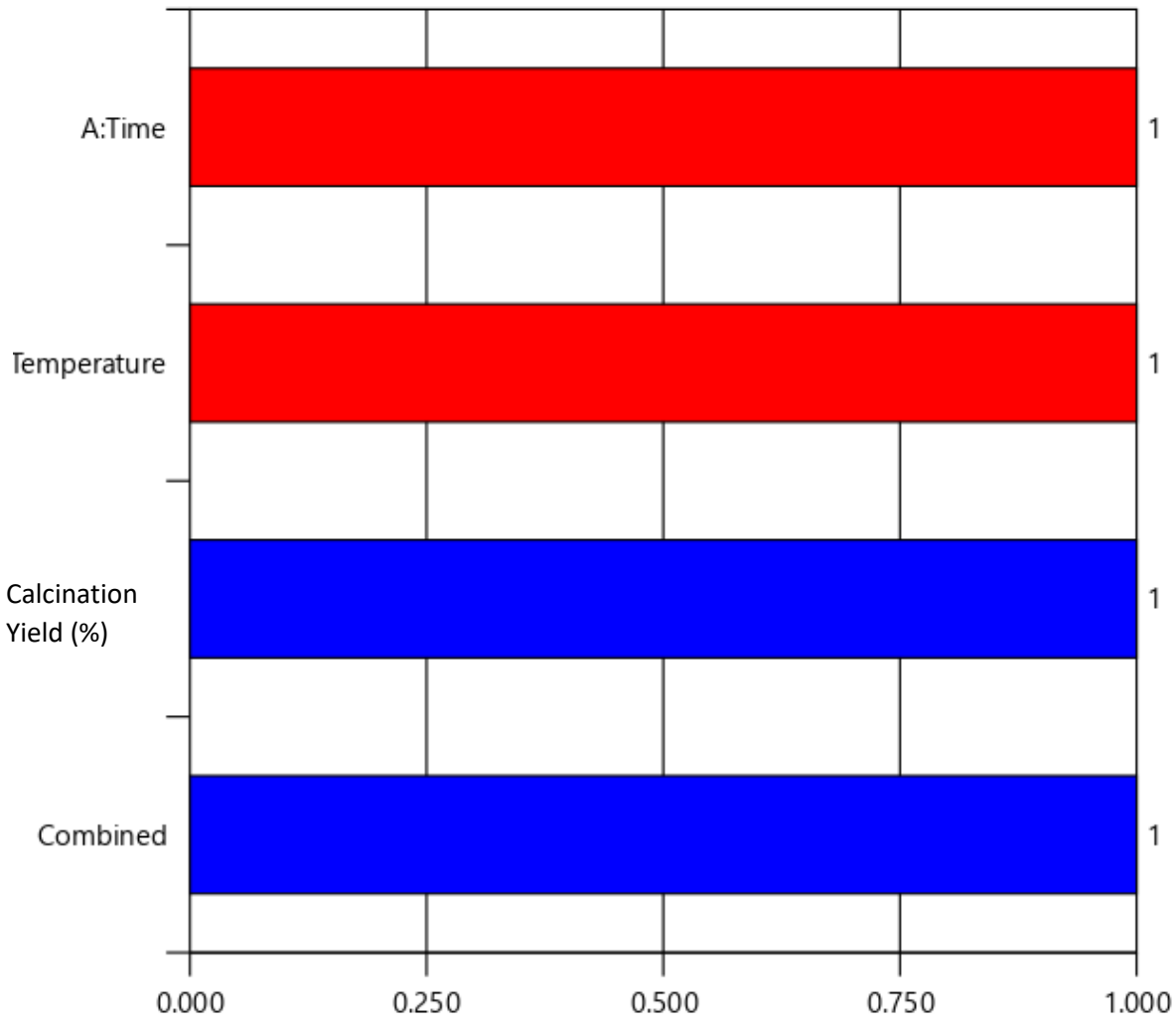

Figure 4.45: Desirability Plot of Calcination Yield of MgO from HPASR

4.10 Characterisation of Dolomite and Synthesized MgO

The following characterisations were carried out to ascertain the synthesized product to be MgO:

4.10.1 X-ray diffraction analysis of the precipitated samples

The mineral diffraction identification in dolomite ore and precipitated samples was carried out following the Joint Committee on Powder Diffraction Standards (JCPDS) using XRD analysis, and the result is presented in Figure 4.46 for NAR, while that of HPASR is presented in Figure 4.47.

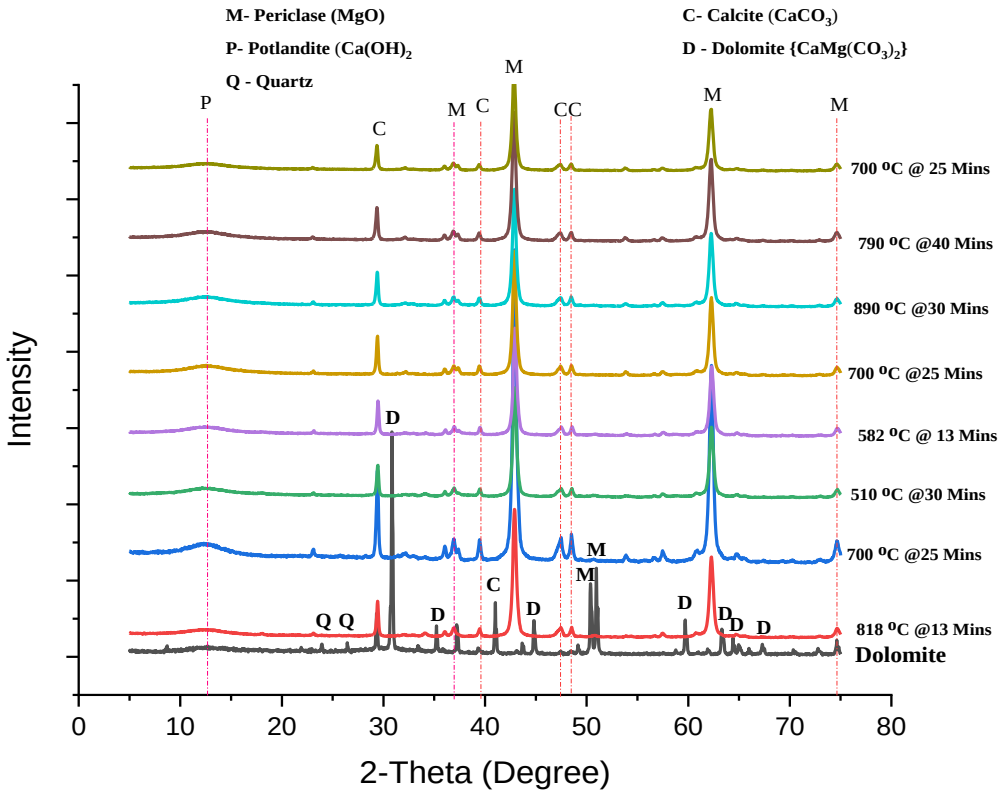

Figure 4.46: X-ray Diffraction Pattern of the Precipitated Samples from NAR

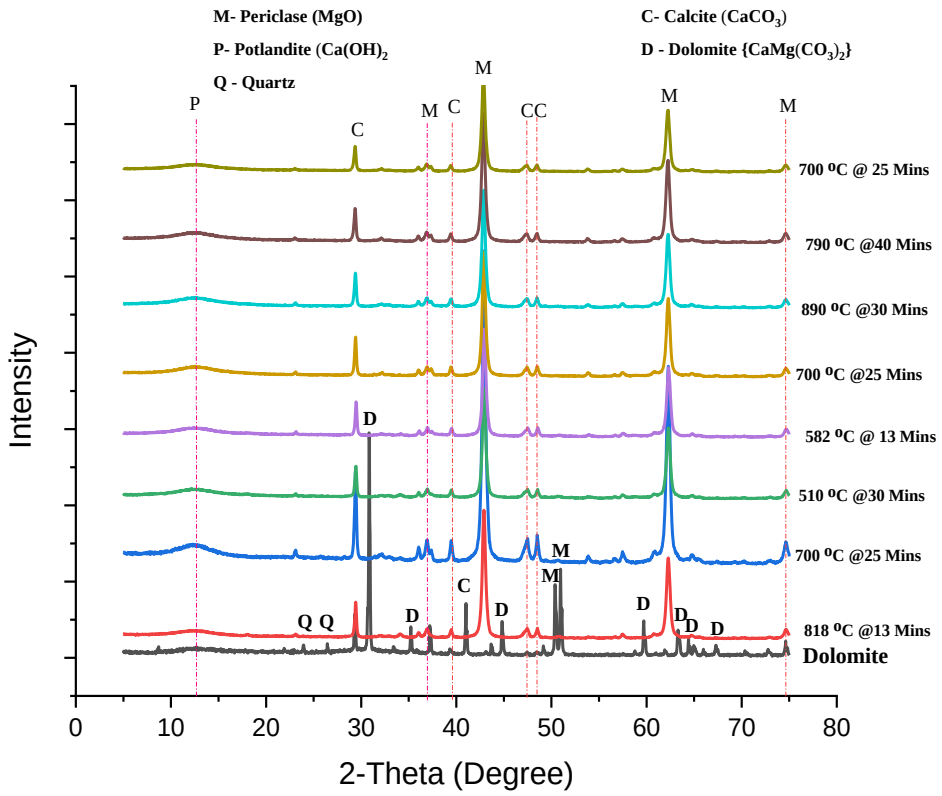

Figure 4.47: X-ray Diffraction Pattern of the Precipitated Samples from HPASR

It can be seen that the most prominent peak of dolomite mineral diffraction (JCPDS 84–1208) falls at a 2θ angle of 30.83º. The other less prominent peaks of the dolomite mineral are also observed at diffraction angles of 35.29 º, 37.28 º, 44.88 º, 59.76 º, and 63.56 º. Almost all the dolomite mineral diffractions are absent in all the samples N1 to N8 and P1 to P8. This implies that the magnesia phase (MgO) was successfully separated from the dolomite. In the dolomite ore, two primary conspicuous periclase (MgO) peaks with mineral diffraction peaks at 50.33º and 51º were found. Prominent MgO diffraction is present at 42.90 º, 62.4 º, 72.8 º, and 74.47 º in the precipitated N1 to N8 samples, while it is present in samples P1 to P8 at diffraction angles of 36.96, 62.4 º, 72.8 º and 74.47. This clearly shows that the method employed in the selective separation process in this study from the saturated solution is

suitable for the production of MgO. Calcite ($CaCO_3$) mineral diffraction (JCPDS 5-0586) was recognized at diffraction angles of 40.91 ^{o} and 29.33 ^{o} in the dolomite ore. While prominent peaks in all the precipitated samples were identified at 29.33^{o}, other calcite diffraction angles at 36.94 ^{o}, 47.36 ^{o}, and 57.44 ^{o} are in traces.

The calcite mineral diffraction angles identified in the dolomite ore are absent in the precipitated samples N1 to N8 and samples P1 to P8. This implies that calcite in the dolomite ore went into solution while the new diffraction angles in the precipitated samples can be attributed to the calcite present in the precipitant as an impurity. The quartz (SiO_2) mineral diffraction angle (JCPDS 83-0539) in the dolomite ore is present at a diffraction angle of 23.87 ^{o} while in the precipitated samples it has faint peaks which help to confirm the removal of the SiO_2 during the filtration process. The portlandite ($Ca(OH)_2$) mineral diffraction identified in accordance to JCPDS 4-0733 is almost unnoticed in the dolomite ore while a slightly prominent peak is noticed in the precipitated samples N1 to N8 and sample P1 to P8. The $Ca(OH)_2$ in the precipitated samples can be considered to be an associate component of the precipitant. An additional mineral known as calcium chloride hydroxide (CaClOH) was identified only in samples P1 to P8 in accordance with JCPDS 36-0983, it can be inferred that the chlorine ion reacted with the calcium ion and hydroxide ions to form the CaClOH.

4.10.2 Quantitative determination of the oxide composition of synthesized MgO and dolomite via XRF analysis

The comparison of the oxide composition of dolomite and the precipitated samples from both the NAR and HPASR is presented in Table 4.31

Table 4.31: Metal Oxide Composition (%) of the Precipitated Samples

Sample	MnO	Cr_2O_3	Fe_2O_3	V_2O_5	CaO	K_2O	P_2O_5	TiO_2	Na_2O	SiO_2	Al_2O_3	MgO	LOI	Sum
N1	0.020	0.000	0.330	<0.01	14.660	0.010	0.500	0.060	<0.010	1.100	0.380	**69.780**	12.410	99.26
N4	0.020	0.010	0.340	<0.01	13.890	0.010	0.460	0.070	0.040	1.080	0.410	**69.200**	14.370	99.87
N7	0.020	0.010	0.350	<0.010	14.640	0.020	0.480	0.060	0.060	1.050	0.490	**72.720**	10.060	99.95
P1	0.01	0.00	0.21	0.00	16.58	0.03	0.33	0.05	0.12	0.67	0.28	**53.70**	17.13	89.13
P4	0.01	0.01	0.24	<0.01	13.51	0.02	0.37	0.05	0.00	0.52	0.28	**49.07**	26.41	90.48
P7	0.01	0.00	0.25	0.00	10.99	0.01	0.35	0.06	<0.01	0.73	0.21	**56.80**	25.58	95.00
Dolomite	0.00	0.00	0.10	0.00	30.62	0.07	0.05	0.02	0.00	1.87	0.44	**18.84**	45.91	97.92

It can be clearly seen in Figure 4.48 that dolomite has the least MgO content of 18.84 % when compared to all the precipitated samples. This implies that the entire process in this study is suitable for the production of MgO. Among the precipitated samples, N7 has the maximum quantity of MgO (72.72 %) followed by N1 (69.78 %) and N4 (69.2 %), while sample P4 has the least. This suggests that the process conditions at N7 favours the synthesis of MgO from $Mg(OH)_2$. All the samples from NAR have higher values of $Mg(OH)_2$ compared to samples from HPASR. This might be due to a reduction in the degree of precipitation of MgO caused by competition from precipitation from CaO and $CaCl_2$ in the presence of a precipitant. The MgO purity of 72.72 % for sample N7 is below the 88 % reported for MgO produced from East Java, Indonesia dolomite. This might be due to a difference in the geological composition of the dolomite (Mubarok and Kumiawan, 2015)

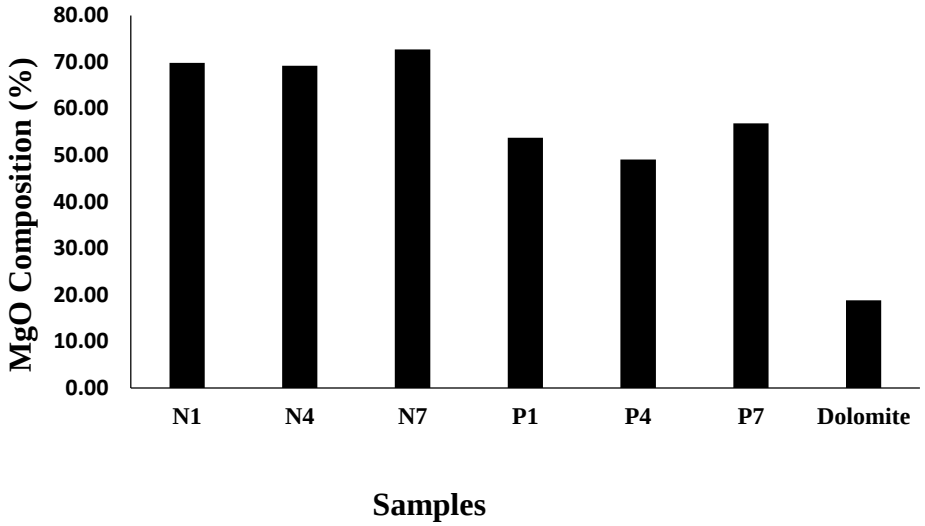

Figure 4.48: MgO composition of Precipitated Samples and Dolomite

The LOI Composition of precipitated samples and that of dolomite is presented in Figure: 4.49**.** The formation of $CaCl_2$ as identified by the XRD can be attributed to the interaction of calcium ion (from dissolved dolomite and $Ca(OH)_2$) and excess chlorine from the mixture of

HCl and $HClO_4$. This can be explained by the higher number of LOI in the P7, P4, and P1 when compared to the N7, N4, and N1. It can therefore be inferred that the $CaCl_2$ present in P7, P4, and P1 was converted to chlorine dioxide on the exposure of the samples to high temperatures during the XRF analysis. This also contributed to the high LOI in the samples. Another factor that can be responsible for the overall content of the LOI is the presence of $CaCO_3$ (identified by the XRD), which can be attributed to impurities in the precipitant. During XRF analysis, the $CaCO_3$ undergoes decomposition and is converted to CaO and carbon dioxide. The carbon dioxide adds up to the LOI content.

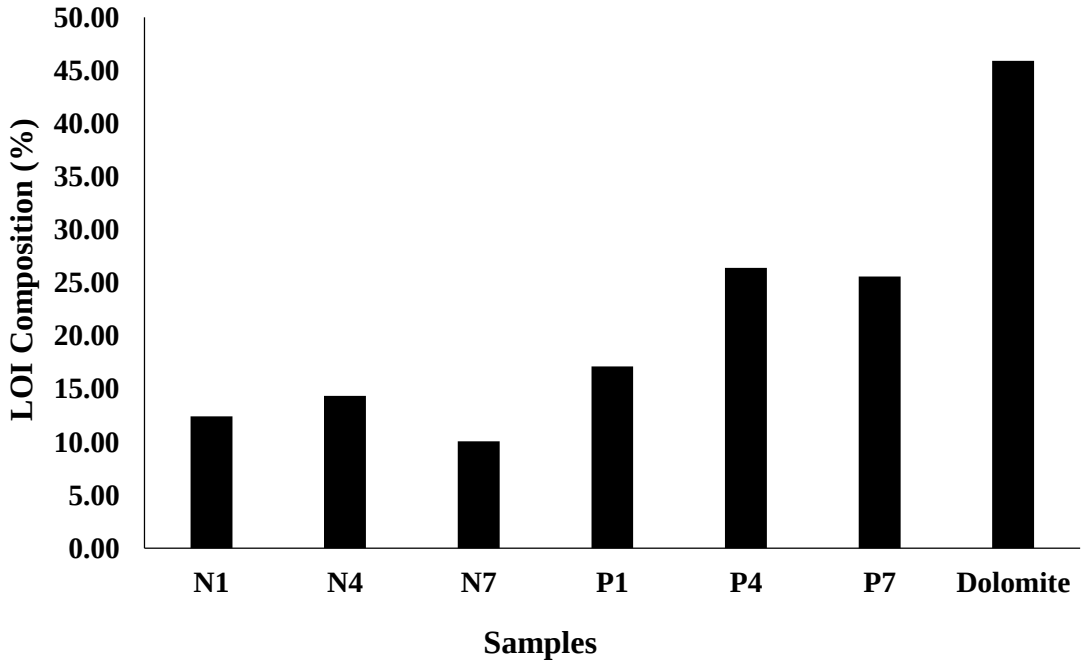

Figure: 4.49: LOI Composition of Precipitated Samples and Dolomite

The amount of CaO present in the calcinated samples as well as in dolomite ore is presented in Figure 4.50. The CaO from the decomposition of $CaCO_3$ adds up to the amount of CaO that is co-precipitated from the saturated solution and the unreacted CaO from the precipitant.

This is what is responsible for the CaO content of all the samples. P1 has the highest CaO of 16.58 % followed by N7 (14.64 %), while P7 (10.99 %) has the least.

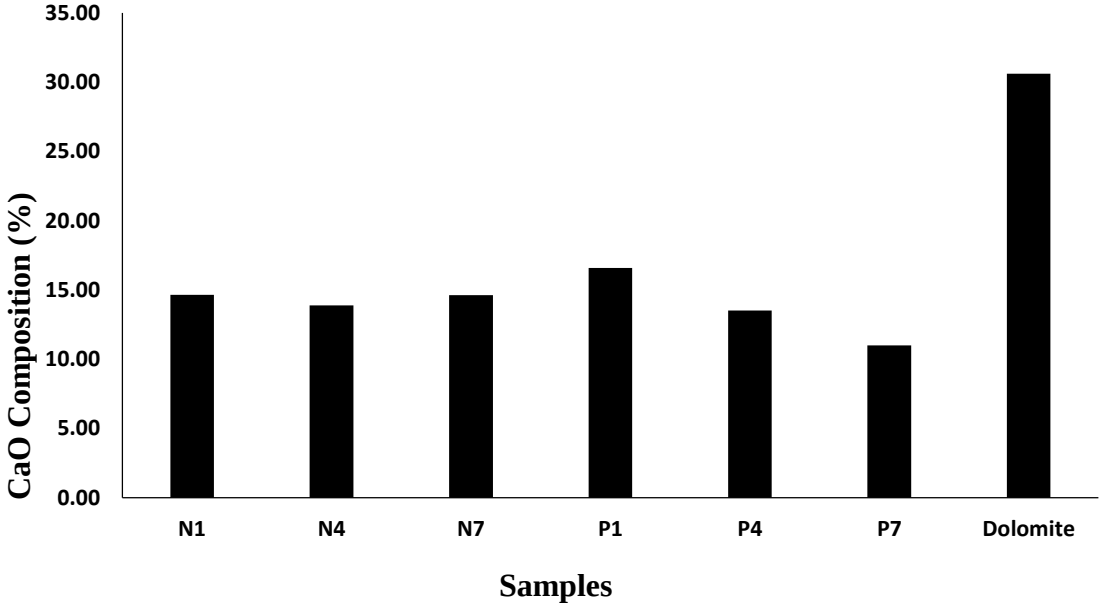

Figure 4.50: CaO composition of Precipitated Samples and Dolomite

The SiO_2 of dolomite (1.87 %) in this study is higher compared to all the precipitated samples. This implies that it does not go into solution during the dissolution process and that the filtration process was efficient. From the precipitated samples, the highest SiO_2 was recorded in N1 (1.1 %), followed by N4 (1.08 %), while P4 (0.52 %) had the least. The SiO_2 content of all samples is significantly low; however, the SiO_2 content of all precipitated samples may be due to the one associated with the precipitant because a small fraction of it settles down at the bottom of the beaker when it is added to the water before precipitation.

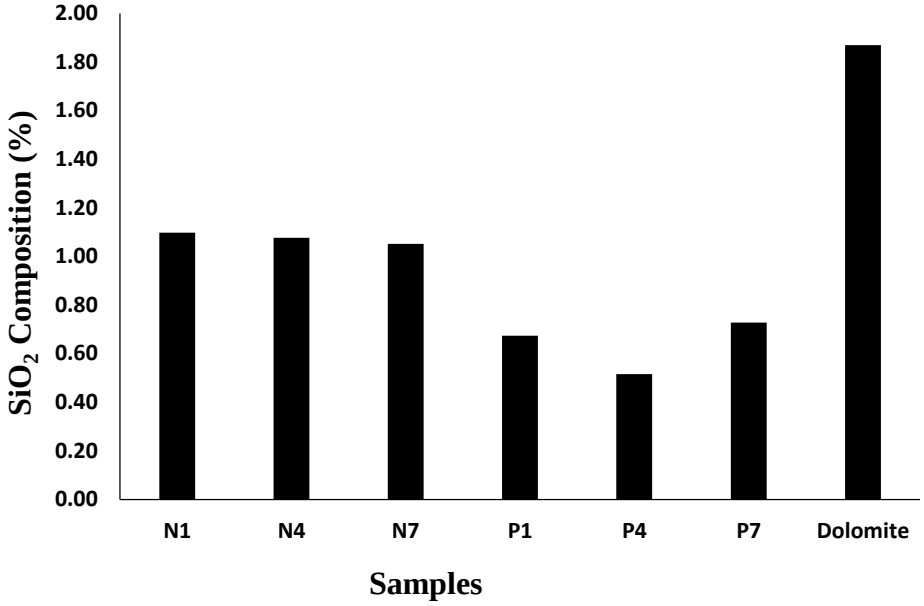

Figure 4.51: SiO_2 Composition of Precipitated Samples and Dolomite

4.10.3 SEM of both $Mg(OH)_2$ and MgO

Plates XIV and XV show SEM images of synthesized $Mg(OH)_2$ and MgO, respectively. It can be seen that there is an agglomeration of most of the particles which accounts for the platelet shape. This is in contrast with the report by Cho *et al.* (2016). However, the image of MgO has a larger pore than that of $Mg(OH)_2$ due to the loss of the water molecule during the breakdown of $Mg(OH)_2$ at high temperatures.

Plate XIV: SEM Image of Synthesized $Mg(OH)_2$

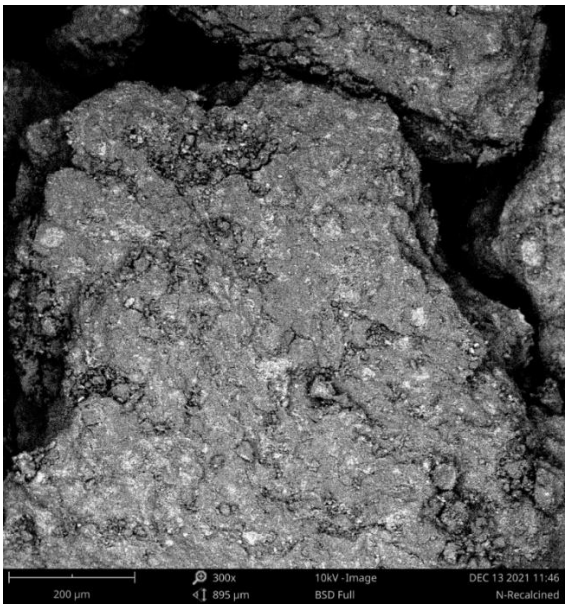

Plate XV: SEM Image of Synthesized MgO

4.10.4 FTIR results of synthesized $Mg(OH)_2$ and MgO

Figure 4.52 depicts the FTIR spectra of synthesized $Mg(OH)_2$ from NU and MgO from NC. The wavelength of the spectrum ranges from 600 to 4000 cm^{-1}.

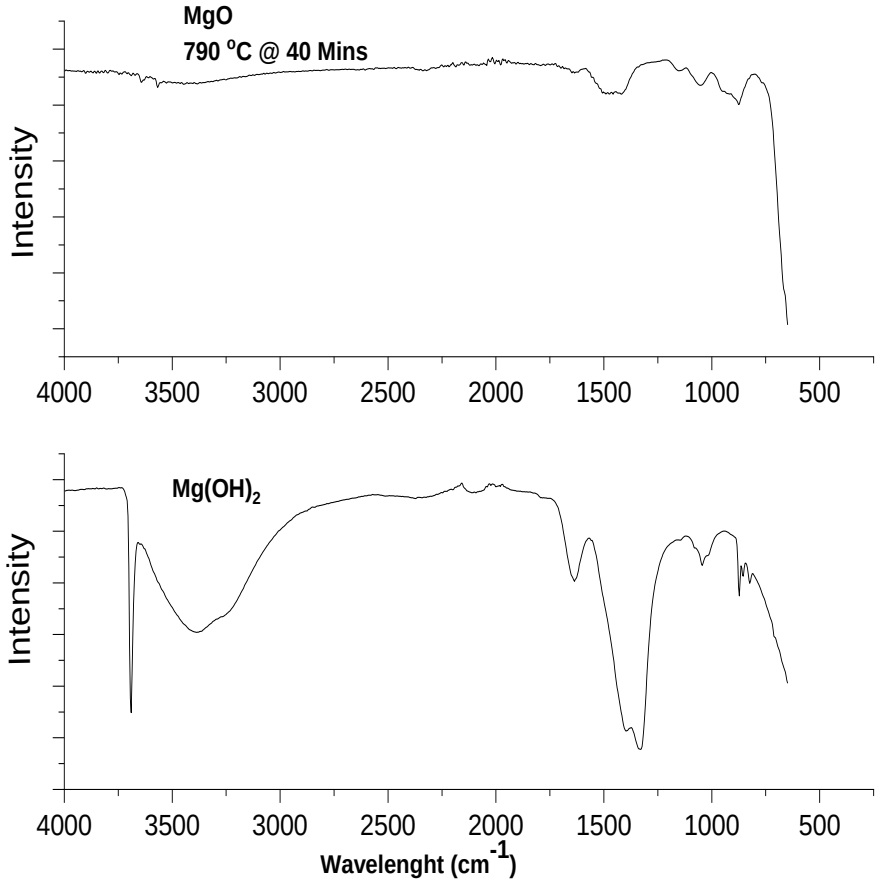

NU: Uncalcined sample from HNO_3 route; NC: Calcined sample from HNO_3 route

Figure 4.52: FTIR of $Mg(OH)_2$ from NU and MgO from NU

In NU, the bond between oxygen and magnesium in $Mg(OH)_2$ has a wavelength of 875.9244 cm^{-1}, whereas the bond in MgO has a wavelength of 872.1971 cm^{-1} (Imani and Safaei, 2019). This implies that there was no disruption of the bond between magnesium and oxygen by the calcination temperature, which accounted for the non-disappearance of the peak at the wavelength. The vibration of the carbonate ion (C-O) group (Imani and Safaei, 2019) is found in calcite and it has a prominent peak at a wavelength of 1043.6546 cm^{-1} in the NU spectral. It is reduced to only small peaks at a wavelength of 1066.0186 cm^{-1}. The disappearance of the prominent peaks in NC could be due to the conversion of the C-O group in calcite to

gaseous carbon dioxide, which was lost during the calcination process. The O-H group adsorbs in NU at wavelengths of 1319.4776, 1643.756, 3350.8767, and 3690.0645 cm^{-1} in $Mg(OH)_2$, whereas a small peak of the O-H group exists only in NC at 1446.2071. The loss of a water molecule from $Mg(OH)_2$ during the calcination process is responsible for the disappearance of the O-H group in NC. Imani and Safaei (2019) reported the OH group in magnesium oxide nanoparticles at the wavelength of 3420 cm^{-1}. Figure 4.53 shows the FTIR spectra of synthesized $Mg(OH)_2$ from PU and MgO from PU. The wavelength of the spectrial ranges from 500 to 4000 cm^{-1}.

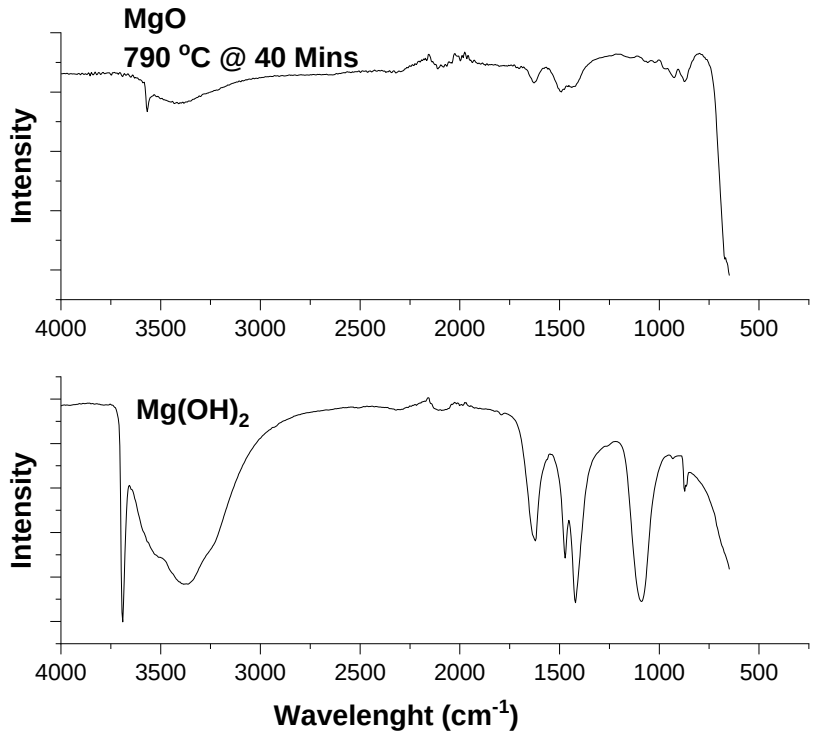

PU: Uncalcined sample from HCl-$HClO_4$ route; PC: Calcined sample from HCl-$HClO_4$ route

Figure: 4.53: FTIR of synthesized $Mg(OH)_2$ from PU and MgO from PU

In PU, the bond between oxygen and magnesium in $Mg(OH)_2$ has a wavelength of 875.80 cm^{-1}, whereas the bond in MgO has a wavelength of 857.2877 cm^{-1} (Imani and Safaei, 2019).

This implies that there was no disruption of the bond between magnesium and oxygen by the calcination temperature, which accounted for the non-disappearance of the peak at the wavelength. The vibration of the carbonate ion (C-O) group (Imani and Safaei, 2019) is found in calcite and it has a prominent peak at a wavelength of 1099.5647 cm^{-1} in the PU spectral. The absence of the prominent peak of the C-O group in PC could be a result of the high conversion of the C-O group in calcite to gaseous carbon dioxide, which was lost during the calcination process. The prominent adsorption of the O-H group in PU is found at wavelength 1423.8431, 1632.574, 2098.4912, 3395.6048, and 3690.0645 cm^{-1} owing to the presence of $Mg(OH)_2$ while a small peak of O-H group only exists in PC at the wavelength of 1461.1164 and 3555.8803. The disappearance of the OH^- group in NC is caused by the loss of a water molecule from $Mg(OH)_2$ during the calcination process. Imani and Safaei (2019) reported the OH- group in magnesium oxide nanoparticles at a wavelength of 3420 cm^{-1}.

4.10.5 Thermogravimetric analysis of MgO

The thermal behavour of the synthesized MgO was studied between 0 to 1000 ^oC (Figure 4.54). The profile shows that the theremal decomposition of MgO can be categorize into three stages. The first stage decomposition is due to lose of about 1.7 % hydrate water at temperature of 200 ^oC. At temperature of 294 ^oC, the weight lose was just 2.03 %. This suggest that the synthesized MgO has low surface water absorption (Hanna *et al.*, 2019). The second stage decomposition experienced a progressive weight lose from 2.2 % at temperature of 297 ^oC to 27.8 % at 356 ^oC. Further thermal exposure of the MgO to temperature of 461.49 0 ^oC resulted in rapid weight lose to 81.32 %, this shows that only 18.64 % was left undecomposed. In the third stage decomposition, increased temperature does not have much contribution on the weight loss as the weight of the MgO left at temperature of 766 ^oC only

dropped to 16.23 %. At decomposition temperature of 880 ^{o}C, only 15.54 % of the initial weight of MgO was left. The curve at the third stage tends toward linarity, as no further significant weight loss was recorded even at elevated temature. The red curve represent the result of differential thermal analysis. The derivative peaks represent the rate of change on the weight loss curve. Temperature of 384.84 ^{o}C and derivative weight percent of -4.63 %/m represent the first derivative peak which is also known as inflection point. This is the point at which the highest rate of change occurs (PerkinElmer, 2015).

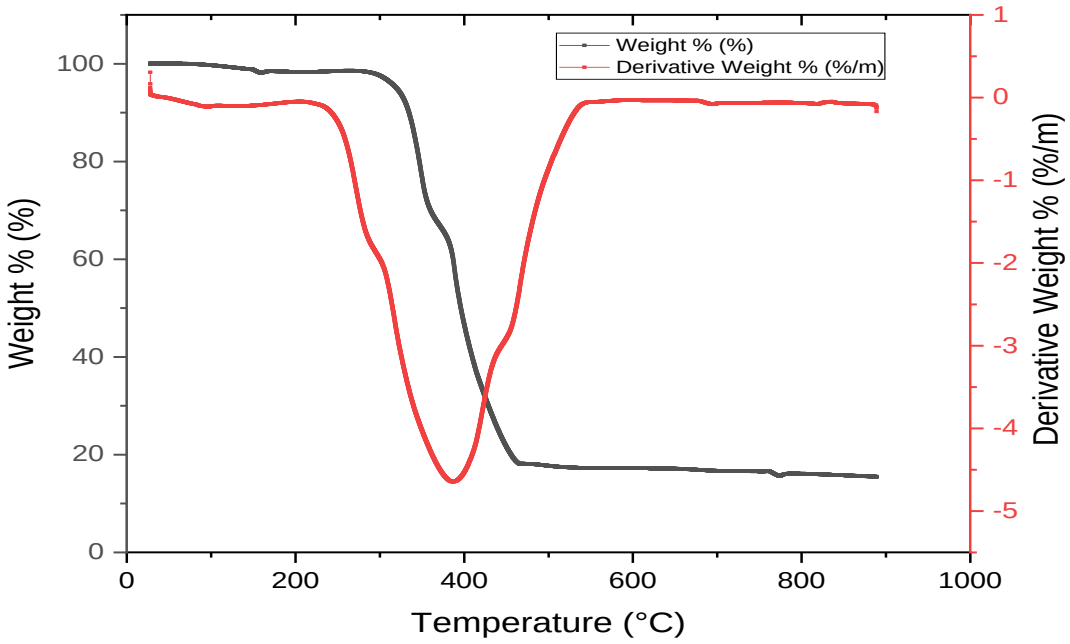

Figure 4.54: TGA/DTA of Magnesium Oxide at Optium (790 ^{o}C 40 mins)

4.11 Comparison between the Synthesized MgO and Naturally Occurring Sources

It is clearly shown in Figure 4.55 that the XRD spectra of both synthesized MgO from dolomite and other sources have almost the same XRD pattern. This implies similar mineral

phases and that the synthesized MgO in this study can compare favourably with synthesized MgO.

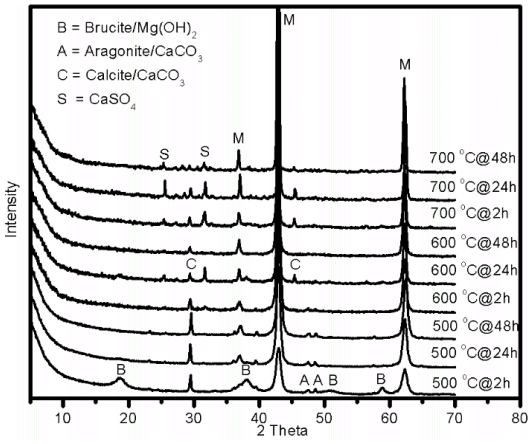

Synthesized MgO from brine
Source : Dong *et al.* (2017)

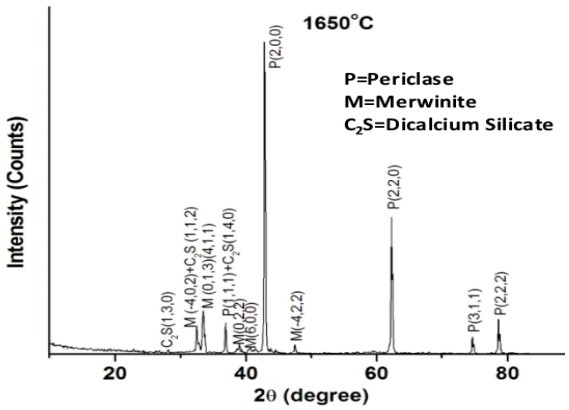

Synthesized MgO from Indian magnesite
Source: Haldar *et al.* (2014)

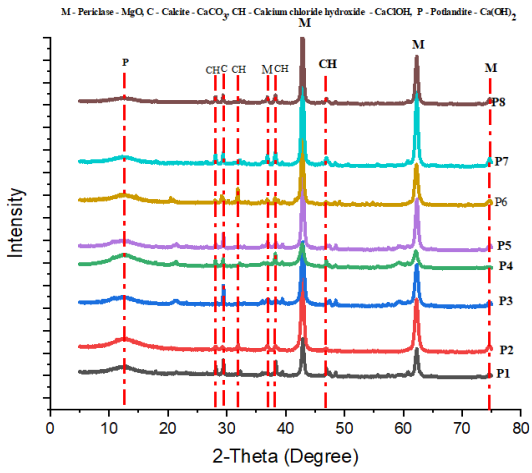

Source: Current Study

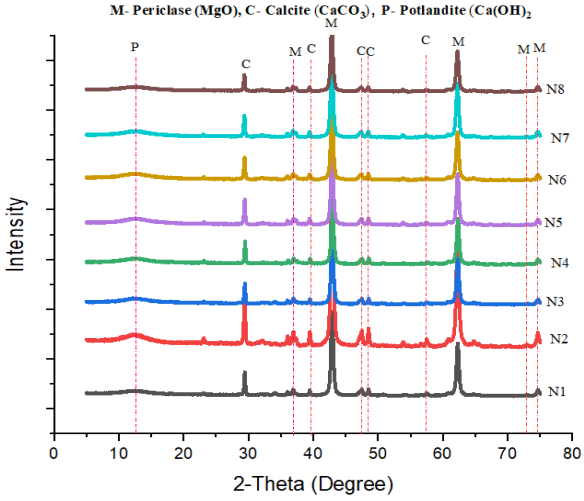

Source: Current Study

Figure 4.55: Comparison between the XRD of Synthesized MgO from Dolomite and other Sources

Table 4.32: XRF Results of Synthesized MgO and Naturally Occurring Sources

Sample (5)	Fe_2O_3 (%)	MnO (%)	Cr_2O_3 (%)	V_2O_5 (%)	TiO_2 (%)	CaO (%)	K_2O (%)	P_2O_5 (%)	SiO_2 (%)	Al_2O_3 (%)	MgO (%)	Na_2O (%)	LOI (%)	Author
N7	0.35	0.02	0.01	<0.01	0.06	14.64	0.02	0.48	1.05	0.49	**72.72**	0.06	10.06	A
P7	0.25	0.01	0.00	0.00	0.06	10.99	0.01	0.35	0.73	0.21	**56.80**	<0.01	25.58	A
Dolomite	0.10	0.00	0.00	0.00	0.02	30.62	0.07	0.05	1.87	0.44	**18.84**	0.00	45.91	A
Pakistan Magnesite	45.4	-	-	-	-	1.18	-	-	0.52	-	**45.4**	-	52.1	B
Indian Magnesite	0.24	-	-	-	0.02	1.41	-	-	2.44	0.17	**45.68**	0.08	49.52	C

A: Current Study, B: Raza *et al.* (2013). C: Haldar *et al.* (2014)

It is a fact that, after iron and aluminum, the third most frequently used structural metal is magnesium. Due to the rapid population growth, magnesium and its compounds have been experiencing unusually high demand. Automobiles, medicinal products, fertilizer, paper, refractory materials, and desulphurizing agents during iron and steel production are all applications for magnesium and its compounds (Raza *et al.*, 2013; Haldar *et al.*, 2014). To meet the demand for magnesium and its compounds, viable sources such as magnesite and dolomite ores must be explored. However, Nigeria doesn't have a viable source deposit of magnesite ore and so is faced with the only available option, which is dolomite. This study has been able to demonstrate that dolomite is a good source of production of magnesium compounds. From Table 4.43, the synthesized MgO from NAR (72.72 %) and HPASR (56.8 %) in this study is far higher than those found in naturally occurring sources such as dolomite (18.84 %) and magnesite (45 % on average). This clearly shows that Nigeria could be among the leading nations in MgO production if harnessed.

4.12 Stage-Wise Reaction Mechanisms Involved in MgO Production from Dolomite

The various reaction mechanisms involved in MgO synthesis from dolomite using HNO_3 as the leachant :

4.12.1 Reaction mechanism of MgO synthesis from NAR

4.12.1.1 Reaction mechanism of dissolution of dolomite ore in HNO_3

$$CaMg(CO_3)_2 + 4HNO_3 \rightarrow Mg(NO_3)_2 + Ca(NO_3)_2 + 2H_2O + 2CO_2 \quad (4.10)$$

$$CaMg(CO_3)_2 \rightarrow CaCO_3 + MgCO_3 \quad (4.11)$$

$$CaCO_3 \rightarrow Ca^{2+} + CO_3^{2-} \quad (4.12)$$

$$MgCO_3 \rightarrow Mg^{2+} + CO_3^{2-} \quad (4.13)$$

$$4HNO_3 \rightarrow 4NO_3^- + 4H^+ \quad (4.14)$$

$$2NO_3^- + Ca^{2+} \rightarrow Ca(NO_3)_2 \quad (4.15)$$

$$Mg^{2+} + 2NO_3^- \rightarrow Mg(NO_3)_2 \quad (4.16)$$

$$4H^+ + 2CO_3^{2-} \rightarrow 2H_2O + 2CO_2 \quad (4.17)$$

4.12.1.2 Reaction mechanism of precipitation of magnesium hydroxide oxide via NAR

$$Mg(NO_3)_2 + Ca(OH)_2 \rightarrow Mg(OH)_2 + Ca(NO_3)_2 \quad (4.37)$$

$$Mg(NO_3)_2 \rightarrow Mg^{2+} + 2NO_3^- \quad (4.38)$$

$$Ca(OH)_2 \rightarrow Ca^{2+} + 2OH^- \quad (4.39)$$

$$Mg^{2+} + 2OH^- \rightarrow Mg(OH)_2 \quad (4.40)$$

$$Ca^{2+} + 2NO_3^- \rightarrow Ca(NO_3)_2 \quad (4.41)$$

4.12.1.3 Reaction mechanism of the decomposition of $Mg(OH)_2$ to MgO

$$Mg(OH)_2 \rightarrow MgO + H_2O \quad (4.56)$$

$$Mg(OH)_2 \rightarrow Mg^{2+} + 2OH^- \quad (4.57)$$

$$OH^- + OH^- \rightarrow H_2O + O^{2-} \quad (4.58)$$

$$Mg^{2+} + O^{2-} \rightarrow MgO \quad (4.59)$$

4.12.2 Reaction mechanism of MgO synthesis from HPASR

4.12.2.1 Mechanism of dissolution of dolomite ore in HCl-$HClO_4$

$$CaCO_3.MgCO_{3(S)} + 4HClO_4 \rightarrow Ca(ClO_4)_2 + Mg(ClO_4)_2 + 2CO_2 + 2H_2O \quad (4.22)$$

$$CaCO_3.MgCO_{3(S)} + 4HCl \rightarrow CaCl_2 + MgCl_2 + 2H_2O + 2CO_2 \quad (4.23)$$

$$4HClO_4 \rightarrow 2H^+ + 2ClO_4^- \quad (4.24)$$

$$CaCO_3 \rightarrow Ca^{2+} + CO_3^{2-} \quad (4.25)$$

$$Ca^{2+} + 2ClO_4^- \rightarrow Ca(ClO_4)_2 \quad (4.26)$$

$$2H^+ + CO_3^{2-} \rightarrow CO_2 + H_2O \quad (4.27)$$

$$2HClO_4 \rightarrow 2H^+ + 2ClO_4^- \quad (4.28)$$

$$MgCO_3 \rightarrow Mg^{2+} + CO_3^{2-} \quad (4.29)$$

$$Mg^{2+} + 2ClO_4^- \rightarrow Mg(ClO_4)_2 \quad (4.30)$$

$$2H^+ + CO_3^{2-} \rightarrow CO_2 + H_2O \quad (4.31)$$

$$HCl \rightarrow H^+ + Cl^+ \quad (4.32)$$

$$Ca^{2+} + 2Cl^- \rightarrow CaCl_2 \quad (4.33)$$

$$Mg^{2+} + 2Cl^- \rightarrow MgCl_2 \quad (4.34)$$

4.12.2.2 Reaction mechanism of precipitation of magnesium hydroxide oxide via HPAR

$$MgCl_2 + Ca(OH)_2 \rightarrow Mg(OH)_2 + CaCl_2 \quad (4.44)$$

$$MgCl_2 \rightarrow Mg^{2+} + 2Cl^- \quad (4.45)$$

$$Ca(OH)_2 \rightarrow Ca^{2+} + 2OH^- \quad (4.46)$$

$$Mg^{2+} + 2OH^- \rightarrow Mg(OH)_2 \quad (4.47)$$

$$Ca^{2+} + 2Cl^- \rightarrow CaCl_2 \quad (4.48)$$

$$Mg(ClO_4)_2 + Ca(OH)_2 \rightarrow Mg(OH)_2 + Ca(ClO_4)_2 \quad (4.49)$$

$$Mg(ClO_4)_2 \rightarrow Mg^{2+} + 2ClO_4^- \quad (4.50)$$

$$Ca(OH)_2 \rightarrow Ca^{2+} + 2OH^+ \quad (4.51)$$

$$Mg^{2+} + 2OH^+ \rightarrow Mg(OH)_2 \quad (4.52)$$

$$Ca^{2+} + 2ClO_4^- \rightarrow Ca(ClO_4)_2 \quad (4.53)$$

4.12.2.3 Reaction mechanism of the decomposition of Mg(OH) to MgO

$$Mg(OH)_2 \rightarrow MgO + H_2O \quad (4.56)$$

$$Mg(OH)_2 \rightarrow Mg^{2+} + 2OH^- \quad (4.57)$$

$$OH^- + OH^- \rightarrow H_2O + O^{2-} \quad (4.58)$$

$$Mg^{2+} + O^{2-} \rightarrow MgO \quad (4.59)$$

CHAPTER FIVE

5.0 CONCLUSIONS, RECOMMENDATIONS, SUGGESTION FOR FURTHER STUDIES AND CONTRIBUTION TO KNOWLEDGE

5.1 Conclusions

The EDS analysis shows that Ikpeshi dolostone ore comprises of magnesium (13.93 %), calcium (20.090 %), and oxygen (65.990 %). The XRF result with 30 % CaO and 18.84 % MgO confirms that the collected sample from Ikpeshi in this study is dolomite. The XRD result further confirmed the collected sample to be dolomite with dolomite mineral phase, calcite, magnesite, and quartz.

The leaching was examined to ascertain the influence of key factors on the leaching efficiency of dolomite in HNO_3. The Box-Behnken design method was used as the outcome of surface methodology with 17 runs of experiments. The second-order quadratic model $[(Y\%) = -111.73625 + 3.64875A + 61.64250B + 2.07825C - 0.14125AB - 0.014875AC - 0.053750BC - 0.022650A^2 - 11.88500B^2 - 0.013275C^2 \quad (4.3)]$ with R^2 of 0.9770 is most appropriate for the prediction of the leaching efficiency. The results of ANOVA show that leaching temperature and nitric acid concentration are the most significant process parameters, while leaching time was less significant in the leaching efficiency. The optimum leaching efficiency was predicted to be 99.16 %, but 98.6 % was validated at the optimum process parameters of leaching temperature at 55.3 ^oC, HNO_3 concentration at 2.22 $moldm^{-3}$, and leaching time at 20 minutes with the desirability of 1. The x-ray diffraction pattern of the residue at optimum compared with that of dolomite ore shows all the dolomite mineral phases are absent in the residue. This implies that almost all the dolomite went into solution during the dissolution process, and this agrees with the 99.16 % optimum dissolution efficiency recorded in the dissolution study.

Similarly, the effect of process conditions such as temperature, dissolution time, and acid concentration on the dissolution of dolomite in a mixture of HCl and $HClO_4$ was studied. A Second-order polynomial model equation was generated, which helped to predict the response of the dissolution of dolomite in a mixture of HCl and $HClO_4$. The ANOVA indicates that the model equation is substantial with a Prob > F of < 0.0001. Temperature, dissolution time, acid concentration, the interactive influence of temperature and acid concentration; interactive effect of time and temperature all have a major influence on the dissolution, while the interactive effect of acid concentration and temperature has no significant effects on the dissolution. At 57 ^oC, 20 minutes of reaction time, and an acid concentration of 2.03 $moldm^{-3}$, a 99.7 % dissolution efficiency optimum point of dolomite in a mixture of HCl and $HClO_4$ was predicted. However, 98.3 % was validated with desirability of 1. The x-ray diffraction pattern of the residue at optimum compared with that of dolomite ore shows all the dolomite mineral phases are absent in the residue. This implies that all the dolomite went into the solution during the dissolution process, and this agrees with the 99.7 % optimum dissolution efficiency recorded in the dissolution study.

The kinetics study also confirms that reaction temperature and nitric acid concentration have a positive contribution to the leaching efficiency. A higher leaching efficiency of 99.5 % was achieved at a temperature of 55.0 ^oC, 2.50 $moldm^{-3}$ of acid, and a mixing speed of 200.0 rpm within a leaching period of one hour. The reaction rate was first order to hydrogen ion concentration [H^+], with 26.6 $KJmol^{-1}$ of activation energy. The leaching of dolomite in HNO_3 is an exothermic reaction and the rate follows a PLDC.

The concentration of HCl-$HClO_4$ and the dissolution temperature have a positive influence on the leaching of dolomite in the acid mixture. In the study of the effect of temperature, an optimum fraction of 0.995 was attained at 2.20 $moldm^{-3}$ of HCl-$HClO_4$, a reaction

temperature of 60 ^{o}C, and a time of 40 minutes. In terms of concentration influence, an optimum dissolution fraction of 0.993 was obtained at a reaction temperature of 57 ^{o}C, a 2 moldm^{-3} acid, and a reaction time of 60 Mins. The reaction order is first order considering hydrogen ion concentration $[H]^{+}$ while the minimum energy requirement is 16.680 kJmol^{-1}. The dissolution of dolomite in HCl-$HClO_4$ is a surface chemical reaction control mechanism. In addition, the precipitation process was optimized to determine the influence of process constraints on the precipitation of $Mg(OH)_2$ from a saturated nitric acid solution. The central composite experimental design (CCD) was used. A linear model [$Magnesium\ ion\ PPT(\%) = +48.47852 + 0.980765A + 1.71455B \quad 4.42)$] with a regression coefficient (R^2) of 0.5180 is most suitable for the prediction of the precipitation outcome. The results of ANOVA show the model is substantial with a prob> 0.026, concentration of calcium hydroxide and time are also significant process parameters. The optimum was predicted to be 98.5 % $Mg(OH)_2$ precipitation, which was confirmed after validation at the optimum conditions of 34 % concentration of calcium hydroxide and time of 8 minutes with desirability of 0.93. Similarly, the effect of process constraints such as concentration of calcium hydroxide and time on precipitation from a saturated solution of HCl/$HClO_4$ was conducted using the central composite design method. The R^2 value of 0.4099 for the second-order polynomial model equation best fits the prediction of $Mg(OH)_2$ from the $HClO_4$/HCl saturated solution. The ANOVA confirmations that the equation is significant with a P-Value of 0.0012. The concentration of calcium hydroxide has a significant effect, while the effect of time has no significant effect. At an optimum condition of 35.3 % calcium hydroxide and a time of 5 minutes, the optimum point prediction of 97.63 % magnesium ion precipitation from the saturated solution of HCl/$HClO_4$ was obtained, with 97.1 % magnesium ion precipitation confirmed after validation. The saturated solution of nitric seems to give a higher yield of

magnesium hydroxide precipitate with that of $HCl/HClO_4$ saturated solution at a lower concentration of calcium hydroxide.

To ascertain the impact of process parameters on the calcination process, the precipitated $Mg(OH)_2$ from the nitric acid-saturated solution was calcined. A pentagonal design with eight runs was used. The calcination yield forecast is the best fit by the quadratic model [Calcination yield (%) $= +43.3806 + 0.53756A + 0.02789B - 0.00051AB - 0.00382A^2 - 7.65723E-06B^2$ (4.60)], which has a regression coefficient of 0.95360. With a p-value of 0.00328, the analysis of variance demonstrates the model's significance. The outcome demonstrates that temperature had a substantial impact, although time did not appear to have a major impact. At the ideal temperature and duration of 10 minutes, 60.590 % of the calcination yield was anticipated, while 60.510 % was confirmed at the ideal temperature and time of 700.0 ^oC with a desirability of 1.0. The precipitation from the $HCl/HClO_4$ saturated solution was also subjected to calcination, and the process was also optimized to affirm the effect of process parameters using a pentagonal experimental design with 8 experimental runs. The calcination yield prediction was most closely matched by the quadratic model, which had an R^2 regression coefficient of 0.996. ANOVA's conclusion demonstrates the model's significance with a P-value of 0.00310. The result also confirms that the effects of time and temperature are significant. The best prediction via numerical optimization methods shows a calcination yield of 68.5 % while 68.1 % was confirmed after validation at best conditions of 582.50 ^oC and precipitation time of 13 minutes. The $HCl/HClO_4$ route yielded a higher yield than the nitric acid route at a lower temperature of 582.5 ^oC.

The mineral phase of the synthesized MgO in this study from HPASR was confirmed by XRD analysis with the most prominent peaks of periclase, while other minor peaks indicate

the presence of calcite, calcium chloride hydroxide, and portlandite. The synthesized MgO from NAR was also confirmed by XRD analysis, which identified it as a periclase phase. Only calcite and portlandite were identified as minor phases. From the XRD results, synthesized MgO from NAR gave the best results, with the minimum minor peaks as impurities.

Further examination of the final product obtained in the investigation was conducted using XRF analysis to determine the chemical compositions as well as the exact amounts of each of the compounds present in the product. The XRF results confirmed the presence of MgO in all the samples from both NAR and HPASR. The exact amounts of other associated metal oxides present were also determined. Sample N7 from NAR has the highest MgO (72.72 %) followed by CaO (14.64 %). Other metal oxides present in the sample are Fe_2O_3 (0.35 %), Cr_2O_3 (0.01 %), V_2O_5 (0.01 %), MnO (0.020 %), TiO_2 (0.060 %), K_2O (0.02 %), P_2O_5 (0.48 %), SiO_2 (1.05 %), Al_2O_3 (0.49 %) and Na_2O (0.06 %). From HPASR, sample P7 has the highest MgO (56.8 %) followed by CaO (10.99 %), while other metal oxides present are Fe_2O_3 (0.25 %), MnO (0.010 %), TiO_2 (0.060 %), K_2O (0.010 %), P_2O_5 (0.35 %), SiO_2 (0.73 %), Al_2O_3 (0.21 %) and Na_2O (<0.01 %). From the XRF results, sample N7 gave the best output in terms of MgO, therefore NAR is preferred for MgO production.

5.2 Recommendations

1. Following the conclusion of this study, which found that Nigerian dolomite is suitable for MgO production, the federal government should explore the huge dolomite deposits for MgO production to increase its gross domestic product.
2. The economic viability of the production process of MgO should be further examined

3. To encourage local content development, highly pure CaO as a precipitant should be synthesized from the abundant calcite deposits in the country rather than importing it. This will further enhance the higher purity of MgO produced.
4. to encourage local production of MgO, the ministry of mines and steel development should sensitize investors on the local production of MgO. Legislators should also enact appropriate legislation to encourage investors in MgO production and gradually reduce the country's reliance on importation.

5.3 Suggestion for Further Studies

1. Further study should consider the variation of pH on the production process of MgO
2. Full factorial design should also be explored for the optimization of the production process.

5.4 Contribution to Knowledge

The study investigated the optimisation of the process parameters for production of magnesium oxide from Ikpeshi dolomite ore in Edo State, Nigeria. The sample collected from the ore deposit in Ikpeshi is dolomite with the major oxide composition being 30 % calcium oxide and 18.84 % magnesium oxide. The result revealed that the second-order quadratic model is suitable for predicting the outcome of leaching of dolomite in nitric acid with optimum leaching efficiency of 99.16 % at temperature of 55.3 ^{o}C, HNO_3 concentration of 2.22 moldm^{-3}, and time of 20 minutes. This implies that a negligible amount of the dolomite will be left undissolved during the industrial processing of dolomite from the study area. Based on the kinetic study, the dissolution of dolomite in nitric acid is 0.77, being a first order, suggestin that large quantities of dolomite ore was processed within 20 minutes at minimum energy consumption of 26.6 KJmol^{-1} activation energy. Optimum precipitation

yield of 98.5 % $Mg(OH)_2$ was achieved at 8 minutes and 34 % calcium hydroxide as precipitant. Linear model with P-value of 0.026 is suitable for predicting the precipitation yield. The quadratic model with P-value of 0.0328 is significant for predicting the calcination of magnesium oxide (MgO) from magnesium hydroxide at optimum conditions of 10 minutes and temperature of 700 ^oC. The production of 72.72 % MgO in this study implies that Nigerian dolomite is a potential raw material for the production of MgO.

REFERENCES

Abali Y., Bayca Salih U., Arisoy Kadir, Vaizogullar Ali I. (2011). Optimization of Dolomite Ore Leaching In Hydrochloric Acid Solutions. *Physicochemical Problems in Mineral. Processing.* 46: 253-262.

Abdel-Aal, E.A. (1995). Possibility of utilizing dolomite ores for production of magnesium oxide by acid leaching. *Fizykochemiczne Problemy Mineralurgii*, 55-56

Abdulkareem, A. S., Uthman, H., Afolabi, A. S., & Awenebe, O. L. (2011). Extraction and optimization of oil from *Moringa oleifera* seed as an alternative feedstock for the production of biodiesel. *Dr. Nayeripour, M. Author, Sustainable Growth and Applications in Renewable Energy Sources*, *1*, 243-268.

Adalbert Lossin "Copper" in Ullmann's Encyclopedia of Industrial Chemistry (2005) Wiley-VCH, Weinheim.

Ahrends, R., Pieper, S., Kuhn, A., Weisshoff, H., Hamester, M., Lindemann, T., & Linscheid, M.W. (2007). A metal-coded affinity tag approach to quantitative proteomics. *Molecular & Cellular Proteomics*, *6*(11), 1907-1916.

Ajemba, R. O. and Onukwuli O. D. (2012). Dissolution kinetics and mechanisms of reaction of Udi clay in nitric acid solution. *American Journal of Scientific and Industrial Research*. 3(3), 115-121.

Akande, J. M., & Agbalajobi, S. A. (2013). Analysis on some physical and chemical properties of Oreke dolomite deposit. *Journal of Minerals and Materials Characterisation and Engineering*. 1, 33-38.

Akanji, L. T., Nasr, G. G., & Bageri, M. (2013). Core-scale characterization of flow in tight Arabian formations. *Journal of Petroleum Exploration and Production Technology*, 3, 233- 241.

Alexander W., (2008). *Electro-deposition a practical Treatise Books. Pp395. ISBN 1-4437-66836*

Al-Zahrani, A. A., & Abdel-Majeed, M. H. (2015). Production of magnesia from local dolomite ores and rejected brines from local desalination plants. In *Saudi Engineering Conference*.

Amlan B. (2016). Estimation of dolomite formation: Dolomite precipitation and dolomitization. *Journal of the Geological Society of India*, *87*(5), 561-572.

Anakoli, K. (2020). Quantification of Uranium and Thorium at Cheptais Anomaly Using Energy Dispersive X-Ray Fluorescence Method for Mineral Content and Evaluation of Associated Radio-ecological Hazards (Doctoral dissertation, University of Nairobi).

Aral, H., Hill, B. D. & Sparrow, G. J., (2004) *CSIR Minerals Report* DMR-2378C. 1-79.

Are, C. T., Suleiman, M. A. T., Yisa, J., Auta, M ., & Joseph, I. A. (2021). Kinetic Study of Reaction between Dolomite Ore and Trioxonitrate (V) Acid (HNO_3). *GeoScience Engineering*, *67*(1), 21-29.

Akarsu, H., & Yildirim, M. (2007). Leaching rates of Icel-Yavca dolomite in hydrochloric acid solution. *Mineral Processing and Extractive Metallurgy Review*, *29*(1), 42-56.

Amrulloh, H., Simanjuntak, W., Situmeang, R. T. M., Sagala, S. L., Bramawanto, R., Fatiqin, A., & Zuniati, M. (2020). Preparation of nano-magnesium oxide from Indonesia local seawater bittern using the electrochemical method. *Inorganic and Nano-Metal Chemistry*, *50*(8), 693-698.

Atomic Absorption spectroscopy (AAS) (2015). *Absorption Spectroscopy*. Wikipedia, the free encyclopedia. Retrieved from http://en.wikipedia.org/wiki/atomic

Baba, A. A., Omipidan, A. O., Adekola, F. A., Job, O., Alabi, A. G., Baral, A., & Samal, R. (2014). Optimization study of a Nigerian dolomite ore dissolution by hydrochloric acid. *Journal of Chemical Technology and Metallurgy*, *49*(3), 280-287.

Babatunde, E. O. (2021). Synthesis and Characterisation of Functionalized Silica Supported Catalyst for the Production of Fatty Acid Methyl Esters from Used Cooking Oil. Unpublished Ph.D. Thesis. Department of Chemical Engineering, Federal University of Technology, Minna, Nigeria.

Balasubramanian A. (2017). Size Reduction by Grinding Methods. Technical Report · March 2017 DOI: 10.13140/RG.2.2.21484.56961

Beruto, D. T., Vecchiattini, R., & Giordani, M. (2003). Solid products and rate-limiting step in the thermal half decomposition of natural dolomite in a CO_2 (g) atmosphere. *Thermochimica Acta*, *405*(2), 183-194.

Binnemans K. & Jones P. T. (2017). Solvometallurgy: An Emerging Branch of Extractive Metallurgy. *Journal of Sustainable Metallurgy*. 3, 570–600.

Bindell, C. R., Wilson, L., Evans, C. A., Wilson, S., & Wilson, G. (1992). *Encyclopedia of materials characterisation: surfaces, interfaces, thin films*. Gulf Professional Publishing.

Boundless."Extractive Metallurgy"."Boundless Chemistry. Boundless, 21 July. 2015. Retrieved 18 Mar. 2016 from https://www.boundless.com/chemistry/textbookks/boundless -chemistry-textbook/metals-20/metallurgic-process-142/extractive-metallurgy-559-3578/.

Brady, G. S., Clauser, H. H., & Vaccari, J. A. (2002). *Materials handbook: an encyclopedia for managers, technical professionals, purchasing and production managers, technicians, and supervisors*. McGraw-Hill Education.

Brent H. (2000). Metallurgy, Survey. *Kirk-Othmer Encyclopedia of Chemical Technology*. Wiley- VCH, Weinheim.

Buckman, J., Donnelly, T., Jiang, Z., Lewis, H., & Ruffell, A. (2020). Methane derived authigenic carbonate (MDAC) aragonite cemented quaternary hardground from a methane cold seep, Rathlin Basin, Northern Ireland: δ13C and δ18O isotopes, environment, porosity and permeability. Geosciences, 10(7), 255

Busenberg, E., & Plummer, L. N. (1989). Thermodynamics of magnesian calcite solid-solutions at 25^{o} C and 1 atm total pressure. *Geochimica et Cosmochimica Acta*, *53*(6), 1189-1208.

Buttrick, D. B., Trollip, N. Y., Watermeyer, R. B., Pieterse, N. D., & Gerber, A. A. (2011). A performance based approach to dolomite risk management. *Environmental Earth Sciences*, 64(4), 1127-1138.

Chang L.LY., Howie, R.A & Zussman, J. (1998). Rock-forming minerals,(Non-silicates). The Geological Society Publishing House, 5B, 2nd edition

Chakrabarti, G., Shome, D., Kumar, S., Armstrong-Altrin, J. S., & Sial, A. N. (2011). Carbon and oxygen isotopic variations in stromatolitic dolomites of Palaeoproterozoic Vempalle Formation, Cuddapah Basin, India. *Carbonates and Evaporites*, *26*(2), 181-191.

Chen, G., & Tao, D. (2004). Effect of solution chemistry on flotability of magnesite and dolomite. *International Journal of Mineral Processing*, *74*(1-4), 343-357.

Cho, K. M., Naing, K., & Khat, K. C. (2016). *Production of Magnesium Hydroxide and Magnesium Oxide Nanoparticles from Bittern and their Industrial Applications* (Doctoral dissertation, MERAL Portal).

Danda S.R., Sumil K.T. and Shivakumar A., (2013). World of mining 5: 318-322

De Viguerie, L., Sole, V. A., & Walter, P. (2009). Multilayers quantitative X-ray fluorescence analysis applied to easel paintings. *Analytical and bioanalytical chemistry*, *395*(7), 2015-2020.

Department of Geology Minnesota Mineral (DGMM) (2018). Dolomite Carboinate Mineral. https://www.esci.umn.edu/courses/1001/minerals/dolomite.shtml

Deer W.A., Howie R.A, Zussman J. (1992). An Introduction to the rock-forming minerals 2nd ed. Longman, London, 641-648

Ding Y., Zhang G., Wu H., Hai B., Liangbin W., Quain Y., (2001). Nanoscale magnesium hydroxide and magnesium oxide powders: control over shape and structure via hydrothermal synthesis. Chemistry Materials. 13, 435-440.

Dong, H., Unluer, C., Yang, E. H., & Al-Tabbaa, A. (2017). Synthesis of reactive MgO from reject brine via the addition of NH4OH. *Hydrometallurgy*, *169*, 165-172.

Drake J. (2021). Magnesium Oxide Structure. https://jdfnet.com/destiny-shadowkeep-ahmam/magnesium-oxide-structure-72867f

Duhaime, P., Mercille, P., & Pineau, M. (2002). Electrolytic process technologies for the production of primary magnesium. *Mineral Processing and Extractive Metallurgy*, *111*(2), 53-55.

Erik P., Anderson, C., Nurjaman, F., Al Muttaqii, M., Handoko, A. S., Bahfie, F., & Mufakhir, F. R. (2020). Monosodium glutamate as selective lixiviant for alkaline leaching of zinc and copper from electric arc furnace dust. *Metals*, *10*(5), 644.

Faraji, F., Alizadeh, A., Rashchi, F., & Mostoufi, N. (2020). Kinetics of leaching: a review. *Reviews in Chemical Engineering*. DOI: https://doi.org/10.1515/revce 2019-0073

Fahad, M., Iqbal, Y., & Ubic, R. (2011). Characteristics of dolomite from swabi, khyberpakhtunkhwa for its use as a raw material in fertilizer production. In *JPMS Conference Issue Materials*.

Fraga M (2020). Magnesium oxide: a forgotten specialty chemical, buck Leat tech. Accessed on 3rd of June, 2020 from https://www.buckman.com/resources/ magnesium-oxide-a-forgotten-specialty-chemical/.

Galai, H., Pijolat, M., Nahdi, K., & Trabelsi-Ayadi, M. (2007). Mechanism of growth of MgO and CaCO3 during a dolomite partial decomposition. *Solid State Ionics*, *178*(15-18), 1039-1047.

Graf, D. L., & Goldsmith, J. R. (1956). Some hydrothermal syntheses of dolomite and protodolomite. *The Journal of Geology*, *64*(2), 173-186.

Gautelier, M., Oelkers, E. H., & Schott, J. (1999). An experimental study of dolomite dissolution rates as a function of pH from− 0.5 to 5 and temperature from 25 to 80 C. *Chemical Geology*, *157*(1-2), 13-26.

Gerald, O., Christopher, N., Ayebatonworio, O., & Martin, O. (2013). Comparative Kinetics of Iron Ore Dissolution in Aqueous HCl-HNO_3 System. *Journal of Minerals and Materials Characterization and Engineering*, 1(4), 153-159. doi: 10.4236/jmmce.2013.14026.

Gonidanga, B. S., Njoya, D., Lecomte-Nana, G., & Njopwouo, D. (2019). Phase Transformation, Technological Properties and Microstructure of Fired Products Based on Clay-Dolomite Mixtures. Journal of Materials Science and Chemical Engineering, 7(11), 1-14.

Geochemical Instrumentation and Analysis (2022). Instrumentation and Analysis. Accessed on 23rd, May, 2022. https://serc.carleton.edu/research_education/geochemsheets/techniques/XRF.html

Green, D.W., Perry, R.H., (2008) Perry's chemical engineers' handbook, 8th edition, McGraw-Hill companies. 18.59-18.6

Gregg, J. M., Bish, D. L., Kaczmarek, S. E., & Machel, H. G. (2015). Mineralogy, nucleation and growth of dolomite in the laboratory and sedimentary environment: a review. *Sedimentology*, *62*(6), 1749- 1769.

Griffiths, P.; de Hasseth, J.A. (2007). Fourier Transform Infrared Spectroscopy (2nded.). Wiley- Blackwell.ISBN 0-471-19404-2.

Haldar, M. K., Ghosh, C., & Ghosh, A. (2014). Studies on synthesis and characterisation of magnesia based refractory aggregates developed from Indian magnesite. *Journal of Materials Science and Chemical Engineering*, *2*(10), 1-8.

Hamilton minerals and Metals Ltd (2013). web page <metals.com/minerals/dolomite.html>as on January, 2013

Hanna, A.A, Abdelmoaty, A.S and Sherief M.A (2019). Synthesis, Characterisation, Thermal Behavior of Nanoparticles of $Mg(OH)_2$ to be Used as Flame Retardants *Journal chemistry*

Haynes, W., (2011). Handbook of Chemistry and Physics. CRC. Pp 474 ISBN 1439855110

Herman, J. S., & White, W. B. (1985). Dissolution kinetics of dolomite: effects of lithology and fluid flow velocity. *Geochimica et Cosmochimica Acta*, *49*(10), 2017-2026.

Hips, K., & Árgyelán, G. B. (2007). Controls on Diagenesis of the Triassic Kurrachine Dolomite, Syria. *GeoArabia*, 12(2), 41-64.

Hobart M, K. (2020). A sedimentary Rock Similar to Limestone. Also Known as 'Dolomite' and Dolomite Rock. Retrieved on February10th, 2020 from https://geology.com/rocks/dolomite.shtml

Hussain, A., Hasan, A., Javid, A., & Qazi, J. I. (2016). Exploited application of sulfate-reducing bacteria for concomitant treatment of metallic and non-metallic wastes: a mini-review. *Biotechnology*, *6*(2), 1-10.

Hosten, C., & Cırak, M. (2013). Flocculation behavior of clayey dolomites in borax solutions. *Powder technology*, *235*, 263-270.

Hycnar, E., Ratajczak, T., & Sęk, M. (2020). Dolomites as SO_2 Sorbents in Fluid Combustion Technology. Resources, 9(10), 121.

Imani, M. M., & Safaei, M. (2019). Optimized synthesis of magnesium oxide nanoparticles as bactericidal agents. *Journal of Nanotechnology*, .

Jakic, J., Labor, M., & Martinac, V. (2016). Characterisation of Dolomitic Lime as the Base Reagent for Precipitation of $Mg(OH)_2$ from Seawater. *Chemical and Biochemical Engineering Quarterly*, *30*(3), 373-379.

Joseph, I.A., Eterigho, E.J., Okafor, J.O. and Are, C.T., (2022). Alternative approach of gold extraction using modified borax. Iranian Journal of Chemistry and Chemical Engineering, 41(7), 2288-2299.

Kaczmarek, S. E., Gregg, J. M., Bish, D. L., Machel, H. G., Fouke, B. W., MacNeil, A., & Wood, R. (2017). Dolomite, very-high magnesium calcite, and microbes: implications for the microbial model of dolomitization. In Characterisation and Modeling of Carbonates–Mountjoy Symposium (1) 7-20).

Kaufmann J., (2013) sinkholes at the wayback machine USGS fact Sheet. Retrieved on 2013

Khan Academy. Activation energy, transition state, and reaction rate. [Online]. 2018 [Accessed 2020-01-02] www.khanacademy.org/science/biology/energy-and-enzymes/introduction-to-enzymes/a/activation-energy?modal=1

Kirk-Othmer. (2005). *Encyclopedia of Chemical Technology*, 5th Edition. **(**15**),** 398-414.

Kozhevnikov, E. K., Kropanev, S. I., & Baranovskii, N. I. (1973). Beneficiation of dolomites. *Refractories*, 14(3-4), 152-153.

Leaching and adsorption resource book, (2012), [online],Available: http://rsteyn.files.wordpress.com/2010/07/leaching-adsorption-basics-and-example.pdf, [2012, May 5].

Lhoist North America, Inc (2018). Safety Data Sheet (Dolomite. Retrieved on 24/03/2021 from https://www.lhoist.com/sites/lhoist/files/lna_sds_dolomite_2018.pdf

Li, G., Li, Z., & Ma, H. (2013). Synthesis of aragonite by carbonization from dolomite without any additives. *International Journal of Mineral Processing*, *123*, 25-31.

Lingling, X., & Deng M. (2005). Dolomite used as raw material to produce MgO-based expansive agent. *Cement and Concrete research*, *35*(8), 1480-1485.

Lund, K., Fogler, H. S., & McCune, C. C. (1973). Acidization: The dissolution of dolomite in hydrochloric acid. *Chemical Engineering Science*, *28*(3), 691 -700.

Lottering, C. (2016). Leaching of secondary zinc oxides using sulphuric acid. Doctoral dissertation, Metallurgical Engineering Department, Stellenbosch University.

Mahmut, A., Mehmet, Y., and Turan, Y. (2016). Leaching of Mersin/Ayincik Dolomite Ore in Hydrochloric Acid. Dissolution Rate. *Physicochemical Problem Mineral Processing*. 52(2), 536-550.

Manivannan S. (2016). Metallurgical sludges, bio/leaching and heavy metals recovery (Zn, Cu). Doctoral dissertation, Environmental Engineering, Université Paris-Est.

Martinac, V., Labor, M. and Petric, N. (2004). Boric Oxide in Seawater Derived Managesia. *Indian Journal of Marine Sciences*. 33(3) 226-230.

McCarthl, G.J. and Walsh, (2012) Alan-Biographical entry. Encyclopedia of Austalian Science. Retrieved 22 May, 2012.

Mertens, J., Lepaumier, H., Rogiers, P., Desagher, D., Goossens, L., Duterque, A. & Webber, M. (2020). Fine and ultrafine particle number and size measurements from industrial

combustion processes: Primary emissions field data. *Atmospheric Pollution Research, 11*(4), 803-814.

MSMD (Ministry of Solid Minerals Development) (2003). Inventory of Minerals and Mines in Nigeria.

Mohammed, M. A. A., Salmiaton, A., Wan Azlina, W. A. K. G., Amran, M., & Taufiq-Yap, Y. H. (2013). Preparation and characterisation of Malaysian dolomites as a tar cracking catalyst in biomass gasification process. *Journal of Energy, 2013*.

Moorkah, H. I., & Abolarin, M. S. (2005). Investigation of the properties of locally available dolomite for refractory applications. *Nigerian Journal of Technology, 24*(1), 79-86.

Nowak, A., Lubas, M., Jasinski, J. J., Szumera, M., Caban, R., Iwaszko, J., & Koza, K. (2022). Effect of Dolomite Addition on the Structure and Properties of Multicomponent Amphibolite Glasses. Materials, 15(14), 4870.

Mubarok, M. Z., & Adi Kurniawan, C. (2015). Synthesis of magnesia powder from East Java dolomite through leaching, precipitation and calcination. In *Advanced Materials Research* (1112, pp. 550-554). Trans Tech Publications Ltd.

Mubashir M., Yaseen, M., Khan, E. U., & Khan, M. J. (2018). Dolomite and dolomitization model- a short review. *International Journal of Hydrology, 2*(5), 549-553.

NORDFEED (2021). Magnesium Oxide Fertilizer, Agriculture, Fused, Dead Burned Magnesia, Technical and Feed Grade. http://www.nordfeed.com/magnesium-oxide-fertilizer-agriculture-fused-dead-burned-grade.html

Ohtaki, H., & Radnai, T. (1993). Structure and dynamics of hydrated ions. Chemical reviews, 93(3), 1157-1204.

Olaiya K. A., Yekinni A. A., Abubakre O. K. and Rabiu T. O. (2015). Experimental Investigation and Suitability of Alagutan Dolomite Deposit as Refractory Raw Materials. *International Journal of Engineering Innovation & Research.* 4(5), 720-725

Olivia, R., Jamarun, N., Arif, S., & Sirin, Y. A. (2017). The utilization of dolomite as catalyst in biodiesel production. *Rasayan Journal of Chemistry*, 10, 160.

Olokesusi, F. (2010). An evaluation of the history, evolution and geography of the solid mineral industry in Nigeria. In NEITI, *An evaluation of the nature and character of the Nigerian extractive industries. solid minerals 2)* 6-66). Abuja, Nigeria.

PerkinElmer (2015). Thermogravimetric Analysis (TGA). www.perkinelmer.com

Pichler, T., & Humphrey, J. D. (2001). Formation of dolomite in recent island-arc sediments due to gas-seawater-sediment interaction. *Journal of Sedimentary Research, 71*(3), 394-399.

Pultar, M., Vidensky, J., & Sedlarova, I. (2019). Study of the reaction between dolomite and nitric acid. *Physicochemical Problems of Mineral Processing*, *55*.

Priya P. (2014). Development of Dolomite Bricks with Positive Plc. Master of Technology Thesis. Department of Ceramic Engineering, National Institute of Technology, Rourkela. (Unpublished).

Rahimi, A., Adabi, M. H., Aghanabati, A., Majidifard, M. R., & Jamali, A. M. (2016). Dolomitization mechanism based on petrography and geochemistry in the Shotori Formation (Middle Triassic), Central Iran. *Open Journal of Geology*, 6(9), 1149-1168.

Rahman, M. U., Gul, S., Odhano, A. A., Hafeez, Tareen, I. R. B. and Yasinzai, M. M (2011). Optimization of Concentration of Medium Ingredients for Production of Citric Acid using Statistical Methods. *Bangladesh Journal of Scientific and Industrial Research.* 46(4), 549-560

Raza, N., & Zafar, Z. I. (2013). An analytical model approach for the dissolution kinetics of magnesite ore using ascorbic acid as leaching agent. *International Journal of Metals*. 2(23), 23-27

Rizwan S. (2018). Process Used to Manufacture Ball Mills by Grinding Plant Manufacturer. Engineering product info. http://engineeringproductsinfo.com/2018/12/04/ball-mills-by-grinding-plant-manufacturer/

Robert W.L., Cambell T.J and Rapp G.E, (1990) Encyclopedia of mineral, Van Nostrand-Reinhold New York, Ny, USA 2nd ed.

Roy, P., & Sardar, A. (2015). SO_2 emission control and finding a way out to produce sulphuric acid from industrial SO_2 emission. *Journal of Chemical Engineering Process Technology*, *6*(2).

Salleh, M. N., Kasim, F. H., Ismail, K. N., Ghazali, C. M. R., Saad, S. A., & Daud, S. (2006, July). Characterization and application of dolomite rock in Perlis. In Proceedings of the 1st International Conference on Natural Resources Engineering & Technology. 465-470.

Sanni, R.O. (2016) Preparation of Some Industrial Copper Compounds from a Nigerian Malachite Mineral. M.Sc Project thesis, Department of Industrial Chemistry, University of Ilorin, Ilorin, Nigeria.

Samtani, M., Dollimore, D., Wilburn, F. W., & Alexander, K. (2001). Isolation and identification of the intermediate and final products in the thermal decomposition of dolomite in an atmosphere of carbon dioxide. *Thermochimica Acta*, *367*, 285-295.

Scholle A. Peter & Dana U. (2013). Cements and cementation. DOI**:** https://doi.org/10.1007/978-1-4020-3609-5_40

Sefiu O. A., Ahmed, H. A., & Ahmed, H. (2020). Methods of ore pretreatment for comminution energy reduction. *Minerals*, *10*(5), 423.

Shamsuddin M. (2016). Electrometallurgy. Physical Chemistry of Metallurgical Processes.

Online ISBN: 9781119078326. Wiley online Library.

Shen, Z., Konishi, H., Brown, P. E., & Xu, H. (2013). STEM investigation of exsolution lamellae and "c" reflections in Ca-rich dolomite from the Platteville Formation, western Wisconsin. American Mineralogist, 98(4), 760-766.

Sitando, O., Senanayake, G., Dai, X., Nikoloski, A. N., & Breuer, P. (2018). A review of factors affecting gold leaching in non-ammoniacal thiosulphate solutions including degradation and in-situ generation of thiosulphate. Hydrometallurgy, 178, 151-175.

Sirajo, M. Z. (2008). Characterisation of Koto-karfe iron ore pellets for pig iron production in Nigeria. Ahmadu Bello University, Zaria, Metallurgical Engineering. Zaria: Unpublished.

Sivrikaya O. (2018). A Study on the Physicochemical and Thermal Characterisation of Dolomite and Limestone Samples for Use in Iron Making and Steelmaking. Institute of Materials, Minerals and Mining. 45(8), 764-772.

Solihin, Indriani, & Mubarok, Z. M. (2018). Dissolution Profile of Dolomite in Chloric Acid Solution: The Effect of Chloric Acid Concentration and Pulp Density. AIP Conference Proceedings https://doi.org/10.1063/1.5038304

Souza, A.D., Pina, P.S, Lima, E.V.O., da Silva, C.A. & Leão, V.A., (2007) Kinetics of sulphuric acid leaching of a zinc silicate calcine, *Hydrometallurgy*. 89, 337-345.

Songtao Y., Weidong T., Mi Z., Tao J., Xiangxin X., & Weijun Z. (2017). Effects of Dolomite on Mineral Compositions and Metallurgical Properties of Chromium-Bearing Vanadium–Titanium Magnetite Sinter. *Minerals*. doi:10.3390/min7110210

Sunil K.T., S. K., Murthy, Y. R., Panda, L., Singh, V., & Bhatnagar, A. (2013). A review on dolomite: genesis, application and processing. *Journal of Mines, Metals and Fuel, 4*, 93-102.

Szilveszter, S., Szabados, M., Kónya, Z., Kukovecz, Á., Pálinkó, I., & Sipos, P. (2020). Differential Precipitation of Mg $(OH)_2$ from $CaSO_4 \cdot 2H_2O$ Using Citrate as Inhibitor: A Promising Concept for Reagent Recovery from $MgSO_4$ Waste Streams. *Molecules*, *25*(21), 5012.

Trend Economy (2022). Nigeria Importation of Natural magnesium carbonate, fused-magnesia and magnesium-oxide. Accessed on 2nd September, 2022 from https://tradingeconomics.com/nigeria/imports/netherlands/natural-magnesium-carbonate-fused-magnesia-magnesium-oxid

Thomas, D. G. (2007). *Development of a process route for the beneficiation of koton-karfe iron ore deposit.* Ahmadu Bello University, Zaria, Metallurgical Engineering. Zaria: unpublished

Toma, M., Chiuta, F., Vintila, M., Burlacu, R., Hoza, D., Popescu, S., & Moise, D. (2021). Bio Cultivation and Capitalization of Premial Strawberries in Condition of Nowadays Climate Change. *World Journal of* Pharmaceutical Research. 10 (14), 101-129.

Umaru, M., Aris, M. I., Munnir, S. M., Aliyu A. M., Aberuagba, F. and Joseph, I. A. (2016). Statistical Optimization of Biolubricant Production from Jatropha Curcas Oil using Trimethylolpropane as a Polyol. *Proceedings of the World Congress on Engineering and Computer Science.*

Walton, R. (2005). Zinc cementation. *Developments in Mineral Processing*, *15*, 589-601.

Warren, J. (2000). Dolomite: occurrence, evolution and economically important associations. *Earth-Science Reviews*, *52*(1-3), 1-81.

Web book in hydrometallurgy, (2012). Available: www.biomine.skelleftea.se/ biomine/leaching/letheo_11.htm, (2012, April 29).

Whitaker, F. F., & Xiao, Y. (2010). Reactive transport modeling of early burial dolomitization of carbonate Plate forms by geothermal convection. *AAPG bulletin*, *94*(6), 889-917.

Wulandari, W., Subagjo, A. R., & Istiadi, P. (2015). Characterisation and Treatment of Dolomite as Raw Material for Producing Magnesium Metal. *Sustainable Energy and Mineral Processing for National Competitiveness.* 12-13 October, 2015.

Xiaoli, L., Sun, Q., Yuan, H., Li, X., Chu, Y., Ruan, Y. & Lian, B. (2016). A feasible way to increase carbon sequestration by adding dolomite and K-feldspar to soil. *Cogent Geoscience*, *2*(1), 120-124.

Yildirim, M. (2008). Dissolution kinetics of Icel-Aydincik dolomite in hydrochloric acid. *South African Journal of Chemistry*, *61*, 127-132.

Yildirim, M., & Akarsu, H. (2010). Preparation of magnesium oxide (MgO) from dolomite by leach-precipitation-pyrohydrolysis process. *Physicochemical Problems of Mineral Processing*, *44*, 257-272.

Younesi, S. R., Alimadadi, H., Alamdari, E. K., & Marashi, S. P. H. (2006). Kinetic mechanisms of cementation of cadmium ions by zinc powder from sulphate solutions. *Hydrometallurgy*, *84*(3-4), 155-164.

Yu, Y. (2015). *Electrowinning of Zinc for the anode of Rechargeable Hybrid Aqueous Batteries (ReHABs)*. Master's thesis, University of Waterloo.

Zvir, Y., Pimentel, C., & Pina, C. M. (2021). The Effect of Stoichiometry, Mg-Ca Distribution, and Iron, Manganese, and Zinc Impurities on the Dolomite Order Degree: A Theoretical Study. Minerals, 11(7), 702.

APPENDICES

APPENDIX-A

Kinetics Plots for NAR

Appendix-A1: Fraction of dolomite that reacted at various reaction times and HNO_3 concentration

Time (Min)	Fractions of dissolved dolomite at different concentration					
	0.5 moldm^{-3}	**1 moldm^{-3}**	**1.2 moldm^{-3}**	**1.5 moldm^{-3}**	**2 moldm^{-3}**	**2.5 moldm^{-3}**
10	0.57	0.65	0.75	0.853	0.9	0.93
20	0.613	0.71	0.812	0.92	0.963	0.98
30	0.631	0.727	0.836	0.95	0.98	0.984
40	0.652	0.73	0.867	0.965	0.983	0.987
50	0.682	0.747	0.884	0.973	0.987	0.987
60	0.696	0.77	0.893	0.98	0.99	0.995

At a temperature of 55 ^{O}C

Appendix-A2: Dolomite Fractions that Reacted at Various Reaction Times and Temperatures

Time (Min)	Fractions of dissolved dolomite at the different reaction temperatures				
	30 ^{O}C	**40 ^{O}C**	**50 ^{O}C**	**60 ^{O}C**	**70 ^{O}C**
0	0	0	0	0	0
20	0.777	0.95	0.967	0.983	0.993
30	0.89	0.96	0.983	0.993	0.993
40	0.9367	0.983	0.987	0.993	0.993
50	0.95	0.987	0.99	0.993	0.993
60	0.983	0.99	0.992	0.993	0.993

At concentration of 2.2 moldm^{-3}

Appendix-A3: Film diffusion control at the different acid concentrations for NAR

Time (Min)	Fractions of Dissolved Dolomite at Different Concentrations					
	0.5 $moldm^{-3}$	1 $moldm^{-3}$	1.2 $moldm^{-3}$	1.5 $moldm^{-3}$	2 $moldm^{-3}$	2.5 $moldm^{-3}$
20	0.613	0.71	0.812	0.92	0.963	0.98
30	0.631	0.727	0.836	0.95	0.98	0.984
40	0.652	0.73	0.867	0.965	0.983	0.987
50	0.682	0.747	0.884	0.973	0.987	0.987
60	0.696	0.77	0.893	0.98	0.99	0.995
Slope	0.00220	0.00140	0.00210	0.00140	0.00060	0.00030
R^2	0.9782	0.8727	0.9198	0.8214	0.6721	0.6235

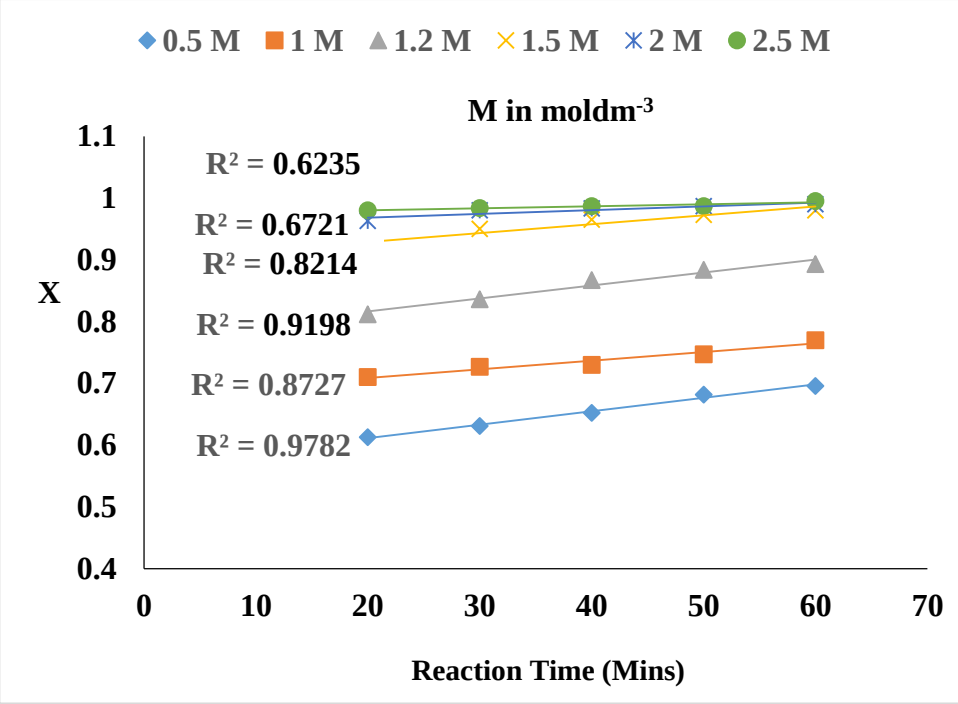

Appendix-A4: Plot of film diffusion control at different acid concentration for NAR

Appendix-A5: Chemical reaction control at different acid concentration for NAR

Time (Min)	Fractions of Dissolved Dolomite at Different Concentration					
	0.5 moldm^{-3}	1 moldm^{-3}	1.2 moldm^{-3}	1.5 moldm^{-3}	2 moldm^{-3}	2.5 moldm^{-3}
20	0.2712	0.3381	0.4271	0.5691	0.6667	0.7285
30	0.2827	0.3513	0.4526	0.6316	0.7285	0.748
40	0.2966	0.3536	0.4895	0.6729	0.7428	0.7648
50	0.3174	0.3593	0.5123	0.7	0.7648	0.7648
60	0.3246	0.3675	0.5252	0.7285	0.7845	0.829
R^2	0.9829	0.9482	0.9749	0.9154	0.9656	0.8327
Slope	0.00142	0.00067	0.00256	0.00387	0.00272	0.00218

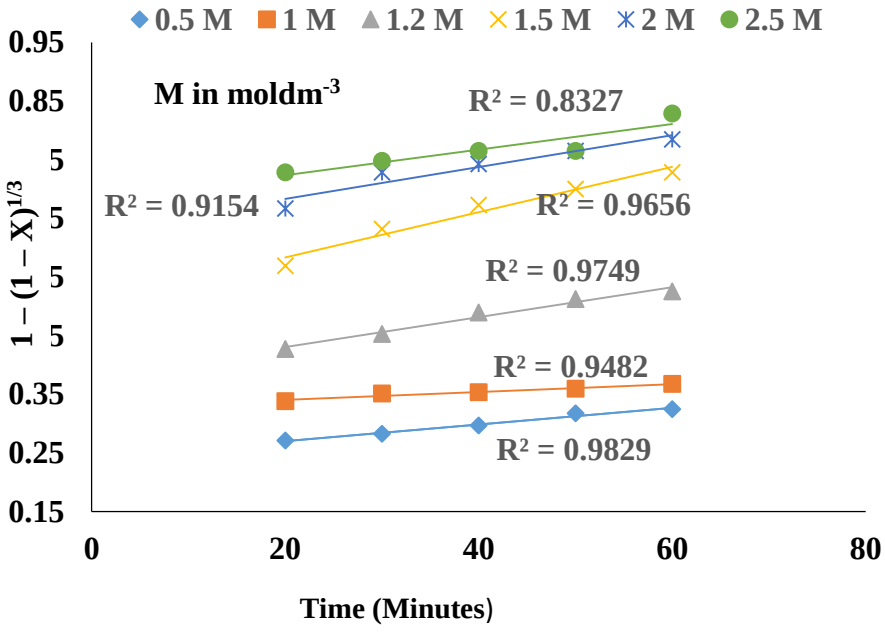

Appendix-A6: Plot of chemical reaction control at different acid concentration for NAR

Appendix-A7: Product layer diffusion control at different acid concentration for NAR

	Fraction of Dissolved Dolomite at Different Concentration					
	0.5	**1**	**1.2**	**1.5**	**2**	**2.5**
Time	**moldm^{-3}**	**moldm^{-3}**	**moldm^{-3}**	**moldm^{-3}**	**moldm^{-3}**	**moldm^{-3}**
20	0.1808	0.2658	0.3915	0.6031	0.7409	0.819
30	0.19467	0.2836	0.4292	0.6929	0.819	0.8415
40	0.2384	0.2868	0.4844	0.749	0.8357	0.8602
50	0.2384	0.2946	0.5185	0.784	0.8602	0.8602
60	0.2517	0.306	0.5379	0.819	0.8808	0.8808
slop (K)	0.00124	0.00142	0.00283	0.00351	0.00392	0.00394
R^2	0.8924	0.9502	0.9753	0.9535	0.9363	0.9363

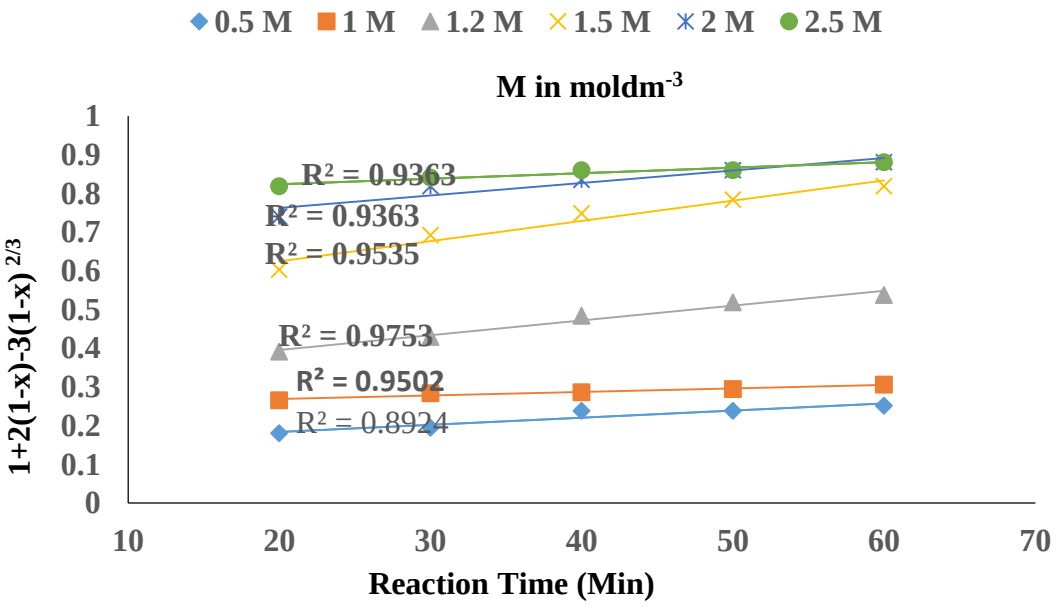

Appendix-A8: Plot of product layer diffusion control at different acid concentration for NAR

Appendix-A9: Film diffusion control at different temperature for NAR

Time (Mins)	Fractions of Dissolved Dolomite at Different Temperatures				
	30 ^{O}C	40 ^{O}C	50 ^{O}C	60 ^{O}C	70 ^{O}C
20	0.777	0.95	0.967	0.983	0.993
30	0.89	0.96	0.983	0.993	0.993
40	0.9367	0.983	0.987	0.993	0.993
50	0.95	0.987	0.99	0.993	0.993
60	0.983	0.99	0.992	0.993	0.993
Slope	0.00472	0.00107	0.00057	0.0002	0.0000
R^2	0.8670	0.8959	0.8147	0.5000	0.000

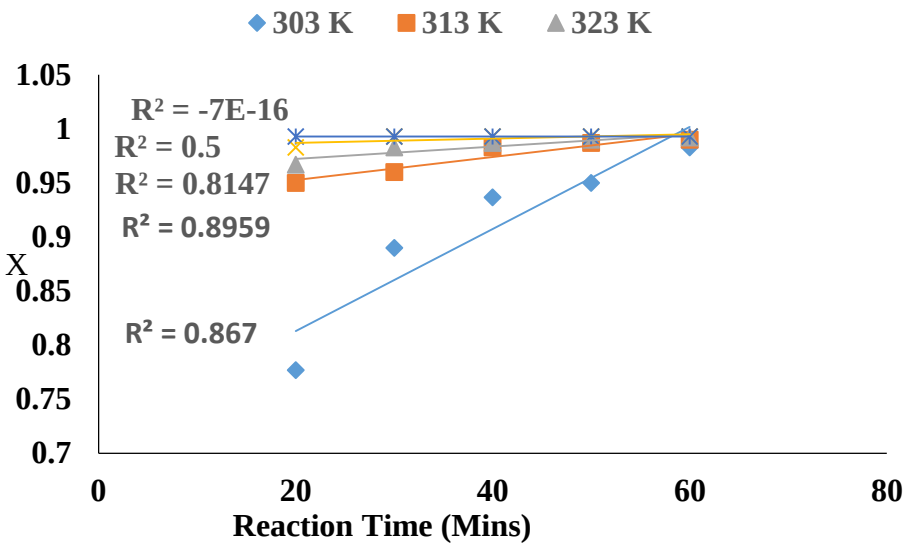

Appendix-A10: Plot of film diffusion control at different temperature for NAR

Appendix-A11: Chemical reaction control at different temperature for NAR

Time (Mins)	Fractions of Dissolved Dolomite at Different Temperature			
	30 ^{O}C	40 ^{O}C	50 ^{O}C	60 ^{O}C
20	0.3943	0.6316	0.6792	0.7428
30	0.5208	0.658	0.7428	0.8087
40	0.5958	0.7428	0.7648	0.8087
50	0.6316	0.7648	0.7845	0.8087
60	0.7428	0.7845	0.8000	0.8087
Slop (K)	0.00808	0.00413	0.00283	0.00132
R^2	0.9687	0.9313	0.9035	0.5000

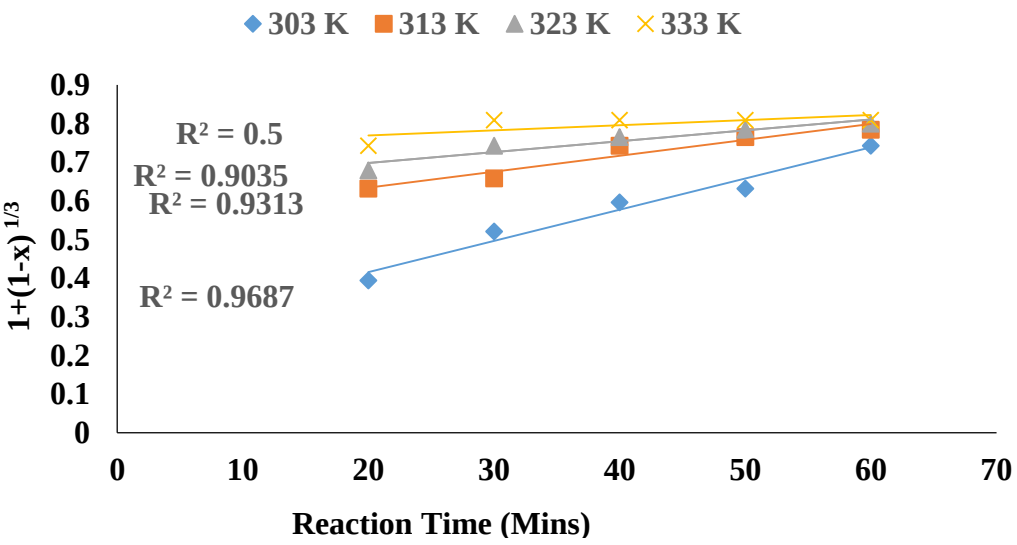

Appendix-A12: Plot of chemical reaction control at different temperature for NAR

Appendix-A13: Product layer diffusion control at different temperature for NAR

Time (Mins)	Fractions of Dissolved Dolomite at Different Temperature			
	30 ^{O}C	40 ^{O}C	50 ^{O}C	60 ^{O}C
20	0.3428	0.6938	0.7574	0.8357
30	0.4813	0.7292	0.8057	0.8804
40	0.6427	0.8057	0.8602	0.9042
50	0.6929	0.8602	0.8808	0.9042
60	0.8357	0.8808	0.8960	0.9042

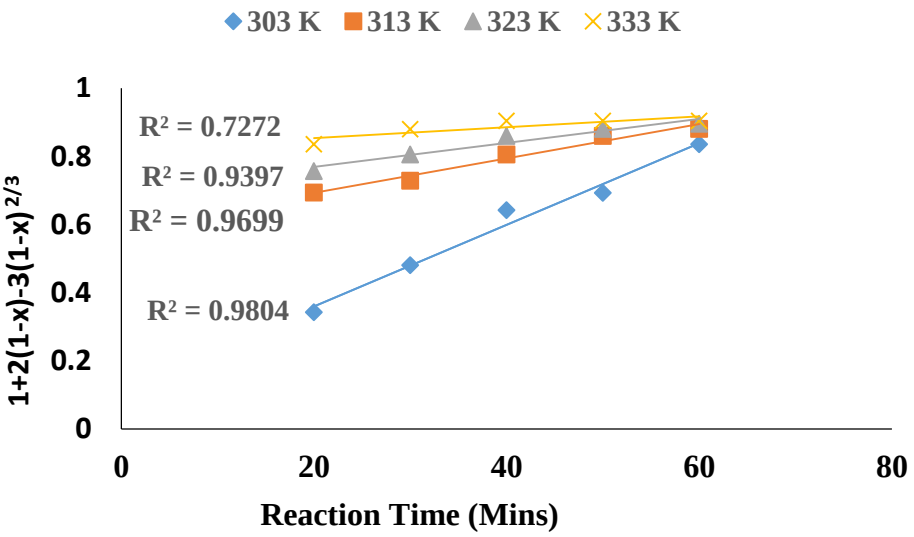

Appendix-A14: Plot of product layer diffusion control at different temperature for NAR

Appendix-A15: Natural Logarithm of HNO_3 Concentration and Apparent Rate Constant

Concentration[HNO_3]	ln[HNO_3]	K	InK
0.5	-0.6932	0.00124	-6.6899
1	0.0000	0.00142	-6.5568
1.2	0.1823	0.00283	-5.86724
1.5	0.4055	0.00351	-5.65354
2	0.6931	0.00392	-5.54148

Appendix-A16: Activation Energy for Dissolution of Dolomite in HNO_3

	T (K)	1/T	Lnk
	303	0.0033	-6.6899
	313	0.0032	-6.5568
	323	0.0031	-5.86724
	333	0.003	-5.65354
	342	0.0029	-5.54148
		slope	**-3200.1**

APPENDIX-B:

Kinetics Data from HPASR

Appendix-B1: Effect of concentration on dissolution of dolomite in HCl- $HClO_4$

	Fractions of Dissolved Dolomite					
Time (Min)	0.5 $moldm^{-3}$	1 $moldm^{-3}$	1.2 $moldm^{-3}$	1.5 $moldm^{-3}$	2 $moldm^{-3}$	2.5 $moldm^{-3}$
0	0	0	0	0	0	0
10	0.61	0.7	0.74	0.878	0.93	0.95
20	0.72	0.82	0.85	0.97	0.972	0.983
30	0.733	0.861	0.87	0.983	0.987	0.987
40	0.743	0.873	0.887	0.985	0.989	0.993
50	0.752	0.882	0.899	0.988	0.991	0.993
60	0.763	0.882	0.899	0.988	0.993	0.993

at temperature of 55 ^oC

Appendix-B2: Effect of temperature on dissolution of dolomite in HCl- $HClO_4$

	Fractions of Dissolved Dolomite at Different Temperature				
Time (Min)	30 ^OC	40 ^OC	50 ^OC	60 ^OC	70 ^OC
0	0	0	0	0	0
20	0.830	0.900	0.970	0.987	0.995
40	0.917	0.970	0.986	0.995	0.995
50	0.947	0.977	0.988	0.995	0.995
60	0.960	0.989	0.993	0.995	0.995
70	0.972	0.992	0.994	0.995	0.995

Apendix-B3: Film diffusion control at different HCl-$HClO_4$ concentration

Time (Min)	Fraction of dissolved dolomite at different concentration					
	0.5 $moldm^{-3}$	1 $moldm^{-3}$	1.2 $moldm^{-3}$	1.5 $moldm^{-3}$	2 $moldm^{-3}$	2.5 $moldm^{-3}$
20	0.72	0.82	0.85	0.97	0.972	0.983
30	0.733	0.861	0.87	0.983	0.987	0.987
40	0.743	0.873	0.887	0.985	0.989	0.993
50	0.752	0.882	0.899	0.988	0.991	0.993
60	0.763	0.882	0.899	0.988	0.993	0.993
Slope	0.00249	0.00317	0.00274	0.00173	0.00107	0.00072
R^2	0.9961	0.7865	0.7545	0.7545	0.7579	0.7972

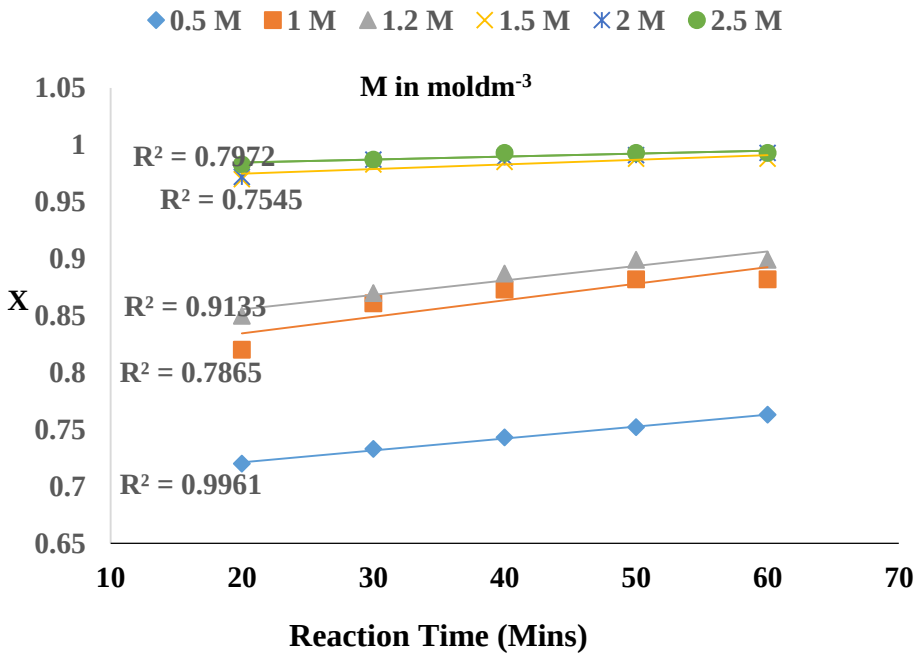

Apendix-B4: Plot of film diffusion control at different HCl-$HClO_4$ concentration

Apendix-B5: Chemical reaction control at different HCl-$HClO_4$ concentration

Time (Min)	Fraction of dissolved dolomite at different concentration					
	0.5 moldm^{-3}	1 moldm^{-3}	1.2 moldm^{-3}	1.5 moldm^{-3}	2 moldm^{-3}	2.5 moldm^{-3}
20	0.3457	0.4353	0.4686	0.6892	0.6963	0.7428
30	0.346	0.482	0.4934	0.7428	0.7648	0.7683
40	0.3642	0.4973	0.5165	0.7533	0.7776	0.8087
50	0.3717	0.5095	0.5343	0.771	0.792	0.8087
60	0.3811	0.5095	0.5343	0.771	0.8087	0.8087
R^2	0.9453	0.8108	0.9245	0.8106	0.8495	0.7982
Slope	0.00097	0.00176	0.00172	0.00192	0.00252	0.00172

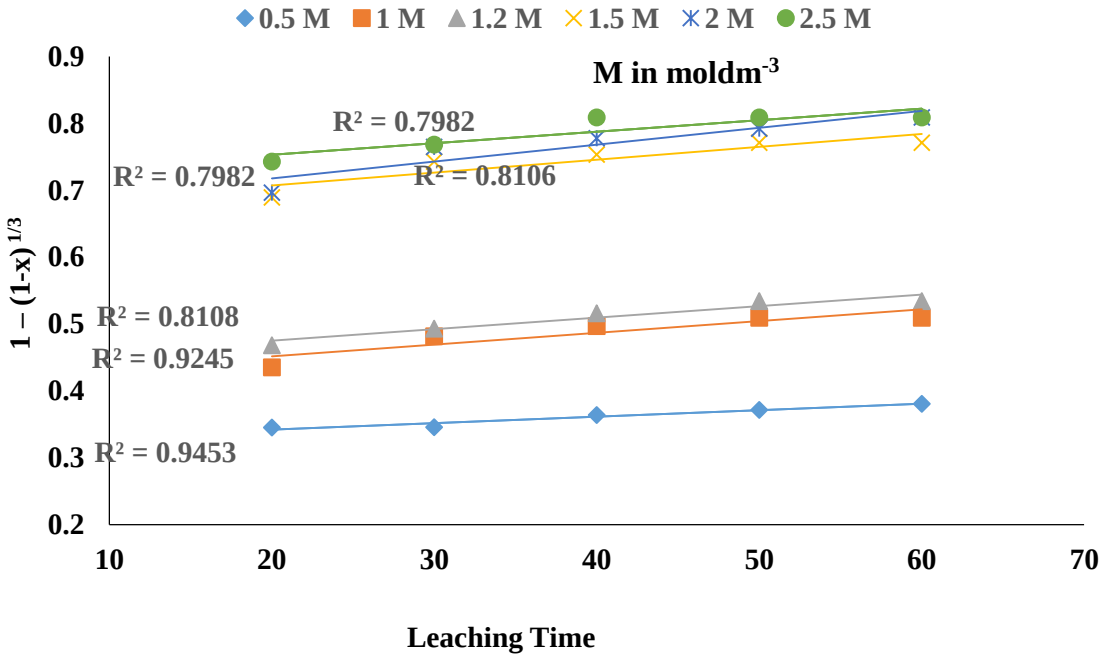

Apendix-B6: Plot of chemical reaction control at different HCl-$HClO_4$ concentration

Apendix-B7: Product layer diffusion control at different HCl-$HClO_4$ concentration

Time (Mins)	Fraction of dissolved dolomite at different concentration					
	0.5 $moldm^{-3}$	1 $moldm^{-3}$	1.2 $moldm^{-3}$	1.5 $moldm^{-3}$	2 $moldm^{-3}$	2.5 $moldm^{-3}$
20	0.2761	0.4034	0.4531	0.7704	0.7794	0.8357
30	0.2901	0.473	0.5162	0.8357	0.8602	0.8602
40	0.3014	0.4961	0.5249	0.8476	0.8736	0.9042
50	0.3119	0.5143	0.5514	0.8668	0.8882	0.9042
60	0.3251	0.5143	0.5514	0.8668	0.9042	0.9042
slop (K)	0.00112	0.00263	0.00232	0.00224	0.00278	0.00181
R^2	0.9977	0.8287	0.8116	0.7926	0.7996	0.7996

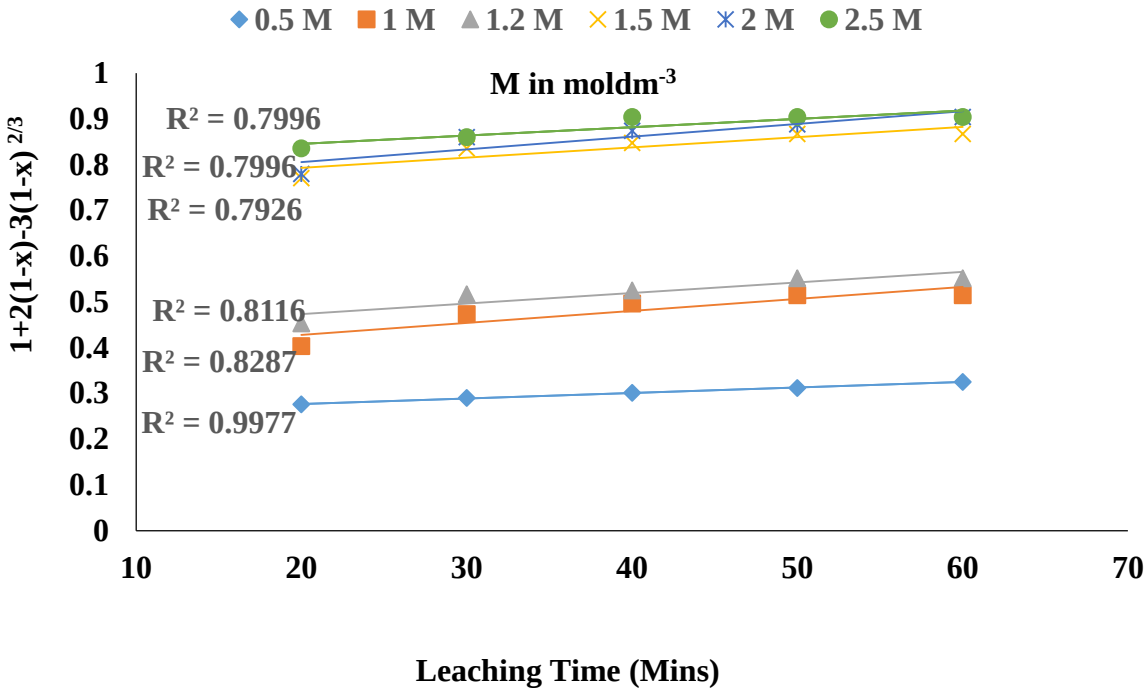

Apendix-B8: Plot of product layer diffusion control at different HCl-$HClO_4$ concentration

Apendix-B9: Film diffusion control at different temperature for HPASR

Time (Mins)	Fraction of dissolved dolomite at different temperature				
	30 ^{O}C	40 ^{O}C	50 ^{O} C	60 ^{O} C	70 ^{O} C
20	0.83	0.9	0.97	0.987	0.995
30	0.917	0.97	0.986	0.995	0.995
40	0.947	0.977	0.988	0.995	0.995
50	0.96	0.989	0.993	0.995	0.995
60	0.972	0.992	0.994	0.995	0.995
Slope	0.00327	0.00203	0.00055	0.00016	0.0000
R^2	0.8221	0.7233	0.8114	0.5000	0.0000

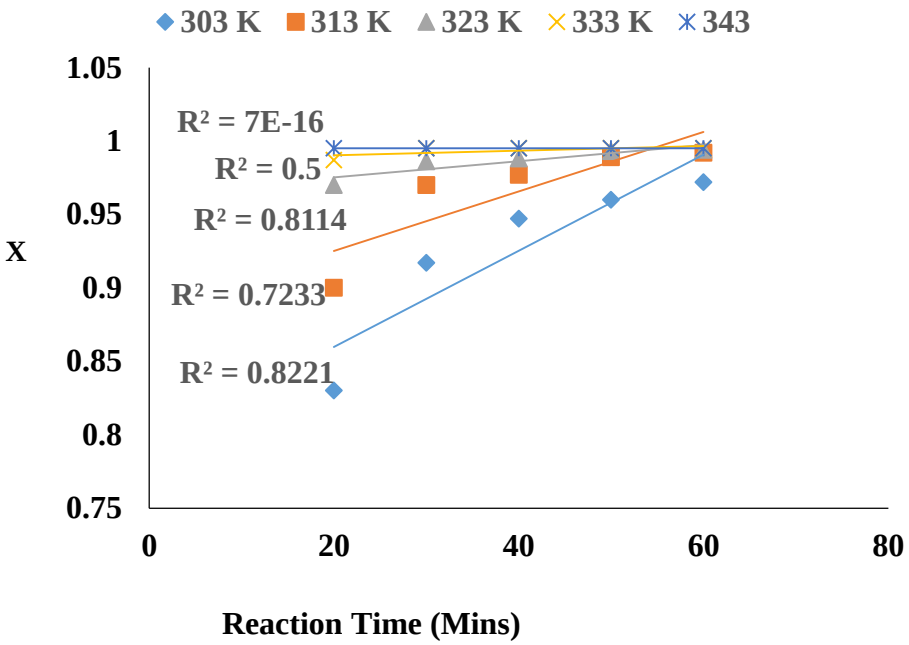

Apendix-B10: Plot of film diffusion control at different temperature for HPASR

Apendix-B11: Chemical reaction control at different temperature for HPASR

Time (Mins)	Fraction of dissolved dolomite at different temperature			
	30 ^{O}C	40 ^{O} C	50 ^{O}C	60 ^{O}C
20	0.4460	0.5358	0.6892	0.7648
30	0.5638	0.6892	0.759	0.829
40	0.62433	0.7156	0.771	0.829
50	0.6580	0.7776	0.8087	0.829
60	0.6963	0.8000	0.8183	0.829
Slope	0.00595	0.00617	0.00308	0.00128
R^2	0.9254	0.8791	0.9047	0.5000

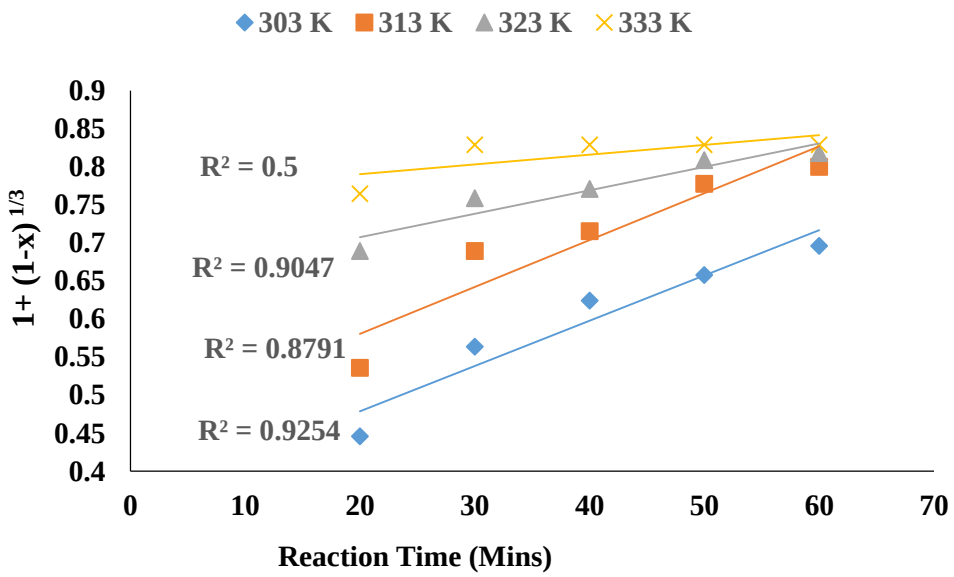

Apendix-B12: Plot of chemical reaction control at different temperature for HPASR

Apendix-B13: Product layer diffusion control at different temperature for HPASR

Time (Mins)	Fraction of dissolved dolomite at different temperature			
	30 ^{O}C	40 ^{O}C	50 ^{O}C	60 ^{O}C
20	0.4194	0.5537	0.7704	0.8602
30	0.5952	0.7704	0.8538	0.9223
40	0.6828	0.8034	0.8668	0.9223
50	0.7292	0.8736	0.9042	0.9223
60	0.7794	0.896	0.913	0.9223
Slop	0.00854	0.00788	0.00336	0.00124
R^2	0.9130	0.8379	0.8757	0.5000

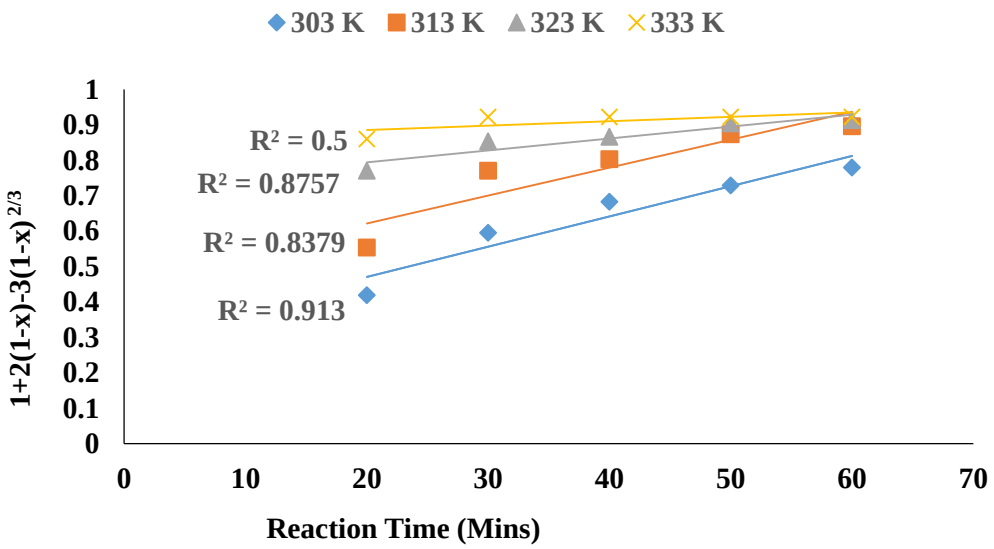

Apendix-B14: Plot of product layer diffusion control at different temperature for HPASR

Apendix-B15: Natural logarithm of HCl-$HClO_4$ concentration and apparent rate constant

K	Conc.[HCl-$HClO_4$]	ln[HCl-$HClO_4$]	InK
0.00097	0.5	-0.6932	-6.9434
0.00176	1	0.000	-6.3430
0.00172	1.2	0.1823	-6.3637
0.00192	1.5	0.4055	-6.2565
0.00252	2	0.6932	-5.9835
Slope			**0.6583**

Apendix-B16: Activation energy for dissolution of dolomite in HCl-$HClO_4$

T (K)	1/T	lnk
303	0.0033	-6.9434
313	0.0032	-6.3430
323	0.0031	-6.3637
333	0.003	-6.2565
342	0.0029	-5.9835
	Slope	-2006.3

APPENDIX-C:

AAS Precipitation Data from NAR

Run	Conc. of $Ca(OH)_2$ (%)	Time (Mins)	Mg ion Concentration (mg/l)	Mg ion in PPT (%)	Ca ion Concentration (mg/l)	Ca ion in PPT (%)
			Initial Conc = 9.48		Initial Conc. 12.97	
1	32	2	0.205716	97.83	12.68855	12.68855
2	22	5	2.017344	78.72	10.20998	10.20998
3	29	5	1.41252	85.1	11.03747	11.03747
4	34	8	0.112812	98.81	12.81566	12.81566
5	24	2	2.33682	75.35	9.772895	9.772895
6	29	5	1.422	85	11.0245	11.0245
7	29	9	0.226572	97.61	12.66002	12.66002
8	29	5	1.40304	85.2	11.05044	11.05044
9	29	5	1.410624	85.12	11.04006	11.04006
10	29	5	1.422	85	11.0245	11.0245
11	36	5	1.934868	79.59	10.32282	10.32282
12	24	8	1.585056	83.28	10.80142	10.80142
13	29	1	2.388012	74.81	9.702857	9.702857

APPENDIX-D:

AAS Precipitation Data from HPASR

Run	Conc. of $Ca(OH)_2$ (%)	Time (Mins	Mg ion Concentration (mg/l) Initial Con: 9.21	Mg ion in PPT (%)	Ca ion Concentration (mg/l) Initial Con: 12.91	Ca ion in PPT (%)
1	36	5	0.97634	97.6341	12.6046	2.3659
2	32	8	0.85839	85.8385	11.0818	14.162
3	36	1	0.80719	80.7188	10.4208	19.2812
4	39	2	0.90279	90.279	11.6550	9.7210
5	36	5	0.975418	97.5418	12.5927	2.4582
6	31	5	0.72810	72.81	9.39977	27.190
7	40	5	0.96611	96.6113	12.4725	3.3887
8	36	5	0.97428	97.4278	12.5779	2.5722
9	32	2	0.80353	80.3529	10.3736	19.647
10	39	8	0.92806	92.8057	11.9812	7.1943
11	36	5	0.97353	97.3531	12.5683	2.6469
12	36	10	0.82587	82.5874	10.66203	17.413
13	36	5	0.975215	97.5215	12.59003	2.4785